ABSTRACT

Title of Dissertation: CHARACTERIZATION AND ANALYSIS OF FLUIDIC ARTIFICIAL MUSCLES

Jonathan Chambers
Doctor of Philosophy, 2021

Dissertation Directed By: Professor Norman M. Wereley
Department of Aerospace Engineering

Fluidic artificial muscles (FAMs) are a form of soft actuator that have been applied to an expanding number of applications, due to their unique characteristics such as low weight, simple construction, inherent compliance, and high specific force and specific work capabilities. With energy sourced from a pressurized fluid, contractile FAMs provide a uniaxial contractile force, while their morphing geometry allows them to contract in length. In a design environment where actuators have tight spatial requirements and must provide precise force and position control, it is becoming more important than ever to have accurate mathematical representations of FAM actuation behavior and geometric characteristics to ensure their successful implementation. However, geometric models and force analyses for FAMs are still relatively crude. Geometric models of FAMs assume a cylindrical geometry, the accuracy of which is suspect because there are no documented methods for effectively measuring FAM shape. Actuation force analyses are also relatively inaccurate unless they are adjusted to fit to experimental response data. Research has continu-

ally pursued methods of improving the predictive performance of these analyses by investigating the complex working mechanisms of FAMs.

This research improves these analyses by first, making improvements to the experimental characterization of a FAM's actuation response, and then using the more comprehensive data results to test long-held modeling assumptions. A quantitative method of measuring FAM geometry is developed that provides 0.004 in/pixel resolution measurements throughout a characterization test. These measurements are then used to test common assumptions that serve as sources of uncertainty: the cylindrical approximation of FAM geometry, and assumption that the FAM's braid is inelastic. Once these sources of modeling error are removed, the model's performance is then tested for potential improvements. Results from this research showed that the cylindrical approximation of the FAM's geometry resulted in overestimations of the FAM's average diameter by 4.7%, and underestimations of the FAM's force by as much as 37%. The inelastic braid assumption resulted in a maximum 4% underestimation of average diameter and a subsequent 5% overestimation in force, while the use of softer braid materials was found to have the potential for much larger effects (30% underestimation in diameter, 70% overestimation in force). With subsequent adjustments made to the force model, the model was able to achieve a fit with a mean error of only 2.8 lbf (0.3% of maximum force).

This research demonstrates improvements to the characterization of a FAM's actuation response, and the use of this new data to improve the fidelity of existing FAM models. The demonstrated characterization methods can be used to clearly define a FAM's geometry to aid in the effective design and implementation of a

FAM-actuated mechanism, or to serve as a foundation for further investigation into the working mechanisms and development of FAMs.

CHARACTERIZATION AND ANALYSIS OF FLUIDIC ARTIFICIAL MUSCLES

by

Jonathan Michael Chambers

Dissertation submitted to the Faculty of the Graduate School of the
University of Maryland, College Park in partial fulfillment
of the requirements for the degree of
Doctor of Philosophy
2021

Advisory Committee:
Dr. Norman Wereley, Chair/Advisor
Dr. David Akin
Dr. Craig Carignan
Dr. Ross Miller
Dr. Anindo Roy

Acknowledgments

I would first like to acknowledge the support of my advisor, Dr. Wereley, for his guidance through a wide-range of projects. The experience I garnered through these projects will surely prove to be invaluable. I would also like to thank Dr. Fourney for the opportunities he provided me at the beginning of my graduate studies.

I would like to thank Dr. Akin, Dr. Carignan, Dr. Miller, and Dr. Roy for their support as my doctoral committee members. I would like to acknowledge some of the external funding that supported my research, including: NAVAIR–Patuxent River (Exoskeleton project: Research and Educational Development Program N00421-13-2-0001); the Office of Naval Research Basic Research Challenge (SEASTAR project: ONR BAA Announcement N00014-16-S-BA10); and, the Army (SBIR Topic A17-115, Contract Number: W56HZV-17-C-0178). I would also like to thank Dr. Carignan, Dr. Kothera, and Dr. Choi for assisting me through these projects, and Mike Perna for his machinist expertise and guidance.

I would also like to thank many of the fellow graduate students I spent time with through the years. Special thanks to Ami, Andrew, Caitlin, Chinonso, Frank, Jacek, Rebecca, Sai, and Steve, for their company in the lab, and for the insights they provided me towards my research. I would like to especially thank Tom for passing all of his knowledge of FAMs down to me.

And finally, I would like to thank my family and friends who have encouraged me throughout this long and arduous process. I especially would like to thank my Dad, my Sister, and Rebecca for their support.

Table of Contents

Acknowledgements ii

List of Tables viii

List of Figures x

List of Abbreviations xv

1 Introduction 1
- 1.1 Problem Statement . . . 1
- 1.2 Fluidic Artificial Muscle Actuators . . . 3
  - 1.2.1 Background . . . 4
    - 1.2.1.1 History . . . 6
    - 1.2.1.2 Working Mechanism . . . 10
  - 1.2.2 Experimental Characterization . . . 11
  - 1.2.3 Modeling . . . 13
    - 1.2.3.1 Geometric Model . . . 15
    - 1.2.3.2 Actuation Force Model . . . 17
    - 1.2.3.3 Review of Literature . . . 19
- 1.3 Contributions of Dissertation . . . 22
- 1.4 Overview of Dissertation . . . 26

2 Design, Fabrication, and Failure Testing of a Swaged End-fitting FAM 29
- 2.1 Introduction . . . 29
  - 2.1.1 Background . . . 33
- 2.2 Component Descriptions . . . 35
  - 2.2.1 Internal Fitting . . . 36
  - 2.2.2 Swage Tube . . . 39
  - 2.2.3 Bladder . . . 40
  - 2.2.4 Braid . . . 42
  - 2.2.5 Epoxy . . . 44
- 2.3 Determination of FAM Component Sizing . . . 45
  - 2.3.1 Sizing of FAM to Achieve Desired Response . . . 45

2.3.1.1 Models for Estimation of FAM Radial Expansion and Force Response . . . 47
2.3.1.2 FAM Force Response Approximation . . . 49
2.3.1.3 FAM Contraction Approximation . . . 50
2.3.1.4 FAM Component Sizing Constraints . . . 51
2.3.1.5 Selection of Target FAM Sizing . . . 54
2.3.2 Sizing of Components for Swaged end-fittings . . . 55
2.3.2.1 Steps for Sizing Components of Swaged end-fitting . . . 56
2.3.3 Final Sizing of FAM . . . 61
2.4 FAM Method of Fabrication . . . 61
2.4.1 Material Preparation . . . 63
2.4.2 Assembly . . . 67
2.4.3 Swaging . . . 69
2.4.4 Finishing Process . . . 70
2.4.5 Modification to swaging process . . . 72
2.5 Testing Swaged FAMs . . . 76
2.5.1 Characterization Test . . . 77
2.5.2 Ultimate Tensile Failure Test . . . 78
2.5.3 Burst Test . . . 81
2.5.4 Extended Use Failure . . . 82
2.5.5 Subsequent Improvements to end-fitting . . . 84
2.6 Conclusion . . . 86

3 Improvements in FAM Characterization Through Accurate Control of Pressure 88
3.1 Introduction . . . 88
3.1.1 Basis of Work . . . 91
3.2 Experimental Test Setup . . . 93
3.2.1 FAM Test Specimens . . . 94
3.2.2 Pressure Systems . . . 95
3.2.2.1 Pneumatic Pressure System . . . 99
3.2.2.2 Hydraulic Pressure System . . . 99
3.2.3 Pressure System Control . . . 101
3.2.3.1 Pneumatic Pressure Control . . . 103
3.2.3.2 Hydraulic Pressure Control . . . 104
3.2.4 Controller Tuning . . . 105
3.3 Results . . . 108
3.3.1 Pressure Control Results . . . 109
3.3.2 Characterization Results . . . 110
3.3.3 Modeling Results . . . 111
3.4 Conclusion . . . 114

4 A Photogrammetric Method for Measuring FAM Shape 116
4.1 Introduction . . . 116
4.2 Test Methods . . . 123
4.2.1 Image Acquisition . . . 124
4.2.2 Image Analysis . . . 125
4.2.2.1 Color Model . . . 125
4.2.2.2 Boundary Detection . . . 128
4.3 Procedure . . . 132
4.3.1 Image Acquisition . . . 133
4.3.2 Image Analysis . . . 137
4.3.2.1 Step 1 . . . 140
4.3.2.2 Step 2 . . . 141
4.3.2.3 Step 3 . . . 141
4.3.2.4 Step 4 . . . 142
4.3.2.5 Step 5 . . . 142
4.3.3 Characterization Test Parameters . . . 143
4.4 Results . . . 146
4.4.1 Calibration . . . 146
4.4.2 Force-Contraction Response . . . 147
4.4.3 Shape Profile Characterization . . . 148
4.5 Analysis . . . 151
4.5.1 Shape Profile Analysis . . . 152
4.5.1.1 Profile Average Diameter . . . 152
4.5.1.2 Profile Fourier Series Fit . . . 153
4.5.1.3 Comparison to Previous Cylindrical Profile Estimates 157
4.5.2 Volume Approximation . . . 160
4.5.3 Testing of Different FAMs . . . 164
4.6 Conclusion . . . 169

5 Investigation of the Inelastic Braid Modeling Assumption 172
5.1 Introduction . . . 172
5.2 Experimental Testing . . . 174
5.2.1 Description of Tested FAM . . . 175
5.2.2 Characterization of the FAM's Actuation . . . 176
5.2.3 Characterization of the FAM's Braid . . . 176
5.3 Analysis of Braid Elasticity Using Measurements of FAM . . . 179
5.3.1 Analysis of Measured Elasticity Values . . . 182
5.4 The Effect of Braid Elasticity on Geometry and Actuation Force . . . 185
5.4.1 Effects of Elasticity with Kevlar-49 Braid . . . 186
5.4.2 Estimated Effects of Lower Stiffness Braid Materials . . . 188
5.5 Conclusion . . . 192

6 Investigation of the Cylindrical Approximation Assumption 194
6.1 Introduction . . . 194
6.2 Geometric Dimensions Definitions . . . 198
6.2.1 Estimated Dimensions – Cylindrical Approximation . . . 200
6.2.2 Measured Dimensions . . . 202
6.2.3 Measured Dimensions – Cylindrical Approximation . . . 203
6.3 Analysis of the Cylindrical and Measured Geometries . . . 204
6.3.1 Comparison of Braid Dimensions . . . 205
6.3.2 Comparison of Bladder Dimensions . . . 207
6.3.2.1 Comparison of Bladder Thickness . . . 209
6.3.2.2 Comparison of Longitudinal Strain . . . 211
6.3.2.3 Comparison of Circumferential Strain . . . 214
6.4 Effect of Geometry Profile on Force Model Results . . . 217
6.4.1 Gaylord Actuation Force Term (F_G) . . . 219
6.4.2 Bladder Actuation Force . . . 220
6.4.2.1 Bladder Stiffness Characterization . . . 221
6.4.2.2 Longitudinal Bladder Force Term ($F_{bld,z}$) . . . 225
6.4.2.3 Circumferential Bladder Force Term ($F_{bld,c}$) . . . 227
6.4.2.4 Combined Effect of Bladder Forces . . . 230
6.4.3 Overall Effect of Geometry on Estimated Force . . . 231
6.4.4 Comparison To Experimental Data . . . 233
6.5 Conclusion . . . 238

7 Modeling Improvements 242
7.1 Introduction . . . 242
7.2 Background on Model . . . 244
7.2.1 Baseline Modeling Results . . . 249
7.3 Model Improvements . . . 253
7.4 Model Results and Analysis . . . 258
7.4.1 Comparison of Experimental and Model Values of E_n . . . 259
7.4.2 Parametric Analysis for Optimal Model Fit . . . 261
7.4.2.1 Effect of Number of E_n Terms Used . . . 262
7.4.2.2 Effect of Variation of E_n with Pressure . . . 265
7.4.2.3 Best-fit Model Selection . . . 266
7.5 Conclusion . . . 269

8 Conclusion 273
8.1 Summary of Key Work and Conclusions . . . 273
8.1.0.1 FAM Design and Fabrication . . . 273
8.1.0.2 Characterization Improvements - Pressure Control . 274
8.1.0.3 Characterization Improvements – Profile Measurements . . . 275
8.1.0.4 Testing the Inelastic Braid Assumption . . . 276
8.1.0.5 Testing the Cylindrical Approximation . . . 277
8.1.0.6 Analysis of Improved Actuation Model . . . 278

8.1.1 Contributions to Literature 279
8.1.2 Future Work 282

Bibliography 286

List of Tables

1.1 Comparison of direct-drive actuator technologies 6

2.1 List of swaged and comparable Flexo crimped FAMs, and their specifications for comparison to the 7/8 inch FAM developed in this work 33
2.2 Braid thickness, t, and range of achievable diameters, D, and range of braid angles, θ, for Kevlar braids of three nominal braid sizes (defined in 45 deg. braid orientation) (Source: Soller Composites, LLC) 52
2.3 The initial braid angle for each combination of FAM size and nominal braid diameter. Red entries are at the threshold of the achievable range of the braid, while blank entries are non-feasible combinations (Reference Table 2.2) 52
2.4 Construction of the 7/8 in diameter swaged FAM 61
2.5 Specifications of swaged FAMs used for testing 78

3.1 Construction and specifications of the 3/16 in and 7/8 in diameter FAMs 95
3.2 The gains used for testing each FAM in water and air (psi pressure input, PWM control output) 107
3.3 Average pressure and standard deviation for the force response characterization test at each test pressure (3/16 in FAM) 108
3.4 Average pressure and standard deviation for the force response characterization test at each test pressure (7/8 in FAM) 108
3.5 The force response root-mean-square error (RMSE) at each test pressure. 111

4.1 Construction of the 7/8 in diameter FAM 143
4.2 The effect of the number of Fourier series fit terms used for fitting the profile data on the maximum and Root-Mean-Square Error (RMSE) averaged between all tested pressures 155
4.3 Coefficient values for the three-term Fourier Series fit performed in Figure 4.17(a) 157

5.1 Geometric dimensions calculated for the FAM in the resting length state 181

5.2 Comparison of effects of braid stretch for different braid materials . . 192

6.1 Longitudinal Bladder Strain, ϵ_z^n (Free-contraction, $100\,psi$) 213
6.2 Circumferential Bladder Strain, ϵ_c^n (Free-contraction, $100\,psi$) 217
6.3 Gaylord Force Term, F_G ($100\,psi$) 220
6.4 Longitudinal Bladder Stress, σ_z ($100\,psi$) 226
6.5 Longitudinal Bladder Force Term, $F_{bld,z}$ ($100\,psi$) 227
6.6 Circumferential Bladder Stress, σ_c ($100\,psi$) 229
6.7 Circumferential Bladder Force Term, $F_{bld,c}$ ($100\,psi$) 230
6.8 Combined Bladder Force, F_{bld} ($100\,psi$) 232
6.9 FAM Actuation Force (Model), F_{act} ($100\,psi$) 234
6.10 Mean Absolute Error (MAE) - Experimental versus Model Results . . 237
6.11 Blocked Force - Experimental versus Model Results 237
6.12 Free-Contraction - Experimental versus Model Results 237

7.1 Model Error with Respective Stress-Strain Constraints – 100 psi (Experimental Blocked Force: 1058 lbf, Experimental Free-Contraction: 0.354) 256
7.2 Model Error with Respective Stress-Strain Constraints – Averaged Across All Pressures 256
7.3 Material Coefficient Values, E_n (Fixed with respect to pressure) . . . 259
7.4 Average Model Error Using Experimental Versus Optimized E_n Values (E_{1-3} Fixed With Respect to Pressure) 260
7.5 Fit Coefficient Values, E_n, For "Best-Fit" Model 268
7.6 Error of the "Best-Fit" Model with Respect to Experimental Data for All Tested Pressures 270

List of Figures

1.1 Actuation of a contractile FAM . . . 2
1.2 FAMs with 1/8 in, 7/8 in, and 2 1/4 in diameters . . . 4
1.3 Examples of FAM actuated mechanisms . . . 7
1.4 Historical images of FAMs . . . 9
1.5 The braid acting as the working surface of the FAM transforms the working fluid pressure forces into an actuation force expressed at each end-fitting . . . 11
1.6 Braid angle θ, and its effect on actuation force . . . 12
1.7 Experimental characterization of FAMs . . . 13
1.8 Comparison between the FAM's geometry, and the commonly used cylindrical approximation of its geometry . . . 14
1.9 Triangle relationship commonly used to define the relationship between the FAM's geometric parameters . . . 15
1.10 Free-body diagram of forces acting on and within a FAM [1] . . . 18
1.11 Overview of the FAM's actuation force model development through the following representative literature: Gaylord (1958) [2], Schulte (1961) [3], Chou and Hannaford (1994) [4], Chou and Hannaford (1996) [5], Tondu (1997) [6], Klute and Hannaford (2000) [7], Tsgarakis and Caldwell (2000) [8], Tondu (2000) [9], Ferraresi (2001) [1], Colbrunn (2001) [10], Davis et al. (2003) [11], Davis and Caldwell (2006) [12], Kothera (2009) [13], De Volder (2011) [14], Solano (2011) [15], Tiwari (2012) [16], Tondu (2012) [17], Hocking (2012) [18], Meller (2014) [19], Robinson (2015) [20], Wang (2015) [21] . . . 23

2.1 Comparison of the refinement of wire wound, hose clamped, crimped, and swaged end-fittings . . . 30
2.2 Cross-Sectional view of a swaged FAM's end-fitting . . . 36
2.3 Side and isometric views of the internal fitting . . . 37
2.4 The effect of initial diameter and braid angle on estimates of maximum force and maximum diameter of the FAM. The surface represents the unconstrained design space, while points indicate options in the constrained design space . . . 50

2.5 The estimated force and diameter of the FAM for an assumed contraction of 40%. Results compare the response of FAMs with different combinations of available braid and bladder sizes 50
2.6 Dimensioned cross-section of the die used for swaging 58
2.7 Dimensions of internal fitting used for the 7/8 in swaged FAM 61
2.8 Swage tools (bolded) and FAM assembly in alignment prior to swaging 62
2.9 Components of FAM and swage tools prepared prior to assembly . . . 63
2.10 Steps of the assembly process prior to swaging 68
2.11 Progression of producing a swaged FAM end-fitting 71
2.12 Buckled swage tube of failed swaging attempt 73
2.13 Modified Swage Assembly 76
2.14 Labeled components of modified swage assembly 76
2.15 Swaging progression with modified assembly. Per methodology, the tube support and the standoff extension have been removed between frames 2 and 3, prior to continuation of extrusion. 77
2.16 Tested 7/8 in swaged FAMs 78
2.17 Isobaric force-contraction response of the three tested FAMs 79
2.18 Ultimate tensile failure test conducted on FAM 2 80
2.19 Burst test conducted on FAM 3 83
2.20 FAMs with failure due to internal fitting slipping out of end-fitting assembly 85

3.1 Illustrations of the components of the force-balance model given in Equation 3.1 93
3.2 The FAMs used in this study with outer diameters of 7/8 in (top) and 3/16 in (bottom) 95
3.3 3/16 in FAM characterization testing with (black lines) and without (colored lines) the addition of a controllable valve for accurate pressure control 97
3.4 7/8 in FAM characterization testing with (black lines) and without (colored lines) the addition of a controllable valve for accurate pressure control 98
3.5 Pneumatic pressure control system 100
3.6 Hydraulic pressure control system 101
3.7 Controller block diagrams 103
3.8 Open loop input, $v(P_{set})$, for hydraulic control of each tested FAM . . 105
3.9 Measured pressure for each force response characterization 109
3.10 Measured actuation force for each characterization 112
3.11 Comparison between the averaged characterization data, and the force response model 113

4.1 FAM with its shape profile traced in green along the edge of the braid 117
4.2 Variation of the FAM's shape profile for (a) a single FAM in different states of contraction, and for (b) three different FAMs in their free-contraction states 119

4.3 The actual profile that has a varying radius along its length (left) versus the cylindrical approximation of this shape profile with a constant radius along its length (right) . . . 120
4.4 Cylindrical HSV color space . . . 127
4.5 Example depiction of Moore-Neighbor tracing of a boundary . . . 132
4.6 FAM with sensors, MTS fixtures, and masking applied prior to mounting in the MTS machine . . . 133
4.7 Views of FAM mounted in the MTS machine with the photogrammetric test setup (camera, lights, and backdrop) . . . 134
4.8 Image captured by camera for photogrammetric analysis with calibration ruler . . . 139
4.9 The method of identifying the distance (in pixels) between 1/8 inch increments on the calibration ruler is illustrated. Each hatch mark has its left (blue), right (green), and then center (red) located on a segment of the ruler image (top), and respective brightness gradient plot (bottom). . . . 139
4.10 Identification of the FAM in the image (Steps 1-2) . . . 144
4.11 Identification of the end-fittings in the image (Steps 3-4) . . . 145
4.12 The resulting shape profile of the braid along the FAM's length . . . 146
4.13 Actuation diagram of the 9-9/32 in, 7/8 in diameter test FAM . . . 147
4.14 Comparison between contraction of image data, and displacement recorded by the MTS machine for a single contraction cycle . . . 149
4.15 Evolution of the shape profile for a complete contraction cycle (100 psi) 150
4.16 Average diameter of the FAM's shape profile for all tested pressure-contraction states . . . 154
4.17 Comparison of assumed profiles to the measured shape profiles of the FAM at 0, 8.75, 17.5, 26.25, and 35 (maximum) percent contraction at 100 psi . . . 156
4.18 Comparison of the average measured diameter values, D_{avg}, against estimated diameters, $D_{est,1}$ and $D_{est,2}$ . . . 161
4.19 Internal FAM volume with respect to contraction for all tested pressures 164
4.20 Tested 7/8 in FAMs in free contraction and blocked force (resting length) states at 100 psi . . . 166
4.21 Shape profile comparison of the three tested 7/8 in diameter FAMs at 0, 8.75, 17.5, 26.25, and 35 percent contraction . . . 166
4.22 Characterization of the 2-1/4 in diameter FAM at 26 psi . . . 167

5.1 Tested 7/8 in diameter FAM . . . 175
5.2 Characterization testing of the FAM's actuation and geometry . . . 177
5.3 Testing of Kevlar-49 thread samples . . . 178
5.4 Triangle relationship of FAM dimensions, and subsequent effect with consideration of braid elasticity . . . 179
5.5 Analysis of the braid threads through *in situ* analysis . . . 183

5.6 Comparison of the stress-strain relationship calculated from (1) the tensile test measurements of the Kevlar threads, and (2) estimates from the *in situ* measurements of the FAM's braid. 184
5.7 Thread tension and length with respect to contraction and internal pressure 187
5.8 Estimated braid dimensions for the Kevlar-49 braid ($E_{brd} = 11.6 \times 10^6\, psi$) – Comparison between elastic (colored lines) and inelastic (black dashed lines) braid assumptions 189
5.9 Gaylord actuation force estimates for the Kevlar-49 braid ($E_{brd} = 11.6 \times 10^6\, psi$) – Comparison between elastic (colored lines) and inelastic (black dashed lines) braid assumptions 189
5.10 Estimated braid dimensions for a lower stiffness braid ($E_{brd} = 1.16 \times 10^6\, psi$) – Comparison between elastic (colored lines) and inelastic (black dashed lines) braid assumptions 191
5.11 Gaylord actuation force estimates for a lower stiffness braid ($E_{brd} = 1.16 \times 10^6\, psi$) – Comparison between elastic (colored lines) and inelastic (black dashed lines) braid assumptions 191

6.1 Comparison between the profile of the FAM, and the profile assumed with the commonly used cylindrical approximation 195
6.2 Various assumed geometry profiles used for modeling of FAMs 196
6.3 Definitions of dimensions for the analyzed geometries 200
6.4 The Triangle Relationship, enabled by the cylindrical geometry approximation, used to estimate the dimensions of the FAM between states of contraction 201
6.5 Comparison between the profiles defined from acquired image data, and the Fourier-series fit equations that are used to define the profiles for analysis 203
6.6 Comparison of dimensions obtained from the cylindrical approximation of the measured geometry (colored lines), estimated cylindrical geometry with elastic braid (gray lines), and estimated cylindrical geometry with inelastic braid assumption (black dashed lines) 206
6.7 Bladder longitudinal and circumferential stress directions 208
6.8 Bladder thickness calculated for each geometry ($100\, psi$) 211
6.9 Geometry-dependent longitudinal length assumed for longitudinal bladder strain calculations 212
6.10 Longitudinal bladder strain calculated for each geometry ($100\, psi$) . . 213
6.11 Geometry-dependent radial profile assumed for circumferential bladder strain calculations 215
6.12 Circumferential bladder strain calculated for each geometry ($100\, psi$) 216
6.13 Comparison of the Gaylord force term estimates obtained for the cylindrical approximation of the measured geometry (colored lines), the estimated cylindrical geometry with elastic braid (gray lines), and the estimated cylindrical geometry with inelastic braid assumption (black dashed lines) 220

6.14 Latex bladder tensile test specimen . . . 222
6.15 Tensile testing of the latex bladder used in FAM construction . . . 223
6.16 Engineering and True Stress values acquired from tensile test data . . 224
6.17 Longitudinal bladder stress, and longitudinal force term, calculated for each geometry (all tested pressures) . . . 227
6.18 Circumferential bladder stress, and circumferential bladder force term, calculated for each geometry (all tested pressures) . . . 229
6.19 Combined bladder force calculated for each geometry (all test pressures) 231
6.20 Combining individual actuation force model terms to obtain overall model results for each geometry . . . 234
6.21 Comparison between model and experimental test results . . . 235

7.1 Free-body diagram of the FAM used in derivation of the force model [1] 244
7.2 Model results (7/8 inch FAM) using the approach of Hocking (2012) to define E_n values. E_{1-4} values are defined with respect to pressure, and without any constraints on their resulting stress-strain relationships. . . . 251
7.3 Model results (7/8 inch FAM) using the approach of Pillsbury (2015) to define E_n values. E_{1-4} values are constrained to be positive, and as a linear function of pressure. . . . 252
7.4 Comparison of model results using different stress-strain constraints . 257
7.5 Stress-strain curves with the use of the respective constraints for the model at 100 psi (curves vary with pressure) . . . 258
7.6 Comparison between E_{1-3} values obtained through experimental characterization, and those found through optimization. Values of E_{1-3} are independent of pressure. . . . 260
7.7 Model fit error – averaged over all tested pressures – for all tested permutations of defining the material coefficients, E_n . . . 262
7.8 Comparison of model fits with variation in the number of E_n terms used (with respect to pressure) . . . 264
7.9 Comparison of model fits with variation in the relationship between E_n and pressure . . . 267
7.10 Modeling results for the "best-fit" model, which uses terms E_{1-3} that are constrained to vary linearly with pressure, and constrained to comply with the Drucker stability criterion. . . . 269

8.1 Overview of the FAM's actuation force model development through the following representative literature: Gaylord (1958) [2], Schulte (1961) [3], Chou and Hannaford (1994) [4], Chou and Hannaford (1996) [5], Tondu (1997) [6], Klute and Hannaford (2000) [7], Tsgarakis and Caldwell (2000) [8], Tondu (2000) [9], Ferraresi (2001) [1], Colbrunn (2001) [10], Davis et al. (2003) [11], Davis and Caldwell (2006) [12], Kothera (2009) [13], De Volder (2011) [14], Solano (2011) [15], Tiwari (2012) [16], Tondu (2012) [17], Hocking (2012) [18], Meller (2014) [19], Robinson (2015) [20], Wang (2015) [21] . . . 283

List of Abbreviations

a_0	Horizontal shift term (Fourier series equation)
A_{brd}	Cross-sectional area of braid
a_n, b_n	Terms that scale the magnitude of each harmonic of order n (Fourier series equation)
B	Length of each thread of the braid
B_0	Resting length of each thread of the braid
BAM	Braided Artificial Muscle
$B_{elastic}$	Stretched braid thread length (elastic braid)
B_{est}	Estimated braid thread length in estimated cylindrical geometry
B_{meas}	Adjusted braid thread length defined using average of measured diameter $\bar{D}_{meas}$
BPA	Braided pneumatic actuators
b_n	Y-intercept of linear equation that defines E_n
D	Diameter of a FAM
D_0	Diameter of a FAM at rest
D_{brd}	Diameter of the braid
D_{bld}	Diameter of the bladder
D_{cyl}	Diameter of FAM with cylindrical geometry assumed
$D_{elastic}$	Braid diameter - cylindrical geometry with stretched elastic braid
D_{est}	Estimated Braid diameter found using cylindrical approximation
D_i	Diameter of FAM at discrete pixel row i of an image
$D_{meas}(z)$	Measured braid diameter defined along length of FAM
$\bar{D}_{meas}$	Average of measured braid diameter $D_{meas}(z)$
$D_{meas,bld}(z)$	Diameter of the bladder based on $D_{meas}(z)$
$\bar{D}_{meas,bld}$	Average diameter of the bladder based on $\bar{D}_{meas}$
DSLR	Digital Single-lens Reflex (Camera)
e	Error signal
E_{brd}	Elastic modulus of the braid thread material
E_n	Material stiffness coefficient matched with polynomial order n
F_{act}	Actuation force of a FAM
FAM	Fluidic artificial muscle
$F_{bld,c}$	Circumferential bladder force's effect on actuation force
$F_{bld,z}$	Longitudinal bladder force's effect on actuation force
F_{exp}	Experimentally measured actuation force of a FAM
F_{fail}	FAM actuation force at point of failure
F_G	Gaylord force of a FAM
$F_{G,est}$	Gaylord force calculated using estimated cylindrical geometry
$F_{G,meas}$	Gaylord force calculated using measured geometry
F_i	Force measurement within a data set for a single isobaric test

HAM	Hydraulic artificial muscle
HSV	Color model - Hue, Saturation, Value
ISO	International Standards Organization (camera sensitivity)
K_p	Proportional control gain
K_i	Integral control gain
L	Length of braided section of a FAM
L_0	Resting length of braided section of a FAM
L_{bld}	Length of the bladder
$L_{bld,0}$	Length of the bladder at rest
L_{cyl}	Length of bladder based on a cylindrical geometry approximation
L_{meas}	Length of bladder based on the measured geometry
MAE	Mean Absolute Error
m_n	Slope of linear equation that defines E_n with respect to pressure
n	Order of the bladder's stress-strain relationship
N	Number of turns that a single thread of the braid makes about the circumference of a FAM
n_{brd}	Number of threads the braid is composed of
N_i	Total number of data points at each tested pressure
N_p	Total number of experimentally tested pressures
$OD_{fit,brd}$	Internal end-fitting outer diameter for braid compression surface
$OD_{fit,bld}$	Internal end-fitting outer diameter for bladder compression surface
OD_{swg}	Outer diameter of swage tube after being swaged
P	Pressure applied to a FAM
PAM	Pneumatic Artificial Muscle
PET	Polyethylene terephthalate
P_{fail}	FAM internal pressure at point of failure
PI	Proportional-integral (control)
P_{meas}	Measured pressure
P_{set}	Desired set pressure
PWM	Pulse-width modulation
R	Radius of a FAM
$R(z)$	Braid radius defined along length of FAM
R_0	Radius of a FAM at rest
R_{bld}	Radius of the bladder
$R_{bld,0}$	Radius of the bladder at rest
R_{cyl}	Radius of FAM with cylindrical geometry assumed
R_{est}	Estimated braid radius found using cylindrical approximation
RGB	Color model - Red, Green, Blue
$R_{meas}(z)$	Measured braid radius defined along length of FAM
$R_{meas,bld}(z)$	Radius of the bladder based on $R_{meas}(z)$

RMSE	Root mean square error
t_{bld}	Bladder thickness
$t_{bld,0}$	Bladder thickness at rest
t_{brd}	Braid thickness
T_{brd}	Tension in the each braid thread
t_{swg}	Thickness of swage tube
u	Control input signal
v	Open-loop control input
V_{bld}	Bladder volume
V_{brd}	Braid volume
V_{int}	Internal working fluid volume of bladder
V_{prof}	Volume of FAM as estimated from measured shape profile of FAM
w	Fundamental frequency of harmonic (Fourier series equation)
w_i	Probability of a image pixel value being in class i (Otsu's Method)
w_p	Width of each pixel in a photographic image
α	Force magnification factor
ϵ_{brd}	Strain in threads of braid
ϵ_c	Circumferential bladder strain
ϵ_z	Longitudinal bladder strain
$d\epsilon$	Strain increment tensor (Drucker Stability)
μ_i	Mean value of image pixels in class i (Otsu's Method)
μ_T	Mean value of all image pixels values (Otsu's Method)
σ_b	Inter-class variance (Otsu's Method)
σ_{brd}	Stress in threads of braid
σ_c	Circumferential bladder stress
σ_z	Longitudinal bladder stress
$d\sigma$	Stress increment tensor (Drucker Stability)
θ	Angle of the FAM's braid defined with respect to the normal of the longitudinal axis of the FAM
$\theta(z)$	Braid angle defined along length of FAM
θ_0	Angle of the FAM's braid in the FAM's resting length state
$\theta_{elastic}$	Braid angle - cylindrical geometry with stretched elastic braid
θ_{est}	Estimated braid angle found using estimated cylindrical geometry
θ_{meas}	Braid angle defined using average of measured diameter $\bar{D}_{meas}$
$\theta_{meas}(z)$	Actual braid angle defined along length of FAM
$\%Comp_{brd}$	Percent compression of braid for swaged end-fitting
$\%Comp_{bld}$	Percent compression of bladder for swaged end-fitting

Chapter 1: Introduction

1.1 Problem Statement

Today, robotic systems have continually-increasing requirements and expectations to execute demanding tasks with precision and seamless motion. The burden of these expectations lies especially on the actuators that drive these systems, which must consistently deliver exact control of their position and force outputs. Many of the most commonly used actuator types, such as electric motors and hydraulic actuators, have predictable and well understood qualities, but their overall packaging – especially when gearsets are required – can add a lot of weight, inertia, complexity, and impedance to a robotic system. High-impedance robots produced by those actuators types are common in industrial settings that value precision, speed, and task repeatability; however, the stiffness and bulk of these actuators is less desirable for use in the increasing number of robotic systems designed for human interaction or for bio-inspired mechanisms, where an actuator's low profile, compliance, and low weight, are prioritized.

An alternative to bulky and rigid actuators is the fluidic artificial muscle (FAM) soft actuator. With energy supplied by a pressurized working fluid, FAMs provide a uniaxial contractile force and stroking motion that is enabled by its mor-

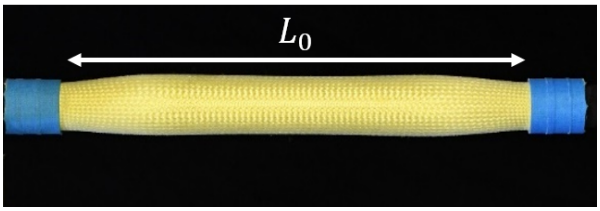

(a) Resting length state (deflated)

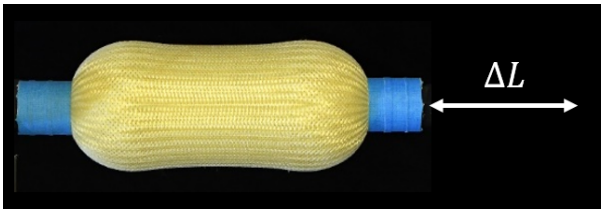

(b) Maximum contraction state (inflated)

Figure 1.1: Actuation of a contractile FAM

phing inflatable structure (Fig. 1.1). Interest in FAMs has been continually expanding due to their unique set of characteristics, including their low weight, simple construction, inherent compliance, and high specific force and specific work capabilities. However, there are remaining challenges that have inhibited their widespread use in robot systems and mechanisms. Further improvements are needed in their design, fabrication, characterization, and modeling.

Effective application of an actuator in a manipulator requires a clear understanding of actuator force, stroke, spatial requirements, and required energy supply. For FAMs, these specifications are difficult to know *a priori*, and must be ascertained by characterization testing. FAM characteristics can be hard to predict due to the complex interactions and nonlinear material properties of their components, as well as variance from FAM-to-FAM that arise during fabrication.

The interdependence of the FAM's pressure, force, contraction, and geometry dictates that they should all be measured to obtain a complete characterization of a

FAM. Geometric measurements, however, are typically not obtained due to the lack of available methods for capturing the changing bulbous shape of the FAM during testing. Almost all FAM research has, instead, relied on a cylindrical estimation of the FAM's geometry. The amount of error ensconced in these estimates is uncertain, yet these estimates are relied upon as bases for design decisions, and for multiple inputs in all actuation force models. The bulk of FAM research has worked to improve the accuracy of these empirically-based actuation force models, and to take steps towards making the model more predictive. Despite these focused efforts, multiple geometry-based assumptions have remained uninvestigated while also being frequently cited as likely sources of error.

The goal of this research, therefore, is to produce a method of providing a complete and accurate characterization of FAMs. With the acquisition of this characterization data, the error that arises from common FAM modeling assumptions is tested, and improvements are made to the existing actuation force model. This dissertation aims to provide an additional dimension to the characterization of FAMs for improved model design, and provide quantitative geometric data of FAMs, in order to improve the ability to design mechanisms and systems around FAM actuation characteristics.

1.2 Fluidic Artificial Muscle Actuators

This section contains an overview of fluidic artificial muscles (FAMs). A general background, history, and details on the experimental characterization and mod-

eling of FAMs, is discussed to provide context for the presented research.

1.2.1 Background

A fluidic artificial muscle (FAM) is a form of soft actuator that provides a uniaxial force. Its simple construction consists of an elastomeric bladder, a surrounding braided sleeve, and two end-fittings. Upon internal pressurization, a FAM produces a contractile or extensile actuation force depending on the orientation of its braided sleeve. Because contractile FAMs are able to produce higher forces and are less prone to buckling than extensile FAMs, contractile FAMs are more commonly used [22]. The term FAM, therefore, typically refers to the contractile actuator type that is the focus of this work.

The simple construction of FAMs make them lightweight(< 0.5 lbm), low cost, and tolerant to bending and axial misalignments. Their soft construction and inherent compliance provide FAMs with their muscle-like qualities that make them especially attractive for use in applications with human interaction or bio-inspired designs [10, 23–26].

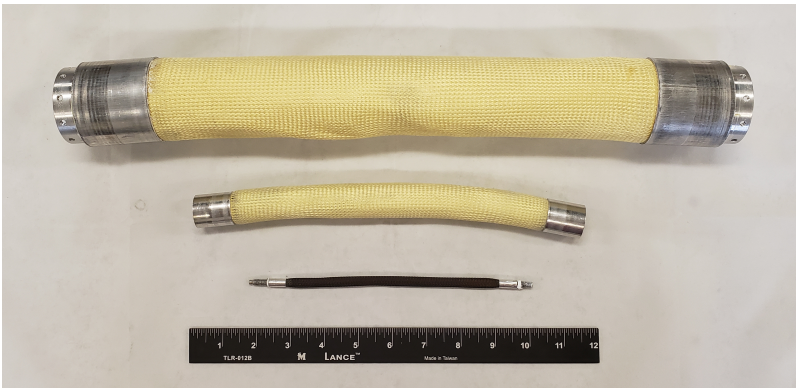

Figure 1.2: FAMs with 1/8 in, 7/8 in, and 2 1/4 in diameters

FAMs have been developed with diameters ranging from 1/16 inch to 2 1/4 inch [15]. With typical operating pressures below 100 psi, they produce actuation forces ranging from tens of pounds to thousands of pounds, while also being able to provide length contractions of up to 30-40% (Fig. 1.2) [27]. Coupled with their low weight, these high force and stroke capabilities give them high force-to-weight ratios (1000s lbf/lbm), and specific work capabilities (1000s ft-lbf/lbm) [28]. Table 1.1 shows the maximum strain (stroke divided by length), actuation stress (force divided by cross-sectional area), and specific work (work divided by mass) of several types of direct-drive actuators [29]. In comparison to the other actuator types, FAMs are able to produce a good balance of actuation strain and stress (stroke and force) capabilities. The direct-drive actuation of FAMs also provides them benefits over actuators that require gearboxes, such as motors; FAMs are backdrivable, have zero backlash, and are lower in weight and complexity. Researchers have reported specific power values of FAMs ranging from 500-2000 W/kg (225-900 W/lbm) [30], while electric motors are just on the order of 100 W/kg (50 W/lbm) [31]. With all of the aforementioned positive attributes of FAMs, it should be noted that challenges remain in refining the FAM's durability, modeling, and control of position and pressure.

The FAM's attributes make it well-suited for a wide-range of applications. Typical applications include prosthetics and assistive technologies (Fig. 1.3(a)) which can take advantage of the low weight and compliance of FAMs [23,28]. Among other attributes, their mechanical flexibility also makes them popular and uniquely suited for use in bio-inspired mechanisms and appendages (Fig. 1.3(b)) [24]. Their lack of moving parts, seals, lubrication, and electric power, makes them operable in

Actuator Type	**Maximum Strain**	**Actuation Stress,** MPa (psi)	**Specific Work,** J/kg (ft-lbf/lbm)	**Maximum Frequency,** Hz
Shape Memory Alloy (SMA)	0.07	700 (101,500)	4,500 (1,500)	7
Piezoelectric	10^{-4}	10 (1,450)	1 (0.33)	10^7
Magnetostrictive	0.002	10 (1,450)	20 (6.7)	10^7
Solenoid	0.4	0.1 (14.5)	5 (1.7)	80
Hydraulic Cylinder	1	70 (10,150)	35,000 (11,700)	100
Pneumatic Cylinder	1	0.9 (131)	1,200 (400)	100
FAMs (UMD)	**0.4**	**16 (2300)**	**4,400 (1,470)**	**100**
Human Muscle	0.5	0.4 (58)	0.8 (0.27)	100

(Adapted from Huber et al., 1997) [29]

Table 1.1: Comparison of direct-drive actuator technologies

environments that are difficult for other types of actuators [32,33]. Unique examples include aerospace [34–37] (Fig. 1.3(c)), subterranean (DARPA Underminer), and subsea [24] applications.

1.2.1.1 History

The invention of the fluidic artificial muscle was reached through the evolution of many similar technologies that preceded it. Reportedly, the first mechanisms of this general type were developed in the 1930s by a Russian inventor named S. Garasiev [39]. Similar devices can be found in patents from the era, including: a rubber tube covered in a braided fiber exterior for use in mining (Pierce, 1940) [40]; a fluid-driven linear tension device (Haven, 1949) [41]; and an elastic diaphragm

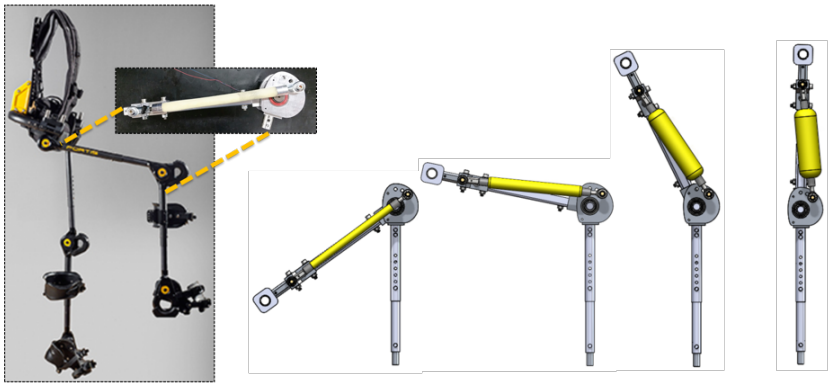

(a) Exoskeleton with FAM actuated assistance [28]

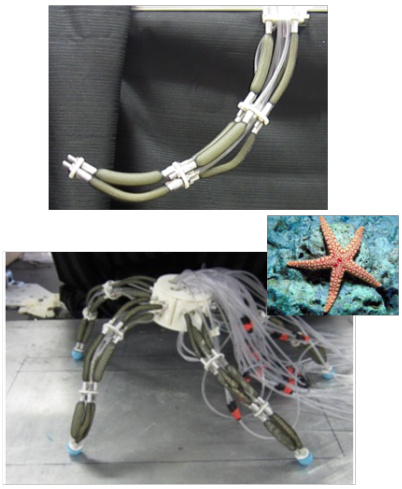

(b) Brittle star inspired FAM actuated appendages [24]

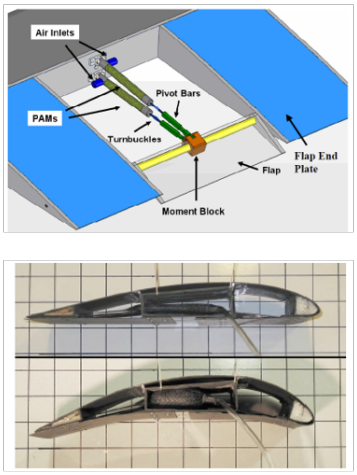

(c) FAM actuated trailing-edge flap [38], and morphing wing concept [36]

Figure 1.3: Examples of FAM actuated mechanisms

covered with stiff threads (Morin in 1953) [42]. Richard Gaylord is often attributed with the invention of the fluidic artificial muscle in 1958 with his patent titled *Fluid Actuated Motor System and Stroking Device* (Fig. 1.4(a)) [2]. This patent included the first equation to describe the force-pressure relationship of FAMs. In 1960, Joseph McKibben used FAMs in an assistive device that he developed for his polio-stricken daughter (Fig. 1.4(b)) [43]; *Life* magazine highlighted his device which helped popularize FAM technology. However, FAM development stalled not long

after this due to needed improvements in pneumatic valve and storage technology, along with the emergence of the miniaturized electric motor [17]. It was not until the 1980s that industrial automation applications renewed an interest in FAMs. Bridgestone developed the first commercialized FAM called the *Rubbertuator*, which was used in the actuation of an industrial robotic arm (Fig. 1.4(c)) [44, 45]. Only a few companies, including the Shadow Robot Group [46], and Festo [47], have since developed commercialized versions of FAMs. Widespread adoption of FAMs in industrial and commercial settings has been stymied by the need for further refinement and maturation of the technology.

From the mid-1990s to the present, development of FAMs has occurred mainly in research settings, and has been spurred on by rising interest in humanoid and bioinspired robotics that FAMs are well-suited for. Research efforts have focused on improvements in the modeling and control of FAMs, and on making adjustments to the construction and selection of materials, in attempts to improve their performance and durability.

Over time, slight variations in the construction, form, or application of FAMs, has garnered them a variety of names in literature. While fluidic artificial muscle (FAM) is the preferred nomenclature in this work, they are also often called McKibben actuators. Other names in literature include: braided artificial muscle (BAM), fluidic flexible matrix composite, rubber muscle actuator, and rubbertuator (trademarked by Bridgestone Company). Some names specify the working fluid used, including: pneumatic artificial muscle (PAM), hydraulic artificial muscle (HAM), braided pneumatic actuator (BPA), and air muscle.

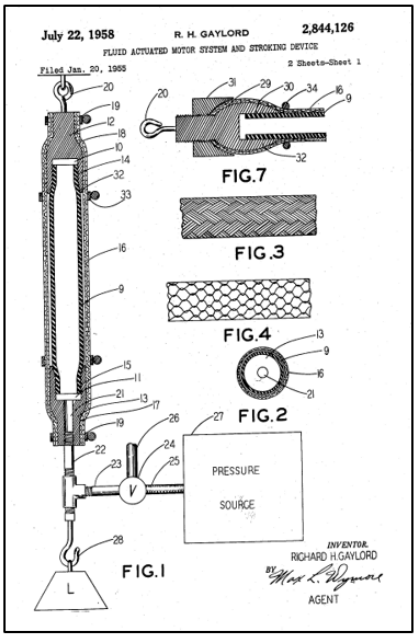

(a) Patent submitted by R.H. Gaylord [2]

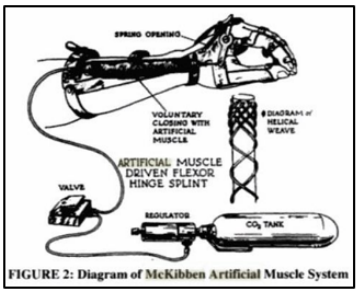

(b) Device developed by McKibben to assist his polio stricken daughter

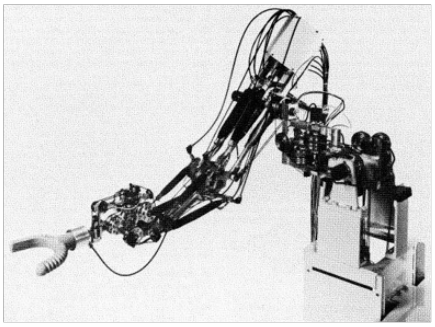

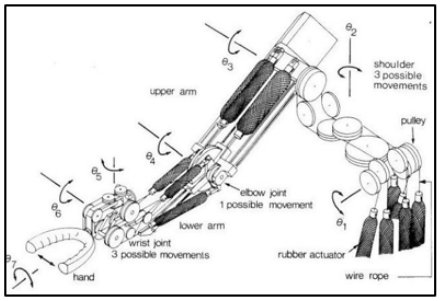

(c) Rubbertuator robotic arm

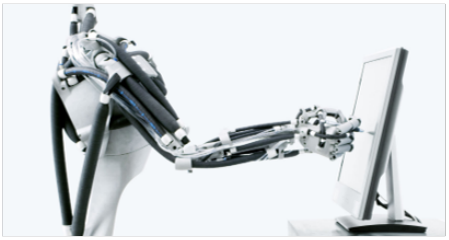

(d) Festo commercial FAMs

Figure 1.4: Historical images of FAMs

1.2.1.2 Working Mechanism

A FAM consists of an elastomeric bladder that contains the pressurized working fluid, a surrounding helically-braided sleeve that acts as the main load-bearing component, and two end-fittings that act as mounting points at each end of the FAM; one of the two end-fittings also acts as a conduit for the working fluid to flow into and out of the FAM. Upon pressurization (by air, water, oil, etc.), the bladder expands radially against the stiff braided sleeve. Radial expansion of the sleeve causes the sleeve to contract axially, and the radial pressure force from the bladder is transformed into an axial force which is transmitted through the sleeve and then end-fittings (Fig. 1.5). Motion of the braid is enabled by the changing angle of its threads that occurs as the FAM contracts in length; the braid angle θ – defined with respect to the normal of the longitudinal axis – begins at a maximum in the resting length state, and reduces as the FAM contracts in length and expands radially (Fig. 1.6(b)).

The braid angle and concomitant radius of the braid – both defined by the length state – largely determine the actuation characteristics of the FAM. Actuation force can be estimated as a function of the FAM's instantaneous internal pressure P, braid angle θ, and radius R, using the following equation:

$$F_G = P\pi R^2(2tan^2\theta - 1) \tag{1.1}$$

This equation, typically attributed to Gaylord [2], can be separated into two parts: the $P\pi R^2$ term defines the force of a cylinder actuator, and the $(2tan^2\theta - 1)$ term

defines the force magnification (α) that the braid provides. The amplification of actuation force that the FAM provides over a traditional cylinder actuator (where $\alpha = 1$), is enabled by the larger working area of the FAM (i.e., the braid surface) in comparison to the working area of a traditional cylindrical actuator (i.e., the piston area) (Fig. 1.5). As seen in Figure 1.6(a), the multiplication factor increases dramatically at higher braid angles. A typical initial braid angle of 70 degrees provides a 14.1 magnification of force over that of a cylindrical actuator with an equivalent initial diameter. Also of interest is the braid angle value that returns a magnification factor of zero; this braid angle ($\theta = 35.3$ deg.) demarcates whether a FAM will contract or expand in length upon pressurization, and therefore, defines the principle difference between contractile and extensile FAMs.

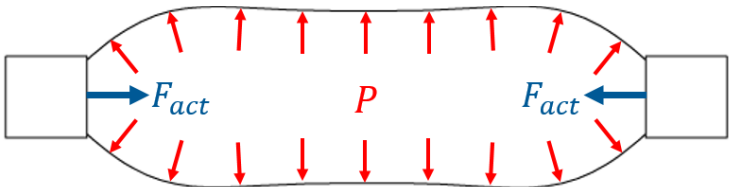

Figure 1.5: The braid acting as the working surface of the FAM transforms the working fluid pressure forces into an actuation force expressed at each end-fitting

1.2.2 Experimental Characterization

The actuation of a FAM is characterized by defining its pressure-dependent force-contraction response. The response is typically measured on a test apparatus such as the material test machine shown in Figure 1.7(a). This machine directs a controlled motion of the FAM, while pressure is controlled with a regulator, and force is measured by a load cell. Testing is performed by quasi-statically cycling the

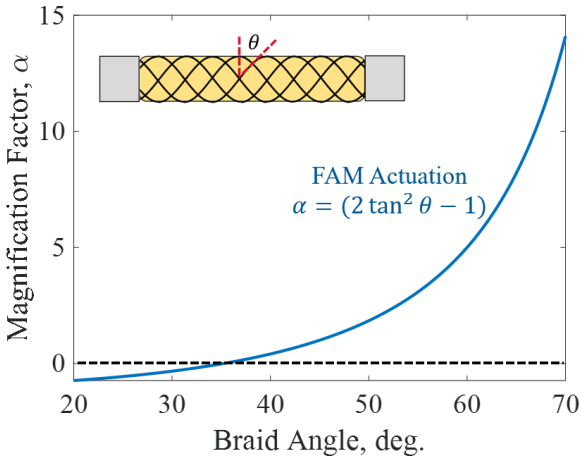

(a) Braid angle dependent magnification of actuation force. Estimated actuation force equals $P\pi R^2\alpha$

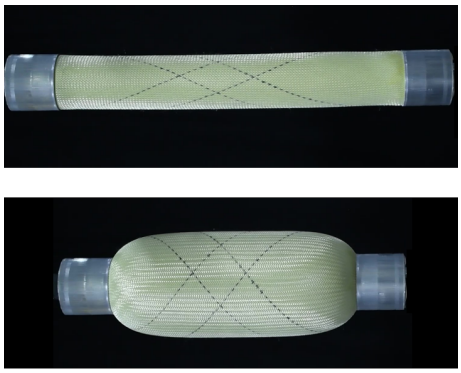

(b) Decrease in braid angle between resting length and maximum contraction states (threads marked on FAM)

Figure 1.6: Braid angle θ, and its effect on actuation force

FAM between its resting length and maximum contraction states at fixed pressures. A complete characterization requires repeating this test for multiple discrete set-pressures within the standard operating range of the FAM.

The experimental characterization results shown in Figure 1.7(b) illustrate the typical actuation characteristics of FAMs. A FAM provides its maximum force when in its resting length state, termed the *blocked force* state; its force decreases with its contraction until a pressure-dependent maximum contraction state, also known as a *free-contraction* state, is reached. Actuation force is nominally proportional with pressure, as implied by the Gaylord force equation. Each isobaric test exhibits hysteresis due to friction within the FAM, with higher forces observed during eccentric motion. The eccentric and concentric motion curves are typically averaged to create a single curve at each pressure to simplify modeling and analysis.

While experimental characterization of a FAM typically entails defining its isobaric force-contraction response, other useful characterizations include measur-

ing the change in volume with contraction [19], and failure testing to quantify the maximum strength or pressure capabilities of a FAM [37].

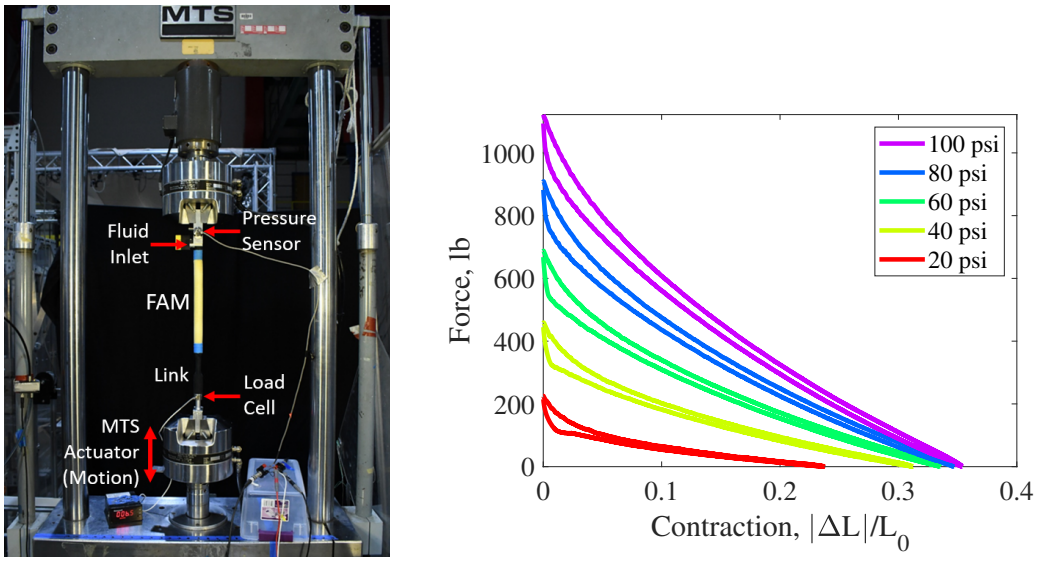

(a) Test machine often used for characterization testing of FAMs

(b) Actuation response of a 7/8 inch diameter FAM

Figure 1.7: Experimental characterization of FAMs

1.2.3 Modeling

Obtaining accurate models of a FAM's actuation is pivotal to effectively designing a mechanism for FAM actuation and for accurate control of the FAM. Because of this, much of the research has focused on incremental improvements to the accuracy of FAM models. While acquiring models of the FAM's actuation force response is often the main focus of these studies, modeling the changing geometry of the FAM – which acts as an input into the actuation force model – is also of primary importance.

Despite their complex geometry, virtually all modeling and analysis efforts have assumed a cylindrical geometry (Fig. 1.8) [1–3, 5, 8–10, 13, 16, 18–21]. This sim-

plifying assumption assumes a constant diameter and braid angle along the length of the FAM. By using a cylindrical approximation, cylindrical dimensions of the FAM are easily estimated for all states of contraction, and have been used as an input in almost every model formulated for FAMs. The cylindrical assumption has been used in the derivation of models representing the FAM's internal volume [19], friction [9], bladder strain [13], and actuation force [17]. Researchers have long acknowledged this inaccurate representation of FAM geometry – inherent when using the cylindrical approximation – is a likely source of modeling error [13]. Few attempts, however, have been made to address this issue.

An overview of the standard modeling practices of FAMs is provided in the following subsections.

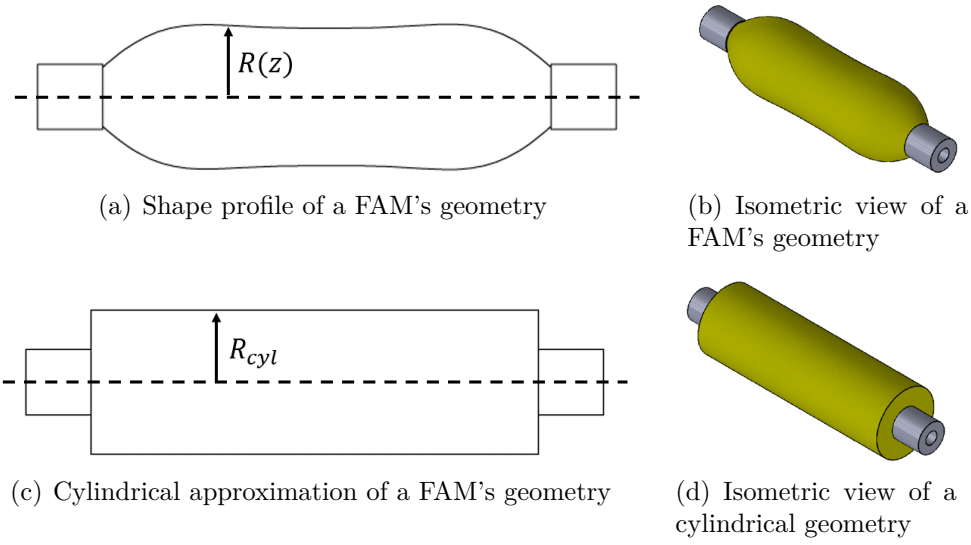

(a) Shape profile of a FAM's geometry

(b) Isometric view of a FAM's geometry

(c) Cylindrical approximation of a FAM's geometry

(d) Isometric view of a cylindrical geometry

Figure 1.8: Comparison between the FAM's geometry, and the commonly used cylindrical approximation of its geometry

1.2.3.1 Geometric Model

An accurate measure of a FAM's geometry is important for: (1) ensuring proper clearances within an actuated mechanism, and (2) ensuring accurate inputs for the actuation force model. FAM research has lacked a method of accurately measuring a FAM's geometry, and has therefore relied on a cylindrical approximation for the model to extract estimates of the geometry in all length states.

The geometry of the FAM is defined by its instantaneous length L, diameter D, braid angle θ, along with braid parameters defining the length of each braid thread B (assumed fixed), and the number of turns of each braid thread about the circumference of the FAM N (fixed) (Fig. 1.9). The braid diameter and angle are a function of both the position along the FAM, and the contraction state of the FAM. Notably, the geometry of the FAM unpredictably varies between otherwise identical FAMs.

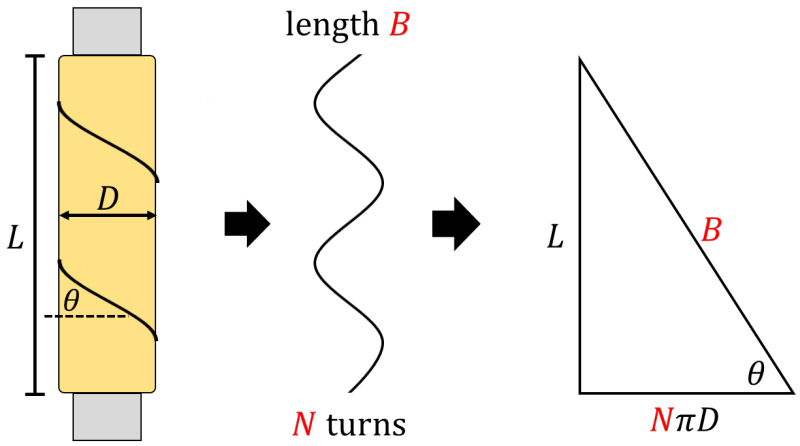

Figure 1.9: Triangle relationship commonly used to define the relationship between the FAM's geometric parameters

The cylindrical geometry assumption fixes D and θ along the length of the

FAM; the geometry parameters can then be related through a *triangle relationship* [4] (Fig. 1.9), which allows for D and θ to be estimated for all length states L, using the following equations:

$$D = \frac{\sqrt{B^2 - L^2}}{\pi N} \tag{1.2}$$

$$\theta = sin^{-1}\left(\frac{L}{B}\right) \tag{1.3}$$

Values of B and N are typically estimated using the the resting length dimensions L_0, D_0, and θ_0, with the following equations:

$$B = \frac{L_0}{sin(\theta_0)} \tag{1.4}$$

$$N = \frac{L_0}{\pi D_0 tan(\theta_0)} \tag{1.5}$$

Instantaneous bladder thickness t_{bld} – which varies with straining of the bladder – is also estimated using the cylindrical approximation through the following equation:

$$t_{bld} = R - \sqrt{R^2 - \frac{V_{bld}}{\pi L}} \tag{1.6}$$

where R is the radius ($R = D/2$), and V_{bld} is the bladder volume which is assumed incompressible (i.e., fixed) and is estimated in the resting length state configuration. Bladder radius is assumed equivalent to braid radius R due to the negligible thickness of the braid.

Estimates of bladder internal volume (i.e., the working fluid volume) are also made by assuming an estimated cylindrical geometry. Estimation of instantaneous volume can be a required input for some actuation force models, but is also useful for estimating fluid flow rate requirements to aid in pressure control of the FAM, and for sizing fluid handling equipment and storage. Very few researchers have

experimentally characterized internal volume due to the specialized test equipment required to do so [19].

1.2.3.2 Actuation Force Model

Models relating the force, contraction, and actuation pressure, have been developed using both force-balance [1] and energy method derivations [4]. Basic forms of the developed models are largely independent of the derivation method used, however the force-balance method is more widely adopted because it has been shown to provide more opportunities for model refinement.

The force-balance form of the actuation force model was originally derived by Ferraresi (2001) [1]. Many authors have since improved upon this model by adding or adjusting terms to better represent the FAM's dimensions, or components' interactions and material properties. The model takes a mechanistic approach, and is based on a free-body diagram which accounts for pressure, bladder, and braid forces (Fig. 1.10). From this, force-balance equations for equilibrium in the FAM's longitudinal (z) and circumferential (c) directions are obtained:

$$PRL = \sigma_c t_{bld} L + N T_{brd} cos(\theta) \tag{1.7}$$

$$F_{act} + \pi R^2 P = \sigma_z (V_{bld}/L) + T_{brd} sin(\theta) \tag{1.8}$$

These equations include: unknown values for actuation force (F_{act}) and braid thread tensions (T_{brd}); a working fluid parameter for pressure (P); bladder parameters for volume (V_{bld}), thickness (t_{bld}), longitudinal stress (σ_z), and circumferential stress (σ_c); and braid geometry-based parameters for active length (L), radius (R),

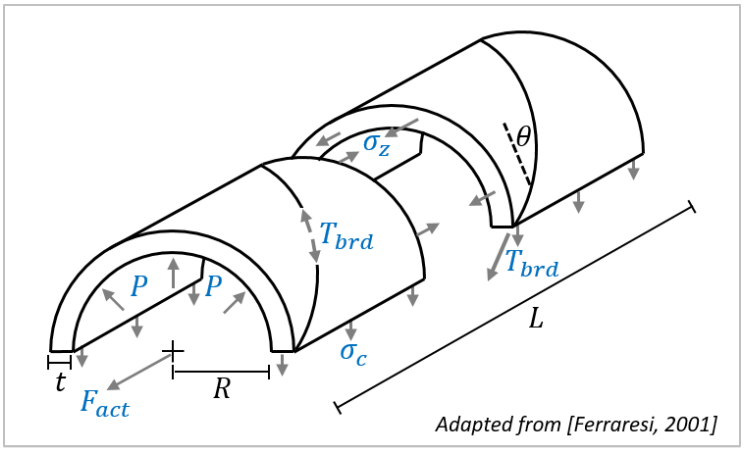

Figure 1.10: Free-body diagram of forces acting on and within a FAM [1]

braid angle (θ), and number of turns of each thread about the circumference of the FAM (N). Through substitution for the unknown value of T_{brd}, the system of equations is used to solve for F_{act}. The following expression for actuation force of the FAM – as a function of length L – is then defined as follows:

$$F_{act} = P\pi R^2(2tan^2\theta - 1) + \sigma_z\left(\frac{V_{bld}}{L}\right) - \sigma_c\left(\frac{t_{bld}L^2}{2\pi RN^2}\right) \tag{1.9}$$

The model has three basic terms. The first term – which is the Gaylord force equation – accounts for the actuation force produced by the internal fluid pressure acting on the braid. The second and third terms of Equation 1.9 are bladder force terms; these terms account for actuation force losses due to the stretching of the bladder during actuation. Attempts at making model improvements have often focused on these bladder force terms, and specifically in accurately estimating bladder stresses σ_c and σ_z which rely on accurate and difficult to obtain models of the bladder's hyperelastic stiffness and geometry-dependent strain estimates. Also note that many of the force model's inputs rely on the geometry estimation model, and therefore inherits the uncertainty in the geometry model's accuracy.

1.2.3.3 Review of Literature

A literature review provides insight on past developments of the FAM's actuation force model. Figure 1.11 provides specific actuation mechanisms or parameters, and the history of their inclusion amongst twenty-one representative works dating back to the first model, in 1958 (the Gaylord equation) [2]. Since the FAM's inception, all FAM models have used the Gaylord force equation, and the cylindrical approximation of the FAM's geometry that it is based on, as a foundation for model development. Energy methods were used for model derivations until the development of the force-balance approach by Ferraresi (2001) [1]; the force balance approach has dominated FAM model development ever since, due to its more flexible and intuitive form that has provided better model accuracy.

Model development has focused on the addition of parameters and correction-terms to better capture effects of the bladder or braid. As previously noted, most additions to the model have been based on a cylindrical approximation of the FAM's geometry.

Energy losses due to bladder strain, and the effect that has on actuation force, has been the focus of much of the research over the past decade [7, 13, 17, 18, 48]. Efforts have focused on accurately characterizing the stiffness of the hyperelastic bladder; stiffness of the bladder can be difficult to capture due to the many dependencies of the bladder's stiffness, and because of the difficulty in experimentally testing hyperelastic materials. Models have included bladder thickness parameters [13] – along with a parameter that defines the bladder's inflation initiation pressure (i.e.

deadband pressure) [14, 18] – since their introduction in the 2000's. The chart in Figure 1.11 also shows that all models have assumed a cylindrical approximation of the bladder's dimensions to obtain the estimates of bladder strain, which are then used to calculate bladder stress and force values. This assumption discounts the variations in bladder strain that result from the varying radius of the FAM along its length.

Researchers have paid less attention to better-representing the braid's effects within the model. Efforts to better model the braid's effect on actuation force have focused on friction from braid-braid and braid-bladder interactions. The effects of braid elasticity have largely been ignored; the inelastic braid assumption is commonly assumed, despite past researchers having demonstrated the effect that braid elasticity can have on the geometry and actuation force of the FAM [11, 13]. The chart also shows how frequently the rounded geometry of the braid is assumed to be cylindrical. This assumption is often made despite commonly being cited as a probable source of modeling error [4,8,9,13,16,18–20,49,50]. More recently, a few researchers have applied shape corrections to the cylindrical approximation (based on assumed shape profiles near each end-fitting), however, the accuracy of those corrections has gone relatively untested [8, 13, 16–18, 20]. The geometry values calculated using the cylindrical approximation have remained unconfirmed experimentally for years, likely due to the lack of available methods for accurately measuring the FAM's geometry.

It should also be noted that the accuracy of the force model is only as good as the accuracy of the experimental characterization that it is based on. Character-

ization testing of the FAM's response often assumes an isobaric contraction of the FAM. Therefore, accurately controlling a constant pressure to the FAM is imperative to an effective characterization. Some past research has had inconsistencies in characterizations or exhibited responses that did not match modeled results; these instances have been attributed to inaccuracies in pressure control during characterization testing [16]. The vast majority of research that has performed isobaric characterization testing, as indicated in Figure 1.11, has not portrayed accurate control of pressure (including pressure tolerances), as should be done for assurance of the accuracy of their experimental findings.

Overall, the chart in Figure 1.11 highlights physical aspects of the FAM that have been neglected in the model. Almost all FAM models, developed over the past six decades, have relied on two modeling assumptions – the cylindrical approximation, and the inelastic braid assumption – as methods of simplifying analysis. Both assumptions have been questioned on multiple occasions, but have yet to be comprehensively addressed, likely due to the lack of a method for accurately measuring the FAM's geometric profile.

This work acts to address areas where the current actuation force models are lacking: the representation of the braid's elasticity, and the effects of the bladder and braid's non-cylindrical geometry. Improvements are first made to the methods of experimentally characterizing FAMs; accurate pressure control is assured, and then a method of accurately measuring the geometric shape profile of the FAM is developed. The acquired geometric measurements of the FAM are then used to test the cylindrical approximation and inelastic braid assumption. Uncertainty in the

model – due to inaccurate or incomplete characterizations, and the aforementioned modeling assumptions – is thereby substantially reduced, and an updated version of the FAM model is then analyzed for potential improvements in accuracy.

1.3 Contributions of Dissertation

The objective of this research was to improve the characterization and modeling of FAMs. Special emphasis was placed on acquiring geometric measurements of the FAM, and then using that data to test long-held modeling assumptions. Several contributions were made to the state-of-the-art in FAM design, fabrication, characterization, and modeling.

Previous work developed a swaged end-fitting design that improves a FAM's durability, working lifetime, and refinement. Swaged end-fitting FAMs had been made in a limited number of diameter sizes (5/8, 3/4, and 1 inch diameters), which limited the number of applications they could be applied to [51]. In this work, a method of scaling the design and fabrication of swaged end-fitting FAMs is developed, and is used to produce a new 7/8 inch diameter FAM that improves upon the force and stroke capabilities of previous swaged end-fitting FAMs. The developed 7/8 inch FAM was used in this research, and has since been applied to multiple robotic applications.

The accuracy of a model is only as good as the experimental data that it is based on. An accurate characterization of a FAM, therefore, is important to producing an accurate model of its actuation response. Prior to this research, char-

KEY:

●	Included
○	Partially Included
	Not Included
–	Not Specified

Actuation Force Models (Terms/effects included)	Gaylord, 1958	Schulte, 1961	Chou and Hannaford, 1994	Chou and Hannaford, 1996	Tondu, 1997	Klute and Hannaford, 2000	Tsagarakis and Caldwell, 2000	Tondu, 2000	Ferraresi, 2001	Colbrunn, 2001	Davis et al, 2003	Davis and Caldwell, 2006	Kothera, 2009	De Volder, 2011	Solano, 2011	Tiwari, 2012	Tondu, 2012	Hocking, 2012	Meller, 2014	Robinson, 2015	Wang, 2015
1) Modeling Approach (F=Force Balance; E=Energy Methods)	–	E/F	E	E	E	E	E	E	F	E	–	–	E/F	E/F	F	E	E	F	E	F	F
2) Gaylord Force - Cylindrical Approx.	●	●	●	●	●	●	●	●	●	●	●	–	●	●	●	●	●	●	●	●	●
4) Bladder Elasticity		○				●	○		○		–	–	●	○	○		●	●		●	●
5) Bladder Geometry												–									
6) Bladder Thickness												–	●		●			●		●	●
7) Bladder Deadband pressure							○					–		●	●			●		●	
8) Braid Elasticity											○	–	○								
9) Braid Geometry							○				–	–	○			○	○	○		○	
10) Friction		○	○	○			○	○				●				●	●	○		○	
11) Pressure Control	–	–	–	–	–	–	–	–	–	–	–	–	–	○	–	○	–	–	–	–	–

Figure 1.11: Overview of the FAM's actuation force model development through the following representative literature: Gaylord (1958) [2], Schulte (1961) [3], Chou and Hannaford (1994) [4], Chou and Hannaford (1996) [5], Tondu (1997) [6], Klute and Hannaford (2000) [7], Tsgarakis and Caldwell (2000) [8], Tondu (2000) [9], Ferraresi (2001) [1], Colbrunn (2001) [10], Davis et al. (2003) [11], Davis and Caldwell (2006) [12], Kothera (2009) [13], De Volder (2011) [14], Solano (2011) [15], Tiwari (2012) [16], Tondu (2012) [17], Hocking (2012) [18], Meller (2014) [19], Robinson (2015) [20], Wang (2015) [21]

acterization of a FAM's response was done by setting a fixed feed-pressure to the FAM, and measuring its actuation force at different states of contraction. This method of characterization often had two faults that would lead to errors in subsequent modeling efforts: they (1) often lacked the assurance of accurate control of the assumed isobaric feed-pressure during testing; and (2) did not include a measure of the FAM's geometry. With standard pressure-regulators, the pressure to the FAM can drift with working fluid flow into and out of the FAM; if the pressure is assumed fixed, this can result in inaccurate predictions of the FAM's force response. Secondly, the geometry of the FAM is typically estimated based on a cylindrical approximation; this can result in error of the geometric parameter inputs used for the actuation force model, but also leaves uncertainty in design requirements such as the required space allowance for the actuator within a mechanism, or the working fluid flow-rate requirements for actuation of the FAM.

This present work provides improvements to the characterization of FAMs. Accurate pressure control systems are developed – for both air and water working fluids – that ensure accurate control of pressure as the volume of the FAM fluctuates during eccentric and concentric motions of the FAM. These systems ensured accurate characterization data for the modeling efforts performed in this research, but were also used to prove the independence of the quasi-static actuation response to changes in the compressibility of the working fluid used. This work also presents a novel photogrammetric method to accurately measure FAM geometry during testing. The photogrammetric method can be used to generate accurate geometric parameter values for the force model, but also provides a non-intrusive method

of obtaining volume measurements of the FAM – important for defining actuation efficiency and flow-rate requirements. These geometric measurements provide an opportunity to improve the understanding of FAM actuation, and aid in making model improvements – as is done in this work.

Previous FAM actuation models have long relied on simplifying assumptions. Two of those simplifications – the cylindrical approximation, and the inelastic braid assumption – have been used in actuation response models since the development of the first FAM model in 1958. The cylindrical approximation neglects the curvature of the FAM by approximating the geometry of the FAM as a cylinder. The inelastic braid assumption neglects the compliance of the braid, and the effect that this could have on the geometry and force of the FAM. Each of these assumptions have remained – despite often being cited as likely sources of error – in part, due to the lack of methods for accurately quantifying their effects on the actuation of FAMs. These assumptions, therefore, have persisted as a source of uncertainty in FAM models.

In the presented work, photogrammetric measurements of FAM geometry make it possible to quantify the error in the cylindrical approximation and inelastic braid assumption. Furthermore, these geometric measurements can be used in place of cylindrical approximation values in geometry and actuation force models to improve their accuracy. The geometric measurements also enable the magnitude of braid stretch during actuation to be quantified *in situ*, and provide an avenue for analyzing the effect of braid stretch on the geometry and actuation force of the FAM. Removing the uncertainties instilled into FAM models by the assumptions

tested here improves the accuracy of the FAM model's outputs, and also provides new opportunities for further improvement.

1.4 Overview of Dissertation

This dissertation is organized into eight chapters, each presenting a different aspect of the research performed.

Chapter 1: Introduction. This chapter presents the motivation for the research. An overview of FAMs is provided, and current methods of characterization and modeling them are introduced. Assumptions within current characterization and modeling methods are presented. A literature review of past modeling improvements is provided for context of this research.

Chapter 2: Development of the Swaged End-Fitting FAM. The design, fabrication, and testing of a new 7/8 inch diameter swaged end-fitting FAM is presented. A standard procedure for scaling the design and fabrication of FAMs with swaged end-fittings is introduced. Adjustments are made to the swaging process to ensure efficient, safe, and repeatable fabrication. The 7/8 inch diameter FAM developed in this chapter is then used for the research performed in the subsequent chapters.

Chapter 3: Improvements in FAM Characterization Through Accurate Control of Pressure. Pressure control systems – for both air and water working fluids – are developed to ensure accurate pressure control during characterization testing of FAMs. The assurance of fixed set-pressures during testing is paramount

to the production of accurate empirically-based force response models. A detailed description of each pressure control system is presented, and are then used to characterize both a large and small-scale FAM. The new pneumatic control system is compared to the previous system, and subsequent improvements in the force characterization are reported. Data from the air and water tests are compared to test if the FAM's quasi-static response is independent of working fluid. The acquired characterization data is used for analysis in subsequent chapters.

Chapter 4: A Photogrammetric Method for Measuring FAM Shape. This chapter presents a method of measuring a FAM's geometry (i.e. shape profile). The photogrammetric method developed for acquiring measurements is detailed including the test setup, image analysis, and data analysis techniques. Geometric measurement data of a FAM is acquired, and then used to perform a preliminary analysis. Initial analysis of the data brings into question previous modeling assumptions – including the cylindrical approximation and inelastic braid assumptions – which motivates the work of subsequent chapters.

Chapter 5: The Inelastic Braid Assumption. In this chapter, the validity of the commonly used inelastic braid assumption is tested. Stretch in the braid is quantified using the shape profile measurement data acquired in Chapter 4. This data is used to approximate the stiffness of the braid's threads while on the FAM, and is compared to the stiffness measured through a tensile test performed on a single braid thread. The effect of the braid's elasticity on geometry and actuation force is investigated for the tested Kevlar braid, and for a hypothetical braid with lower stiffness.

Chapter 6: The Cylindrical Approximation Assumption. The error in the commonly used cylindrical approximation of the FAM's geometry is tested through comparison with measured geometry data of a FAM. Since geometric parameters serve as inputs to the actuation force model, the measured and cylindrically assumed geometries are compared for their effect on estimated force. This comparison is used to gauge potential improvements in model accuracy through the use of the measured geometries.

Chapter 7: Model Performance with Reduction in Modeling Assumptions. In this chapter, the force model is updated – based on the findings from previous chapters – and then its performance is analyzed. To ensure the model accurately represents the FAM's force response, the model uses optimized fit-parameters – as used in many other recent works – that are embedded into the model's bladder material stiffness terms. Optimization constraints on the fit-parameters from previous works are made more realistic while also improving model accuracy. The optimized fit-parameter values are compared to the experimental material coefficient values found in Chapter 6, and are also modified and analyzed for their effect on model accuracy.

Chapter 8: Conclusion. This final chapter summarizes the key conclusions from this research. The original work contribution to literature is identified, and future work topics are discussed.

Chapter 2: Design, Fabrication, and Failure Testing of a Swaged End-fitting FAM

2.1 Introduction

Despite the promising and unique performance capabilities of fluidic artificial muscles (FAMs), expanding their adoption hinges on improving their reliability, their consistent and efficient fabrication, refinement in their design, and scalability in size. The ability of FAMs to serve as a viable option for robotic and actuated mechanism applications depends on whether they can prove to be reliable and versatile in comparison to common forms of actuation such as pneumatic and hydraulic cylinders, and electric motors. Much of the current work with FAMs remains in research settings, where refinements in design, size, and cost are not often prioritized.

Refinements to FAM construction, especially in the end-fitting design, have improved markedly through the years. Earlier FAMs – including many used just for research purposes – have used end-fittings held together by wire winding or hose clamps. Few options of FAMs exist today that offer a refined and low-profile end-fitting design. The crimped fittings of Festo FAMs [47] have a refined – but somewhat bulky – design, while the swaged end-fitting design developed jointly

through work done by the University of Maryland and InnoVital Systems Inc. [37,51] has been shown to produce a refined and strong end-fitting construction (Fig. 2.1). Research on swaged FAMs, resulting in a patent on the technology [51], has shown that the swaged end-fitting design provides dramatic increases in the strength and durability of FAMs while providing a functional and aesthetic form factor. Woods (2012), for example, demonstrated the capabilities of a swaged 5/8 in diameter FAM that could withstand pressures beyond 1000 psi, and forces of 3170 lb. The durability of this FAM was also demonstrated by successfully cycling a 1 in swaged FAM for 120 million cycles with only minimal wear, compared to the 10 million cycle service life of the Festo FAMs [47], and a maximum of 14,000 cycles for the next best FAM after that [37].

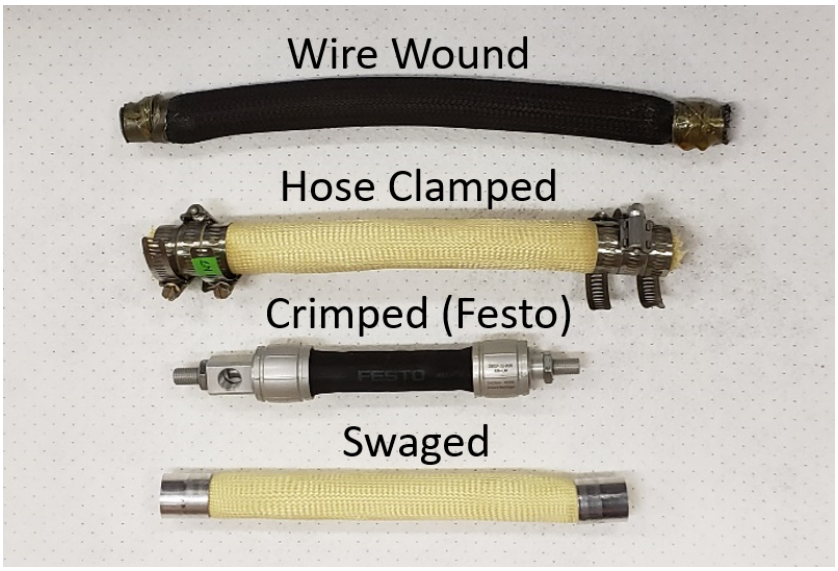

Figure 2.1: Comparison of the refinement of wire wound, hose clamped, crimped, and swaged end-fittings

FAMs with swaged end-fittings have been previously developed with nominal

diameters of 5/8 in, 3/4 in, and 1 in using the same approximate design formula (Table 2.1). Their force capabilities increase with diameter, but are also largely effected – as are their contraction capabilities and radial expansion – by the braid angle of the braided sheath that is a principal component of the FAM. The sizing of the components of the FAM, critical to the FAM's resultant performance, is also constrained by what is available through manufacturers and vendors. This constraint limits the number of possible component combinations that could be constructed to achieve a desired actuation response, and serves as a unique design challenge of FAM development.

Numerous calls for research proposals and projects involving actuated mechanisms have requirements that would necessitate the development of a FAM actuator that improves upon previously developed swaged FAMs. We considered the following design requirements:

- Actuation force of about 1,000 lbf
- Percent contraction greater than 30%
- Minimize radial expansion and respective change in internal volume
- Operating range of 0–100 psi

Secondary Considerations include:

- Minimize deadband pressure
- Maximize end-fitting internal airflow cross-sectional area

A newly-designed FAM should produce a maximum actuation force of about 1,000 lbs, and a contraction of greater than 30%. The FAM will be applied to applications where the pressurized air will come from shop air supply systems that commonly provide pressures of about 100 psi for use with pneumatic tools. Therefore, the

operating range of the designed FAM will be 0 to 100 psi. A factor-of-safety of at least two is desired for the maximum pressure and actuation force to ensure safety and robustness of the FAM. These requirements should be met while minimizing the FAM's radial expansion and respective volume required for actuation to facilitate the application of FAMs in mechanisms with space constraints. The FAM is expected to have refined end-fittings, and good reliability and durability traits as have been provided by previous swaged FAMs. Manufacturing the FAM should be an efficient and repeatable process, with the goal of producing FAMs having nearly identical actuation characteristics to improve the interchangeability of FAMs, as well as the efficiency and coherence of FAMs used in parallel such as for variable recruitment schemes. Development of detailed methods for readily scaling the production of swaged FAMs can also aid in future development.

This research details the development of a 7/8 in swaged FAM that improves upon the capabilities of previous FAMs to achieve the above-stated objectives. Through the development process, a methodical approach to FAM sizing and fabrication is presented, which includes improvements devised and applied to methods used previously in the fabrication of swaged FAMs. A method of determining the required sizing for a FAM for desired actuation attributes – while considering practicalities and constraints on sizing – is provided as a general guide for FAM development, and it also provides a background to the motivation of developing the 7/8 in FAM. A breakdown of the swaged FAM's components is provided. The process of fabricating a swaged FAM is detailed as an enumerated sequence to aid in future swaged FAM design efforts. Difficulties with both fabrication inconsistencies and failures led to

the development of improvements to the swaging process that are introduced and detailed in this research. Finally, tests were performed on three FAMs – fabricated using these improvements – to demonstrate the consistency and integrity of the FAM's performance, and to test their failure strength to determine safety factors. The failure mechanisms discovered through these tests were investigated for possible improvements.

FAM Diameter, in	**Max Force, lbf**	**Max Percent Contraction**	**Braid Angle**	**Weight, lbm**
5/8 in, UMD [52]	600 (90 psi)	34 % (90 psi)	72.5°	0.17
3/4 in, UMD [20]	950 (100 psi)	36 % (100 psi)	76.5°	0.18
0.79 in, FESTO [47]	337 (87 psi)	25 % (87 psi)	64.5° (est.)	0.52 (est.)
7/8 in, UMD	**1049 (100 psi)**	**35 % (100 psi)**	**71.6°**	**0.19**
1 in, UMD [37]	450 (90 psi)	27 % (90 psi)	55.5°	0.25
1.58 in, FESTO [47]	1037 (87 psi)	25 % (87 psi)	62.0° (est.)	1.83 (est.)

Table 2.1: List of swaged and comparable Flexo crimped FAMs, and their specifications for comparison to the 7/8 inch FAM developed in this work

2.1.1 Background

The three essential components of a FAM are an elastomeric bladder, a surrounding braided sheath, and some form of rigid fitting at each end. The bladder serves to encapsulate the pressurized working fluid, while the braid serves to transmit the radial pressure force into an axial force expressed at each end-fitting. These rigid end-fittings serve multiple roles for the FAM: They provide a rigid point of connection for the braid and bladder at each end; they serve as rigid mounting points for external hardware connections; they provide an air tight seal, and; they serve as a conduit for the working fluid to flow into and out of the FAM.

Various methods have been pursued in efforts to form a viable connection between an end-fitting, and the braid and bladder. Most methods include a rigid internal fitting that sits internal to the braid and bladder at each end, and an external component that encircles the braid, bladder, and internal fitting, and acts to compress and hold the bladder and braid against the internal fitting to provide a non-slip and pressure-tight seal. The cylindrical internal fitting often has some type of textured surface – such as barbs – to increase the resistance to slipping of the braid and bladder. Examples of external clamping components used include hose clamps [1,52], wire windings [38], compression fittings [38], barbed fittings [19], crimped tubes [18], and swaged tubes.

The end-fitting construction must balance between providing sufficient clamping force while not creating stress concentrations on the surface of the braid and bladder. Points of high stress concentrations can lead to premature wear and eventual failure of the FAM at or near the end-fittings. This can happen with sharp or abrupt edges, non-uniform clamping action, and overall relatively small clamping regions. It is desirable to have an end-fitting that can evenly distribute the clamping force at all points of contact with the braid and bladder within the fitting.

Swaging is the method of extruding a piece of metal – in this case the external end-fitting tube – through a die to reduce its diameter in what is commonly performed as a cold-working process. For the construction of FAMs, the external tube of the end-fitting, or *swage tube*, is forced through the die with the internal fitting, and with the braid and bladder sandwiched in between them (Fig. 2.2). The reduction in diameter of the swage tube, therefore, produces a permanent clamping force

on the braid and bladder as its outer and inner diameter are reduced. The method of swaging the external fitting component onto the internal fitting was introduced through the work done by Woods [37, 51].

Swaging of the end-fitting provides some key advantages over other end-fitting designs. Swaging provides a continuous clamping force along the entire length and circumference of the fitting. This increases the effective clamping area for a stronger hold, and the uniform clamping force reduces the peak stress on the braid and bladder. The swaged end-fitting design also provides a very low-profile and clean fitting design that does not create an obstruction beyond the diameter of the FAM. The internal fitting of the swaged end-fitting provides two distinct regions of clamping action. The difference in stiffness between the braid and bladder necessitates the use of two separate clamping regions for an effective clamping action. The smaller diameter of the internal fitting serves as a contact surface for the bladder to ensure a pressure-tight seal. The larger diameter of the internal fitting serves as a contact surface for only the braid. This ensures a strong connection between the major load bearing elements.

2.2 Component Descriptions

FAMs are composed of four primary components: two internal fittings, two swage tubes, braid, and a bladder (Fig. 2.2). At each end, the end-fitting, comprised of the internal fitting and swage tube, is used to clamp the bladder and braid. The end-fitting is designed to provide a maximum holding strength to ensure that the

FAM can withstand high loads and pressures. Additionally, epoxy adhesive is used during fabrication of each end-fitting to further enhance their holding strength. The braid and bladder are selected to be a balance between maximum actuation force and stroke, and durability. The design attributes and material selection considerations are detailed in the following subsections for each of these components.

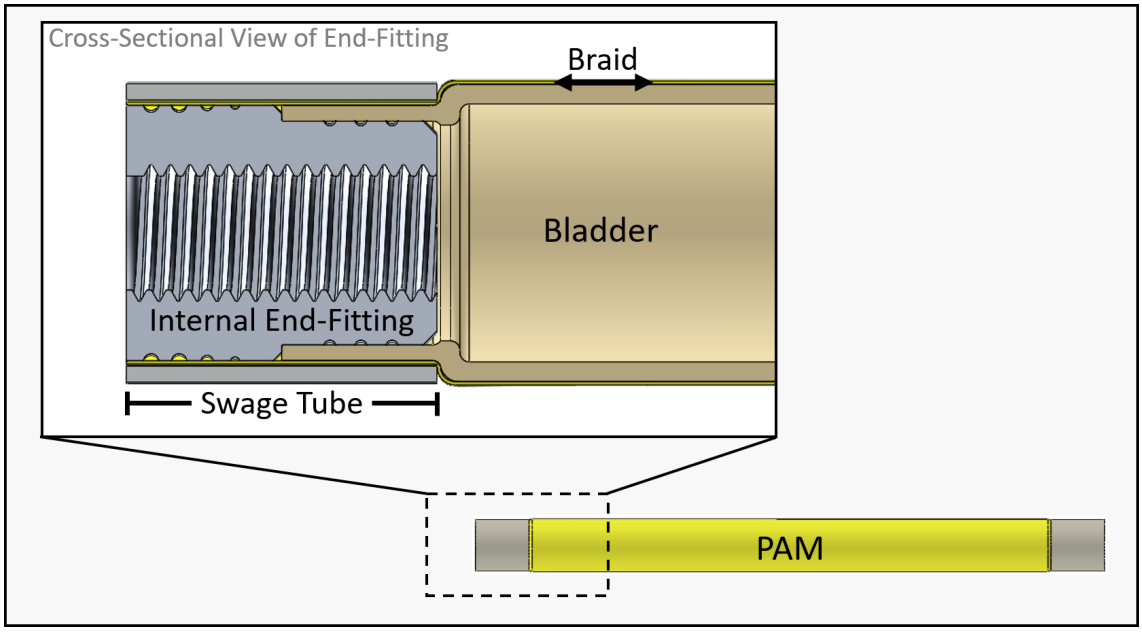

Figure 2.2: Cross-Sectional view of a swaged FAM's end-fitting

2.2.1 Internal Fitting

The internal fitting acts as a clamping surface for the bladder and braid to be clamped to by the swage tube. Each internal fitting has three distinct features that help it serve its unique role: a stepped clamping surface, annular grooves, and an external connection interface.

Swaging the swage tube onto the internal fitting in a single pass requires the swage tube to have a fixed diameter along the length of the end-fitting. The

difference in stiffness between the braided sleeve and the bladder requires different amounts of compression to provide the required clamping force. Controlling the amount of compression to the bladder and braid individually requires a stepped design, with the bladder clamped in one region, and the braid in a second region. The lower modulus of elasticity of the bladder requires a larger displacement to achieve the required clamping force compared to the stiffer braid. This design also enables the braid, which carries the actuation force of the FAM, to have its own dedicated clamping region.

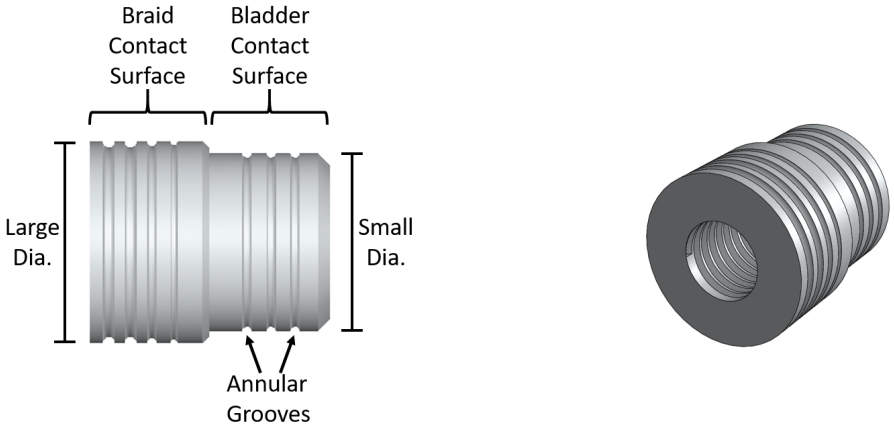

Figure 2.3: Side and isometric views of the internal fitting

The stepped design of the internal fitting is shown in Figure 2.3, while its orientation with respect to the bladder and braid is shown in Figure 2.2. The small diameter step is the contact surface for the bladder, while the large diameter step is the contact surface for the braid. The diameter of each step is sized to dictate the desired amount of compression for both the bladder and braid based on the inner diameter of the swage tube. Each of the stepped sections are typically made equal in length. Increasing the length of the entire end-fitting can increase its holding

strength, but at the expense of decreasing the percentage of the FAM's total length that is active for actuation.

Prior internal fitting designs with flat contact surfaces allowed the braid to pull out of the end-fitting at relatively low loads. Woods et al., therefore, introduced an internal fitting design with annular grooves and chamfered edges [37]. The annular grooves provide intermittent recessed regions where the bladder or braid are uncompressed, resulting in thickness variations that serve as a locking mechanism which increases the pullout strength of the end-fitting. The grooves also provide small reservoirs for the epoxy to bond to the bladder and braid, further increasing the pullout strength. The chamfered edges aid in reducing stress concentrations at the edge of each stepped surface of the fitting. The pullout strength of various end-fitting designs were tested to failure; those that had the updated internal fittings – with the annular grooves and chamfered edges – exhibited a 550% advantage in their holding strength, compared to the former designs with internal fittings that did not have these features. Through finite element analysis of the stress on the braid, a 40% decrease in the average stress on the braid, and a decrease in the maximum stress of 30% was found with the updated internal fitting design [37].

The connection interface of the internal fitting provides a point of mechanical connection to external components at each end of the FAM (Fig. 2.3). This interface is typically a concentric tapped hole that accepts a threaded stud for external connection. At least one internal fitting must have a tapped through-hole that extends through the entire length of the end-fitting. With a hollow threaded stud, this end-fitting serves as a conduit for the working fluid to flow into and out of

the FAM. The hollow stud is connected to a tube fitting or manifold that channels the pressurized working fluid from the fluid source to the inlet of the FAM. It is desirable to maximize the cross-sectional area for the flow of fluid channeling into the FAM to maximize flow rates to improve the dynamic response of the FAM. The cross-sectional area of the through-hole is constrained by the small-diameter step of the internal fitting.

The internal fittings are commonly made of a rigid material that can be easily formed to have the required features. Aluminum 6061-T6 has commonly been used for its combination of strength and machinability.

With a large percentage of the FAM's weight in the internal fittings, weight saving in this area can have a significant effect on the force-to-weight ration of the FAM. Therefore, lightweight materials – such as 3-D printed plastics – have also been considered for applications with lower force and pressure requirements.

2.2.2 Swage Tube

The swage tube is a thin-walled cylindrical tube that provides the clamping force of the FAM's end-fitting. They are commonly made of a ductile metal, such as aluminum, that can easily be formed through the swaging process. In order to provide a clamping force through swaging, the diameter of the tube is reduced by extruding it through a confining die. The confining die is designed for use with the specific outer diameter of the swage tube, and reduces the diameter of the swage tube by a prescribed amount to provide the desired clamping action onto the braid

and bladder. The wall thickness of the swage tube is assumed to be fixed through the swaging process. Therefore, it is assumed that the inner diameter of the swage tube is reduced by the same amount as its outer diameter.

Sizing options of swage tube diameter and thickness are often constrained by what is available through vendors. Typical swage tube thicknesses have ranged from 0.035 – 0.065 in. Choice of wall thickness is often driven by what is required to get the desired levels of compression of the bladder. The effect of the wall thickness on the tube's stiffness during swaging must also be considered. A thinner wall, for example, requires less force to push the tube through the die, but also makes it more susceptible to buckling in the process. The selected swage tube must also have tight wall thickness and diameter tolerances from the manufacturer. A variation of just a few thousandths of an inch can result in significant variations in the compression applied to the bladder and braid resulting in a diminished strength of the overall end-fitting.

2.2.3 Bladder

The bladder serves as an internal membrane that confines the pressurized working fluid within the FAM. The bladder is typically a cylindrical tube that helps define the dimensions of the FAM. The bladder is subjected to large strains from diameter increases that are often greater than 2.5 times the initial diameter. Energy consumed to strain the bladder is energy that would otherwise go towards actuation of the FAM. The bladder, therefore, is often thin and is made of a low

modulus, highly elastic elastomer. Wear on the bladder over time, especially for very thin wall thicknesses, can lead to pin-hole leaks and catastrophic ruptures of the bladder. Therefore, care must be taken to choose a wall thickness that is not so thin as to limit the operating life and resilience of the FAM.

Common bladder materials include silicone, polyurethane, latex, and natural gum rubber [48, 51]. Material selection is often limited by the availability of materials from vendors in the desired dimensions. Some researchers, however, have used molds to make custom bladders to the dimensions of their choice [48, 52]. As discussed above, it is desirable to have a bladder with a low modulus of elasticity. Unfortunately, the stiffness of elastomers is not often provided by vendors due to, in part, their unpredictable, non-linear response. The Shore Hardness, however, is often provided for elastomers and can be used as a relative measure of stiffness of available bladder materials. Elastomeric tubes are often manufactured through extrusion or mandrel formed techniques that provide a seamless design with constant wall thickness. Some cylindrical bladders, especially with larger diameters, have seams produced from manufacturing techniques such as mandrel wrapping. These seams produce potential points of weakness and non-uniform thickness that can lead to uneven inflation and premature failure of the bladder. Compatibility of the bladder material with the working fluid to be used must also be considered. For example, some bladder materials – such as many natural rubbers – can deteriorate when exposed to hydraulic oils. For petroleum based working fluids, alternate materials such as Viton and a non-rubber, low-density polyethylene (LDPE) bag bladder have been used [19].

Comparing the force response and free contraction of FAMs with bladders made of different materials has been a popular topic of research [19, 48]. Latex has commonly been used as a baseline of comparison. Latex is often available in a wide range of sizes, while also providing a good combination of durability and low stiffness. Silicone is a common alternative that is often used to make custom sizes of bladders, using molds, but it has also been found to exhibit large amounts of strain-stiffening which blunts the maximum contraction capability of the FAM [48]. Latex, therefore, is used for the development of the FAM presented in this research with the opportunity to adjust the bladder material in future iterations if required.

2.2.4 Braid

The helical braid serves as the primary load-bearing element of FAMs. The braid fibers transfer the radial pressure force of the internal working fluid into an axial force expressed at each end-fitting, while they also enable axial contraction of the FAM through the reorientation of its fibers. The braid material, therefore, must have a high tensile strength while also being pliant to allow for the relative braid movement.

The actuation characteristics of FAMs are highly dependent on the angle of their braid. The *braid angle* – defined with respect to the circumference of the FAM – decreases as the FAM contracts in length and expands in diameter. For contractile FAMs, the initial braid angle must be greater than 35.26 degrees [22]. FAMs with a braid angle that is less than 35.26 degrees form an *extensile FAM* that extends

upon internal pressurization. This is proven through the Gaylord Force equation (Eq. 2.5), which also demonstrates the strong relationship between braid angle and the actuation force. A larger initial braid angle also results in a larger achievable stroke of the FAM [13]. The maximum achievable initial braid angle, however, is limited by the physical jamming constraint of the braid [53].

Examples of braid materials include Kevlar, polyester (PET), nylon, and fiberglass [11,37,51,52]. Braid materials with a high elastic modulus and tensile strength are preferable to provide a braid that does not stretch or break under load. Elongation of the braid fibers results in energy losses, and also limits the application of rigid fiber assumptions used in many models. It is also desirable to have a braid with low friction characteristics. Braid-on-braid friction, and potential braid-on-bladder friction, have been shown to contribute to the hysteretic force response of FAMs that is indicative of additional energy losses [5, 9]. As with other components of the FAM, the choice of braid material is often limited by the sizing and materials available through vendors.

Kevlar and PET braids are frequently used for FAMs, and are often the subject of comparison tests. Kevlar often provides better performance than PET with greater stiffness (Young's modulus of 24,650 kpsi (170 GPa) compared to 1,600 kpsi (11 GPa)), and a higher failure stress (232,000 kpsi (1600 MPa) compared to 116,000 kpsi (800 MPa)) [54]. PET, however, is less expensive and can provide better performance than Kevlar with a few FAM diameters where PET braid can provide a higher braid angle [48]. Kevlar is selected as the preferred material for this research due to its durability and proven performance, as well as its availability in a range of sizes.

2.2.5 Epoxy

Epoxy is used to augment the holding strength of the end-fitting provided by swaging. Epoxy is applied to the inside of the end-fitting prior to swaging to produce a high-strength bond between the internal fitting, bladder, braid, and swage tube. WEST SYSTEM 105 resin-based epoxy is used in conjunction with the slow-curing WEST SYSTEM 206 hardener [55] in this research. The slow-curing hardener was selected, among other options, for its cited thin-film working time of 90-110 minutes. When the epoxy resin and hardener are mixed, self-heating of the mixed epoxy occurs which reduces its working time down to about one hour. Since the complete process of applying epoxy and swaging both ends of the FAM takes 30-60 minutes, there is typically just enough time to make a FAM with each mixed batch of epoxy. After swaging of the FAM is done, the epoxy requires 10-15 hours of curing time to get to a solid state, and 1-4 days to reach working strength. When fully cured, the epoxy becomes a high-strength plastic that has a tensile strength of about 7,300 psi.

By using epoxy in conjunction with swaging, improvement in the component's holding strength has been demonstrated [56]. A comparative tensile test was performed on two 1/4 in FAMs that were crimped with and without the addition of epoxy. Vocke et al. demonstrated that a FAM with epoxy had a three-fold improvement in holding strength over a FAM without epoxy.

2.3 Determination of FAM Component Sizing

Sizing of FAM components is a methodical and iterative process that requires consideration of not only the desired actuation response of the FAM, but also the holding strength of the end-fittings. The braid and bladder sizing drive the characteristic response of a FAM. Sizing of all the FAM components must be considered together to ensure an acceptable level of compression of the bladder and braid within the end-fitting for the required strength of the FAM's construction.

2.3.1 Sizing of FAM to Achieve Desired Response

Preliminary sizing of the FAM's diameter and braid angle are essential to estimating the force, contraction, and radial expansion of the FAM prior to performing detailed design efforts. Note that the diameter and length parameters of a FAM are defined as the FAM's outer diameter and the length of its bladder at rest, respectively. While determining the approximate sizing of FAM components, it is important to consider the limited and discrete availability of the bladder and braid sizes from vendors, and how those constrained sizing options will affect the resultant sizing configuration and respective response characteristics of the FAM.

The presented force and radial expansion models were used for initial sizing of the FAM with the following design objectives (as stated in the introduction) in mind:

- Actuation force of about 1,000 lbf
- Percent contraction greater than 30%

- Minimize radial expansion and respective change in internal volume
- Operating range of 0–100 psi

Secondary Considerations include:

- Minimize deadband pressure
- Maximize end-fitting internal airflow cross-sectional area

An actuation force of about 1,000 lb with a minimum of 30% contraction at a maximum operating pressure of 100 psi was deemed sufficient for most projected applications of the FAM. Many applications have space constraints that limit the radial expansion allowed for the FAM, while larger values of radial expansion also detrimentally increase the required volume and flow requirements of the source air. Minimizing the *pressure deadband* – the minimum pressure required to initiate actuation – is desirable to ensure maximum responsiveness and efficiency of the FAM. This objective can be met if the bladder and braid diameters are equivalent in the resting length configuration. Maximizing the cross-sectional flow area within the FAM's end-fitting should be considered with the other design objectives to aid in maximizing the dynamic response of the FAM.

Basic models of the expected force response and radial expansion of the FAM are presented to aid in initial sizing of the FAM. Parameters that take into account the stiffness of the bladder – such as material modulus of elasticity and wall thickness – are significant to the resulting actuation characteristics of the FAM. However, consideration of the effects of the bladder on the response characteristics of the FAM have been left out of initial FAM sizing exercises due to the modeling complications they introduce. The presented models are based on the geometry of the FAM alone

without consideration of material properties of the FAM's components. The outer diameter of the bladder is assumed to be equivalent to the diameter of the braid for all length states of the FAM. This is a reasonable modeling assumption, considering that actuation of the FAM requires the bladder to be in contact with the braid to transmit pressure forces to the braid. The models use the *cylindrical approximation*, which assumes that the FAM takes on a perfectly cylindrical shape along its entire length for all states of contraction. This cylindrical shape characteristic is used as the basis for most force and geometric modeling efforts of FAMs [1, 9, 13].

2.3.1.1 Models for Estimation of FAM Radial Expansion and Force Response

The cylindrical approximation leads to a geometric relationship, termed the *triangle relationship*, which correlates the diameter and respective braid angle to the length of the FAM for all states of contraction. With an assumption made for the maximum percent contraction of the FAM, this leads to estimations of radial expansion and internal volume. The triangle relationship is found by first defining the fixed length of each braid fiber, B, and the number of turns of each braid fiber about the circumference of the FAM, N, defined by the following equations:

$$B = \frac{L_0}{sin(\theta_0)} \tag{2.1}$$

$$N = \frac{L_0}{D_0 \pi tan(\theta_0)} \tag{2.2}$$

where L_0 is the initial active length, D_0 is the initial diameter, and θ_0 is the initial braid angle of the FAM. The FAM diameter, D, can then be found for any length state, L, using the following equation:

$$D(L) = \frac{\sqrt{B^2 - L^2}}{\pi N} \tag{2.3}$$

For some calculations, such as force, it is necessary to have an approximation of the instantaneous braid angle. The relationship between diameter and braid angle is fixed in accordance with the following equation:

$$\frac{cos(\theta_1)}{D_1} = \frac{cos(\theta_2)}{D_2} \tag{2.4}$$

where the braid angle, θ_n, and diameter, D_n, are related between states 1 and 2. Manufacturers commonly provide a nominal diameter with respective braid angle for the delivered braid. This information, along with the diameter for any given state as found from Equation 2.3 can be used to find the braid angle for the given state.

Figure 2.4(b) illustrates the relationship between the initial braid angle, FAM diameter, and the final diameter using Equations 2.2–2.3. The plot calculates radial expansion of the FAM at an assumed 35% maximum contraction, and is independent of the length of the FAM. Discrete points using braids of different nominal diameters are included for later analysis of the radial expansion under constrained availability of bladder and braid of sizing.

2.3.1.2 FAM Force Response Approximation

The cylindrical approximation also serves as the basis for most FAM force response models. The Gaylord force, F_G, provides an estimation of force based on the geometry and internal pressure of the FAM; It uses the braid angle, θ, radius, R, and internal pressure, P, to approximate the actuation force in the following equation:

$$F_G = P\pi R^2(2tan^2\theta - 1) \tag{2.5}$$

Values of R and θ can be found using Equations 2.3 and 2.4 respectively. Energy expended through radial expansion of the bladder is not factored into the model, but it would act to reduce the value of the actuation force estimated from the Gaylord force equation. The Gaylord force calculation is, therefore, most accurate at low levels of radial expansion that occur at low levels of FAM contraction.

Figure 2.4(a) illustrates the relationship between the initial braid angle, FAM diameter, and the estimated maximum blocked force of the FAM at 100 psi using Equations 2.4 and 2.5. Notable observations include the steep increase in force with braid angle that is especially noticeable with larger diameter FAMs. Discrete points indicating braids of different nominal braid diameters are included for later analysis of force capabilities under constrained availability of bladder and braid sizing. A red line indicating the 1000 lb mark is included as a reference for comparison to the stated design objective.

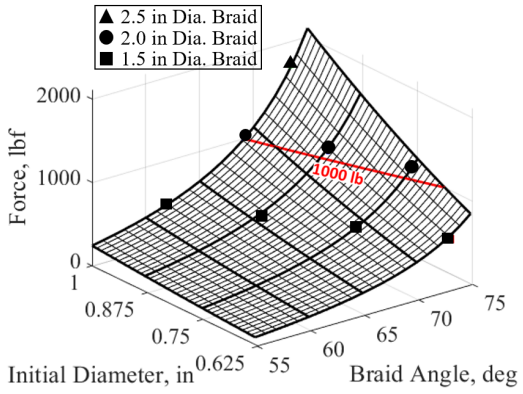

(a) Blocked force at 100 psi

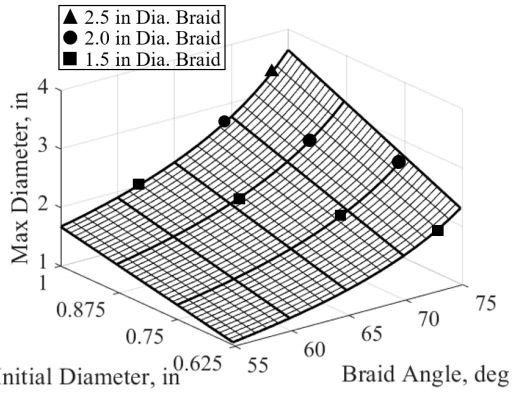

(b) Maximum FAM diameter at an assumed 35% contraction

Figure 2.4: The effect of initial diameter and braid angle on estimates of maximum force and maximum diameter of the FAM. The surface represents the unconstrained design space, while points indicate options in the constrained design space

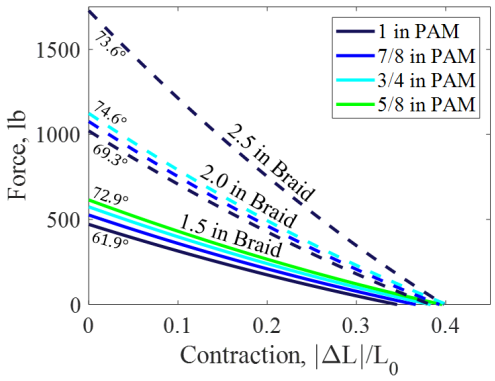

(a) Force with respect to contraction at 100 psi

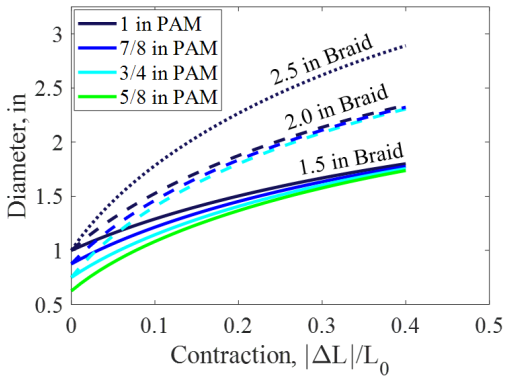

(b) Diameter with respect to contraction

Figure 2.5: The estimated force and diameter of the FAM for an assumed contraction of 40%. Results compare the response of FAMs with different combinations of available braid and bladder sizes

2.3.1.3 FAM Contraction Approximation

The overall length of the FAM is sized based on the contraction required of the FAM for a given application. Contraction of the FAM is defined in terms of a *percent contraction* of the resting length of the FAM. The percent contraction is commonly used to define the contraction of FAMs because the percent contraction

– for a given size and material construction – has been shown to be independent of the resting length of the FAM [13]. Absolute length contraction of a FAM is, therefore, proportional to its length.

The percent contraction of a FAM is primarily dependent on the initial braid angle, and the stiffness of the bladder. Unfortunately, without material properties of the bladder *a priori*, there is no simple model that estimates the contraction of the FAM prior to testing. FAMs have commonly attained between 25-40% contraction. Previously tested FAMs with comparable bladder materials and braid angle can be used to provide an estimate of the attainable percent contraction. The trend between braid angle and percent contraction is evident from the FAMs of Table 2.1.

2.3.1.4 FAM Component Sizing Constraints

When determining target values of FAM diameter and braid angle, it is common to think in terms of a design space without constraints. When thinking in terms of an unconstrained design space, it is easy to think, for example that using a larger diameter would lead to an increase in force and inflated diameter of the FAM. However, in a constrained design space, this is not necessarily the case. It is important to take into account the constraint imposed by the limited availability of components that are only offered in discrete sizes.

Availability of different sizes of components is dependent on the materials and measurement system used (Metric or Imperial). The latex cylindrical tubes used for the bladder are often available in 1/8 in increments for diameters that are around 1

in. For this study, we will consider bladder sizes of 1/2, 5/8, 3/4, 7/8, and 1 in. Braid is commonly sold in 1/2 in diameter increments defined at a set braid angle. The Kevlar used for the development of the FAM comes in nominal diameters of 1/2 in increments with the diameters defined for the braid in the 45 degree orientation. The braid can be stretched or compressed to change its diameter and respective angle in correspondence to the relation defined in Equation 2.4. Each braid has a range of achievable diameters that is limited by jamming of the braid at the extremes. Information on three candidate Kevlar braids are provided in Table 2.2.

	t	$D_{min-max}$	$\theta_{max-min}$
1.5 in Braid Dia.	0.012 in	0.60 - 1.75 in	73.6° - 34.4°
2.0 in Braid Dia.	0.011 in	0.76 - 2.23 in	74.4° - 38.0°
2.5 in Braid Dia.	0.018 in	1.40 - 2.65 in	66.7° - 41.5°

Table 2.2: Braid thickness, t, and range of achievable diameters, D, and range of braid angles, θ, for Kevlar braids of three nominal braid sizes (defined in 45 deg. braid orientation) (Source: Soller Composites, LLC)

	1 in FAM	**7/8 in FAM**	**3/4 in FAM**	**5/8 in FAM**
1.5 in Braid Dia.	61.9°	65.6°	69.3°	72.9°
2.0 in Braid Dia.	69.3°	72.0°	74.6°	–
2.5 in Braid Dia.	73.6°	–	–	–

Table 2.3: The initial braid angle for each combination of FAM size and nominal braid diameter. Red entries are at the threshold of the achievable range of the braid, while blank entries are non-feasible combinations (Reference Table 2.2)

The constructed FAM should have equivalent diameters for the bladder and braid. Every bladder and braid combination, therefore, will have a defined initial diameter and braid angle. Table 2.3 provides the braid angles that can be achieved for each combination of bladder and braid sizing used. There is a clear correlation between reduced FAM diameter and increased braid angle, however the extent of this

is constrained by the diameter limits of the braid indicated in Table 2.2. Therefore, some combinations are not feasible, while other cases are barely feasible (indicated in red) but would result in an undesirable pressure deadband due to the initial looseness of the braid around the bladder.

Figure 2.4 shows where the combinations of bladder and braid sizing lie within the unconstrained design space plots of estimated force and radial expansion. It is apparent that with the constrained sizing options, changes in initial FAM diameter result in relatively little change in the realized force and maximum diameter of the FAM. Figure 2.5 takes a closer look at this observed trend. The sizing combinations are plotted with respect to the percent contraction state of the FAM with an assumed maximum contraction of 40%. A prominent observation for both plots is the apparent grouping of the force and maximum contracted diameter values based on the braid diameters. This makes it clear that in the constrained sizing design space, the nominal diameter of the braid is the key driver of the FAM's characteristic response, with little effect associated with changing bladder diameter.

It is important to consider what effect the inclusion of bladder stiffness as a parameter (which these model approximations do not consider) would have on the results plotted in Figure 2.5. Bladder strain will act to decrease the force and contraction of the FAM. The increase in radial expansion for smaller bladders, observed in Figure 2.5(b), will result in higher levels of strain in the bladder which would act to further reduce contraction and force magnitudes, when compared to larger diameter bladders. This would likely negate some of the slight advantage in force observed with the smaller bladder diameters in Figure 2.5(a).

2.3.1.5 Selection of Target FAM Sizing

To achieve the target force of about 1,000 lbs, Figure 2.5(a) shows that a nominal braid diameter of 2 in should be selected. The 2.5 in diameter braid provides far more force than is necessary with unfavorable increases in radial expansion and air volume expenditure. Selection of the bladder diameter is more nuanced, with considerations of deadband pressure, material strain, air inlet diameter, and component availability.

A larger diameter bladder results in less bladder strain resulting in less energy loss and increased contraction. A larger diameter also does not increase the maximum contracted diameter of the FAM which is beneficial for fitting into tight spaces or for arranging multiple FAMs in parallel. A larger diameter also provides the opportunity for a larger air inlet cross-sectional area to increase volume flow rates, and decreases the expected change in inflation volume with contraction, which together act to improve the dynamic response time of the FAM. A sizing combination of a 3/4 in bladder with the 2 in Kevlar braid was used for the FAM developed by Robinson [20] which skirts the threshold of the achievable range of braid angle according to Table 2.2. This slightly oversized braid resulted in a relatively high pressure deadband of about 10 psi for that 3/4 FAM. As indicated in Table 2.3, defendable choices for FAM size selection can then be pared down to a 1 in or 7/8 in diameter bladder FAM, with little difference in their expected actuation responses. This leaves flexibility for the sizing process required for the design of the swaged end-fitting, as covered in subsequent sections. The 7/8 in FAM with a 2 in nominal

braid diameter configuration was ultimately selected for the FAM used.

2.3.2 Sizing of Components for Swaged end-fittings

The method of sizing a FAM's components has been refined over the years since the introduction of the swaged FAM by Woods [51]. The process of both sizing and fabrication of a FAM is as much of an art as it is a science. That is to say, much of the development of swaged FAMs has entailed a bit of trial and error to produce the desired results. Development of the swaged FAM has been a process of understanding the required compression of the bladder and braid to ensure sufficient strength of the end-fitting, while also finding the limit of compression that the swage tube can withstand without failing when attempting to swage the end-fitting. This includes the limits of force that can be applied to the swage tube before it buckles, and the force that the swage die can withstand, as well as the force that the extrusion press can provide.

The following benchmarks have previously been set for the successful swaging of a FAM. The swage tube experiences a reduction in diameter of 2.7% upon being extruded through the die. The internal fitting is sized to provide 17% compression of the braid, and 30% compression of the bladder. This formula has been used with multiple sizes of FAMs, and has been adjusted as necessary. Subsequent to the fabrication of the FAMs built for this research, the braid compression was increased to 27% compression, upon completion of this work, to improve the holding strength of the end-fitting. The components of the 7/8 in FAM are sized to satisfy these

criteria. It is important to note that one of the biggest challenges in sizing is the limited availability of sizes – especially of the swage tube and bladder – that are available through retailers.

2.3.2.1 Steps for Sizing Components of Swaged end-fitting

The method of sizing for the FAM end-fitting is outlined in the following steps. A detailed explanation of each step follows with a focus on the 7/8 in FAM that is developed for this research.

1. Set Bladder Outer Diameter - *list available wall thickness options,* t_{bld}
2. Set Braid Size - *to maximize braid angle*
3. Set Swage Tube Outer Diameter - *list available wall thickness options*
4. Set Die Inner Diameter - *based on swage tube diameter*
5. Select Test Bladder and Swage Tube Wall Thickness - *from listed options and subject to constraints*
6. Size Internal Fitting - *size to achieve desired end-fitting compression*

The steps should be performed in order. Steps 5 and 6 are iterated for each thickness option in the lists established in Steps 1 and 3 until a feasible solution for the sizing of the FAM is found. If no solution is found, subsequent iterations must incorporate previous steps until a solution is found.

Step 1: Set Bladder Outer Diameter. The outer diameter of the bladder sets the overall diameter of the FAM, and is selected based on the criteria set in the previous section. Bladder diameters are commonly offered in 1/8 in diameter increments. The targeted 7/8 in diameter was found available in wall thicknesses of 1/16 in, 1/8 in, and 3/16 in. Which thickness to use is determined in the subsequent

steps, but preference goes to using a thinner bladder that can help maximize the force and contraction of the FAM.

Step 2: Braid Sizing. The diameter of the Kevlar braid was selected in the previous section as the 2.0 in diameter sleeve, with the diameter defined in the 45 degree braid angle configuration. The relation between diameter and braid angle can then be found using Equation 2.4 as previously mentioned. Relevant to the sizing of the end-fitting components is the thickness of the braid, which is 0.011 in. At 0.011 in, with the braid being so thin, the compression of the braid as a percentage of its thickness is very sensitive to the tolerance that the internal fitting is manufactured to.

Step 3: Set Swage Tube OD. Sizing of the swage tube requires defining its outer diameter and wall thickness. Selection of the wall thickness occurs in later steps where the overall sizing of the end-fitting is iteratively refined. The thin-walled Aluminum 6061-T6 tubing used for the FAM is commonly offered in 1/8 in diameter increments. With the 7/8 in diameter bladder, this drives the swage tube size to an outer diameter of 1 in. Attempting to use a 7/8 in outer diameter swage tube would result in difficulty getting the tube over the bladder, braid, and internal fitting assembly prior to swaging.

Previous swaged FAMs have used tubing with wall thicknesses of 0.035 to 0.065 in. Within this thickness range, 1 in aluminum tubing is offered with wall thicknesses of 0.035, 0.049, 0.058, 0.065 in. It should be noted how the wall thickness affects the swaging process. Buckling of the swage tube in the process of attempting to extrude it through the die is a common issue of concern when swaging. A thinner

wall thickness requires less force to extrude through the die, but has a lower critical buckling load. Conversely, a thicker wall requires more force to extrude, but also has a higher critical buckling load. The thicker wall thickness is likely to be more robust in providing a constant clamping force for the operational life of the FAM. The 1 in outer diameter tube is set for initial sizing with the four wall thicknesses offered serving as viable options for the refinement of the FAM's sizing.

Step 4: Die Sizing. The die is used to reduce the diameter of the swage tube through the swaging process. Previous work established the desired percent reduction in diameter as 2.7%. This requires the die to reduce the 1 in outer diameter of the swage tube down to 0.973 in. The reduction in diameter takes place in the tapered section of the die, as illustrated in Figure 2.6. Sizing of the end-fitting components assumes that the swage tube maintains a constant thickness through the process of being extruded through the die.

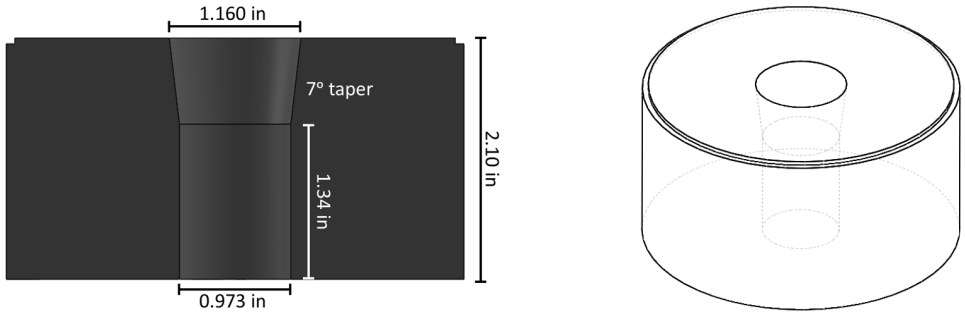

Figure 2.6: Dimensioned cross-section of the die used for swaging

Step 5: Select Bladder and Swage Tube Thickness. Settling on a swage tube and bladder thickness is performed as an iterative process alongside the sizing of the internal fitting. Sizing likely starts with the bladder that has the thinnest wall thickness to provide a maximum force and stroke of the FAM.

Step 6: Size Internal Fitting. Sizing of the internal fitting is the most important step for creating an effective end-fitting design. The outer diameter of each stepped surface of the internal fitting (Fig. 2.3) is sized in conjunction with the swage tube, bladder, and braid, to ensure that the desired compression of the braid and bladder is achieved.

Benjamin Woods, who first made FAMs with swaged end-fittings [51], set the precedent for the compression required of the bladder and braid to successfully swage an end-fitting. The braid requires a compression of 17% of its thickness, while the bladder requires a compression of 30% of its thickness. These criteria are used for sizing the internal fitting in conjunction with the other components.

The equations that define the desired sizing of each stepped surface of the internal fitting are as follows:

$$OD_{fit,brd} = OD_{swg} - 2(t_{swg} + t_{brd}(1 - \%Comp_{brd})) \tag{2.6}$$

$$OD_{fit,bld} = OD_{swg} - 2(t_{swg} + t_{brd} + t_{bld}(1 - \%Comp_{bld})) \tag{2.7}$$

where $OD_{fit,brd}$ is the large diameter of the end-fitting that serves as the contact surface for the braid, and $OD_{fit,bld}$ is the small diameter of the end-fitting that serves as the contract surface for the bladder.

Each equation starts with OD_{swg}, which is the outer diameter of the swage tube after having its diameter reduced by 2.7% through the swaging process. The thickness of the swage tube, t_{swg}, is assumed to remain constant through the extrusion process. The bladder and braid lie in the space between the inner diameter

of the swage tube and the internal fitting. Only the compressed braid, with thickness $t_{brd}(1 - \%Comp_{brd})$), lies in the space between swage tube and the larger step of the internal fitting, $OD_{fit,brd}$. For the smaller diameter step of the internal fitting, $OD_{fit,bld}$, the braid and bladder lie in the region between the internal fitting and swage tube. With the braid considered rigid in comparison to the bladder, this region is occupied by the uncompressed thickness of the braid, t_{brd}, and the compressed bladder thickness, $t_{bld}(1 - \%Comp_{bld})$.

While Equations 2.6 and 2.7 make sizing seem rather trivial, there are constraints on what is considered a feasible design. First, the solution found for $OD_{fit,bld}$ must be a value that is similar to the internal diameter of the bladder. A value of $OD_{fit,bld}$ that is much smaller than the bladder internal diameter would make the bladder bunch up and not lay flat on the internal fitting's surface. On the other hand, if $OD_{fit,bld}$ is much larger than the internal diameter of the bladder, it may not be possible to stretch the bladder over the internal fitting. It is also desirable to have a thin bladder to ensure that $OD_{fit,bld}$ is large enough to enable a large flow area through the internal fitting to maximize the dynamic response of the FAM, among other reasons.

As previously mentioned, the discrete and limited sizing of the bladder and swage tube diameters and thickness options makes sizing of a FAM a challenging design problem with few combinations that can be made to achieve the desired braid and bladder compression values. The sizing process, therefore, is an iterative process that requires different combinations of bladder and swage tube sizes to be tested for feasibility before a final combination of materials and sizing can be settled upon

that obeys the constraints and compression requirements of the end-fitting.

2.3.3 Final Sizing of FAM

The finalized sizing of the 7/8 in FAM's components and respective materials is provided in Table 2.4. A dimensioned drawing of the internal fitting is provided in Figure 2.7. Three FAMs were made to these specifications and tested for this research (Fig. 2.16).

	Material	**Outer Diameter**	**Thickness**
Braid	Biaxial Kevlar Sleeve	2 in	0.011 in
Bladder	Latex Tube	7/8 in	1/16 in
Swage Tube	Aluminum 6061-T6 Tubing	1 in	0.058 in
Internal Fitting	Aluminum 6061-T6	0.838 in, 0.748 in	-

Table 2.4: Construction of the 7/8 in diameter swaged FAM

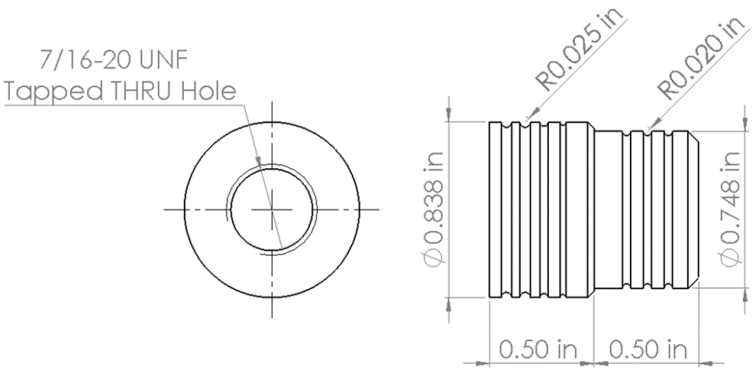

Figure 2.7: Dimensions of internal fitting used for the 7/8 in swaged FAM

2.4 FAM Method of Fabrication

Fabrication of a swaged FAM can be broken down into four basic steps: material preparation, assembly, swaging, and finishing. Material preparation requires

cutting all components of the FAM to length, and fabricating the tools needed for swaging. The FAM is then assembled by putting the FAM's components in place, prior to fixing them in place in the next step through the swaging process. Finally, the excess swage material and braid is removed in the finishing process to complete fabrication of the FAM.

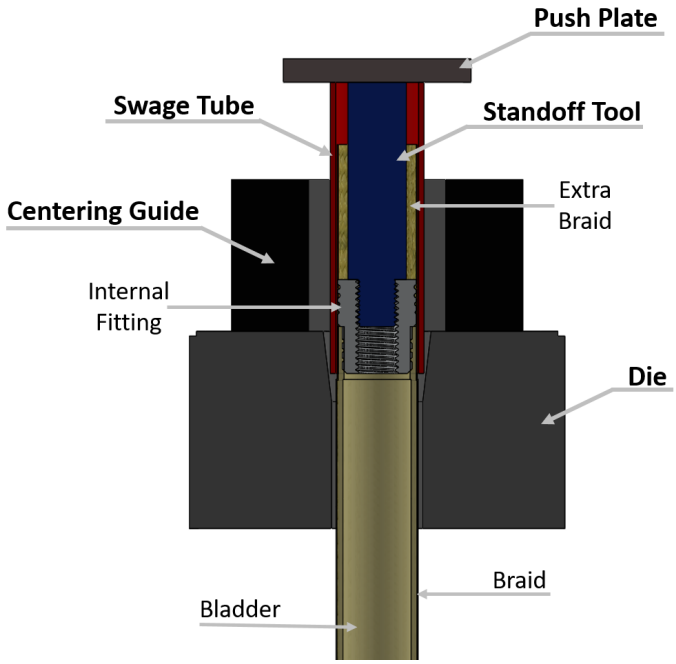

Figure 2.8: Swage tools (bolded) and FAM assembly in alignment prior to swaging

The main components of the swaging process are detailed in Figure 2.8. The tools used for swaging – the swage tube (with extended length), standoff tool, push plate, centering guide, and die – are labeled in the figure. The basic components of the FAM – the braid, bladder, internal fitting, along with the swage tube – are labeled in bold in the figure. It should be noted that the swage tube is initially much longer than the internal fitting. This extra length is necessary for extrusion to ensure that a pushing force can be applied to the top of the tube until the internal

fitting portion is completely extruded through the die. The excess tubing is pushed through the die using a follower tool, and then the excess material is removed later in the process to produce the finalized product.

2.4.1 Material Preparation

Prior to fabricating a FAM, the components of the FAM, as well as the tools required for swaging, must be prepared. Figure 2.9 is an image of these components as they are arranged prior to swaging the FAM. Once made and assembled, the tools used for swaging – the die, centering guide, standoff tool, follower tool, and push plate – can be used to fabricate multiple FAMs. However, the components of the FAM - the internal fittings, braid, and bladder - must be prepared prior to fabrication of every FAM.

Figure 2.9: Components of FAM and swage tools prepared prior to assembly

The two internal fittings are machined to the dimensions defined in Figure 2.7. A cylindrical piece of Aluminum 6061-T6 is reduced to the desired dimensions using a lathe. It is critical that the tolerances on the diameter of the internal fitting are kept within a few thousandths of an inch to ensure the correct compression of the braid and bladder. A deviation of just one-thousandth of an inch from the

prescribed dimensions of the internal fitting would result in a significant 9% change in the compression of the braid.

The length of the bladder dictates the final length of the FAM. The bladder length must account for the active length of the FAM plus the material that covers each lower step of the internal fittings. Approximately 1/8 in of space is left between the edge of the bladder and the step of the internal fitting to allow for axial expansion of the bladder upon compression. For example, with an internal fitting step length of 1/2 in, the bladder is cut to a total length that is 0.75 in longer than the desired active length of the FAM.

A generous amount of braid is used to ensure that there is excess braid to pull on while aligning components prior to swaging. The braid is cut to a length that equals the active length of the FAM, combined with the length of the uncut swage tube and width of two gripped fists. This combined length ensures that there is sufficient space to grab the braid above each swage tube before sliding the swage tube up into place over the internal fitting.

The swage tube is cut to a length that enables the press to apply continual pressure at the push plate until the entire internal fitting exits the bottom of the die (Fig. 2.11(a)). With the 1 in long internal fitting, and the 2.1 in depth of the die, the swage tube must be at least 3.1 in in length. The swage tube is then pushed the rest of the way through the die with the follower tool.

The follower tool is used to push the remaining swage tube out of the die subsequent to swaging the end-fitting (Fig. 2.11(b)). The tool has a diameter that is slightly smaller than the inner diameter of the die, allowing it to push onto the

top of the swage tube while not getting stuck in the die. In cases where the inner diameter of the swage tube is larger than the inner diameter of the die, multiple follower tools with reducing diameters may need to be used. An alternate method of removing the swag tube is to cut the swage tube above the fitting, straighten the cut on a lathe, and then push the swage tube out the way it entered the die with the follower tool. However, this alternate method is more time consuming, and the required cutting can be dangerous with the limited space between the bottom of the die and the fitting.

The standoff tool enables the press to apply force to the swage tube and internal fitting together – via the push plate – to ensure that there is no relative motion between the two components as the tube is extruded through the die. The combined length of the internal fitting and standoff tool are made to be equivalent to the length of the swage tube. The diameter of the standoff tool is reduced to enable space for excess braid between the standoff tool and the inside of the swage tube. The standoff tool is threaded at its bottom to screw into the 7/16-20 UNF tapped hole of the internal fitting. This provides a rigid connection between the internal fitting and standoff tool that ensures the correct alignment between components during the swaging process.

The push plate – alluded to above – is used to provide a surface for the press to apply force to the swage tube and standoff tool together. The push plate is simply a rigid metal plate with dimensions that are greater than the outer diameter of the swage tube.

The die was machined to the dimensions in Figure 2.6. As previously noted,

the inner diameter of the die's bore is sized to provide the desired compression of the swage tube. The die is made of hardened steel to ensure that it can withstand multiple swaging processes. The hardness of the steel, along with the large ratio of the die to bore diameter, help ensure that the bore does not flex and increase in diameter during the swaging process. The bore has a 7 degree tapered section followed by a straight section. A low taper angle ensures a gradual and progressive swaging process. Too shallow of a taper angle, however, requires a taller die and a longer swage tube which is more susceptible to buckling. The 1.35 in straight bore section is used to ensure the final diameter of the end-fitting remains fixed to the bore diameter. This section should be at least as long as the internal fitting to reduce the chances of the swage tube from *rebounding*, the tube increasing slightly in diameter as it exits the bottom of the die.

The centering guide is used to ensure that the swage tube enters the bore of the die straight. Any slight misalignment of the swage tube and bore can easily lead to failure of the end-fitting swage, ruining the entire FAM. The centering guide can be a specially fabricated part, or it can be as simple as machinist V-blocks as is used for swaging the 7/8 in FAMs here.

The last step prior to swaging is to prepare the epoxy. The epoxy is given about 15 minutes to thicken slightly prior to beginning assembly, to facilitate its application onto the end-fitting without excessive dripping.

2.4.2 Assembly

Assembly of the FAM prior to swaging is the most challenging part of making a swaged FAM. To assemble the FAM, the braid is first pulled over the bladder with the bladder centered along its length. A swage tube is then slipped over the braid and bladder. One end of the braid is clamped below the bladder to hold it in place while the other end is worked on (Fig. 2.10(a)). The braid is then folded back onto itself to expose the bladder in preparation for insertion of the internal fitting.

The internal fitting, with the standoff tool attached, has its outer surface coated with epoxy. The small diameter of the internal fitting is then positioned inside of the bladder (Fig. 2.10(b)). While maintaining the positioning of the internal fitting, the braid is then unfolded back over the internal fitting and standoff tool. The braid in the area around the internal fitting is then saturated with epoxy. Prior to applying the epoxy, the swage tube is positioned so its top is aligned with the bottom of the internal fitting to keep epoxy from running down onto the actuated portion of the FAM.

While holding the braid taught with one hand just above the standoff tool, the other hand is used to pull the swage tube up and over the internal fitting until the tops of the swage tube and standoff tube are level with one another (Fig. 2.10(c)). The hand holding the braid is also used to keep the standoff tool and end-fitting in place as the swage tube is pulled up over them. Pulling the swage tube over the internal fitting can take a considerable amount of force, with the required force depending on the amount of clearance allowed between the end-fitting components

prior to swaging.

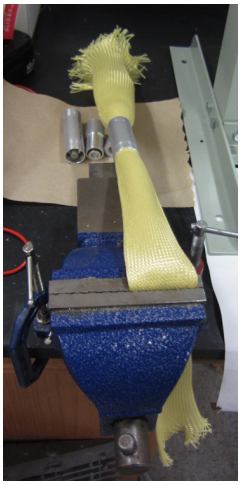

(a) Braid clamped below bladder

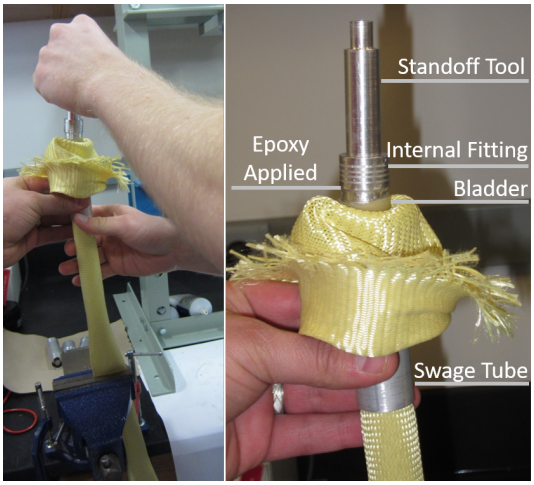

(b) Epoxy covered internal fitting placed inside bladder. The Swage Tube is positioned just below the internal fitting.

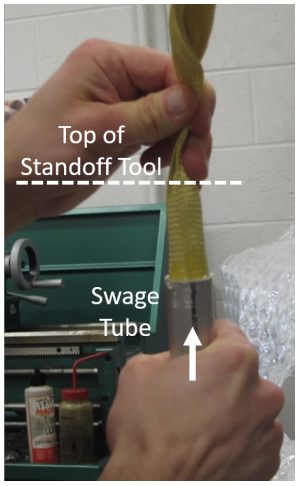

(c) Swage tube is pulled up over the internal fitting until even with top of standoff tool

(d) Braid is unclamped and funneled through die. Die and FAM are placed in press

Figure 2.10: Steps of the assembly process prior to swaging

At this point, the end-fitting components are in their final positions, and are ready to be swaged. The braid is unclamped from the table clamp, and the braid and bladder are fed through the die until the swage tube is resting in position at the entrance of the die's bore (Fig. 2.10(d)). The end-fitting is then swaged.

After swaging the first end, the other end-fitting is swaged following the same steps as with the first end-fitting. But prior to putting the second swage tube on, the die must be slipped onto the FAM. There is no way to get the die below the swage tube after the second swage tube is put onto the FAM. The extra braid that is left below the swaged end-fitting is then clamped into the table clamp, and the process is then repeated for the second end-fitting. It is especially important to pull the braid taught as the swage tube is pulled up over the second end-fitting to maximize the final braid angle of the FAM while ensuring that there is no space between the braid and bladder. Additionally, it is also important to pull on the braid along its longitudinal axis to ensure that the braid fibers are symmetric before the braid is fixed in place by swaging the end-fitting.

2.4.3 Swaging

Swaging is performed by extruding the end-fitting through the die. The extrusion force is provided by a 10-ton press that is actuated by hand through a hydraulic lever-arm. The force of the press is applied to the top of both the standoff tool and swage tube by way of the push plate. The swage components are aligned in-line with the bore of the die –as depicted in Figure 2.8 – before swaging of an end-fitting is performed.

Prior to swaging, a lubricant (e.g. White Lithium Grease) is applied to the outside surface of the swage tube to reduce friction forces between the swage tube and die while swaging. The push plate is then placed on the top of the swage tube

and standoff tool, and the press is lowered to a position that places it just above the push plate. Using the centering guide(s), a final check of alignment is performed to ensure that the swage tube is vertical and oriented in-line with the bore of the die. The press is then lowered to contact the push plate and then begin the swaging process.

The progression of the swaging process is shown in Figure 2.11(a). The FAM assembly is extruded through the die until the push block comes into contact with the die. At this point, with the entire fitting having exited the bottom of the die, the end-fitting is swaged. Excess swage tube still remains in the die, and is extruded the rest of the way through the die using the follower tool (Fig. 2.11(b)). The follower tool is carefully aligned with the swage tube, and then driven down into the swage tube until the swage tube exits the bottom of the die. The follower tool – which is loose in the die – can then be pulled back out of the top of the die by hand. After the swaging process is complete, the FAM is set aside for about 24 hours to let the epoxy cure before the final steps are performed to complete the fabrication of the FAM.

2.4.4 Finishing Process

The excess swage tube and braid that remains with the fitting after swaging is done needs to be removed before the FAM is complete (Fig. 2.11(c)). Removal of this excess material is performed using a lathe. Prior to putting the FAM in the lathe, the midsection of the FAM is covered with protective material (e.g. tape) for

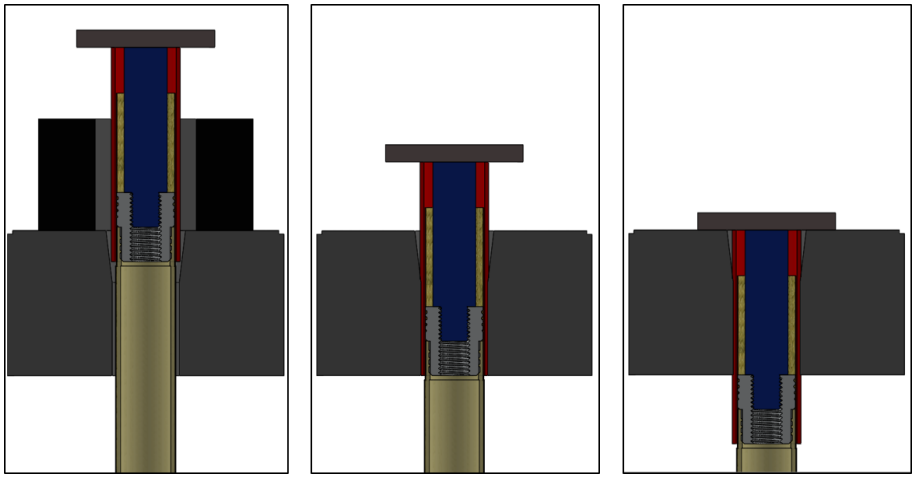

(a) FAM assembly extruded through die until internal fitting is completely through die

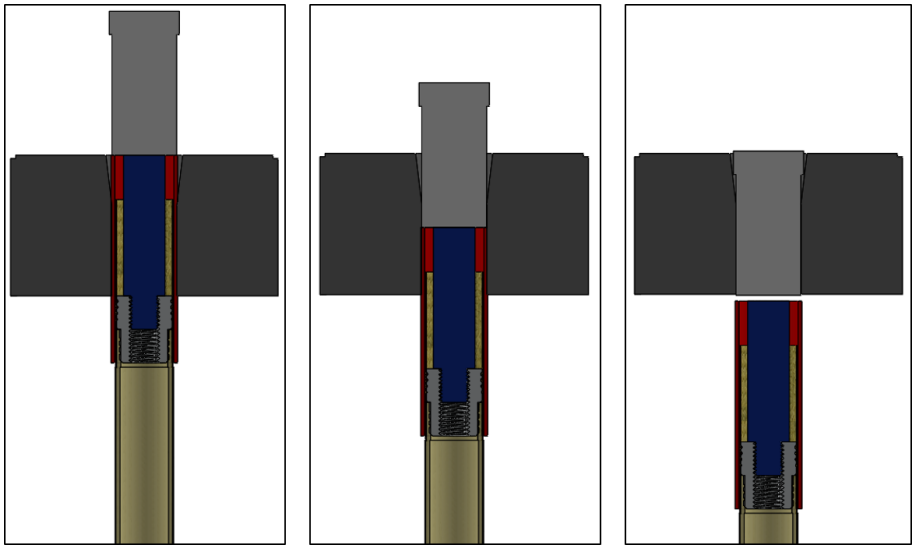

(b) Swage tube that remains in die is driven out using the follower tool

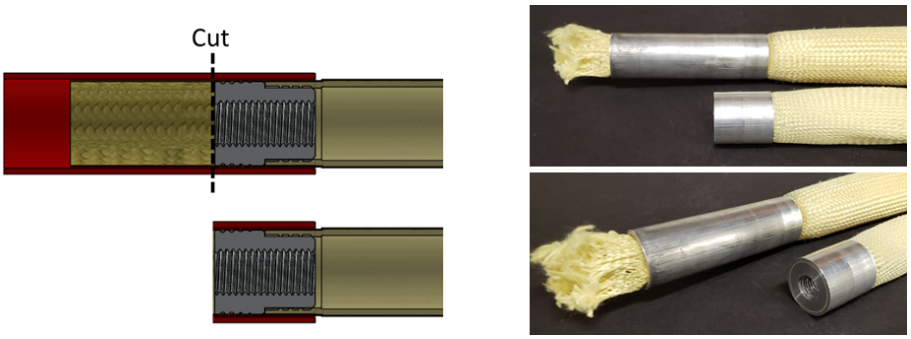

(c) Extra length of swage tube and braid is cut off to produce finished product

Figure 2.11: Progression of producing a swaged FAM end-fitting

its protection and the standoff tool is removed if possible. If the standoff tool can not be removed prior to cutting, it can be removed after carefully cutting away a portion of the swage tube to improve access.

The FAM is clamped by the jaws of the lathe chuck at the bottom of the swage tube, and with the top of the swage tube facing outwards. The rest of the FAM has a cylindrical space behind the chuck where it can lie and be supported while the end-fitting is being trimmed. The excess swage tube is gradually cut away up to the face of the internal fitting. The soft braid is more easily cut near the internal fitting where excess cured epoxy makes it more rigid. With a final pass of the cutting tool across the face of the internal fitting, the braid breaks away cleanly, leaving a nicely finished surface (Fig. 2.11(c)). Once the finishing process is performed on each end-fitting, the fabrication of the FAM is complete.

2.4.5 Modification to swaging process

Initial successes and failures in swaging 7/8 in FAMs resulted in a few modifications to the swaging process. Sometimes, attempts to swage a FAM were unsuccessful, resulting in the FAM being scrapped. The mode of failure was most often due to the swage tube buckling while being forced through the die (Fig. 2.12). A buckled swage tube immediately makes the swaging process impossible to continue with no way to force the end-fitting the rest of the way through the die.

Techniques to reduce the chance of the swage tube buckling during swaging have been learned incrementally through trial and error. Efforts focused on attempt-

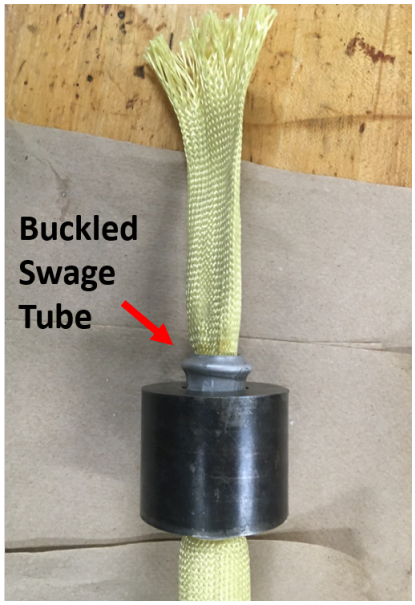

Figure 2.12: Buckled swage tube of failed swaging attempt

ing to reduce the force required to extrude the swage tube through the die, and on supporting the swage tube to increase its critical buckling load. As a note, some of these improvements have already been described in previous sections.

Steps for reducing the required extrusion force were targeted first. A straight, vertical alignment of the swage tube with the bore of the die was initially challenging to do by eye. Any slight misalignment in the swage tube results in the tube and end-fitting jamming in the die, and the resultant non-vertical force of the press on the swage tube reduces the load required for the tube to buckle. The centering guide, which has initially been machinist V-blocks, was devised and employed to ensure a vertical orientation of the swage tube. The use of a lubricant – white lithium grease – was also introduced to decrease the required extrusion force by decreasing the frictional forces between the straight section of the die bore and the swage tube. The grease is applied to the outside surface of the swage tube prior to

swaging. This has dramatically decreased the apparent force required by the press, and greatly improved the smoothness and consistency of the motion of the swage tube as it was extruded through the die.

Subsequent efforts focused on increasing the buckling load of the swage tube. The dimensions of the swage tube – constrained by the dimensions of the die, and by the sizing required to provide the desired compression of the bladder and braid – could not be altered to increase the load-bearing capabilities of the swage tube. Therefore, a means of supporting the swage tube was devised within this research.

The developed solution entails the use of an additional tube that slides within the swage tube for support, but can then be removed prior to entering the die. This revised swage assembly is illustrated in Figure 2.13, and images of the individual components are provided in Figure 2.14. The *tube support* is a 1 in outer diameter, 0.125 in wall thickness tube, that has 1.25 in of its 2 in length turned down to fit within the swage tube with minimal clearance. The tube support increases the area moment of inertia in the overlapped section by 75%, and leaves a maximum of only 1.85 in of unsupported swage tube below it. Overall, based on Euler's buckling load theory, this should approximately double the buckling load of the swage tube. The tube support adds a little bit of height above the swage tube, 0.75 in, that requires a *standoff extension* tool to ensure that force can still be applied to both the internal fitting and swage tube at the push plate. The standoff tool was modified to have a male end that receives the female end of the standoff extension for a secure, but easily removable connection between the two parts.

The entire modified assembly is aligned the same as with the prior basic swage

assembly shown in Figure 2.8, and includes the addition of just the two new parts: the tube support and the standoff extension. The progression of the swage process using the modified swage assembly is provided in Figure 2.15. As the swage tube is extruded through the die, its unsupported length decreases which beneficially increases its critical buckling load. Extrusion of the swage tube is performed with the tube support in place until the tube support begins to enter the die. At this point, the tube support and standoff extension are removed to ensure that they are not swaged within the swage tube as is being done with the internal fitting. Extrusion then continues as is done with the more general assembly until the end-fitting, and then the swage tube, are extruded completely through the die.

Notably, this modified swage assembly, in conjunction with the efforts made to reduce the required extrusion force, has greatly improved the swaging success rate. Furthermore, it has also facilitated an improvement to the strength of the end-fitting. Work on future FAM iterations desired an increase in the compression of the braid to improve the strength of the end-fitting. Targeted improvements in FAM development has included an increase in the compression of the braid to improve the strength of the end-fitting.

This increase in compression entails a slight increase in the diameter of the internal fitting, which further increases the extrusion force required to swage the FAM. The developed improvements to the swaging process have made this possible; Compression of the braid was increased to 27% which further increases the strength of the end-fitting.

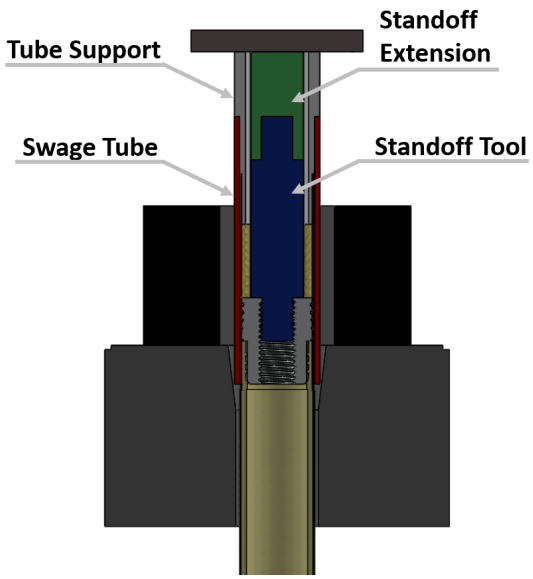

Figure 2.13: Modified Swage Assembly

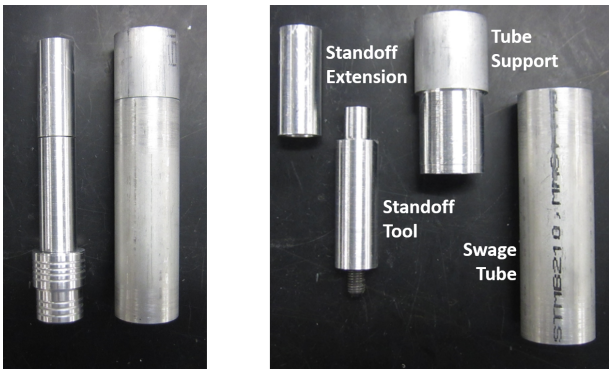

Figure 2.14: Labeled components of modified swage assembly

2.5 Testing Swaged FAMs

Three swaged 7/8 in FAMs were made for initial testing (Fig. 2.16). All three FAMs are identical in their construction, and were all made to similar active lengths. An isobaric force-contraction test was performed to characterize the actuation response of each of the FAMs for comparison. Then, two of the FAMs were tested to failure in an effort to test the strength of the swaged end-fittings. An ultimate

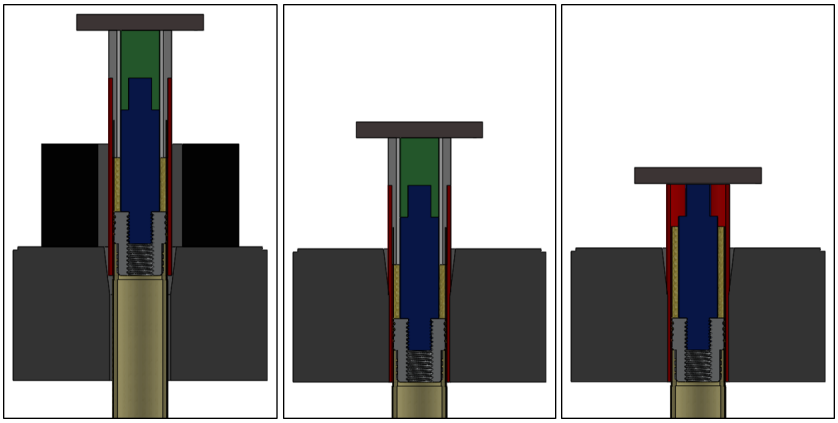

Figure 2.15: Swaging progression with modified assembly. Per methodology, the tube support and the standoff extension have been removed between frames 2 and 3, prior to continuation of extrusion.

tensile test was performed to test the end-fitting's holding strength of the braid. A burst test was performed to test the end-fitting's ability to contain the pressurized internal fluid. A factor of safety is calculated by comparing the maximum force and pressure at failure to the maximum values experienced in the normal range of operation of the FAM.

2.5.1 Characterization Test

The three FAMs were first characterized by testing their characteristic pressure-force-contraction responses. This test was performed on a material testing MTS machine, which controls the length state of the FAM while recording displacement, pressure, and force measurements. The FAM's internal pressure is fixed at a set pressure, and the FAM is then cycled between its maximum force, zero contraction state, called its *blocked force* state, and its zero force, maximum contraction state. The FAMs were redundantly cycled between these bounds three times at each

pressure. For a complete characterization of the FAM's expected pressure operating range, they were tested at pressures of 0 to 100 psi in 10 psi increments. The defining characteristics of the PAMs are provided in Table 2.5. The results of the characterization testing are shown in Figure 2.17. The test results for each FAM are overlayed onto the same plot for ease of their comparison. The consistency of the fabrication method is demonstrated by the fact that the responses of all three FAMs are nearly identical.

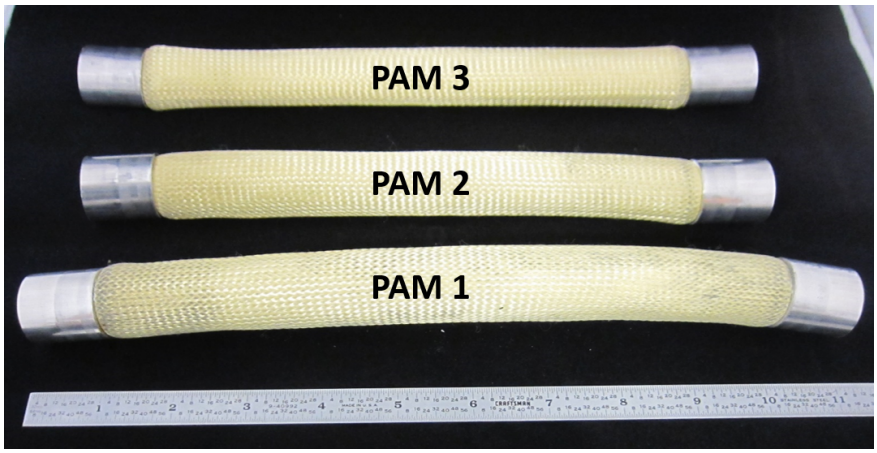

Figure 2.16: Tested 7/8 in swaged FAMs

	FAM 1	**FAM 2**	**FAM 3**
Active Length	9–3/16 in	8–1/64 in	8–29/32 in
Weight	0.190 lb	0.183 lb	0.192 lb
Blocked Force (100 psi)	1037 lb	1029 lb	1049 lb
Free Contraction (100 psi)	34.57 %	35.08 %	35.03 %

Table 2.5: Specifications of swaged FAMs used for testing

2.5.2 Ultimate Tensile Failure Test

An ultimate tensile failure test was conducted on FAM 2 to provide a measure of the maximum load that the FAM can support in tension. Although this is not

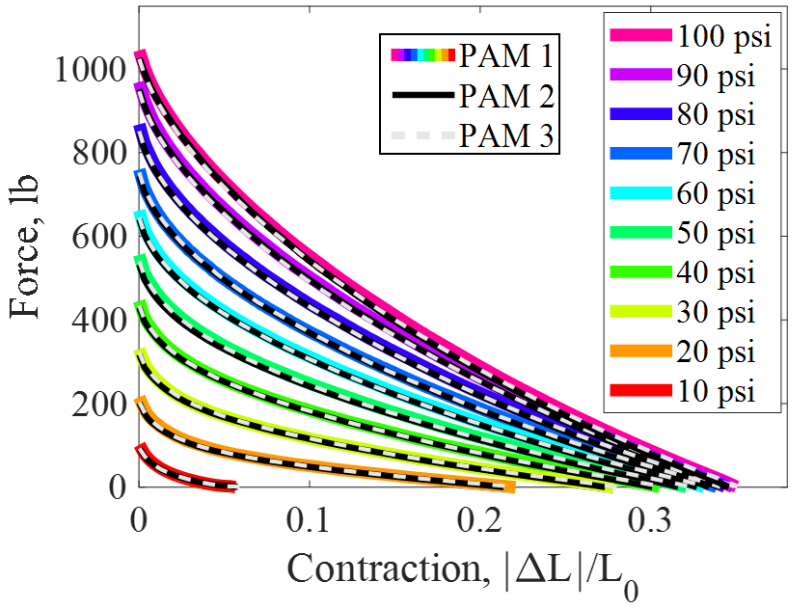

Figure 2.17: Isobaric force-contraction response of the three tested FAMs

within the normal mode of operation, it provides a quantitative measure of the strength of the FAM and its end-fittings. The test is conducted by leaving the FAM unpressurized, and slowly stretching it up to the point of failure. Figure 2.18(a) provides a plot of the test results, while Figure 2.18(b) provides images of the FAM at different stages of the test. This FAM was able to support over 2,147 lb before failing. The failure occured from the internal fitting slipping out of the end-fitting assembly, as can be seen at the top of the FAM in the pictures of Figure 2.18(b). The bladder and braid remained in their original positions within the swage tube after failure (Fig. 2.20). This indicated that the braid clamping region was the main point of failure. With increased compression of the braid, the failure load could likely be increased. This test showed, however, that the FAM can handle double the maximum load that occurs in the 0-100 psi operating range, for a safety

factor of about 2.

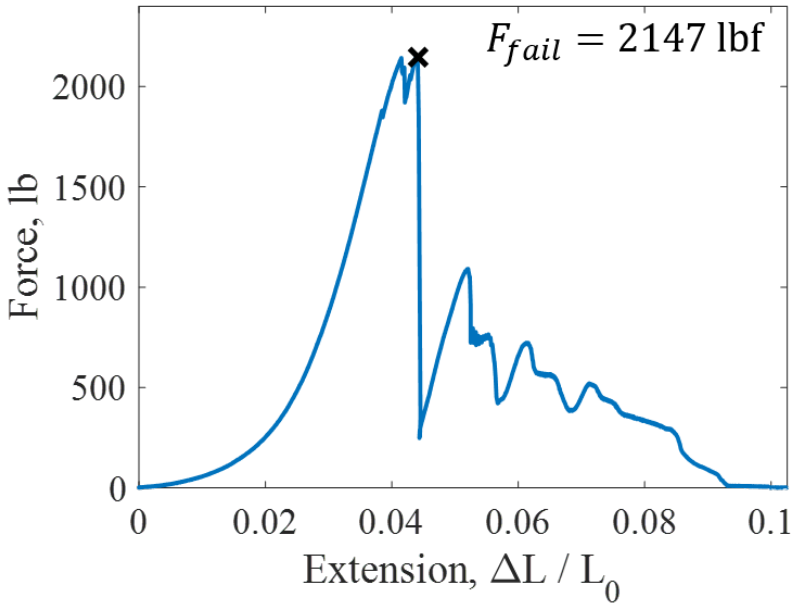

(a) Test results with failure of FAM occurring at 2,147 lbf

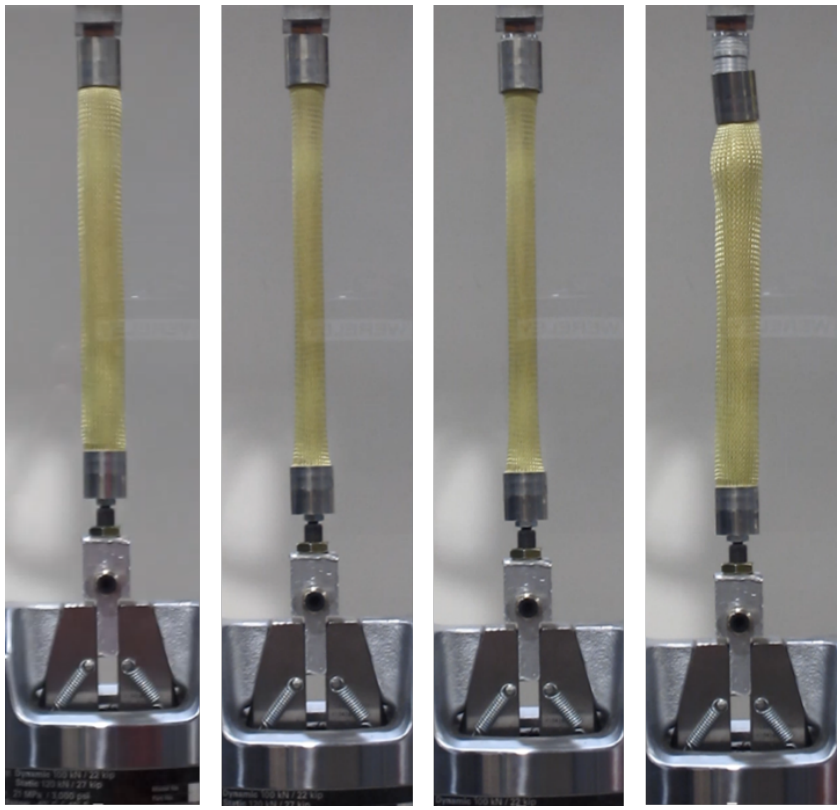

(b) Progression of FAM being pulled apart

Figure 2.18: Ultimate tensile failure test conducted on FAM 2

2.5.3 Burst Test

Additional testing was performed on the swaged FAM to determine the factor of safety with respect to the operating pressure. A burst test was performed on FAM 3. For this test, the FAM is held in its zero contraction state as its internal pressure is slowly ramped up until failure. While similar in nature to the ultimate tensile failure test, this test seeks to focus on the effectiveness of the bladder clamping region of the end-fitting.

The results of the burst test are shown in Figure 2.19(a), while Figure 2.19(b) has images of the FAM before and after failure. The FAM failed at a pressure of 280 psi, which provides the FAM a pressure factor of safety of 2.8 for the 0-100 psi operating range.

Figure 2.19(c) provides an image of the FAM after removal from the MTS machine with the braid rolled back to expose the underlying bladder. As with the ultimate tensile failure test, the mode of failure was separation of the internal fitting from the rest of the end-fitting assembly. The split in the bladder appeared to have occurred subsequent to the separation of the internal fitting from the end-fitting. Although this test targeted failure of the bladder, it is clear that the holding strength of the braid was the point of weakness as it had been with the ultimate tensile failure test. Past tests have displayed an actuation force at the burst pressure that was below that of the ultimate tensile force [37]. This is simply an indication of the fact that every FAM design has different limiting factors in the strength of their design.

With FAM 2 and FAM 3 having the same mode of failure, there would be an

expectation that they would fail at similar loads. It is interesting to note that the actuation force for the burst test was 2,639 lb, 492 lb higher than the maximum force achieved from the ultimate tensile failure test that left the FAM unpressurized. This could be due to any number of reasons. The FAM has a fixed length – and respective fixed braid angle – for the burst test, while the FAM experiences an increase in its length and braid angle for the ultimate tensile failure test leading to reorientation and eventual jamming of the braid prior to failure. It is possible that the relative motion and orientation of the fibers at failure could have detrimental effects on the holding strength of the end-fittings. It is otherwise unknown if the internal pressure of the FAM in the burst test would have any other effects on increasing the strength of the FAM. The discrepancy in failure load could more easily be attributed to slight differences in the fabrication of the two FAMs. An internal fitting of FAM 3 had a braid compression diameter that was two-thousands of an inch larger – due to limits in machinist precision – that resulted in braid compression estimates of 15.9% versus 13.6%. This is compared to the desired design compression of 17%. This slight variation of the braid compression is unavoidable, but may also indicate how a few thousandths of an inch can have a large effect on the holding strength of the FAM's end-fittings.

2.5.4 Extended Use Failure

Many 7/8 in swaged FAMs have been made within this research since the development of the presented swaged fabrication method. Besides the three FAMs

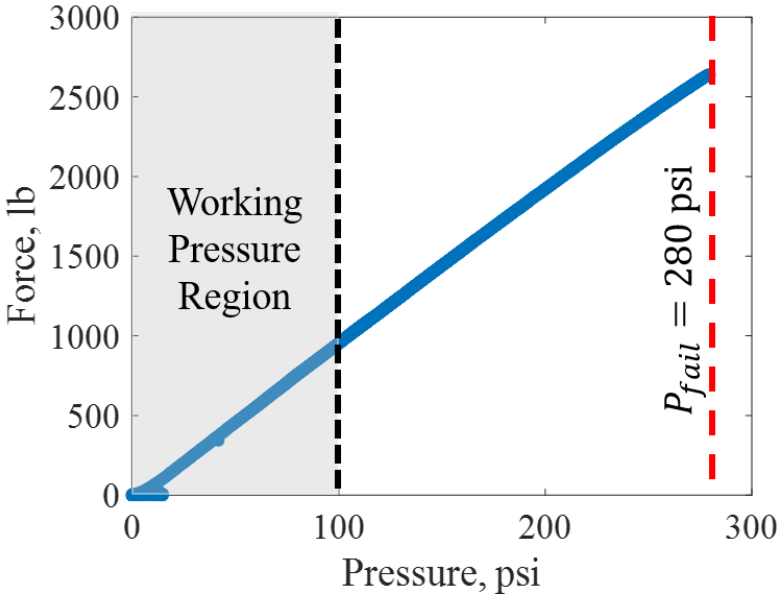

(a) Test Results with failure at 280 psi (2,639 lbf)

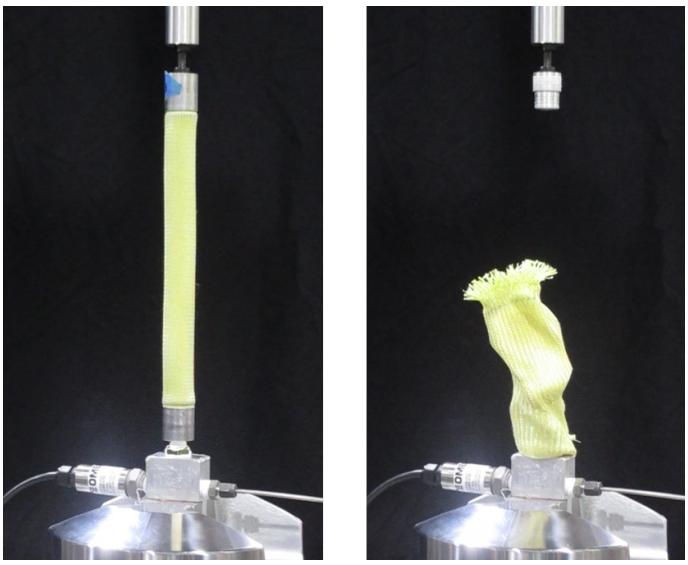

(b) Images of before and after failure of FAM

(c) Failed FAM with braid rolled back to expose bladder

Figure 2.19: Burst test conducted on FAM 3

tested for this research, twelve other FAMs have been fabricated, characterized, and then used for various projects and research. Of the thirteen FAMs that were not intentionally taken to failure, only three of them have failed after months of extensive use.

One of those FAMs failed due to a fabrication flaw; epoxy had unintentionally located on the edge of the braid during the swaging process making it rigid and brittle. Over repeated cycles, braid fibers in this small region near the end-fitting began to sever. This weakness in the braid left the underlying bladder unsupported, leading to a pinhole leak in the bladder that made the FAM unusable.

The other two FAMs displayed a failure mode that was identical in nature to the failures of FAM 2 and FAM 3 (Fig. 2.20). After many cycles of testing, the FAM's internal fittings slipped out of the end-fitting at a point when each FAM was in its blocked force state at 100 psi. This shows that this failure mode was not unique to the methods used to failure test the FAM, but was instead indicative of the realistic failure mode of the FAMs through regular usage. This also made clear that future improvements to increase the strength of the FAM should focus on increasing the compression of the end-fittings. Subsequent efforts were, in fact, made to increase the compression of the braid in the end-fitting.

2.5.5 Subsequent Improvements to end-fitting

Subsequent to the tests performed for this research, the compression of the braid has been incrementally increased in an effort to increase the strength of the

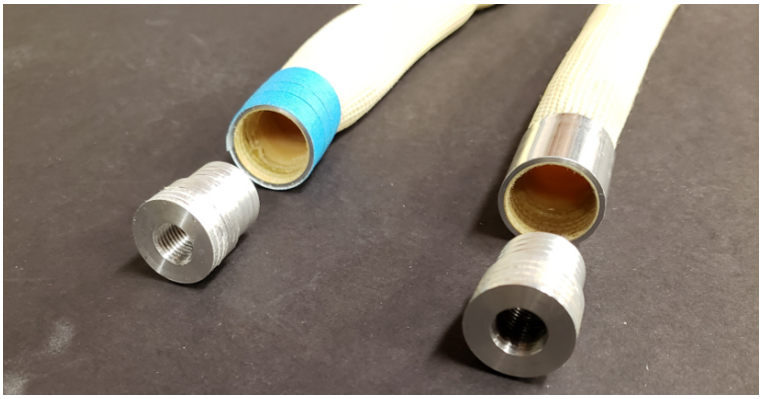

Figure 2.20: FAMs with failure due to internal fitting slipping out of end-fitting assembly

end-fitting. Increasing the compression of the end-fittings increases the extrusion force required to swage them. Therefore, the ability to increase the end-fitting compression is an opportunity now afforded by the modifications made to the swaging process as detailed in Section 4.5.

The compression levels have been increased to a maximum of 27% compression of the braid, and a slight increase to the percent compression of the bladder. At these compression levels, it is difficult to apply any more force through the lever arm of the 10-ton press. Instead of smoothly and continuously moving through the die during the extrusion process as it does at lower levels of compression, the swage tube catches and gives with audible and visual hesitations as the swage tube resists continued motion through the die. At these levels of force, the swage tube is more prone to buckling, and the 10-ton press appears to be approaching the maximum force that it can apply. Attempting to increase the compression of the end-fitting beyond these levels, therefore, would likely require revisiting the design and sizing of the FAM components, as well as require the acquisition of an upgraded press along

with the fabrication of new swaging tools. For fabrication of all future 7/8 in FAMs, the new level of braid compression of 27 % supplants the previous design objective of 17% compression.

2.6 Conclusion

This research works to provide the following contributions: The initial development of swaged FAMs by Robinson and Woods has been extended by this research, with improvements made to the methods of FAM design and fabrication which can serve as a reference for further development. The improvements are demonstrated through the results of the 7/8 in FAM that was developed in this work. This development of the 7/8 in swaged FAM increases the capabilities of FAMs, as well as demonstrates consistency in the manufacturing process, required for greater adoption of FAMs. With a source pressure of 100 psi, the resulting 7/8 in FAMs produced a maximum force of over 1,000 lbs, and a maximum contraction of 35% while providing a safety factor of greater than two. The production of multiple FAMs with nearly identical actuation characteristics speaks to the consistency of the improved swaging process developed here. The improvements to the FAM swaging process yielded an increased success rate and enhanced the efficiency of the FAM manufacturing process, and furthermore, enabled increases in end-fitting compression from 17% to 27% which would yield increases in the failure strength of the FAM.

The 7/8 in FAM developed in this work will serve – and is already serving – as a basis for multiple research efforts. This FAM will be used for research involving

improvements to FAM modeling and characterization methods. This FAM will also be applied to actuate mechanisms being developed in a research setting that have promise to be adopted for commercial use. The fabrication methods developed in this work, with improvements to efficiency and safety of the extant methods, help prepare for the scaling up of production efforts. The sizing and design methods presented in this work can serve as a blueprint for the fabrication of FAMs at different size scales to tailor the characteristics of the FAM depending on the application.

FAMs provide unique actuator characteristics that gives them distinct advantages – in comparison to other common forms of actuation – in an engineering landscape that increasingly sees the adoption of "bioinspired" designs. It is hoped that swaged FAMs, using the improvements presented in this research, will help FAMs to be viewed as a practical and desirable form of actuator for increased adoption in future work.

Chapter 3: Improvements in FAM Characterization Through Accurate Control of Pressure[1]

3.1 Introduction

McKibben actuators are being applied to an increasingly diverse number of applications due to their many desirable characteristics including their high force-to-weight ratio, simplicity, and inherent compliance. Previous work has established McKibben actuators as an ideal form of actuation when specific work, specific power, and power density are of primary importance in actuator selection [18]. With a basic construction consisting of an elastomeric bladder, surrounding load-bearing braided sleeve, and two end-fittings, an internally pressurized McKibben actuator can provide a contractile force of more than ten-thousand times its own weight, and achieve maximum strokes of up to 40% of its resting length [37]. This simple construction makes them readily adaptable to various environments, highly durable with a long fatigue life [37, 57], and easily scalable with diameters ranging from 4 mm (0.15 in) [18] to 40 mm (1.5 in) [27] and forces ranging from several pounds to

[1]Chambers, J.M., and Wereley, N.M., 2021. Influence of hydraulic versus pneumatic working fluids on quasi-static force response of fluidic artificial muscles. Journal of Intelligent Material Systems and Structures 32.3 (2021): 385-396.

several thousand pounds.

Initially conceived by Joseph L. McKibben in the early 1950's as a basic fluid driven stroking device for use with his daughter's arm orthotic, the application of McKibben actuators has expanded to numerous robotic and aerospace mechanisms [6,58]. Since its inception, the McKibben actuator, known more generally as a fluidic artificial muscle (FAM), has typically been operated pneumatically. Incremental improvements in performance and durability have been made through adjustments in FAM geometry, material selection, end-fitting design, and fabrication methods. Research efforts have also been focused on the accuracy and fidelity of modeling pneumatic FAMs for control purposes. Using empirical test data, highly accurate semi-mechanistic models have been developed for pneumatic FAMs [48].

In recent years, research efforts for FAMs has expanded to the use of different working fluids as the source of internal pressure. FAMs have typically been operated pneumatically, however, as their range of applications has expanded to aqueous [59,60] and aerospace environments [34,35,61], it has become necessary to investigate working fluids that are perhaps better suited to these roles. As an example, for typical use in atmospheric environments, surrounding air can easily be obtained, compressed and stored, and vented to the surrounding environment making air a sensible working fluid choice. The same logic can be applied for the use of hydraulic actuation in aqueous environments.

The comparison of working fluid compressibility can also differentiate fluid selection. Fluid compressibility affects the stiffness of FAMs, with air providing more compliance than what hydraulic fluids provide. However, the incompressibility

of hydraulic fluids results in better position control accuracy, a quicker response to load variations, and higher force and pressure bandwidth [33]. Actuation efficiency is also affected, with hydraulic efficiencies shown to be about 60%, compared to about 30% for pneumatics [19, 62, 63]. Other considerations for fluid choice include weight, viscosity, heat capacity, thermal conductivity, and corrosion effects [63]. Comparisons between hydraulic fluids such as water and hydraulic oil have also been drawn. Hydraulic oils provide lubrication and corrosion resistance benefits to the pressure system, but also require specialized FAM bladder materials that do not deteriorate upon contact with oils [19].

Few studies have investigated hydraulically powered FAM actuation [15, 27, 32, 59, 64, 65]. Fewer still have examined the direct comparison between pneumatic and hydraulic FAM actuation [16, 19, 33]. Focchi (2010) performed a comparative study focusing on the dynamics and control of water versus air actuation by analyzing the stiffness variation of water and air with respect to pressure, and experimentally validated that pressure bandwidth, force bandwidth, and position accuracy can be increased using water. Meller (2014) investigated the efficiency of air versus water actuation with results showing 35-60% efficiency with hydraulic actuation, while pneumatic actuation only achieved an efficiency of about 25%.

Tiwari (2012) attempted to back the assumption from past pneumatic FAM (PAM) models that have indicated that pneumatic and hydraulic powered FAMs should provide the same force output independent of working fluid choice in quasi-static operation. With a 1/8 in FAM, Tiwari (2012) conducted constant pressure tests with water and air, but results showed significant discrepancies between their

response curves. The force response discrepancies between tests of the two working fluids was cited as likely being due to inaccurate pressure control. This left their hypothesis of working fluid independence of the quasi-static force response with an uncertain conclusion.

The research described in this chapter is an experimental investigation of the effect of working fluid choice on the quasi-static pressure dependent force-contraction response of FAMs. Using air or water as the working fluid, characteristic isobaric force-contraction response curves are compared for both a large and small scale FAM. Learning from Tiwari's work where inaccurate pressure control resulted in an inconclusive comparison between air and water actuation, in this research, hydraulic and pneumatic pressure systems were developed to provide precise and accurate control of pressure to ensure a reliable comparison of the two working fluids. Back-to-back testing of FAMs using water and then air as the working fluid was conducted to show the independence of working fluid choice on the quasi-static response of FAMs.

3.1.1 Basis of Work

The hypothesis that the quasi-static force response of FAMs is independent of working fluid choice can be explained through analysis of previously developed models of PAMs. These models have been developed and refined over the years to provide an accurate representation of a PAM's quasi-static behavior. Most recently, the fidelity of a semi-mechanistic model based on a force balance approach was im-

proved by including empirically fit coefficients that represent the material properties of the elastic bladder [48]. For this model, force is a function of the working fluid pressure, P, and the PAM actuator length, L, as:

$$F(P, L) = F_G + F_{bld,c} + F_{bld,z} \tag{3.1}$$

where

$$F_G = P\pi R^2(2tan^2\theta - 1) \tag{3.2}$$

$$F_{bld,c} = \sigma_z \left(\frac{V_{bld}}{L}\right) \tag{3.3}$$

$$F_{bld,z} = -\sigma_c \left(\frac{tL^2}{2\pi RN^2}\right) \tag{3.4}$$

where the number of turns of a single braid fiber about the actuator diameter, N, and the volume of the incompressible bladder, V_{bld}, are fixed values that describe the construction of the actuator. Braid angle, θ, bladder thickness, t, actuator radius, R, and bladder stress in the longitudinal and circumferential directions, σ_z and σ_c respectively, are all values that are directly or indirectly functions of the current actuator length, L.

Through examination of the terms of this force model, it can be seen that actuation force is dependent only on PAM geometry (R, θ, V_{bld}, t, L, R, N), material composition (σ_c, σ_z), and on the working fluid pressure (P). The first term of the model, commonly known as the Gaylord force, takes into account the internal pressure acting on the bladder, and how this pressure is transformed into an axial force through the surrounding braid (Fig. 3.1(a)). The second and third terms of the model equation account for energy losses due to straining the bladder during inflation (Fig. 3.1(b)). With no dependencies on fluid properties other than pressure, it can be assumed that this force response model is transferable to use for FAMs with

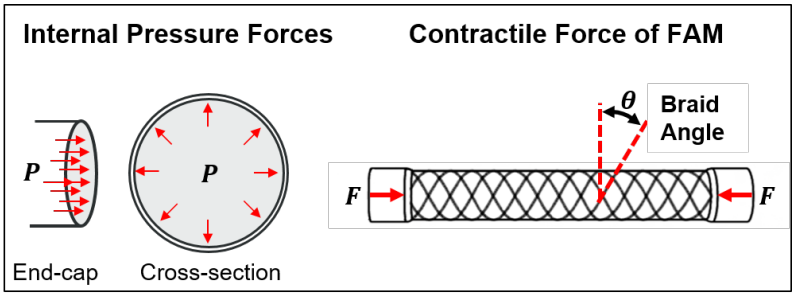

(a) Components that describe transfer of pressure force to axial force through the braid (Equation 3.2)

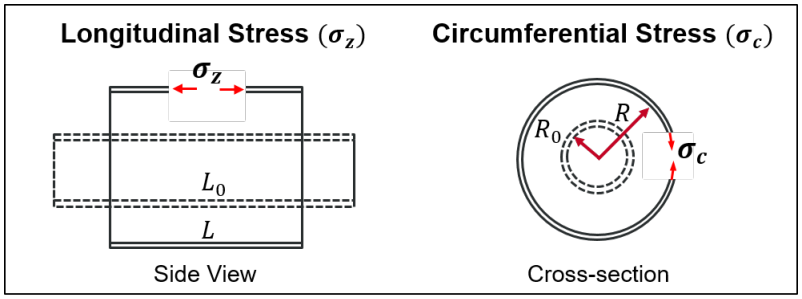

(b) Components that describe energy loss from stretching the bladder (Eqs. 3.3 and 3.4)

Figure 3.1: Illustrations of the components of the force-balance model given in Equation 3.1

working fluids other than air. This research was conducted to confirm the fidelity of this assumption, and therefore extend the use of current PAM models to use with FAMs as a whole independent of the applied working fluid.

3.2 Experimental Test Setup

To compare FAM actuation with different working fluids, the FAM was experimentally tested with both air and water as the working fluid. The method of characterizing the actuators pressure-force-contraction response follows that of previous PAM characterization testing [18]. The FAM is quasi-statically and isobarically stroked from its resting length to its pressure dependent free-contraction

(zero force) length. For this research, the FAM was cyclically tested at set pressures of 20-100 psi in 20 psi increments. Test cycles were performed at 0.02 in/sec, which is slow enough to ensure the quasi-static test assumption holds.

Testing for this research was conducted in a 22 kip MTS servo-hydraulic test machine that directs the stroking of the FAM, while recording external inputs of pressure (Omega PC209-200G5V), and force (Honeywell Model 31 Mid). Testing of each working fluid was conducted successively without removal of the FAM from the test machine in order to retain the FAMs reference length state and alignment. Fixtures attaching the FAM to the test machine were designed to be readily adapted to the hardware required to allow flow of each working fluid into the FAM without removal of the fixtures from the test machine.

3.2.1 FAM Test Specimens

Both a large and small scale FAM were fabricated for comparison testing of air and water driven actuation to ensure size independence of observed phenomenon (Fig. 3.2). The small-scale FAM is a 3/16 in diameter FAM as is used in [18]. This FAM typically produces a maximum force in the blocked force condition of about 50 lbf, and can typically achieve a maximum contraction of 25-35%. The large-scale FAM is a 7/8 in diameter FAM as is used in [28], and typically produces a maximum force of about 1000 lbf, and has typically achieved a maximum contraction of 30-40%. The construction materials and sizing of each FAM is provided in Table 3.1.

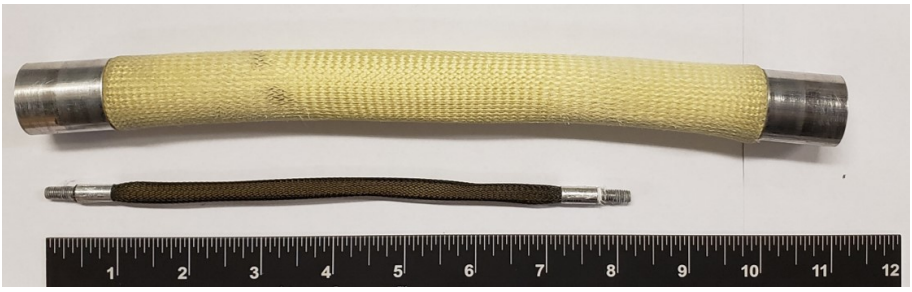

Figure 3.2: The FAMs used in this study with outer diameters of 7/8 in (top) and 3/16 in (bottom)

Table 3.1: Construction and specifications of the 3/16 in and 7/8 in diameter FAMs

	3/16 in Dia. FAM	**7/8 in Dia. FAM**
Active Length	6-27/64 in	8-49/64 in
Braid	Polyethylene Terephthalate (PET)	Kevlar
End-Fitting	Machined Alum. 10-32 Threaded Rod	Machined Alum. 6061-T6
Swage Tube	Alum. 6061-T6 Tubing	Alum. 6061-T6 Tubing
Total Length	6-59/64 in	10-15/16 in
Weight	0.01 lbm	0.18 lbm

3.2.2 Pressure Systems

Direct comparison between the two working fluids requires precise and accurate control of the input pressure to the FAM to maintain a true isobar for each cyclic test. Careful regulation of pressure is imperative to ensure that any discrepancy between the FAM force response for each working fluid can be positively attributed to the working fluid and not to an imprecise feed pressure.

This requirement drove the development of pressure control systems for water and air. For previous PAM testing, air pressure had been controlled by a variable pressure regulator. While using a pressure regulator is commonly sufficient for

holding a fixed volume system at a constant pressure, the inflow/outflow of air required for internal volume changes of a stroking PAM often results in inconsistent control of outlet pressure to the PAM. An inherent drawback to pressure regulators is their tendency to exhibit an observed outlet pressure that is inlet pressure, flow rate, and flow direction dependent [66]. This phenomenon has been apparent in previous PAM tests, where the regulator has constricted air inflow/outflow resulting in higher than set pressures when the PAM internal volume is decreasing (during eccentric motion), and lower than set pressures when the PAM volume is increasing (during concentric motion). If a person were to assume the test pressure was isobaric, this would result in an increase in apparent hysteresis, a decrease of the apparent contraction, and an increase in apparent maximum force. Figures 3.3 and 3.4 show an example of this described phenomenon by comparing the results of testing with (black lines) and without (colored lines) the addition of a controllable proportional valve to accurately control pressure (as will be described in subsequent sections) for a small and large scale PAM respectively. Figures 3.3(b) and 3.4(b) show a clear discrepancy in measured pressure between the use of the pressure regulator with and without the controllable valve. This pressure inaccuracy resulted in the differences in force response as seen in Figures 3.3(a) and 3.4(a), with an appreciable difference in magnitude of the hysteresis and maximum force for each tested pressure. Although the use of a pressure regulator alone was previously deemed sufficient for basic PAM characterization, the examples shown in Figures 3.3 and 3.4 demonstrate how constant pressure characterization tests have not been truly isobaric. With inconsistent pressure variations, this would be an insufficient system for the direct

comparison of different working fluids, and requires an improved pressure control system for handling air.

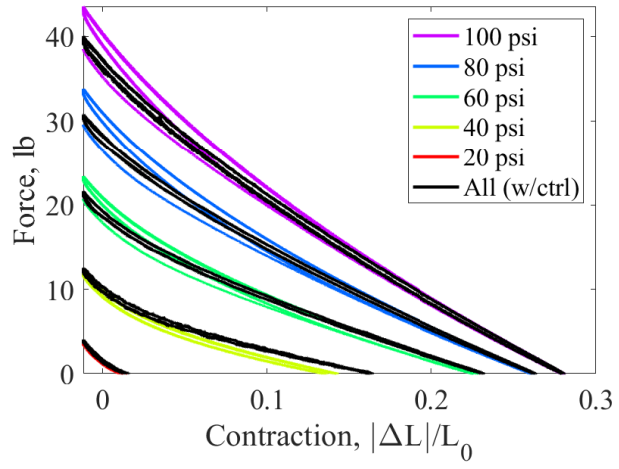

(a) Force-contraction response

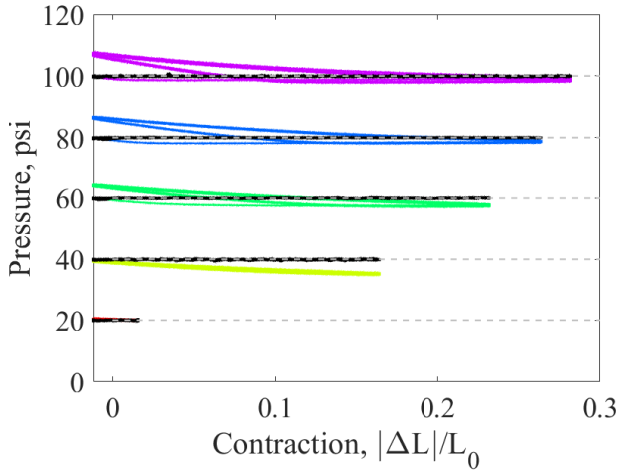

(b) Measured pressure during response testing

Figure 3.3: 3/16 in FAM characterization testing with (black lines) and without (colored lines) the addition of a controllable valve for accurate pressure control

To perform water FAM testing, a hydraulic pressure system had to be developed. The incompressibility of water results in a hydraulic pressure system that is very different in nature to that of the open-circuit air pressure system. There are a few examples of pressure systems that have been developed for hydraulic FAM

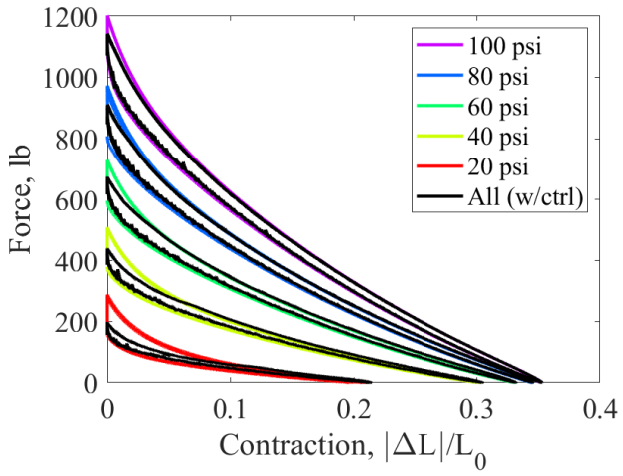

(a) Force-contraction response

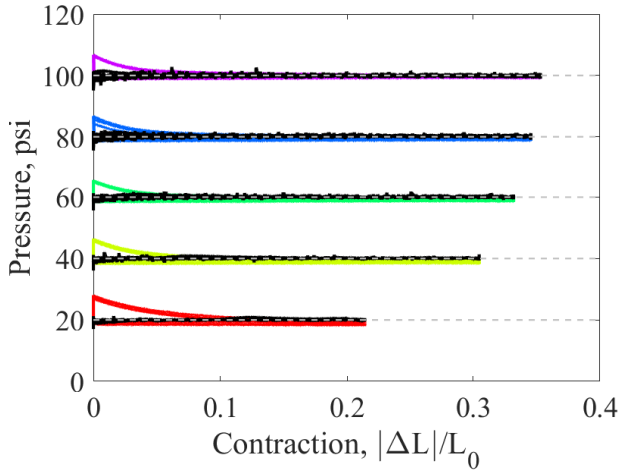

(b) Measured pressure during response testing

Figure 3.4: 7/8 in FAM characterization testing with (black lines) and without (colored lines) the addition of a controllable valve for accurate pressure control

testing by other researchers [15,33,65]. Methods for building water pressure include using a pump with valve restricted flow [65], a pump with accumulator and water compatible proportional valve [33], or a piston-driven, closed-volume system [15]. An overview of the air and water pressure systems used for this research are detailed in subsequent sections.

3.2.2.1 Pneumatic Pressure System

Shown in Figure 3.5, the air pressure system for pneumatic FAM testing is the same as what has been used for previous PAM testing with the addition of a proportional valve to more precisely regulate air flow. A portable 200 psi air compressor (DeWalt D55146) was used to compress and store pressurized air. A pressure regulator (Excelon R73G) with digital pressure transducer (SSI Technologies MGA-9V) was used to set a constant supply pressure of 115 psi, 15 psi above the maximum pressure to be tested. A 5/3-way proportional control valve (Enfield Technologies LS-V05s) was then used to directly control FAM pressure. Airflow in and out of the FAM was directed through the top of the FAM, while the bottom of the FAM was closed. A controller (Arduino Uno) was used to direct proportional valve actuation to control FAM pressure. The Arduino received instantaneous pressure state values for controller feedback through a pressure sensor (Omega PX209-200G5V) mounted to the fixture just above the air inlet of the FAM. A 1000 lbf load cell (Honeywell Model 31 Mid) was fixed in line with the FAM to measure the contraction force output of the FAM.

3.2.2.2 Hydraulic Pressure System

Testing of a water driven FAM required the development of the hydraulic pressure system as shown in Figure 3.6. The incompressible nature of water, along with the limited availability of water compatible components dictated that the hydraulic system would be very different in nature from the pneumatic system. The hydraulic

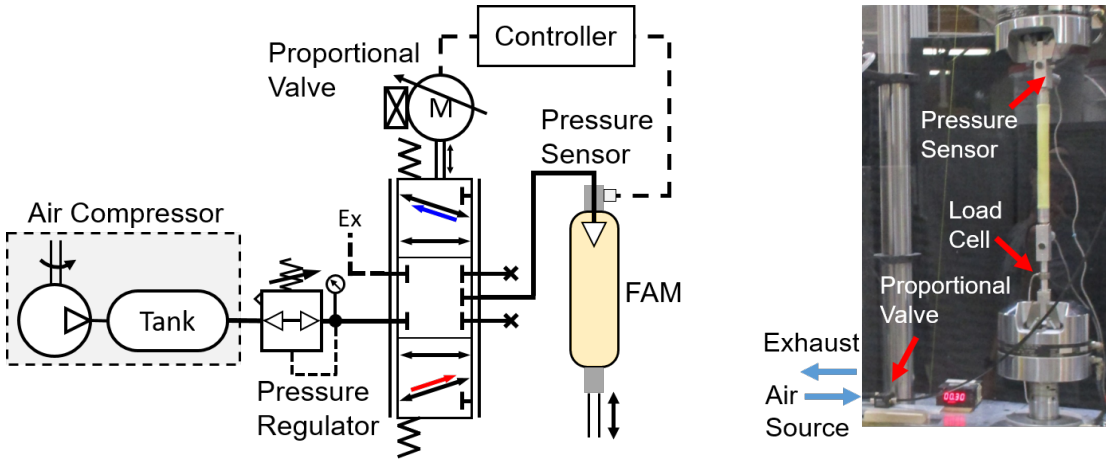

(a) Control system schematic

(b) Experimental test setup

Figure 3.5: Pneumatic pressure control system

circuit uses a continuously running, variable-speed pump. The fixed displacement gear pump (Fluid-o-Tech FG204) requires a fluid reservoir and inline filter to provide circuit pressure. To ensure that the pump does not have to sustain damaging hydraulic hammer effects from constantly switching directions to control pressure about a set-point, the FAM was made open at each end-fitting to allow a continuous flow of water in a single direction. Therefore, for pressure to build up in the circuit, flow is restricted downstream of the FAM by a needle valve (max orifice diameter of 0.175 in). The needle valve orifice diameter is reduced to the point where the pump can provide enough dynamic range without saturating: constrained enough to enable the maximum test pressure to be obtained, yet open enough to allow outflow of the system for FAM internal volume reductions without having to reverse pump direction. As a precaution to avoid sudden spikes in pressure due to the incompressibility of water, an adjustable relief valve (Watts LF 530-C STD) is positioned between the pump and FAM to relieve pressure if it exceeds 110 psi. An Arduino is

used to control pump speed to achieve the desired isobaric pressure.

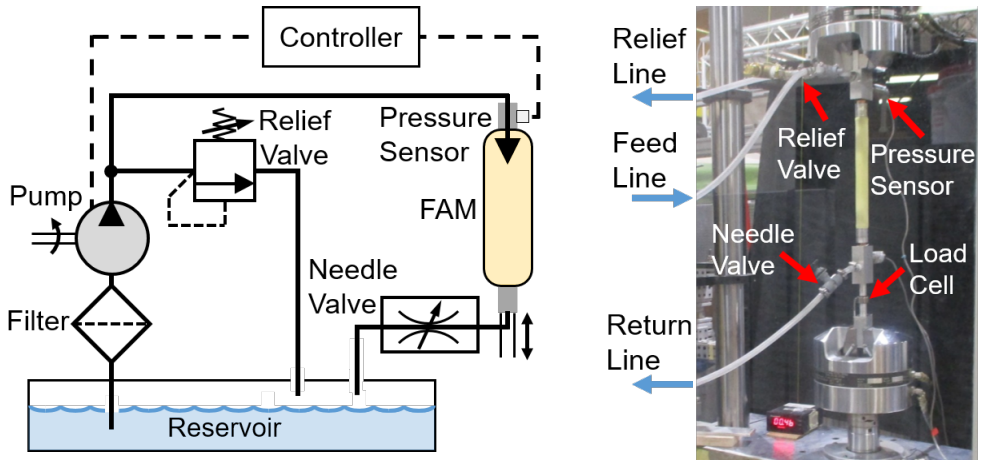

(a) Control system schematic (b) Experimental test setup

Figure 3.6: Hydraulic pressure control system

3.2.3 Pressure System Control

A proportional-integral (PI) closed-loop feedback controller was implemented and tuned to regulate each pressure system to the desired set isobar. The control input to the system acts to minimize the error, $e(t)$, between the desired set pressure, P_{set}, and the measured pressure, P_{meas}. The controller receives a pressure sensor voltage as input, and outputs a control signal in the form of a 5 V pulse-width modulation (PWM) signal. The Arduino produces a control signal value, $u(t)$, of 0-255 as a digital representation of the PWM output that translates to a 0-100% duty cycle. This 0-100% duty cycle produces an approximation of the 0-5 V analog input values required for control of the proportional valve and pump.

The control signal, $u(t)$, is calculated using Equation 3.5 for each control loop iteration as illustrated by the block diagrams in Figure 3.7. The feedback control

signal is manipulated by two user-defined tuning gains: the proportional gain, K_p, and the integral gain, K_i. To limit integral windup and saturation of the control input to the proportional valve/pump, both the integral term and overall control signal are constrained from commanding a value below 0 (0 V) or above 255 (5 V). A derivative term was not included to avoid the effects of noise from the pressure sensor.

The feedback controller is augmented by a system dependent open-loop control component, v, as defined in Equation 3.6. This open-loop control component reduces the role of the feedback controller to disturbance rejection, and results in improved pressure set-point tracking.

$$u(t) \quad = K_p e(t) + K_i \int_0^t e(\tau) d\tau + v \tag{3.5}$$

where

$$v = \begin{cases} v(P_{set}) & \text{if } hydraulic \\ 2.5\,V & \text{if } pneumatic \end{cases} \tag{3.6}$$

Values for the tuning gains, K_p and K_i, as well as the models used for the open-loop control component, v, are dependent on the applied pressure system and FAM, and are detailed in subsequent sections below. Control signal values are presented in the equivalent 0-5 V analog output of the PWM signal (opposed to the 0-255 signal used by the Arduino).

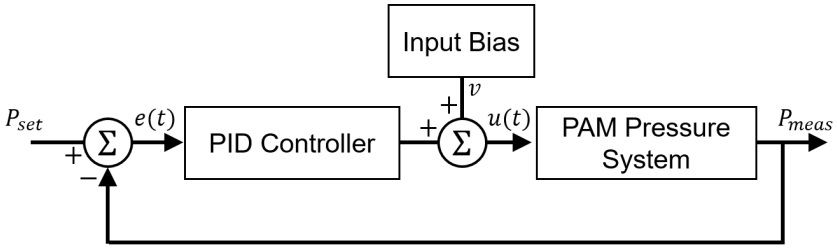

(a) Pneumatic control

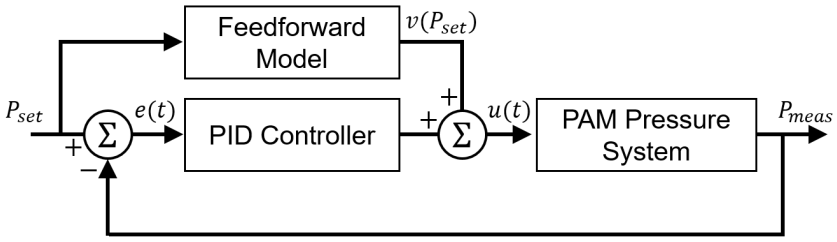

(b) Hydraulic control

Figure 3.7: Controller block diagrams

3.2.3.1 Pneumatic Pressure Control

The proportional valve of the pneumatic system controls inflow/outflow of air to the FAM by accepting a 5 V PWM signal from the controller that dictates the position of its valve spool using a bi-directional linear force motor. Using the valve control diagram in the schematic of Figure 3.5(a) as reference, a command signal of 0 (0 V) positions the valve spool closest to the motor, a signal of 128 (2.5 V) positions the spool in the middle, and a 255 (5 V) signal positions the spool farthest from the motor. For this system configuration, this results in the valve acting to exhaust air from the FAM with a command signal of less than 2.5 V, the valve closed at 2.5 V (with a small deadband), and the valve acting to add pressurized source air to the FAM with command signal voltages greater than 2.5 V.

For the pneuamtic system, the open-loop control component, v, takes the form

of a bias term equal to 2.5 V (Eq. 3.6), which is included to position the spool valve in the middle (valve closed) position when pressure error is equal to zero. Figure 3.7(a) shows the controller block diagram for the pneumatic pressure control system.

3.2.3.2 Hydraulic Pressure Control

The pump providing pressure to the hydraulic system accepts a 5 V PWM signal from the controller, $u(t)$, that correlates to a 0-5000 rpm pump speed (Eqs. 3.5, 3.6). The hydraulic pressure system is a closed-circuit system that requires the pump to continuously displace water to retain system pressure. With the needle valve position fixed, each desired pressure set-point has a corresponding pump speed in the steady-state condition. Therefore, to improve closed-loop feedback control performance, an open-loop model, $v(P_{set})$, was formed by defining the required signal input to the motor (and respective pump speed) to achieve the desired range of set pressures of 0-100 psi in steady state conditions. The characterization results for the large and small scale FAMs are shown in 3.8, where it can be seen that the empirical data was fit to a third-order polynomial to serve as a phenomenological model of the required controller input to achieve desired set pressures in the steady-state condition. The resulting open-loop model equations fit to the data in Figure 3.8 are given for the small and large FAMs in Equation 3.7 respectively.

This model could serve as an open-loop controller on its own, but alone would not be able to rapidly correct for the volume changes of the FAM in the system. Therefore, the controller input serves as a feedforward term for the PI feedback

controller loop (Fig. 3.7(b)). This leaves the PI feedback controller with the sole task of adjusting pump speed according to the pressure error, $e(t)$, to compensate for volume changes of the system as a result of the FAM shape change. It is important to note that the needle valve orifice area was adjusted between testing of the large and small scale FAMs, and that more generally, the characterizations shown in Figure 3.8 are dependent on the position setting of the needle valve.

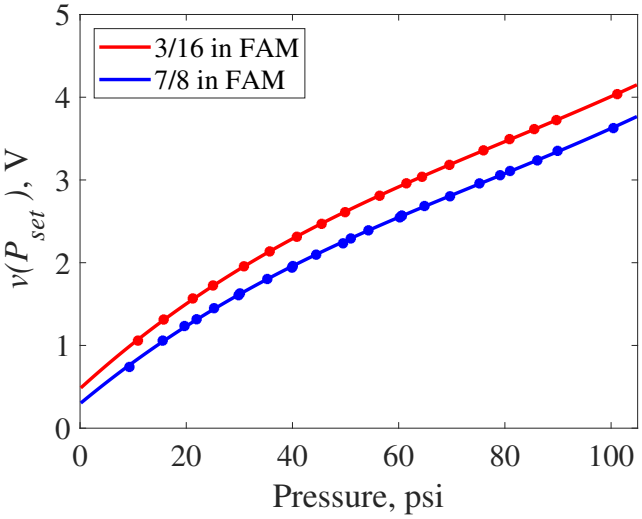

Figure 3.8: Open loop input, $v(P_{set})$, for hydraulic control of each tested FAM

$$v(P_{set}) = \begin{cases} (1.6e{-}6)P_{set}^3 - (3.9e{-}4)P_{set}^2 + 0.06P_{set} + 0.48 & \text{if } 3/16\,in\,dia. \\ (1.6e{-}6)P_{set}^3 - (3.6e{-}4)P_{set}^2 + 0.05P_{set} + 0.30 & \text{if } 7/8\,in\,dia. \end{cases} \tag{3.7}$$

3.2.4 Controller Tuning

The controller was tuned for the pneumatic and hydraulic pressure circuits for both the large and small scale FAMs resulting in a total of four sets of gains. For each of the four cases, the proportional gain, K_p, and integral gain, K_i, were tuned through an iterative process. To get a baseline approximation of the required gains,

the FAMs were initially tabletop tested with zero applied force. Tuning continued with the FAM in the MTS machine, where the ability to hold set pressures was tested in the blocked force state (resting length state) of the FAM. Finally, controller gains were tuned to maintain pressure isobars while cycling the FAM between the blocked force and free contraction states as would be done for the final characterization testing.

To maintain an isobar for the performed cyclic FAM testing, the main task of the controller is to adjust fluid flow rates to account for the change in volume of the FAM. The internal volume of the pressurized bladder of the FAM has been shown to be predominantly a function of the contraction state of the FAM independent of fluid pressure [19]. This made the rates of change of FAM volume with each contraction cycle somewhat predictable during each contraction cycle, and helped clarify points of interest for tuning purposes.

The steady increase in FAM volume with concentric motion, and the steady decrease in volume with eccentric motion, are handled primarily with the slower moving integral term of the controller input. The rapid change in volume that occurs near the resting length state of the FAM is handled primarily by the proportional term of the controller input. Both gains were set to be high enough to react to these changes quickly, but are also restrained to mitigate any detrimental effects of their presence. The proportional gain setting is limited to ensure that it does not overreact to pressure sensor noise, causing the observed pressure to pulsate and bounce around the desired set-point pressure. The integral gain is limited to restrain integral windup that can occur with the sudden change of volume near the resting

length state of the FAM, and where the FAM changes in direction at the maximum contraction state of the FAM for each cycle.

The ratio of the proportional gain to the integral gain for each working fluid was largely affected by the compressibility of each fluid. The compressibility of air made the pressure less reactive to sudden controller inputs from the proportional gain, while the incompressibility of water made it much more reactive to the proportional controller inputs and sensor noise. This resulted in an emphasis on the proportional gain for controlling air pressure, and an increase in the integral gain for controlling water pressure. As expected, the larger changes in volume of the 7/8 in diameter FAM required higher gain values than those required for the 3/16 in diameter FAM. The gains used for the final water and air characterization testing are provided in Table 3.2. Integer value gains were chosen while using units of psi for pressure, P, and the control signal, $u(t)$, in the digital 0-255 PWM value form required by the Arduino (reference Equation 3.5).

Table 3.2: The gains used for testing each FAM in water and air (psi pressure input, PWM control output)

FAM	**Controller Gains**		
	Gain	**Working Fluid**	
		Air	Water
3/16 in Dia.	K_p	1	1
	K_i	2	3
7/8 in Dia.	K_p	4	5
	K_i	2	5

3.3 Results

Accurate pressure control was achieved for both the hydraulic and pneumatic pressure systems, resulting in a high fidelity comparison of the response of the two tested working fluids. The results of the pressure control, as well as the characterization of the FAM response comparing air and water working fluids are detailed in the following sections. The characterization test data is then compared to the force response model to confirm the data's agreement with the model.

Table 3.3: Average pressure and standard deviation for the force response characterization test at each test pressure (3/16 in FAM)

Commanded Set Pressure:	**20 psi**	**40 psi**	**60 psi**	**80 psi**	**100 psi**
Average Pressure, psi (Air)	21.06	41.24	61.25	81.39	101.50
Average Pressure, psi (Water)	21.05	41.22	61.22	81.30	101.41
Standard Deviation, psi (Air)	0.23	0.18	0.21	0.26	0.29
Standard Deviation, psi (Water)	0.15	0.15	0.22	0.29	0.2

Table 3.4: Average pressure and standard deviation for the force response characterization test at each test pressure (7/8 in FAM)

Commanded Set Pressure:	**20 psi**	**40 psi**	**60 psi**	**80 psi**	**100 psi**
Average Pressure, psi (Air)	20.08	40.00	59.89	80.04	100.19
Average Pressure, psi (Water)	19.64	39.96	59.96	80.03	100.11
Standard Deviation, psi (Air)	0.28	0.34	0.31	0.27	0.29
Standard Deviation, psi (Water)	0.39	0.43	0.40	0.42	0.37

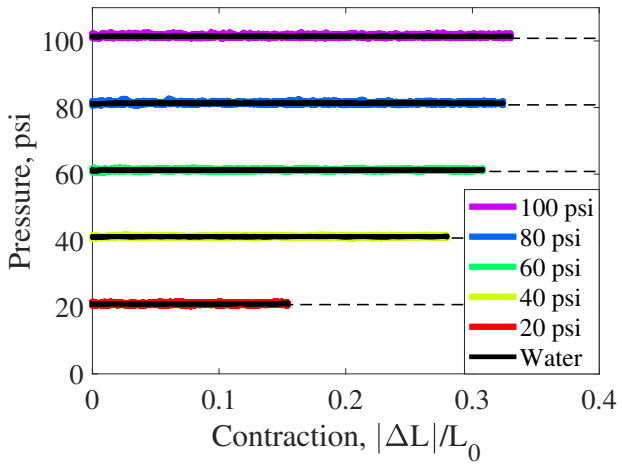

(a) 3/16 in FAM

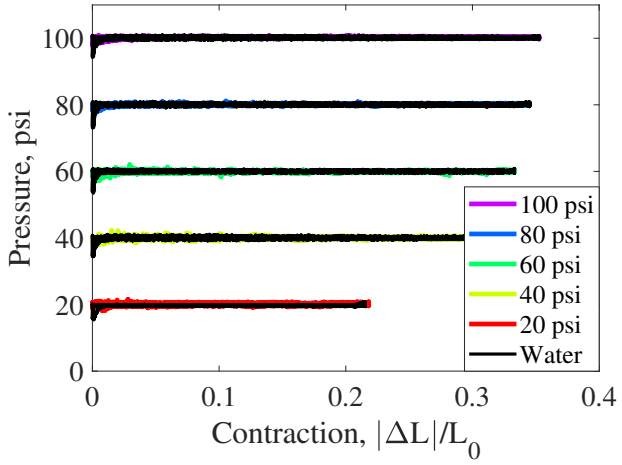

(b) 7/8 in FAM

Figure 3.9: Measured pressure for each force response characterization

3.3.1 Pressure Control Results

Results of the measured pressure during characterization testing for each FAM is given in Tables 3.3 and 3.4. Average pressure and standard deviation values are given for both air and water testing. Together, these values provide a depiction of how well the pressure systems provided a true isobar for each set pressure test to enable a good comparison between each working fluid. Figure 3.9 illustrates the pressure with respect to FAM contraction for each working fluid characterization

test for each size FAM.

Pressure control for the 3/16 in FAM proved to be accurate, with a maximum averaged pressure differential of 0.09 psi. Standard deviation values were all below 0.29 psi, indicating that the pressure didn't vary much around the desired isobar. Figure 3.9(a) provides a qualitative look at how well pressure of the two working fluids corresponded throughout the cycling of the 3/16 in FAM.

Pressure control of the 7/8 in FAM also proved to be very accurate. With exception to the 20 psi test (0.44 psi differential), the maximum averaged pressure differential was 0.08 psi. Figure 3.9(b) provides a depiction of the pressure correlation between the two working fluid tests. The only point of discrepancy in pressure is when the concentric motion of the FAM begins while near the zero percent contraction point. At this point of each pressure test, there is a relatively sudden jump in the required inflow of water due to an instantaneous jump in FAM volume. This effect could be reduced by increasing the proportional gain of the controller at the detriment of increased variation in the pressure about the set-point for the remainder of each test. Overall, this minor discrepancy near the resting length of the FAM did not produce a noticeable effect on the force response results.

3.3.2 Characterization Results

Characterization testing of the two FAMs with each working fluid showed nearly identical results between air and water for all tested pressures. Results from each characterization test are plotted in Figure 3.10. To provide a quantitative

comparison of the force response difference between the two working fluids, the root-mean-square error (RMSE) between the two responses was calculated for each pressure. The RMSE was calculated using the following equation:

$$RMSE_{avg} = \sqrt{\frac{1}{N_i}\sum_i((F_i)_{air} - (F_i)_{water})^2} \tag{3.8}$$

where F is the experimental force for each test, and N is the total number of data points of each test with i representing each respective measurement point from 1 to N. RMSE values for both working fluids at each pressure are given in Table 3.5. The resulting RMSE values are all relatively low, with higher values for the 7/8 in FAM resulting from the overall higher magnitude of forces it achieves. The RMSE values for the results shown in Figures 3.3(a) and 3.4(a) , where the new pressure control system was compared to the previous method of just using a pressure regulator, is provided for a relative point of comparison for RMSE values.

Table 3.5: The force response root-mean-square error (RMSE) at each test pressure.

	20 psi	**40 psi**	**60 psi**	**80 psi**	**100 psi**	**Average**
3/16 in FAM, lbf (Fig. 3.10(a))	0.19	0.27	0.45	0.46	0.75	**0.41**
7/8 in FAM, lbf (Fig. 3.10(b))	2.29	2.39	1.41	4.85	7.65	**3.72**
3/16 in FAM, lbf (Fig. 3.3(a))	0.10	0.98	0.54	0.79	0.86	**0.65**
7/8 in FAM, lbf (Fig. 3.4(a))	19.35	12.18	8.97	8.19	8.41	**11.42**

3.3.3 Modeling Results

The FAM force response model (Eq. 3.1) served as the basis for proving the original hypothesis: the independence of the FAM's quasi-static force response

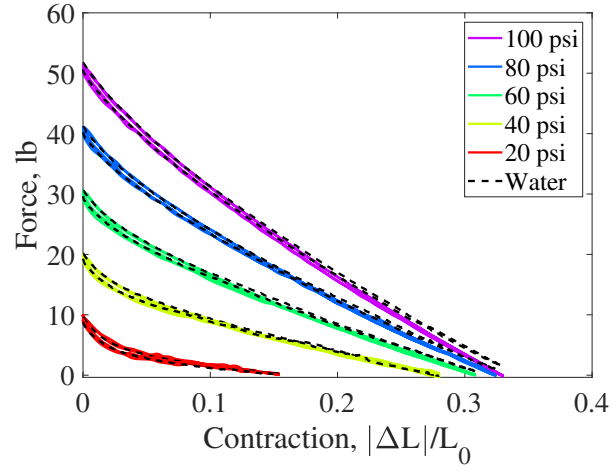

(a) 3/16 in FAM

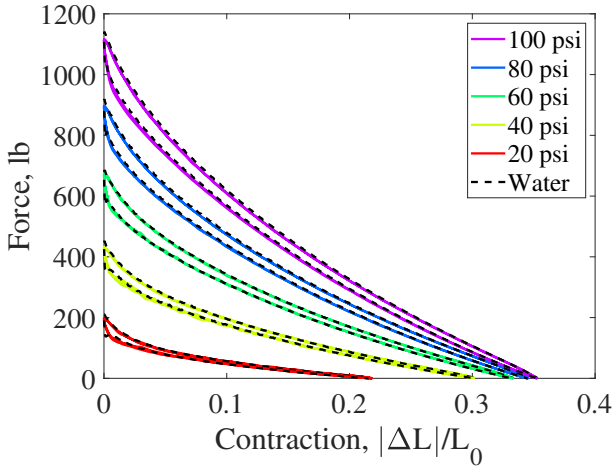

(b) 7/8 in FAM

Figure 3.10: Measured actuation force for each characterization

from the working fluid used. We have shown this independence of working fluid through the results in the previous section. To come full circle, it is now necessary to demonstrate agreement between the characterization data from this research, and the original FAM model used for justification of the hypothesis.

The force response model is applied following the same methods as used in [48]. The longitudinal and circumferential bladder stresses, σ_c and σ_z, are defined using a third-order stress-strain relation as follows:

$$\sigma_c = E_1\epsilon_c + E_2\epsilon_c^2 + E_3\epsilon_c^3 \tag{3.9}$$
$$\sigma_z = E_1\epsilon_z + E_2\epsilon_z^2 + E_3\epsilon_z^3 \tag{3.10}$$

where ϵ_c and ϵ_z are the strains in the bladder in the circumferential and longitudinal directions respectively. As in [48], each of the modulus terms, E_{1-3}, are solved using a least-squares optimization function, and their values are constrained to be a linearly increasing function of pressure.

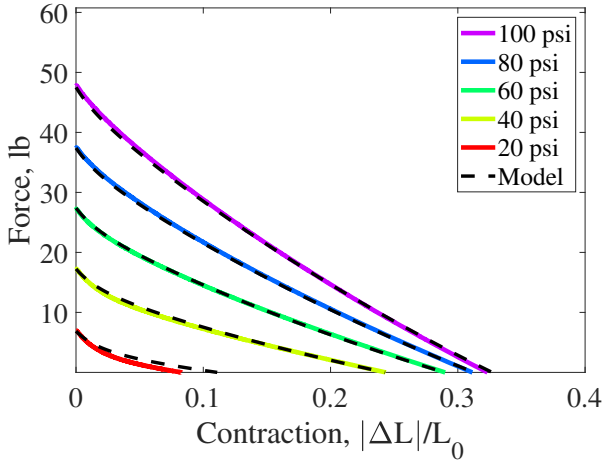

(a) 3/16 in FAM

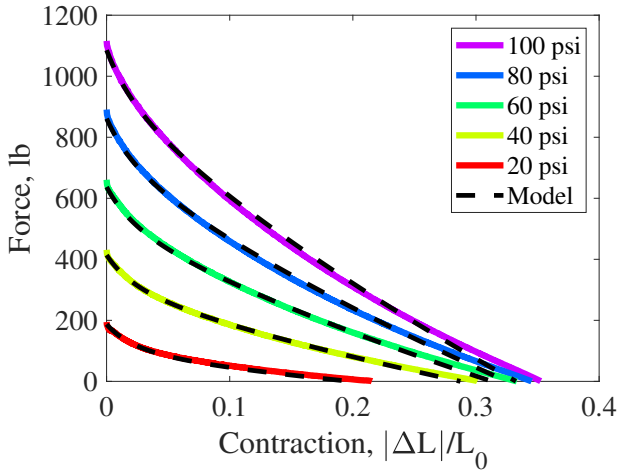

(b) 7/8 in FAM

Figure 3.11: Comparison between the averaged characterization data, and the force response model

The model is compared against the data from the hydraulic actuation characterization tests for both the 3/16 in and 7/8 in FAMs. With the pneumatic and hydraulic test data being virtually identical, it is assumed that the same results would be achieved with application of the pneumatic test data. This form of the model does not capture the hysteresis in the FAM's force response due to friction, so the test data is averaged for each isobaric cyclic test for comparison to the model. The comparison between the averaged data and model, given in Figure 3.11, show a close correspondence in their results. This proves the adherence of the model to the characterization data acquired in this research.

3.4 Conclusion

This work investigated the effect of working fluid choice on the quasi-static force response of FAMs. Past studies have shown how the working fluid used with a FAM can affect its dynamic behavior and efficiency, but none had conclusively demonstrated the assumption that the quasi-static force response is independent of the working fluid used to power it.

To investigate this assumption, a large and small scale FAM was fabricated, and had their quasi-static force response characterized using water and air as the working fluid. To ensure an accurate comparison between the two working fluids, pneumatic and hydraulic pressure control systems were developed to accurately and precisely control fluid pressure for each isobaric force-contraction characterization test. The pressure systems were then used to perform back-to-back air and water

characterization tests which resulted in nearly identical isobaric force-contraction response curves for the two fluids for both FAMs. Finally, agreement between the characterization data and the original force response model was confirmed, completing the adherence of the proven hypothesis to the model. This result confirmed that the FAM's quasi-static force response is independent of working fluid, allowing previously developed pneumatic FAM force response models to be adopted to FAMs using any working fluid, and motivates the use of FAMs with a wider range of application dependent working fluids.

Chapter 4: A Photogrammetric Method for Measuring FAM Shape[1]

4.1 Introduction

Fluidic artificial muscles (FAMs) are a form of soft actuator that have been applied to an expanding number of applications because of their unique characteristics such as low weight, simple construction, inherent compliance, and high specific force and specific work capabilities. In a design environment where optimization techniques are increasingly used for mechanism development and packaging, it is becoming more important than ever to have accurate model representations of device components, including actuators, to accomplish effective design outcomes. Actuator design requirements typically include force and stroke values, while common actuator design constraints include actuator size, energy efficiency, and storage requirements. Models have been developed that address each of these design constraints and requirements for FAMs, but many of those models lack the accuracy required for their use in a world of increasingly constrained design spaces, and improvements to those models have remained stagnant for years.

[1]Chambers, J.M., and Wereley, N.M., 2021. Photogrammetric Measurement and Analysis of the Shape Profile of Pneumatic Artificial Muscles. Actuators. Vol. 10. No. 4. Multidisciplinary Digital Publishing Institute

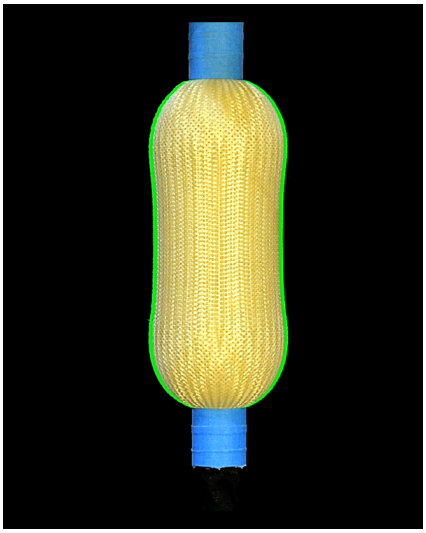

Figure 4.1: FAM with its shape profile traced in green along the edge of the braid

While continual improvements have been made in modeling the force response of FAMs, there has been little recent progress in the development of methods for characterizing the size and overall shape profile of FAMs during operation, parameters commonly used for calculating efficiency, fluid storage, and flow rate requirements. The FAM's shape profile (Fig. 4.1) has long been approximated as a circular cylinder based on visual observations, and has often been cited as a suspected source of modeling error [13, 20]. This research seeks to remedy this by providing a new method of accurately measuring the FAM's shape profile.

With the simple construction of an elastomeric bladder, a surrounding helically braided load-bearing sleeve, and rigid end-fittings at each end, a pressurized contractile FAM can provide a tensile force along its longitudinal axis. Upon internal pressurization of the FAM, the radial pressure force of the internal fluid is transferred through the bladder to the braided sleeve. The braided sleeve transforms that radial force into an axial force expressed at each end-fitting. The actuation force

produced by a FAM is a function of its active length and internal pressure states. The actuation force is at a maximum at its resting length, when the braid angle, defined with respect to the radial axis of the FAM, is at a maximum. As the FAM contracts, the braid angle reduces and the bladder strain increases, resulting in a reduction of actuation force until the FAM reaches a pressure-dependent maximum *free contraction* in its zero-actuation-force state.

The shape profile of a FAM changes with contraction of its length (Fig. 4.2(a)). At its resting length, the FAM has an apparent constant diameter and braid angle along its length. As a FAM contracts in length, its diameter expands and the braid angle reduces as a function of the position along the length of the FAM. The braid geometry is constrained only at each end-fitting where the diameter is equal to the initial diameter. The shape profile is also highly dependent on the FAM, with FAMs of identical material construction having visible differences in their shape profile (Fig. 4.2(b)). FAMs have had shape profiles that range from a more cylindrical mid-section shape to ones that have constant variations in curvature along their entire length. The bulbous shape of a FAM is often approximated as a cylindrical profile with a constant diameter along its entire length (Fig. 4.3). Assuming the braid is inextensible, the cylindrically approximated shape enables a simplification of analysis through the so-called *triangle relationship* that correlates the FAM's diameter, braid angle, and active length. This *cylindrical approximation* serves as the basis for many existing FAM models, including models for volume and actuation efficiency, as well as for force response models that have been developed using both force-balance [1] and principle of virtual work based approaches [5].

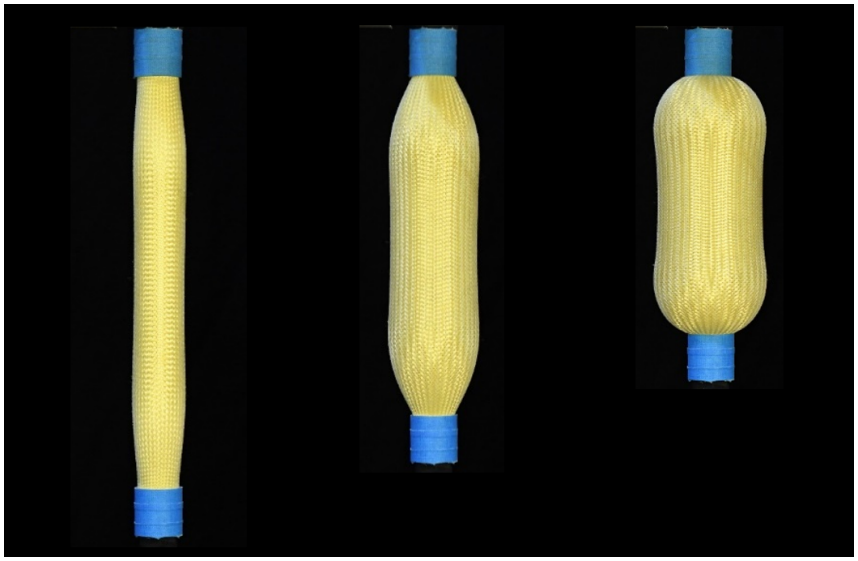

(a) A FAM in its resting length state (left), 17.5% contraction state (center), and 35% (max) contraction state (right)

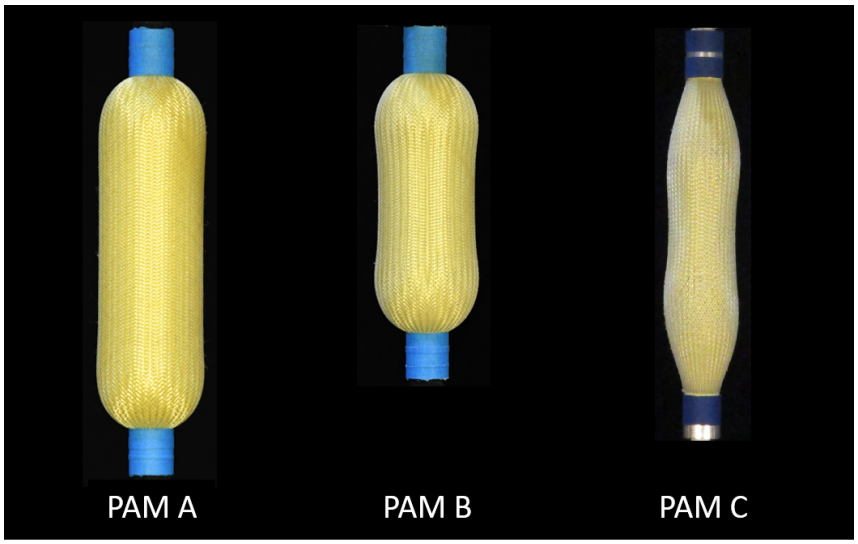

(b) Three different FAMs of identical diameter and construction in their free-contraction state that have noticeably different shape profiles

Figure 4.2: Variation of the FAM's shape profile for (a) a single FAM in different states of contraction, and for (b) three different FAMs in their free-contraction states

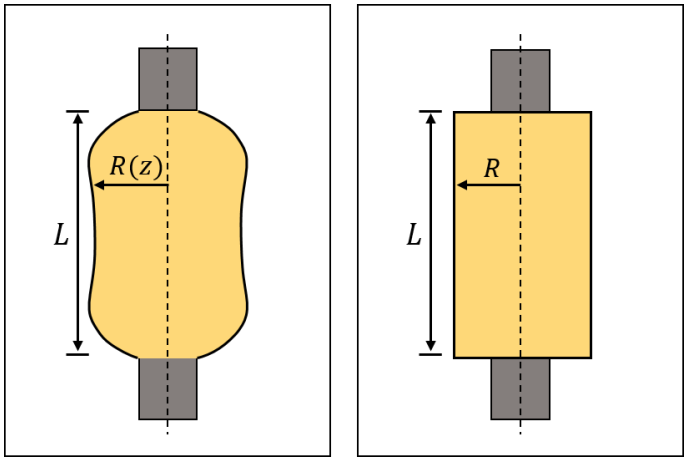

Figure 4.3: The actual profile that has a varying radius along its length (left) versus the cylindrical approximation of this shape profile with a constant radius along its length (right)

Past modeling efforts of FAMs have often centered around rudimentary representations of their shape profile. While the cylindrical approximation of the shape profile simplifies analysis and modeling, it has often been a suspected source of error, thus making it the subject of more detailed modeling efforts [8, 9, 13, 16, 18–20]. Many researchers have inferred that the reduction in diameter near each end-fitting produces what is often termed as *end-effects* that act to decrease the force response of the FAM. Modeling corrections that take end-effects into account for the principle of virtual-work models often seek to more accurately calculate the internal volume of the FAM. Correction efforts for the force-balance modeling method have centered around the effective reduction of active length due to the non-cylindrical shape profile. Tondu and Lopez [9] were the first to use an end-effect correction factor by including a tuning parameter that effectively amplified the contraction ratio in the force response equation. Kothera et al. [13] took a similar approach by reducing the effective active length in the model by two-times the difference of

the current and initial radius. Most models that have taken the shape profile of the FAM into account have maintained a cylindrical approximation for the FAM's midsection, while applying shape corrections to the regions near the end-fittings at each end. Assumed shape profiles have included a stepped cylindrical approximation [8], a 90 deg circular arc [18, 67], a semi-ellipsoid [16, 19], a conic frustum [8], and the partial surface area of an elliptic toroid [20]. These shape profiles are often selected based on qualitative observations and ease of computation. Only Meller et al. [19] has noted that volume measurements appear to show that the cylindrical approximation may be sufficient for modeling the internal volume of the FAM.

Our experience with FAMs has found that the overall shape profile of a FAM is variable, and often exhibits undulating curvature along the full length of the FAM. Having a quantitative method of measuring the shape profile of FAMs would be highly beneficial for improving the accuracy of models that rely on the geometry of the FAM.

Having a more accurate measurement of the shape profile would also aid in characterizing the FAM's internal volume which is often used in defining an actuator's system requirements such as the working fluid flow rate and storage volume requirements. First-cut estimations of internal volume are often made using the cylindrical approximation of the FAM, while end-effects corrections are sometimes included to account for the reduced volume near each end-fitting with unknown improvements to accuracy. Some researchers have turned to quantifying the internal volume through experimental approaches [19]. While experimental methods should provide accurate calculations of internal volume, they often require specialized test

equipment. To date, experimental methods have required either submerging the FAM in water, or pressurizing the FAM using water from a closed graduated cylinder [19], and then tracking the change in water level as the FAM contracts in length. The specialized equipment required for characterizing the volume using these methods not only subject the FAM to fluid that its material composition may not be compatible with, but also requires adjustment, replacement, or even redesign of the test setup components depending on the size and length of the FAM to be tested. Conversely, an experimental method that can test FAMs of all sizes while not requiring specialized equipment is desirable.

It is evident that previous FAM research efforts have relied on multiple different assumed shape profiles without consensus on which ones best fit the observed profiles, and without any conclusive measurement of their accuracy. This research seeks to provide a experimental method that enables quantitative analysis of the shape profile of FAMs for improved accuracy in modeling efforts. In this research, photogrammetry, the science of making dimensional measurements of physical objects from photographic images [68], is adapted for use in the measurement of the FAM's shape profile. An overview of the photogrammetric methods applied in this research are presented first. A test setup for image acquisition is introduced followed by a method of image analysis to render the shape profile measurements from the acquired images. The photogrammetric methods are demonstrated through example by testing a 7/8 in diameter, 9-9/32 in long FAM. The results from testing the FAM are presented, followed by analysis of the FAM using the photogrammetric data. The obtained shape profile data is compared to the profiles assumed by the cylin-

drical approximation. The validity and accuracy of the cylindrical approximation is tested. If more detailed and accurate modeling forms are required, the development of a fit equation is presented for use that accurately replicates the curvature of the FAMs shape profile. Potential improvements to current modeling efforts are also presented, including a demonstration of how easily inaccurate initial geometric conditions can be applied to models without having photogrammetric data available to reference. The profile data is then used to present a simple and accurate method of characterizing the internal volume of FAMs. Finally, the ability of the photogrammetric test method to be universally adopted is demonstrated through shape profile characterizations of FAMs ranging in length from 9-9/32 in to 20 in, and diameters of 7/8 in and 2-1/4 in. Overall, this research aims to provide a new method of characterizing FAMs that has the potential to enlighten future modeling efforts with findings that are not otherwise realizable, and with measurements that have not previously been quantifiable.

4.2 Test Methods

Development of the test setup and methods focused on simplicity to ensure that the photogrammetric characterization would require only an adaptation of current FAM test setups without the need for specialized equipment or photography expertise. The photogrammetric methods performed for this research are detailed in this section to provide context for the test procedure that follows.

4.2.1 Image Acquisition

There are multiple methods of photogrammetric image acquisition that are capable of achieving various levels of image scene reconstruction. Both the number of measurable dimensions of an imaged object, and the requirements for scaling the object in the imaged scene are dependent on the number of cameras used and their relative positioning (i.e. imaging configuration). Imaging configurations include single-, stereo-, and multi-image photogrammetry methods [69]. Stereo-image and multi-image methods provide three-dimensional scene reconstruction and require either the use of multiple cameras or the controlled movement of a single camera. Single-image photogrammetry requires just a single camera in a fixed position, but only provides a two-dimensional planar view of the imaged object. This shortcoming can be overcome, however, by enlisting additional prior knowledge of the imaged object. Three-dimensional measurements can be achieved with just a single camera if geometric relations, measurements, or symmetries of the object are linked to the image.

The scale of an object in an image must be known to acquire its photogrammetric measurements. Scale is defined as the ratio of the size of an object in the imaged world (i.e. in pixels) to its size in the physical world. The scale of an object in an image depends on five things: (a) the object's distance and position with respect to the camera, (b) the lens used by the camera, (c) the distance of the lens from the image sensor plane, (d) optical distortion due to inherent imperfections in the lens, and (e) perspective distortion (i.e. radial distortion) which is dependent on

the angle-of-view of the object in the image [68]. These camera state values can be used for scaling the imaged object, but they can also be arduous and time consuming for the layman to obtain. A simpler method of scaling employs the placement of an object with known dimensions into the image scene to calibrate the scaling of the object. This can be achieved by placing a ruler adjacent to the object of interest in the image scene prior to testing, as is done in this research.

4.2.2 Image Analysis

The goal of the photogrammetric analysis is to obtain the shape profile dimensions of the FAM's braid from photogrammetric images such as in Figure 4.2. In order to do this, image analysis techniques must be applied to isolate the FAM's braid within each photographed image. Image analysis techniques include locating object boundaries, or segmenting image pixels into groups, based on color information such as color values (e.g. brightness, hue, etc.). With potentially thousands of images to be analyzed, it is essential to have automated methods of identifying and outlining objects of interest within images. The image segmentation and object identification techniques used in this research are outlined in the following sections.

4.2.2.1 Color Model

Segmentation of an image is the process of grouping the pixels of an image based on their color values. With color contrast between objects in an image, an image can be segmented and reduced to isolate pixels in an area of interest. With

image segmentation based on the color component values of each pixel, an important first step is the decision of what color model to use.

A color model is the mathematical representation of a color as a tuple of numbers. The RGB color model is commonly used to define pixel color in photographic images, but is often problematic for use in image analysis. The RGB color space is not a perceptual color space which makes it difficult to perceive how changes in color components (R, G, and B) will alter the hue and brightness of the color. This makes it difficult and imprecise to define a range of R, G, or B based on color, hue, or brightness, that would enable a desired segmentation of an image [70]. Another difficulty that arises for image segmentation when using the RGB color model results because normalized RGB component values are not invariant with changes in lighting or shading [71]. This makes the RGB component values vary unpredictably with fluctuations in brightness across an object's surface from shadows, specular reflections, or changes in illumination due to motion of an object.

A color model that is more suitable than RGB for use in image analysis is the hue, saturation, and value (HSV) color space. The HSV color space provides a more intuitive method of defining colors that is beneficial for performing image segmentation [71–73]. As illustrated in Figure 4.4, the HSV color space can be represented as a cylindrical space with *hue*, *saturation*, and *value* represented along respective coordinate axes [70].

Hue is defined as a $0-360$ degree value that correlates to an angular position within the cylinder, and represents a color's position within the color spectrum. Hue is helpful in segmenting an image based on color in a way that is invariant to

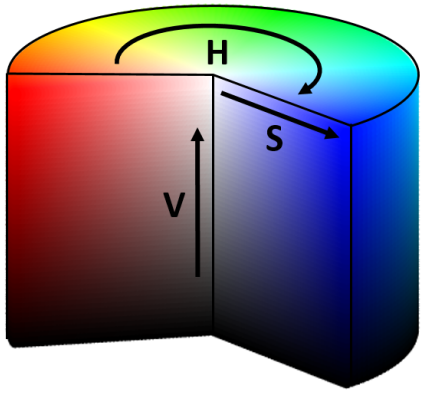

Figure 4.4: Cylindrical HSV color space

changes in lighting conditions. *Saturation*, represented as a $0-100\%$ value along the radius of the cylindrical space, defines the vividness of a color's hue. Desaturation of a color occurs with added white light. Value, which is represented as a $0-100\%$ value along the height of the cylindrical space, defines the perceived brightness of a hue. Sometimes described as *relative brightness*, value can be used to describe a color in varying lighting conditions. Therefore, segmentation using the value color component can be used to segment objects within an image based on their relative brightness [74]. Although photographic image data is often defined using the RGB color space, in can be converted to the HSV color space by using the following equations [75]:

$$M = max(R, G, B) \tag{4.1}$$

$$m = min(R, G, B) \tag{4.2}$$

$$H = 60^\circ * \begin{cases} undefined & \text{if } M = m \\ \frac{G-B}{M-m} mod 6 & \text{if } M = R \\ \frac{B-R}{M-m} + 2 & \text{if } M = G \\ \frac{R-G}{M-m} + 4 & \text{if } M = B \end{cases} \tag{4.3}$$

$$S = \begin{cases} 0 & \text{if }, M = 0 \\ \frac{M-m}{M} & \text{, otherwise} \end{cases} \tag{4.4}$$

$$V = M \tag{4.5}$$

An image can be segmented based on the hue, saturation, or value component of each pixel. The invariance of hue to lighting conditions makes it a good candidate for color-based image segmentation. Care must be taken, however, to avoid use of hue segmentation in areas where pixel colors are near the hue singularity condition. Hue singularity occurs with colors that have saturation and value levels near zero (i.e. grayscale colors). In this color region, imperceptible changes in color can produce large fluctuations in hue. Attempts at hue segmentation near the singularity condition will result in arbitrary and inaccurate segmentation [71]. Those regions are better suited for segmenting based on saturation or value. To aid in avoiding hue singularities, for this research, pixel colors are defined in the HSV color space to segment each image based on relative brightness (i.e. value) and then hue.

4.2.2.2 Boundary Detection

Automated identification of objects within an image boils down to the practice of segmentation through boundary detection. Common methods of boundary detection include edge detection and thresholding. Edge detection methods identify

boundaries of objects by locating the sharp changes in color or light intensity that are characteristic of object boundaries [74]. It is often performed using gradient-based methods such as Canny edge detection [76]. Thresholding techniques, on the other hand, segment an image by grouping image pixels by comparing their color value to a set threshold value. Since thresholding locates areas of an image and not edges, finding boundaries through thresholding requires an additional step of using a method of locating and tracing object boundaries.

Edge detection methods are effective at detecting edges with sharp contrast, but can have difficulty with random specular reflections, or with soft edges that have small color gradients [74]. Identification of the edge of the FAM braid using edge detection methods proved to be difficult due to the soft edges of the FAM's bulbous shape, and random spikes in brightness due to specular reflections off the surface of the Kevlar braid. However, the ruler used for calibration, with its flat surface and high-contrast hatch markings, was found to be an ideal candidate for edge detection methods, as detailed in Section 4.3.2.

Thresholding techniques, when combined with a boundary tracing algorithm, can serve as a more robust method of boundary detection for identification of the FAM's braid. Setting a color threshold can be performed manually through subjective analysis, but automated methods of thresholding have been developed that can identify a suitable threshold in a consistent and time-efficient manner. Automated methods of thresholding are typically based on color histogram analysis. The histogram defines the distribution of the number of instances of each color value in an image. Setting a threshold divides the histogram into two classes (i.e. groups) with

all pixels below the color value threshold grouped into one class, and all pixels above the color value belonging to a second class. An image is commonly transformed into a class-membership based binary image to provide a visual representation of the threshold segmentation, and to serve as an input in many boundary tracing algorithms. Otsu's method is a common method of histogram-based thresholding that is used in this research [74, 77, 78]. This method's algorithm recursively searches for a threshold value that can divide the histogram into classes that have a maximum inter-class variance.

The algorithm is detailed as follows. Let us consider a certain color value (e.g. H, S, or V) to set a threshold on. Each pixel of an image is represented by a color value level of the histogram (e.g. $0-100\%$ for S or V), and within the histogram, the height of each color value bar represents the fraction of the total number of pixels at each respective color value level. For a given threshold, the pixels are separated into two classes ($i = 1, 2$). w_i is equal to the probability of a pixel being in class i, and μ_i and μ_T are the mean value of each class and the total, respectively. Otsu's method then finds the optimal threshold value by maximizing the inter-class variance, σ_b, using the following equation [77, 78]:

$$\sigma_b^2 = w_1(\mu_1 - \mu_T)^2 + w_2(\mu_2 - \mu_T)^2 \tag{4.6}$$

Otsu's method is utilized in Section 4.3.2 for image segmentation, with Figures 4.10(d) and 4.11(d) providing illustrations of the relative brightness and hue histograms, respectively, with thresholds placed using Otsu's method.

With an area of interest identified through threshold segmentation, the bound-

ary of the area must then be traced with a contiguous line. A simple method of boundary tracing used in this research is the Moore-Neighbor algorithm [79, 80]. With a binary image as the input, the Moore-Neighbor tracing algorithm locates any clusters of pixels of the same class, and then traces their boundaries. Starting at a pixel along the boundary of a cluster, the recursive Moore-Neighbor algorithm steps along a boundary until it meets a defined end condition.

The basis of the Moore-Neighbor algorithm is the Moore-Neighborhood of a pixel. A pixel's Moore-Neighborhood (Fig. 4.5(a)) is the set of eight pixels that surround a pixel of interest (pixel C). To advance along a boundary, the algorithm examines the Moore-Neighborhood of a boundary pixel in the clockwise direction, starting from the previously found boundary pixel (pixel P), until it comes upon the next boundary pixel. This process continues recursively until a stopping condition is met. A frequently used stopping condition is the Jacob's stopping criterion. This criterion states that the Moore-Neighbor algorithm shall stop after visiting the start pixel at least twice, or after entering the start pixel from the same direction as it was initially entered.

Figure 4.5(b) provides an example of Moore-Neighbor tracing. A cluster of pixels of the same class (gray) is identified, and a start boundary pixel (pixel 1) located at the boundary of the cluster is established. From pixel 1, the Moore-Neighborhood search begins until the next boundary pixel (pixel 2) is reached. The algorithm repeats until it arrives back at the start boundary pixel from the original direction. The overall boundary traced for this cluster is identified as pixels 1−8.

Through the detection of the boundary of an area of interest (e.g. the braid)

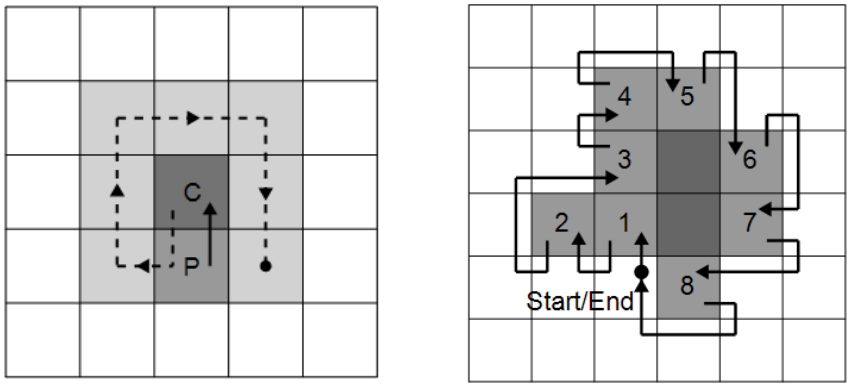

(a) Moore-Neighborhood of pixel C (b) Tracing of a pixel cluster by stepping through pixels 1-8

Figure 4.5: Example depiction of Moore-Neighbor tracing of a boundary

within an image realized, analysis of the size and shape of the boundary can then commence as desired.

4.3 Procedure

The methods of image acquisition and analysis described in the previous section are employed by this research, as detailed in this section. Photogrammetric data is acquired and the image is then reduced down to a traced outline of the FAM braid for further analysis of the shape profile.

Photogrammetric data of the shape profile is acquired while simultaneously characterizing the isobaric force-contraction response of the FAM. Testing of the force response is performed using the same methods as done in past FAM research [18, 22]. The FAM is mounted in a MTS servo-hydraulic test machine, and is quasi-statically stroked between its minimum and maximum contraction length states while maintaining a constant internal working fluid pressure. The MTS machine

directs a controlled stroking motion of the FAM while recording external inputs of pressure (Omega PC209-200G5V), and force (Honeywell Model 31 Mid 1000 lbf. load cell), which provides a complete data set to characterize the isobaric force-contraction response of the FAM. The FAM is mounted in the MTS machine at each end through clamped fixtures (Fig. 4.6). The top fixture serves as both a mounting point for the pressure sensor and as a conduit for air to travel into and out of the FAM. The bottom fixture connects to the load cell that is mounted inline with the FAM.

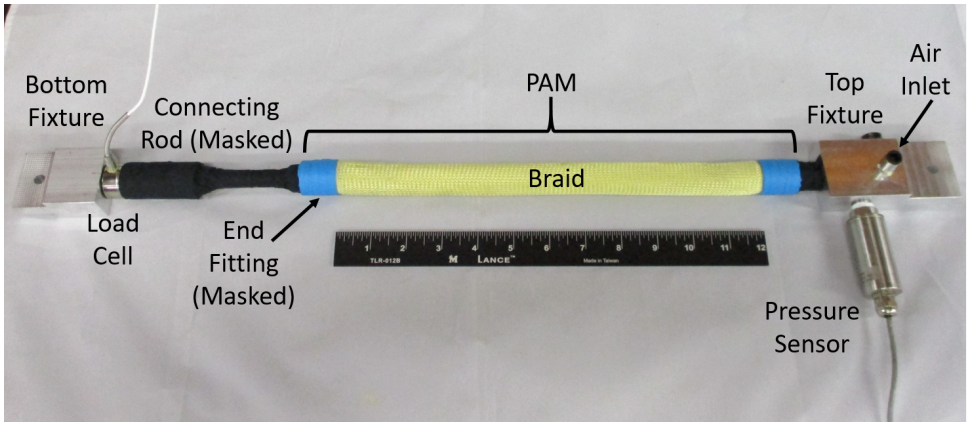

Figure 4.6: FAM with sensors, MTS fixtures, and masking applied prior to mounting in the MTS machine

4.3.1 Image Acquisition

For simplicity of implementation, image acquisition is performed with the single-image photogrammetry configuration. The test setup to perform the force response and shape profile characterization is shown in Figure 4.7. Photogrammetric data acquisition requires the addition of only a camera, a backdrop, lighting, and masking of components. A camera is placed in a fixed position, and photographic

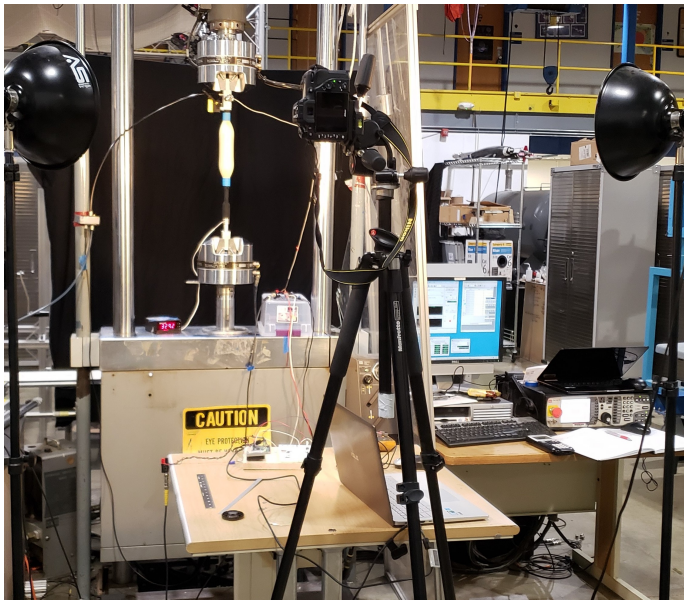

(a) Front view

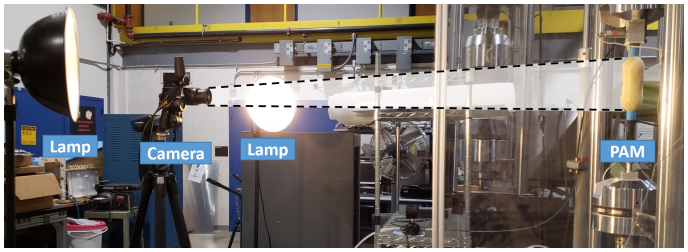

(b) Side view

Figure 4.7: Views of FAM mounted in the MTS machine with the photogrammetric test setup (camera, lights, and backdrop)

images are taken at a regular time interval while the FAM is quasi-statically stroked during force response characterization testing. The camera used is a Nikon D7500 DSLR Camera with a AF-P DX NIKKOR 18-55mm f/3.5-5.6G VR lens. This camera provides a high-resolution image (5,568 $\times$ 3712 pixels) along with manual control of settings including focus and image exposure.

Careful placement of test setup components is required to obtain images that are sufficient for photogrammetric analysis. The scene of the image should be set to promote maximum contrast between the components of the image to be segmented.

The foreground is separated from the background of each image using a threshold of relative brightness, and the end-fittings and braid of the FAM are separated in each image by using a hue threshold. Therefore, the goal for setting the image scene is to aid segmentation by maximizing the brightness differential between the foreground and background, and by maximizing the differential in hue between the end-fittings and the braid of the FAM. To determine the distance from the FAM of the camera placement, a balance must be realized between positioning the camera close to the FAM for maximum resolution, versus maintaining enough distance away from the FAM to minimize the angle-of-view and related perspective distortion. For the tested 9-9/32 in long FAM, the camera was placed 5 ft from the FAM. The height of the camera is set to a level that makes it level with the mid-height of the FAM in its resting length state. This results in a relatively small angle-of-view of the FAM of 8.84 degrees when the FAM is at its resting length (Fig. 4.7(b)). Contrast in brightness between the foreground and background is heightened by maximizing the distance between the foreground and background. A 5×5 ft black cloth backdrop is placed 4 ft behind the FAM. The FAM is front-lit by two fluorescent lamps (Smith-Victor 10 inch Adapta-Light) positioned to each side of the camera (Fig. 4.7(a)). The lamps act to further increase brightness contrast between the foreground and background, and ensure complete, shadow-free lighting of the half of the FAM that is facing the camera. Black gaffers tape is applied to everything but the FAM in the foreground to enable these objects to be segmented out with the background by the brightness threshold (Fig. 4.6). To maximize the contrast of hue between the yellow braid and the aluminum end-fittings of the FAM, the end-fittings are wrapped in

blue tape (yellow's color complement). Non-reflective materials are selected for all applied surfaces to minimize specular reflections that can affect the image brightness and hinder hue identification of pixels (due to the aforementioned hue singularity conditions).

Camera settings are adjusted to ensure accurate coloration and ideal exposure of images. The lens is set to its longest focal length of 55 mm (2.2 in) to maximize the size and resolution of the FAM's image. The camera's auto-focus functionality is used to obtain a sharp focus of the FAM in the image plane. However, a change in the focus would result in a change in the scaling of the image, so the focus must be set prior to scale calibration and testing. Additionally, the camera's auto-focus functionality is turned off prior to testing to ensure that the camera does not change focus by reacting to the changing shape of the FAM.

The aperture's f-stop is set to a minimum to achieve a narrow depth-of-field which enables the background to be out of focus [68]. The motion of the FAM will be very slow (less than 0.1 in/sec), so the choice of shutter speeds is minimally constrained. Therefore, exposures can be iteratively tested until the desired result is achieved through adjustments of the shutter speed and ISO sensitivity. For the scene setup in this research, desired exposure is achieved with the f-stop set at f/5.6, the shutter speed of 1/160 sec, and the ISO sensitivity at ISO 3200. To provide an accurate color representation in the artificially lit indoor laboratory, white balance is set to the incandescent setting which equates to a color temperature of 3000 K.

Calibration of the scale of the FAM is acquired by taking a picture of a ruler in the image frame prior to testing. The 12 in ruler is positioned in the image alongside

the FAM as seen in Figure 4.8. Placement of the ruler in close proximity to the FAM helps ensure accurate calibration of scale, and enables the ability to correct for any optical distortion as a function of its position along the ruler. The ruler attaches to the top MTS fixture by a rigid mounting plate that ensures a vertically fixed orientation of the ruler. Since the ruler would obstruct the radial expansion of the FAM during testing, it must be removed prior to testing after the calibration picture is taken. It is very important that the calibration ruler is placed at the mid-plane of the FAM to ensure that the scale is calibrated at the same depth as the shape profile outline to be measured. Prior testing for this test setup revealed that scale calibration would change by about 2% of the mid-plane calibration value per inch of depth change from the FAM's mid-plane. This indicates that performing the scale calibration with the ruler at the mid-plane of the FAM is critical to acquiring accurate shape profile measurements of the FAM.

4.3.2 Image Analysis

Prior to analysis of the photogrammetric data, the scale of the FAM in the images must be determined for the camera settings and position used. First, a photograph is taken with a ruler placed adjacent to the FAM in the image scene (Fig. 4.8). This image is rotated by 90 degrees and then cropped to retain only the 1/8 inch hatch marks of the 12 in calibration ruler. The scale is then determined by finding the number of pixels between each 1/8 inch hatch mark of the ruler. The location of each hatch mark is pinpointed by using an edge detection method. The left and right

edges of each hatch mark are located as the maximum and minimum points of the brightness gradient. The midpoint between the minimum and maximum gradient points is then identified as the center of each hatch mark. Figure 4.9 provides an example of this hatch mark identification; the maximum and minimum brightness gradient points are marked in blue and green respectively, and the center of each hatch mark is marked in red. The distance between each hatch mark, measured in pixels, indicates the scale of the FAM in the image. The scale can be averaged along the ruler for the length of the FAM, or can be found as a function of the height along the ruler if distortion of the image is considered appreciable.

Analysis of the photogrammetric test data begins with the original 5568 x 3712 pixel images (Fig. 4.8(a)). All images are then cropped to a size that cuts out the metallic surfaces of the MTS machine and fixtures while retaining the entire length of the FAM (Figs. 4.8(b), 4.10(a)). What remains in each image is the FAM (braid and end-fittings), the connecting rod (masked in black), and the background. This image is then analyzed to obtain the originally stated goal of outlining and measuring the shape profile of the FAM's braid. A sample image of the tested FAM is shown in Figure 4.10(a) to serve as an example of the developed method. The braid's profile is acquired from each image through the following five steps:

1. Isolate the FAM in the image using a threshold on relative brightness, V
2. Trace the boundary of the FAM (braid and end-fitting) using the threshold segmented image
3. Within the traced outline of Step 2, isolate the end-fittings using a threshold on hue, H
4. Trace the boundary of the end-fittings from the threshold segmented image of Step 3

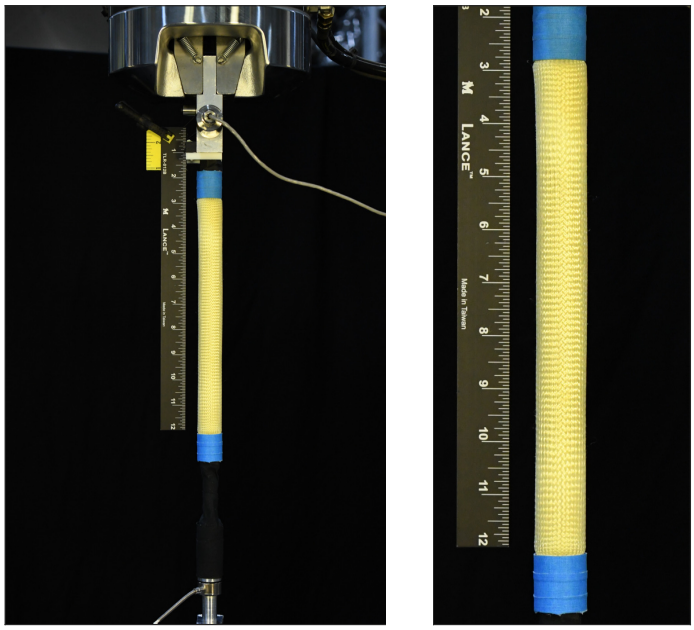

(a) Original image view, 5568x3712 pixels

(b) Cropped image view, 2650x1100 pixels

Figure 4.8: Image captured by camera for photogrammetric analysis with calibration ruler

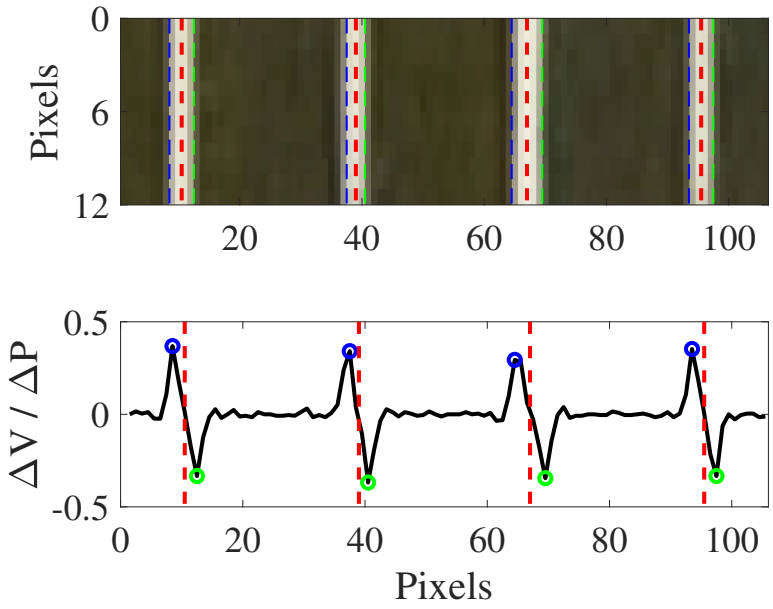

Figure 4.9: The method of identifying the distance (in pixels) between 1/8 inch increments on the calibration ruler is illustrated. Each hatch mark has its left (blue), right (green), and then center (red) located on a segment of the ruler image (top), and respective brightness gradient plot (bottom).

5. Using the outline of the FAM from Step 2, retain only the region between the outlined end-fittings from Step 4

Details of each step in this process are described below. Using a sample image of the tested FAM, each step is accompanied by an illustration of the described analysis. The process of isolating the braid's profile from each image is detailed below, and is accompanied with an illustration of each step of the analysis using a sample image of the tested FAM (Figs. 4.10−4.12).

4.3.2.1 Step 1

The FAM is first isolated in the image from the connecting-rod and background through segmentation using a threshold on relative brightness, V. The histogram in Figure 4.10(d) illustrates the relative brightness distribution of the pixels in the image, and includes the threshold that separates the pixels into two classes (i.e. groups). The dark pixels of the black background and masked connecting-rod are in the class that is to the left of the threshold, while the light pixels of the FAM are to the right of the threshold. The brightness contrast in the image, illustrated by the separation of the two pixel groupings to each side of the threshold, indicates the effective segmentation of the image. A binary form of the segmented image is created (Fig. 4.10(b)), with pixels in the class below the threshold value presented in black, and pixels in the class above the threshold value presented in white.

4.3.2.2 Step 2

Using the binary image created in Step 1 (Fig. 4.10(b)), the Moore-Neighborhood algorithm is used to trace the boundary of the FAM (Fig. 4.10(c)). The Moore-Neighborhood algorithm locates and bounds all pixels of the image that have a relative brightness that is above the threshold. This may include small areas from random specular reflections, or other objects that come into the scene of the image. These areas are located and traced by the Moore-Neighborhood algorithm as well, but are rejected on the grounds of being a smaller area than the traced boundary of the FAM.

4.3.2.3 Step 3

The end-fittings of the FAM must be separated from the braid. A threshold segmentation is performed on the area within the outline of the FAM from Step 2 (Fig. 4.11(a))). A hue threshold value is set using Otsu's formula to separate the blue hue of the end-fittings from the yellow hue of the braid in the image. The histogram in Figure 4.11(d) displays the threshold's effective separation of the blue and yellow pixels of the FAM. Just as in Step 1, a binary form of the image is created for use by the boundary tracing algorithm (Fig. 4.11(b)). Pixels in the class below the threshold are black, while pixels in the class above the threshold are white and can be found in the image in the area of the end-fittings.

4.3.2.4 Step 4

Using the binary image created in Step 3 (Fig. 4.11(b)), the Moore-Neighborhood algorithm is applied to trace the boundary of each end-fitting (Fig. 4.11(c)). Just as in Step 2, any extraneous areas located and traced by the Moore-Neighborhood that are smaller than the areas of the two end-fittings are not considered in further analysis.

4.3.2.5 Step 5

The final step is to outline the outer edges of the braid. For analysis of the shape profile of the FAM, we are only concerned with a single left and right boundary of the FAM in the area between the two end-fittings.

The top and bottom of each end-fitting appear to be perfectly horizontal if viewed head-on. However, due to perspective distortion in the image, the top and bottom of each end-fitting can appear to be rounded. Since we are interested in the shape profile of the FAM at its mid-plane, we only consider the outline of the braid to the inner edge of each end-fitting. To do this, the outline of the FAM obtained in Step 2 (Fig. 4.10(c)), and the outline of the end-fittings from Step 4 (Fig. 4.11(c)), are compared. The areas where the FAM and end-fitting outlines overlap is subtracted from the outline of the FAM to retain only the outline of the FAM that lies between the two end-fittings. What remains are two contiguous lines that delineate the left and right edges of the braid (Fig. 4.12(a)). Figure 4.12(b) provides a depiction of the shape profile data to be used in subsequent analysis of

the FAM's profile.

4.3.3 Characterization Test Parameters

As a proof-of-concept of the presented photogrammetric method, a 9-9/32 in long, 7/8 in diameter FAM was selected for initial testing and analysis. The material composition of this FAM, as detailed in Table 4.1, is identical to that of FAMs used in other research [28] resulting in comparable actuation characteristics.

Table 4.1: Construction of the 7/8 in diameter FAM

	Material
Braid	2 in Biaxial Kevlar Sleeve
Bladder	7/8 inch Latex Tube (1/16 in Thickness)
end-fitting	Machined Aluminum 6061-T6
Swage Tube	Aluminum 6061-T6 Tubing

Photogrammetric data was acquired while the isobaric force-contraction response of the FAM was tested in the MTS machine. The FAM was stroked three times between a maximum and minimum length state for each isobaric test to ensure accuracy and consistency of the characterization data. The minimum tested length state of each test is the pressure-dependent free contraction, zero force state, of the FAM. To ensure a quasi-static characterization, the FAM was stroked at 0.04 in/sec. For the photogrammetric analysis, photographs were taken at 1 second intervals for the first cycle of testing, resulting in shape profile data for every 0.04 in change in length of the FAM. Testing was performed at isobaric pressures of $10-100$ psi in 10 psi increments, for a total of ten tests. Pressure was controlled to be constant

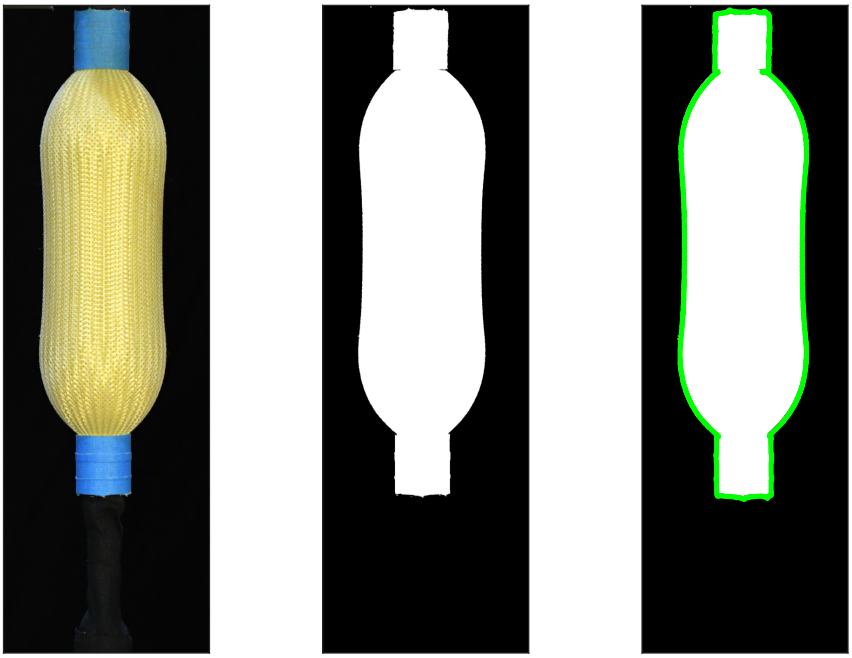

(a) Initial Image

(b) Step 1b: V segmented binary image

(c) Step 2: Traced outline of FAM

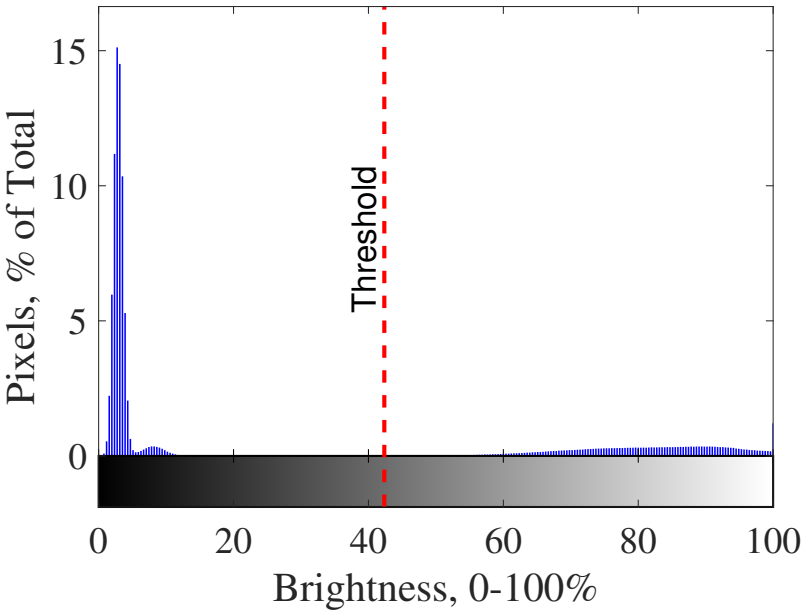

(d) Step 1a: Brightness pixel segmentation using Otsu's Method

Figure 4.10: Identification of the FAM in the image (Steps 1-2)

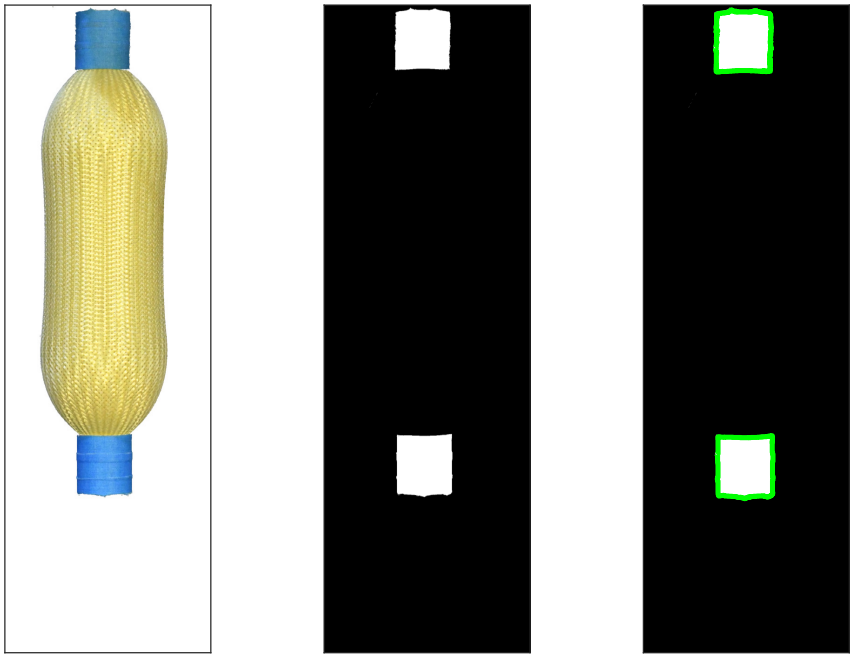

(a) Image with FAM only (b) Step 3b: H segmented binary image (c) Step 4: Outline of end-fittings

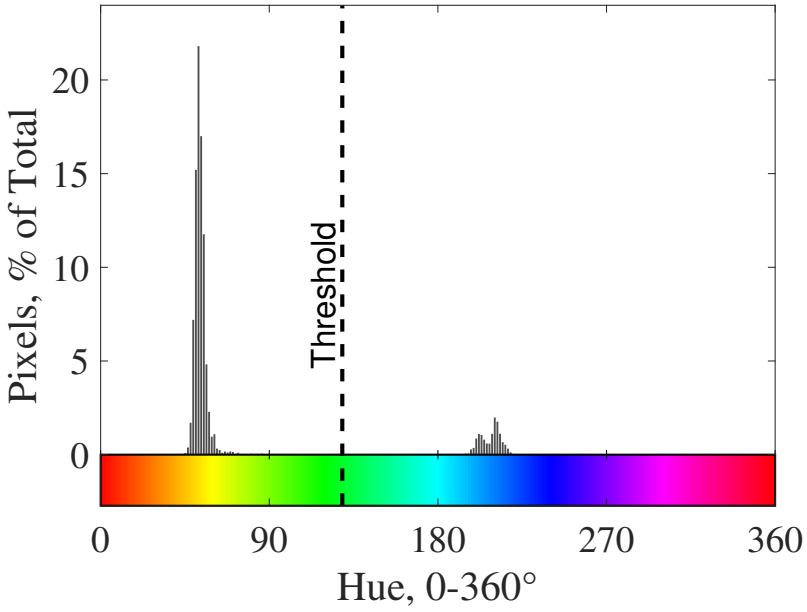

(d) Step 3a: Hue pixel segmentation using Otsu's Method

Figure 4.11: Identification of the end-fittings in the image (Steps 3-4)

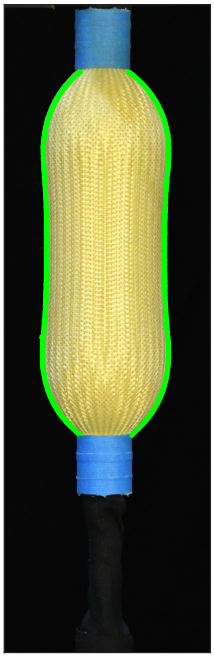

(a) Step 5: Profile

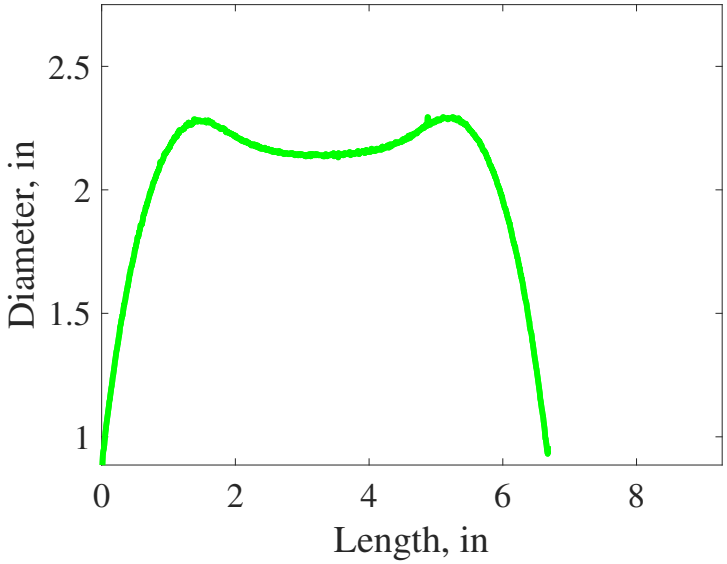

(b) Diameter of shape profile with respect to length

Figure 4.12: The resulting shape profile of the braid along the FAM's length

during testing using the air pressure control system developed in Chapter 3.

4.4 Results

4.4.1 Calibration

The first image to be processed is the calibration image (Fig. 4.8) used to calibrate the scale of the FAM in the images. The scale of the FAM was found to be 226.63 pixels/in, resulting in high resolution measurements from each image. Care was taken to not change any settings of the camera (e.g. focus, position) subsequent to this calibration being performed to ensure that the scale remained constant for each photographed image. It is worth noting that since the scale was found to be uniform along the entire length of the FAM, there was no compensation of scaling

due to image distortion used for this test.

4.4.2 Force-Contraction Response

The isobaric force-contraction response of the tested FAM is shown in Figure 4.13. These results closely replicate those of other FAMs of the same size and construction. The characteristic hysteretic response of FAMs, as seen in Figure 4.13, results in the FAM expressing higher forces in eccentric motion than in concentric motion. Despite this fact, subsequent analysis of the shape profile of the FAM has found no dependency of the shape profile on the direction of motion. When comparing the shape profile of the FAM for the full contraction range at 100 psi, there was found to be an average differential of only 0.00051 in between the profiles for concentric and eccentric motion.

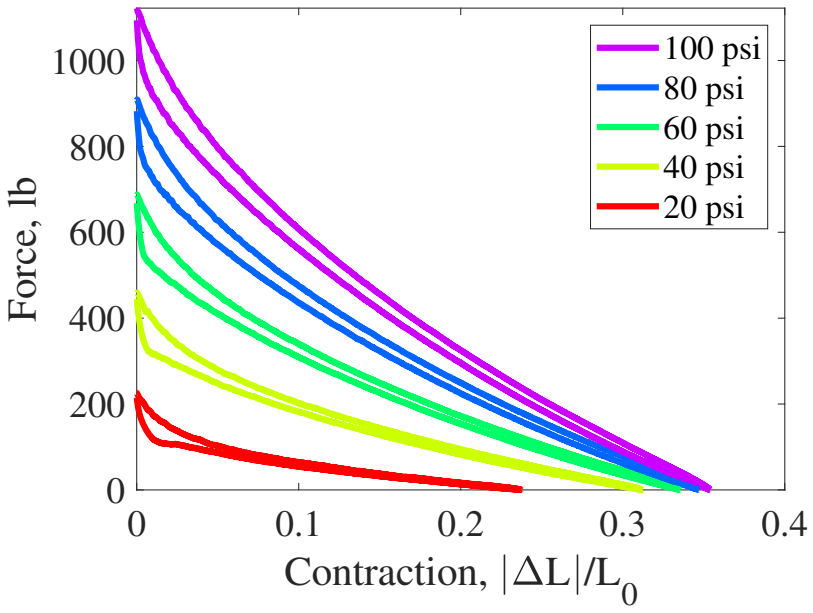

Figure 4.13: Actuation diagram of the 9-9/32 in, 7/8 in diameter test FAM

4.4.3 Shape Profile Characterization

The developed image analysis methods are applied to get measurements of the shape profile for every image acquired during the characterization testing of the force-contraction response. As a first step, the timing of the photogrammetric data must be synchronized with that of the force-contraction response data recorded by the MTS machine. This was done in this research by comparing the contraction of the FAM, as directed by the MTS machine, to the contraction as found through the shape profile data. To do this, the recorded time of the MTS data was shifted to produce a minimum error between the MTS and photogrammetric contraction data. With measurements of the MTS machine recorded every 0.02 seconds, fine adjustment of the time shift can be made to synchronize the time between the two measurement systems accurately.

The comparison of the photogrammetric and MTS contraction data also provides a method of ensuring the fidelity of the photogrammetric results. The photogrammetric measurements can be checked through comparison to manually acquired measurements taken during testing. However, manually acquiring measurements would be time consuming and difficult to perform accurately. The MTS machine controls and records the contraction of the FAM length during testing to the ten-thousandth of an inch. Therefore, if we consider these contraction values as the true contraction of the FAM, a simpler and more accurate method of checking the photogrammetric measurements would be to compare the contraction as found through the photogrammetric data to that of the MTS machine. This comparison

of the time synchronized data is shown in Figure 4.14.

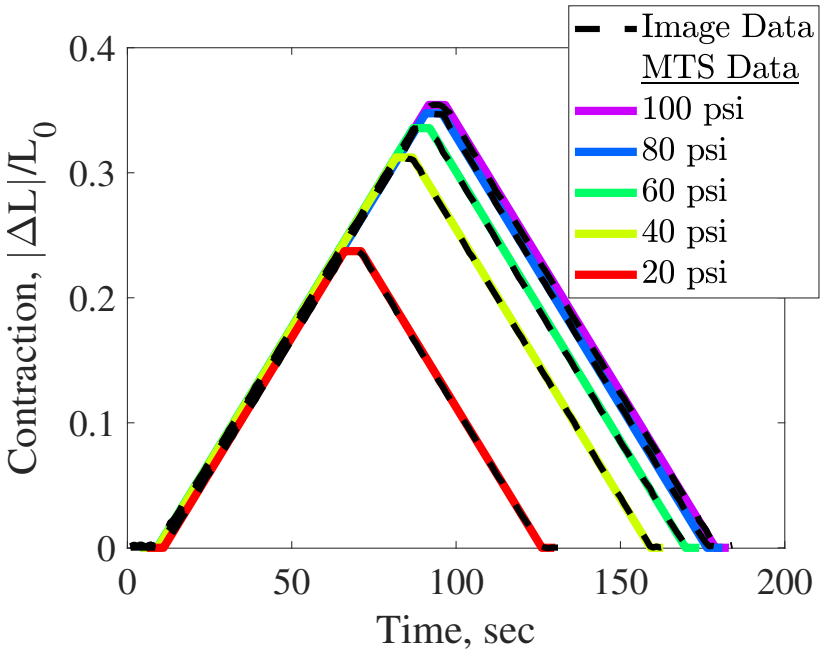

Figure 4.14: Comparison between contraction of image data, and displacement recorded by the MTS machine for a single contraction cycle

Figure 4.14 shows that the photogrammetric data tracks that of the MTS machine very well, with a maximum differential between the two of 0.02 in occurring at the FAM's resting length, which results in an error of the length measurement of 0.25%. With a measurement resolution of 0.004 in/pixel, a portion of this error is a limitation of the resolution of the image. A portion of this measurement error can also be attributed to the slightest amount of distortion along the length of the FAM. The diameter measurements of the shape profile, with an even narrower angle-of-view, would be subject to even less perspective distortion which would result in even less measurement error. Therefore, the 0.25% error of the photogrammetric measurements can be treated as an absolute maximum. With this comparison, the photogrammetric measurements of this research can be received as a high-fidelity

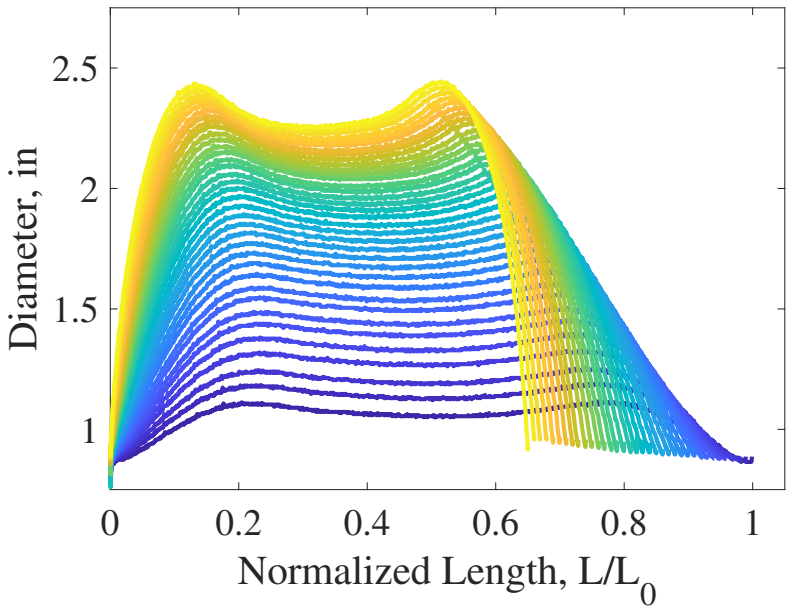

Figure 4.15: Evolution of the shape profile for a complete contraction cycle (100 psi)

representation of the true dimensions of the FAM's braid. The shape profile of the FAM is now analyzed with confidence in the accuracy of the photogrammetric measurements.

With the maximum contraction achieved at the highest test pressure, the 100 psi test serves as a good starting point for analysis of the FAM's shape profile. Figure 4.15 provides snapshots of the FAM's shape profile in 1% contraction increments up to the maximum contraction of about 35% at 100 psi.

There are a few observations to be made from the shape profiles in Figure 4.15. The distinct shape, with a maximum diameter at each end of the midsection, resembles the shape of a peanut. The profile near each end-fitting is also of interest, with a slope of the braid that dramatically changes as the FAM contracts. The slope is close to zero at low levels of contraction, but rapidly increases with increased contraction. This distinct change in the shape of the braid makes it difficult to have

a single assumed shape for the profile near each end-fitting, as has been assumed by other authors (e.g. circular arc, toroid, etc.), that can accurately represent the shape profile for the entire contraction range. Observation of other FAMs of the same material construction have shown that this characteristic shape is not unique to this FAM. Some of those FAMs have exhibited a midsection with a more severe peanut shape than others, but all have exhibited the change in profile slope in proximity to each end-fitting that is observed here.

This section demonstrated the successful measurement of the FAM's shape profile using photogrammetric analysis. Subsequent sections provide a preliminary analysis of these profiles that demonstrates the added value that photogrammetric characterization of FAMs can provide.

4.5 Analysis

Photogrammetry provides the first quantitative measurements of the shape profile of FAMs, and opens the door for new and improved modeling efforts. As a first step towards analysis of these shape profiles, each shape profile – which is comprised of thousands of data points – must be defined in simpler terms. One method could be to define each shape profile by a single value such as the average or maximum diameter of the profile. Defining the profile by a single diameter value assumes a cylindrical profile, and enables the measured data to be used with current modeling frameworks that have an input of a single approximated cylindrical value. Now, if a more detailed analysis of the shape profile is desired, each profile dataset

can be defined by a fit equation. A Fourier series fit equation is presented as a good candidate for accurate representation of the FAM's shape profile.

The shape profile data can also be compared to the cylindrical diameters that have been assumed in previous work. Prior to the quantitative analysis methodology presented here, the cylindrical diameter could only be estimated based on approximations derived from the resting (uncontracted) geometry of the FAM. We will term these the *estimated cylindrical shape profiles*. The accuracy of these shape profile estimates has gone relatively unchecked. Using the measured shape profile data, we now have the ability to test the accuracy of these estimated cylindrical approximation shape profiles.

Finally, analysis of the measured shape profile provides the unique opportunity to define the internal volume of FAMs. Using an assumption of axisymmetry along the longitudinal axis of the FAM, two-dimensional photogrammetry measurements can be used to approximate the internal volume through a non-intrusive method that is much simpler than previous methods that have required costly and intrusive measurement setups.

4.5.1 Shape Profile Analysis

4.5.1.1 Profile Average Diameter

The average diameter is easily calculated from the raw shape profile data, and is the simplest representation of a shape profile for analysis. With the average defining a single diameter value for each profile, the resulting assumed cylindrical profile

is in contrast to the complex curvature of the measured profile (Fig. 4.17(b)). The average profiles result in average diameters that are about 10% below the maximum diameter due to the dramatic decrease in diameter at each end of the FAM in proximity to the end-fittings. The average diameter was calculated for the entire contraction range of the FAM at each pressure (Fig. 4.16). The results suggest that the radius is nominally independent of internal pressure. Closer inspection of the average diameters, however, reveals small increases in diameter with pressure. This is especially apparent in the zero-contraction state, where the diameter swells by about 0.02 in from 20 psi to 100 psi. This appears to capture the affect of tensile stretching of the braid, a phenomenon that had not previously been captured. Stretching of the braid has often been ignored with a rigid braid assumption, but has also been accounted for – without the benefit of having quantitative data – in some modeling efforts [11, 13]. Further investigation of the apparent increase of the braid diameter at fixed length states with increases in pressure warrants further investigation in future work.

4.5.1.2 Profile Fourier Series Fit

Previously assumed shape profiles have failed to accurately capture the complex curvature of the FAM's shape profile. Previously piece-wise profile definitions used for attempted corrections on the cylindrical profile approximation – which typically use separate equations to define the profile of the midsection and the region near each end-fitting – increase modeling complexity with unvalidated improvements

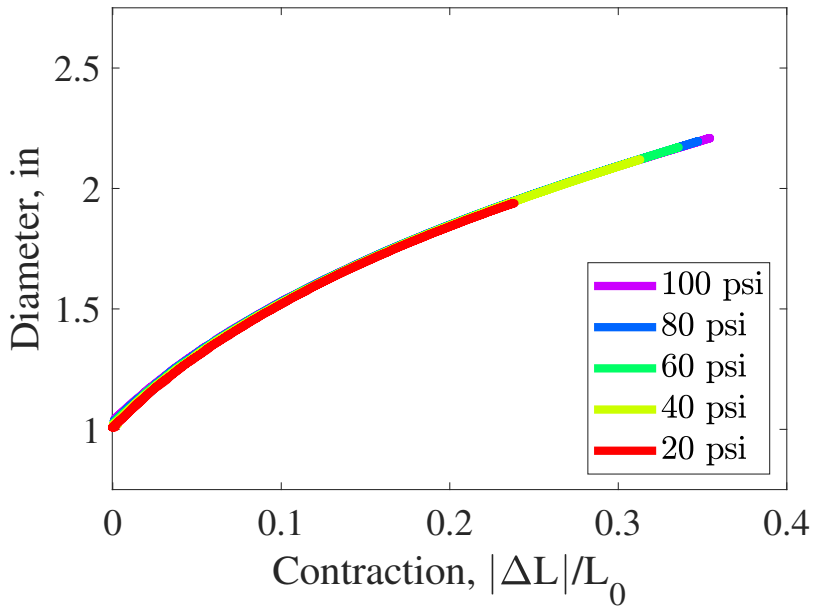

Figure 4.16: Average diameter of the FAM's shape profile for all tested pressure-contraction states

in accuracy. A single equation representation of the measured shape profiles is desired for simplicity of analysis.

Curve fit equations are used to fit the measured shape profiles. With multiple forms of fit functions to choose from (e.g. polynomial, exponential, etc.), it is important to select a function with a characteristic shape that resembles the shape of the observed profiles to enable an accurate and low-order fit equation. Since the observed profiles draw a resemblance to a half-sine pulse with higher order harmonics, a Fourier series curve fit equation was selected. The form of the fit equation is given as:

$$y = a_0 + \sum_{n=1}^{3} a_n cos(nxw) + b_n sin(nxw) \tag{4.7}$$

where x represents the position along the length of the shape profile, a_0 provides a horizontal shift, n indicates the order of the harmonic, and a_n and b_n are terms

that scale the magnitude of each harmonic. The number of terms used for the fit is adjusted to achieve a good fit while also keeping the number of terms to a minimum for simplicity. A third-order Fourier series fit was found to achieve a very good fit of the shape profile data (Fig. 4.17(a)). The resulting fit has a low combined average error for all tested states of contraction. The accuracy of the fit of this FAM begins to plateau with the use of three or more terms. Table 4.2 provides a comparison of the accuracy of the fit depending on the number of terms used. Values for each term of the three-term Fourier series fit performed in Figure 4.17(a) are provided in Table 4.3. The profiles for all tested states of pressure and contraction can be fit for a complete characterization of the shape profiles. As noted from previous observation of Figure 4.16, the profile is predominantly a function of the contraction state with little variation with changes in pressure. This enables a reduction in the number of required fits to fully define the shape profile of the FAM by only needing to characterize the shape profiles of the maximum pressure tested.

Table 4.2: The effect of the number of Fourier series fit terms used for fitting the profile data on the maximum and Root-Mean-Square Error (RMSE) averaged between all tested pressures

Number of Terms:	**1**	**2**	**3**	**4**	**5**
Max Error (avg.), in	0.509	0.069	0.036	0.035	0.021
RMSE (avg.), in	0.108	0.015	0.005	0.005	0.003

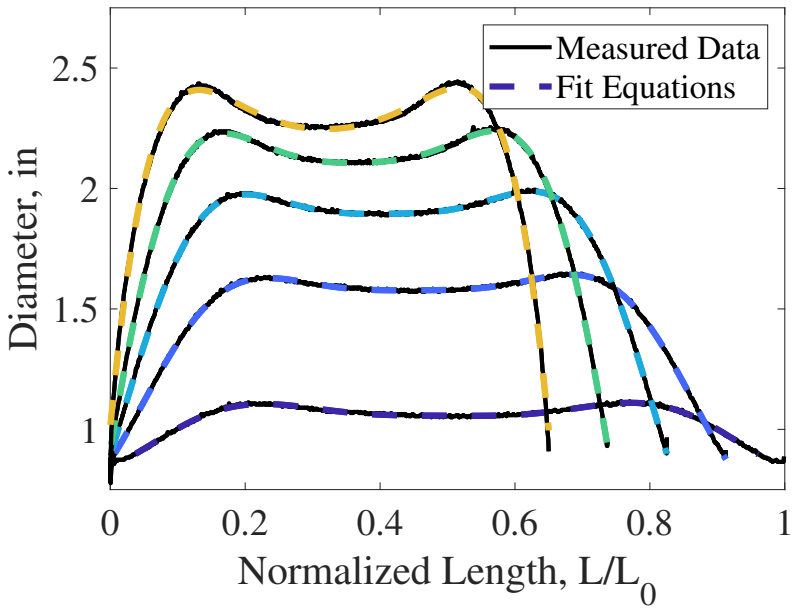

(a) Comparison of the measured shape profiles to the three-term Fourier Series fit equation profiles

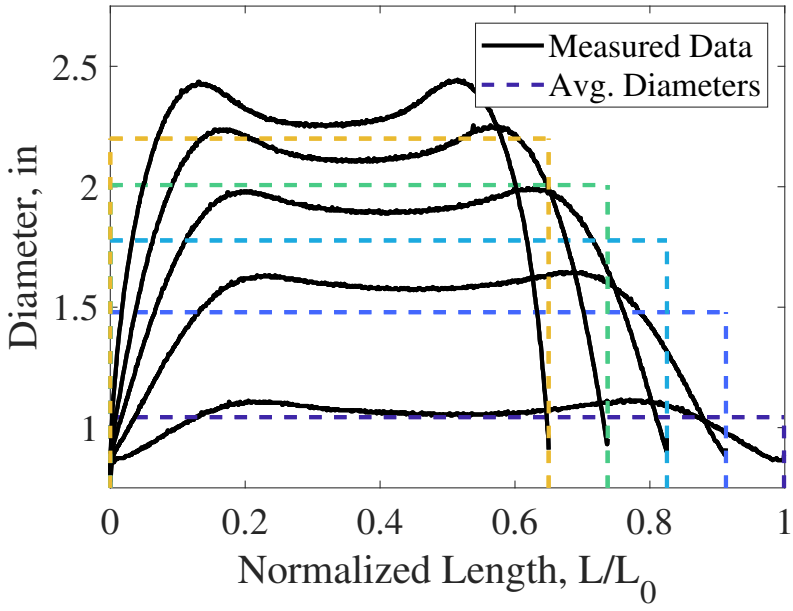

(b) Comparison of the measured shape profiles to assumed cylindrical profiles that have a diameter equal to the average diameter of the measured shape profile at each respective contraction state

Figure 4.17: Comparison of assumed profiles to the measured shape profiles of the FAM at 0, 8.75, 17.5, 26.25, and 35 (maximum) percent contraction at 100 psi

Table 4.3: Coefficient values for the three-term Fourier Series fit performed in Figure 4.17(a)

$\%L_0$	a_0	a_1	a_2	a_3	b_1	b_2	b_3	w
0%	1.02	-0.09	-0.07	-0.01	0.03	0.06	0.02	5.62
8.75%	1.37	-0.35	-0.15	-0.01	-0.17	-0.19	-0.06	-5.86
17.5%	1.51	-0.56	-0.10	0.04	0.43	0.41	0.10	6.00
26.25%	1.27	-0.83	0.29	0.18	1.20	0.75	0.04	5.89
35%	-32.74	24.82	12.82	-3.90	44.44	-18.47	-0.5	3.35

4.5.1.3 Comparison to Previous Cylindrical Profile Estimates

The shape profile of FAMs has traditionally been modeled as a cylindrical profile. The diameter of the FAM can be estimated for all states of contraction by using this cylindrical approximation and an assumed initial geometry. The estimated profile diameter has long been assumed to be nominally accurate enough for use in almost all modeling efforts of FAMs. However, with no previous method of measuring the actual shape profile of FAMs, there has not been any quantifiable data to check the accuracy of these estimated cylindrical profiles until now. With the shape profile measurements acquired using photogrammetry, the accuracy of the cylindrical shape profile approximation can now be tested.

The cylindrical approximation has served as the basis of most FAM modeling since the inception of the FAM in 1958 [2]. The cylindrical approximation, prior to the addition of any applied correction factors, makes the following assumptions:

- The shape profile is cylindrical (constant diameter with respect to length)
- The braid angle is constant with respect to length

- There is no strain in the braid fibers

With these qualifying assumptions, the geometry of the FAM can be defined using the *triangle relationship* which defines a set trigonometric relationship between the active length, L, diameter, D, and braid angle, θ, of the FAM through fixed values that are the length of each braid fiber, B, and the number of turns of each braid fiber around the circumference of the FAM, N [5]. The fixed values of N and B, can then be found using the initial geometry of the FAM defined by the initial braid angle, θ_0, the initial diameter, D_0, and the initial active length, L_0, through the following relations:

$$N = \frac{L_0}{D_0 \pi tan(\theta_0)} \tag{4.8}$$

$$B = \frac{L_0}{sin(\theta_0)} \tag{4.9}$$

Finally, the diameter of the FAM can be estimated as a function of active length through the following relationship:

$$D_{est}(L) = \frac{\sqrt{B^2 - L^2}}{\pi N} \tag{4.10}$$

The established direct relationship between D_{est} and L produces estimated diameter values – commonly used as an input parameter to models – through relatively simple geometric relationships. However, it is also relatively sensitive to the assumed initial geometry of the FAM. The value of D_0 is commonly assumed to be equal to the resting outer diameter of the bladder (assuming a thin braid), or the braid diameter at its point of insertion into the end-fitting. The value of θ_0 can then be determined using the method covered in Pillsbury (2015) [48] which uses the linear relationship

between blocked force and pressure to solve for θ_0. It should be noted that the value of θ_0 found through this method is a function of the estimated value of D_0.

The average diameter of the measured profile data will be compared to the estimated cylindrical profile. The assumed cylindrical profiles for both the estimated and average of the measured data provide a basis of direct comparison. An accurate estimated profile diameter should match the average of the measured profiles.

The value of D_0 for the tested FAM is equal to the outer diameter of the bladder at 7/8 in. An estimated value of θ_0 was found using the blocked force with respect to pressure data to be 72.27 degrees. The resulting estimated diameter values, labeled as $D_{est,1}$, are compared to the results of the measured data in Figure 4.18(a) for a single stroke of the FAM. There is an observed error in the estimated value of D_0 which is about 0.15 in below the initial measured average diameter of about 1.025 in. This initial increase in diameter was not due to any noticeable slack in the braid prior to pressurization, with the braid being taut prior in the resting length state. The resulting discrepancy between the estimated and measured diameters is especially large at low levels of contraction.

With knowledge of the actual value of D_0, using the measured data we can attempt to estimate the shape profile again with corrected values of D_0 and θ_0. Since there is a slight range of the measured initial diameter values with respect to pressure, the average of these measured values of 1.025 in can be used for this comparison. This value of D_0 results in a value of 69.04 degrees, a significant difference from the previous value of 72.27 degrees. Estimated diameter values, $D_{est,2}$, are calculated using the new initial geometry conditions (Fig. 4.18(b)). With

proper alignment of the curves at low levels of contraction, there is now a sizeable error in the maximum contraction state. The resulting error between curves could be the result of the estimated value of θ_0 being too high. A lower value of θ_0 would result in lower values of estimated maximum contraction. If the value of θ_0 is reduced to 68-68.5 degrees with D_0 still equal to 1.02 in, the estimated and measured diameter curves match very well. However, an accurate physical measurement of the value of N for the tested FAM found that the braid angle should be around 68.9 - 69.7 degrees which coincides well with the value of θ_0 used to define $D_{est,2}$. It is therefore likely that the discrepancy between the values of D_{avg} and $D_{est,2}$ are a result of error from using the cylindrical approximation for the estimated diameter values. The cylindrical approximation, in estimating a diameter from the initial geometry state, neglects the length of the braid that is effectively lost to the curvature of the FAM's braid resulting in overestimations of diameter. This research serves as an initial comparison of these estimated and measured diameter values, with the resulting discrepancy between these values deserving of further investigation.

4.5.2 Volume Approximation

Measurement of a FAM's internal volume is often required for actuation system design and modeling efforts. Estimates of volume are necessary to determine requirements of the system such as the working fluid flow rate and storage requirements. Modeling efforts also use values of internal volume for force response models (e.g. virtual work method), as well as for providing estimates of actuation efficiency.

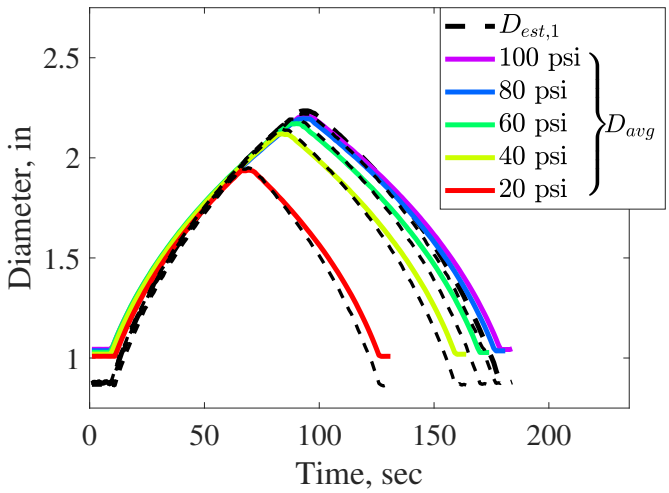

(a) Comparison of D_{avg} against estimated diameters, $D_{est,1}$, using initial geometry $D_0 = 7/8$ in, and $\theta_0 = 72.27$ deg.

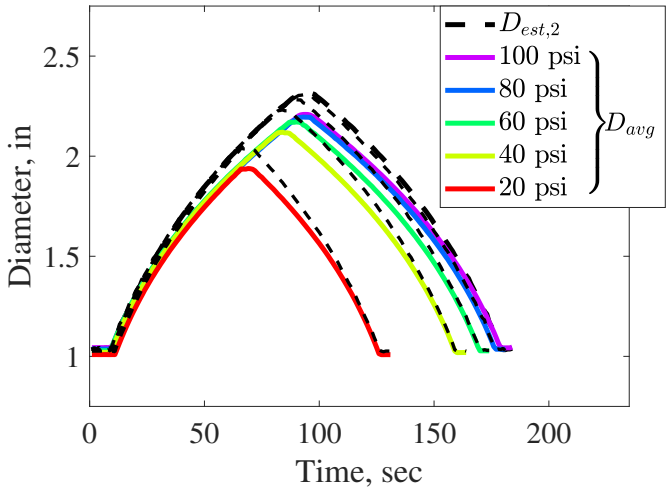

(b) Comparison of D_{avg} against estimated diameters, $D_{est,2}$, using initial geometry $D_0 = 1.02$ in, and $\theta_0 = 69.04$ deg.

Figure 4.18: Comparison of the average measured diameter values, D_{avg}, against estimated diameters, $D_{est,1}$ and $D_{est,2}$

The acquisition of accurate volume measurements has often proved difficult for researchers due to the specialized equipment that is often required to do so. As a consequence, researchers have often settled for using dimensions provided by using the estimated cylindrical approximation diameter.

The photogrammetric data acquired in this research provides the opportu-

nity to easily obtain an accurate estimation of the internal volume of the FAM for all tested pressure and contraction states. Since the profiles only provide a two-dimensional depiction of the FAM, a three-dimensional measurement of volume requires the assumption that the FAM is axisymmetric about its longitudinal axis. The symmetry of many previously tested FAMs usually makes this a reasonable assumption. Appreciable deviations from symmetry have only been observed for FAMs with flaws in their fabrication.

Using the shape profile data, the internal volume of the FAM, V_{int}, can be found using the following basic equation:

$$V_{int} = V_{prof} - V_{bld} - V_{brd} \tag{4.11}$$

where,

$$V_{prof} = \begin{cases} w_p \sum_{i=1}^{L_p} \frac{\pi}{4} D_i^2, & \text{discrete profile} \\ \\ \pi \int_0^L \left(\frac{D(x)}{2}\right)^2 dx, & \text{continuous profile} \end{cases} \tag{4.12}$$

V_{prof} is the volume encased within the outline of the shape profile of the FAM, V_{bld} is the volume consumed by the incompressible bladder, and V_{brd} is the volume of the braid. Therefore, equation 4.11 states that the internal volume of the FAM is equal to the volume within the shape profile minus the volumes of the bladder and braid that are also contained within the shape profile volume. The bladder and braid volumes are fixed values that can easily be found using their cylindrical dimensions in the FAM's resting length configuration (i.e L_0). For the FAM used in this research, the braid has an assumed resting diameter of 0.863 in equal to that of the end-fitting at each end, and a thickness of 0.011 in resulting in a value for V_{brd}

of 0.273 in^3. The incompressible bladder has a resting outer diameter of 7/8 in and thickness of 1/16 in, resulting in a bladder volume, V_{bld}, of 1.481 in^3.

The volume V_{prof} can be found through integration of the defined shape profile (Eq. 4.12). The method of integration is dependent on how the shape profile is defined. In this research, the diameter of the shape profile has been defined as a discrete function D_i, with the width of the FAM defined for each pixel i along the length of the FAM, and as a continuous function, $D(x)$, defined by the Fourier series fit equations used to describe the shape profile of the FAM. To find V_{prof} for the discrete definition of the shape profile, integration is performed as a summation of the volume of each pixel-width slice of the FAM. This discrete integration is shown in Equation 4.12, where w_p is the width of each pixel, and L_p is the current length (in pixels) of the FAM. The continuous function definition of the shape profile provides a much simpler method of calculating the volume of the FAM. As shown in equation 4.12, disc integration is performed to calculate the volume V_{prof} using the continuous function form of the shape profile, $D(x)$. The cylindrical approximated diameter of the FAM, $D_{cyl,fit}$, having been shown to accurately represent the average diameter of the FAM, can also be used to calculate the volume V_{prof} of the FAM.

Using the discrete form of the shape profile data, the internal volume of the tested FAM is calculated as shown in Figure 4.19. As is predicted from the average shape profile diameter results of Figure 4.16, the volume is a function of the length state of the FAM and is effectively independent of internal pressure. There is only a slight deviation in volume with respect to pressure due to the assumed stretch in the braid. These results can be easily adjusted to provide values for the change in

volume required for contraction of the FAM as would be needed for flow rate and efficiency calculations.

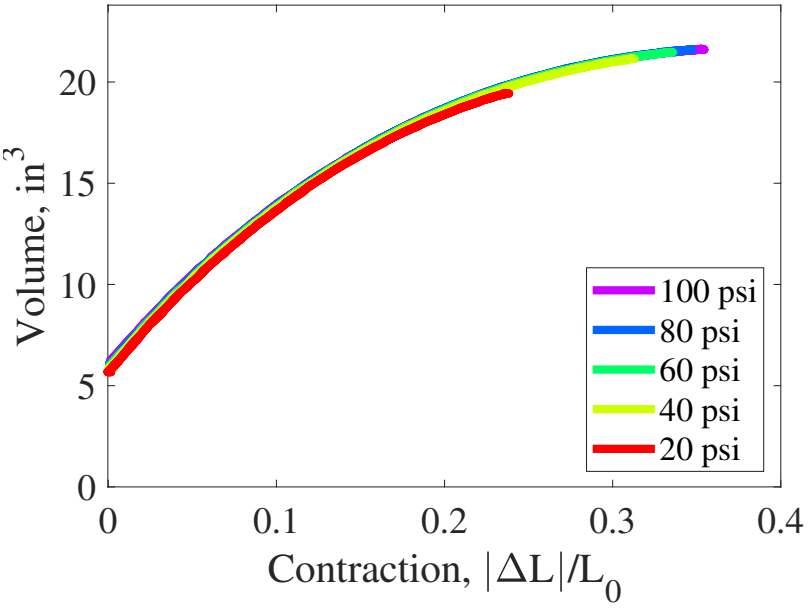

Figure 4.19: Internal FAM volume with respect to contraction for all tested pressures

4.5.3 Testing of Different FAMs

A few other FAMs have been characterized thus far using the photogrammetric methods as described above. Three 7/8 in diameter FAMs and one 2-1/4 in diameter FAM have been characterized using photogrammetry. The three 7/8 in diameter FAMs have identical material construction. The 9-9/32 in long FAM has been used to demonstrate the photogrammetric methods up to this point, but FAMs with lengths of 12 in and 20 in have also been tested (Fig. 4.20). These FAMs were tested to compare their shape profiles while also demonstrating the ability of the photogrammetric test setup to characterize FAMs of varying length scales. Analysis of the 2-1/4 in diameter by 13-13/16 in long FAM (Fig. 4.22) further demonstrates

the capability of the test method to characterize FAMs of a wide range of diameters.

The shape profiles of the 7/8 in diameter FAMs are compared in Figure 4.21 for the same five states of percent contraction. Despite their slight differences in shape, their resulting diameters are very similar. The three FAMs were all able to achieve nearly identical free contraction values at 100 psi of 35.43%, 35.55%, and 35.36% for the 9-9/32 in, 12 in, and 20 in FAMs respectively. Each of their profiles has an undulation at each end of the FAM that resembles the previously noted peanut-like shape which seems to be a characteristic of many FAMs. The shape profile of the 20 in (longest) FAM has an additional small undulation at its mid-length that is barely visible. A Fourier series fit was conducted on the three FAMs resulting in an accurate representation of their profiles. A three-term Fourier series provides an accurate fit for the 9-9/32 in and 12 in long FAMs, while the additional undulation of the 20 in long FAM profile requires a four-term Fourier series to achieve a good fit. The largest discrepancy between the profiles comes in the zero-percent contraction state, where the 9-9/32 in FAM has the largest average diameter of the three. The difference in initial diameters is reflected by the difference in their estimated initial braid angles. The three FAMs had estimated initial braid angles of 69.4, 71.1, and 71.9 degrees for the 9-9/32 in, 12 in, and 20 in FAMs respectively. With all three FAMs using the same braid, the differences in initial braid angle and diameter indicates slight differences in their fabrication or identification of their resting length. As previously noted from observation of Figure 4.16, the diameter of the FAM is much more sensitive to changes in length at lower states of contraction, so a small deviation in length or braid angle near the resting length state results in a relatively

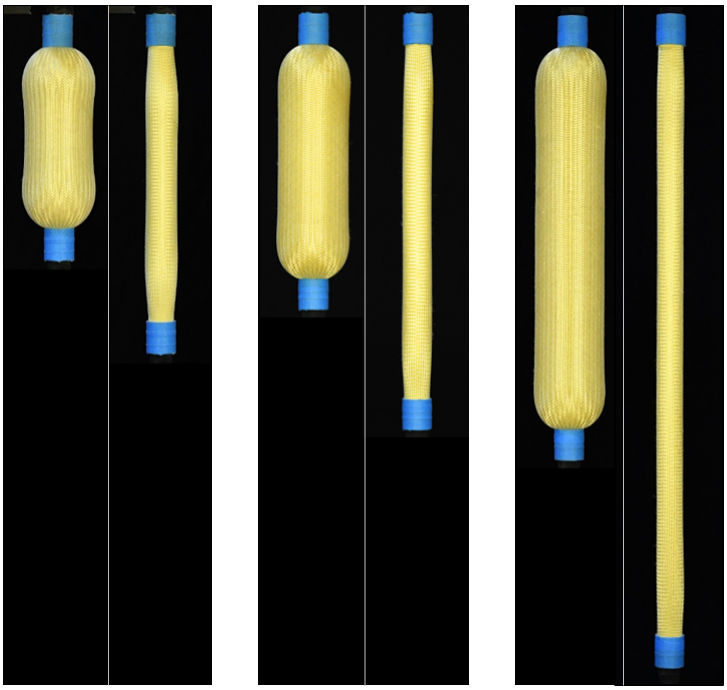

(a) $L_0 = 9\frac{9}{32}$ in (b) $L_0 = 12$ in (c) $L_0 = 20$ in

Figure 4.20: Tested 7/8 in FAMs in free contraction and blocked force (resting length) states at 100 psi

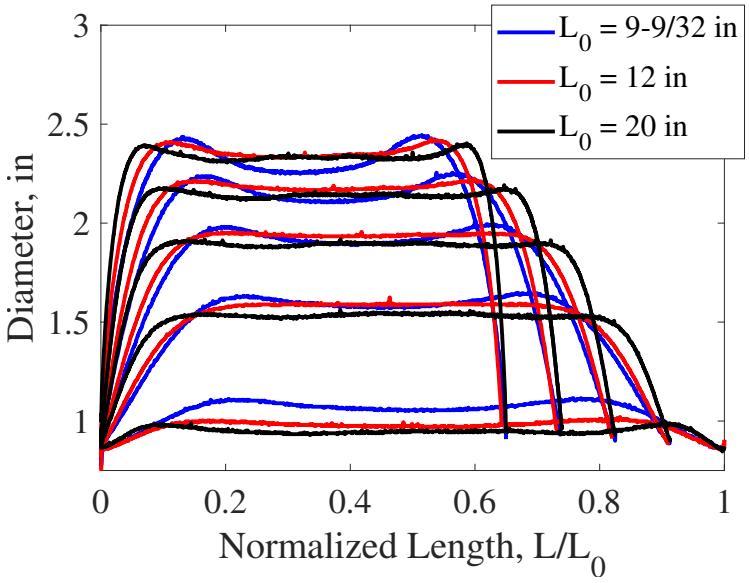

Figure 4.21: Shape profile comparison of the three tested 7/8 in diameter FAMs at 0, 8.75, 17.5, 26.25, and 35 percent contraction

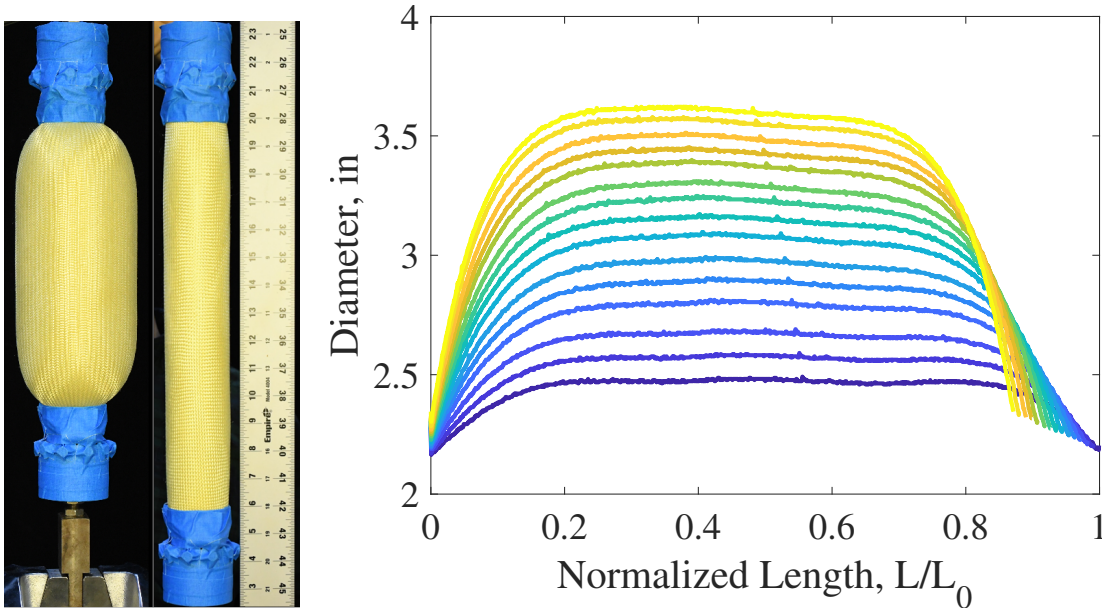

(a) Free contraction and resting length states

(b) Evolution of shape profile

Figure 4.22: Characterization of the 2-1/4 in diameter FAM at 26 psi

large change in the expected diameter.

The shape profiles of the 2-1/4 in diameter FAM, as captured in Figure 4.22(b), are also accurately captured using the described photogrammetric methods. The simpler rounded shape of its profile allows for an accurate Fourier series fit of the profiles to be achieved with the use of only two terms.

Testing of both the 7/8 in diameter by 20 in long FAM, and the 2-1/4 in diameter by 13-13/16 in FAM, represents the maximum extent of what has been produced with regard to sizing of FAM lengths and diameters, respectively. Although the photogrammetric measurement of FAMs of different sizes might seem trivial, many previous test setups for FAM volume testing have required modifications or redesigns in order to administer tests for FAMs of different sizes. Photogrammetric characterization is capable of testing FAMs with a large range of sizes by just repositioning

the camera to capture and fill each image with the entire FAM. As mentioned earlier, the positioning of the camera will effect the accuracy of the photogrammetric measurements. The accuracy is dependent on the competing effects of attempting to reduce the angle-of-view by distancing the camera from the FAM, while also keeping the distance at a minimum to maximize measurement resolution. For the 7/8 in diameter FAMs, the camera was setup at the distance of 60.0 in for the shorter 9-9/32 in length FAM, and it was placed 3.0 in farther away for the longer 20 in FAM to capture its entire length. Those two camera placements resulted in angle-of-views of 8.84 and 18.04 degrees respectively, and measurement resolutions of 216.35 pixels/in and 226.63 pixels/in respectively. Both tests achieved a high degree of accuracy despite the slight changes in resolution and angle-of-view. Comparing the contraction measurements of the MTS machine and photogrammetric data, as performed in Figure 4.14 for the 9-9/32 in FAM, resulted in a maximum error of 0.042 in (0.21%) for the 20 in long FAM. This is in comparison to the 0.024 in (0.25%) error previously cited for the 9-9/32 in FAM. Similarly, measurement of the 2-1/4 in diameter FAM achieved results with a maximum error in the length contraction measurement of 0.05 in (0.36 %). It is assumed that even with the larger diameter of this 2-1/4 in FAM, its diameter is still significantly smaller than the length measurement that is used here to cap the maximum expected error in the measurement.

The accurate characterization of the shape profiles of the four FAMs demonstrates that the photogrammetric methods presented in this research can be readily adapted to FAMs of different length and diameter scales. A new method of experimentally characterizing the volume of FAMs has been presented that can be per-

formed without the need for specialized test equipment, and can be easily adapted for the measurement of FAMs of different sizes.

4.6 Conclusion

This research presents an approach for characterizing the shape profile of FAMs through photogrammetric measurement. The method of measuring the FAM's shape profile is described including a basic test setup, method of image acquisition, and a process of abstracting measurements from the image data. A 7/8 in diameter FAM served as an example for describing the presented test method and analysis.

The photogrammetric testing was performed in parallel with the isobaric force-contraction characterization that is typically performed to define the actuation of FAMs. The photogrammetric test setup requires the addition of only a camera, backdrop, lighting, and masking to acquire measurement data. The complete method of acquiring measurements from the image data, including a background on the methods used, was provided in detail to ease the adoption of this characterization method for future research efforts.

Some preliminary analysis of the shape profile data was then performed. The average diameter and volume of the FAM were found to be primarily a function of the contraction state. However, there was an indication of strain in the braid fibers from the small but appreciable increase in FAM diameter with increased pressure. This strain in the braid fibers had not been quantifiable prior to the characterization performed in this testing.

The measured shape profiles were redefined from a set of data points to a cylindrical approximation or fit equation. The average of each measured profile was used to define each profile as a single value. This assumes a cylindrical shape profile that can be readily applied to previously existing models. If the assumption of a cylindrical shape profile is not sufficient for a high-fidelity modeling effort, the complex curvature of the shape profiles can be defined to a high-degree of accuracy using Fourier series fit equations. Working with equations instead of the raw shape profile data greatly simplifies usage of the shape profile information garnered from the photogrammetric testing.

The estimated diameters found using the cylindrical approximation and initial geometry have long served as the basis for most FAM modeling. These estimates were tested by comparing them to the measured average diameters of the tested FAM. The comparisons resulted in discrepancies between the estimated and measured diameters, with the first comparison finding an inaccuracy in the initial estimated diameter. After this initial offset in diameter was corrected, the estimated diameters still did not match the measured diameters, warranting further future investigation of the effect of the cylindrical approximation on these estimates.

A new method of characterizing the internal volume of FAMs using the acquired shape profile data was also presented. This new non-contact method of calculating the internal volume is desirable compared to current methods which often require specialized test equipment that must be altered in order to test FAMs of different sizes.

Finally, the accuracy and adaptability of the presented test method is demon-

strated through the shape profile characterization of multiple FAMs of different sizes. A comparison of three 7/8 in diameter FAMs was performed, demonstrating some of the similarities in their contraction-diameter characteristics, and also the slight differences in the undulations and curvature of their profiles. A wide 2-1/4 in FAM was also accurately characterized with the same test setup without the need for any modifications. The Fourier series fit was able to accurately replicate the profile data for all tested FAMs with an observed correlation between the number of undulations of the profile's curvature, and the number of terms required to provide an accurate fit.

The presented method was developed out of a need to be able to quantify modeling unknowns and long used approximations of diameter, but also out of the necessity to define the dimensions of FAMs for implementation into mechanism designs, to define actuation system requirements, and develop accurate models for open-loop control of FAMs. It is the authors hope that this method of characterization can aid in the discovery, confirmation, and necessary adjustments for improved modeling efforts, as well as enlighten and ease the adoption of FAMs by providing a more complete characterization of their actuation.

Chapter 5: Investigation of the Inelastic Braid Modeling Assumption

5.1 Introduction

To date, most of the methods used to model the actuation force and geometry of FAMs have been based on the original modeling strategies used from when FAMs were first in invented back in 1958 [2]. These models have continued to rely on assumptions while having little or no investigation of their accuracy. Many of these assumptions have been retained due to the modeling simplifications they provide, or due simply to an inability to make further improvements to the accuracy of the models.

One of the most prevalent modeling assumptions used with FAMs is the *inelastic braid assumption*, which assumes that the fibers of the braid do not stretch under the tensile loads that are applied to them during actuation. This assumption – commonly used in conjunction with the *cylindrical geometry approximation* – enables a simplification of the geometric and actuation force models of FAMs.

A lack of investigation into the effects of braid elasticity has persisted, in part, due to an inability to experimentally capture and quantify the stretch of the braid during actuation of the FAM. Stretching of the braid is often visually imperceptible, and has consequently often gone unnoticed or ignored. Previous methods of mea-

suring the dimensions of the braid – such as using a ruler to measure the braid at discrete points along the length of the FAM – have been rudimentary and lack the resolution and accuracy required for an effective investigation of braid stretch.

A wide-reaching survey of previous FAM modeling efforts was conducted, and found that very few researchers have investigated the effects of braid elasticity on actuation. A few papers have included a cursory investigation of braid elasticity and, absent the use of supporting experimental data, have subsequently assumed the effects to be negligible [81]. Just two authors were found to have included factors that directly account for braid elasticity in their actuation force models, and they have both noted subsequent improvements in the accuracy of their models. Davis et al. [11] added a term to their force-balance based model to account for the estimated braid stretch during actuation after observing the radial expansion of a FAM in isometric states with changes in pressure. Similarly, Kothera [13] used an energy-method modeling approach, adding a term that accounted for the elastic energy storage due to the stretch of the braid. With the inclusion of their braid-stretch terms, both studies demonstrated improvements in the accuracy of their actuation force models. However, they both lacked experimental evidence to support the magnitude of the braid stretch assumptions used in their models.

Now, development of a photogrammetric method for measuring the FAM's external dimensions provides the degree of resolution and accuracy required of measurements to analyze the stretch of the braid during FAM actuation. Initial analysis of the photogrammetric measurement data (Ch. 4) found a slight increase in the average diameter of the FAM as it was isometrically pressurized. It was hypothesized

that this radial expansion is primarily due to the stretch of the braid fibers, and not simply attributable to a reorientation and initial tensioning of the braid fibers as has been noted in previous testing of FAMs. Further investigation is necessary to affirm this hypothesis.

The goal of this research, therefore, is to investigate the effects of the braid's elasticity on the resulting geometry and actuation force of FAMs. The stretch of the braid is calculated using an accurate representation of the FAM's dimensions obtained through photogrammetric measurement. Calculations of braid stretch and tension are then used to calculate an approximate modulus of elasticity of the braid material which is then compared to cited and experimentally-obtained values. Agreement of all of the obtained elasticity values indicates that the braid elasticity is, in fact, the source of the observed radial expansion. The result of that elasticity is then tested by approximating its effects on the resulting dimensions and actuation force of the FAM. An assessment is then made on whether the inelastic braid assumption should be maintained as a baseline in future work.

5.2 Experimental Testing

To investigate the effects of braid elasticity, characterization of both the braid and the FAM's actuation are needed. An actuation response was characterized by performing isobaric force-contraction tests on the FAM while simultaneously measuring its geometric dimensions. The braid was characterized in isolation by performing tensile tests on individual threads of the aramid braid.

5.2.1 Description of Tested FAM

The tested FAM is composed of a latex inner bladder, an aramid braided sleeve, and swaged aluminum end-fittings (Ch. 2) (Fig. 5.1(a)); It has a diameter of 7/8 in, and a length of 9-9/32 in. The braid is defined by two parameters that are the resting length of each braid thread, B_0, and the number of turns of each thread about the circumference of the FAM, N. For the tested FAM, values for B_0 and N were found – through direct measurement of the FAM – to be 9.89 in and 1.09 respectively (Fig. 5.1(b)). Direct measurement of those two values ensured accuracies within $\pm 1/32$ in, and ± 0.005, respectively.

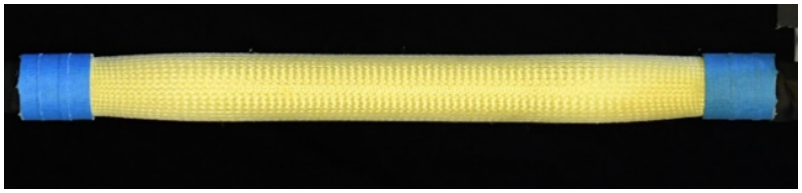

(a) Constructed FAM

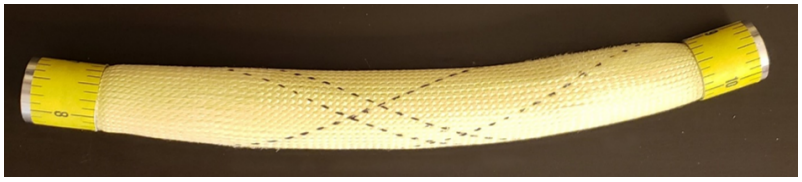

(b) FAM threads marked for measurement of N and B_0

(c) Kevlar braid used in FAM construction

Figure 5.1: Tested 7/8 in diameter FAM

5.2.2 Characterization of the FAM's Actuation

The actuation response of the FAM was characterized using a 22 kip MTS servo-hydraulic test machine (Fig. 5.2(a)). The MTS machine records the displacement of the cyclic motion, along with the external inputs of force (Honeywell Model 31 Mid) and pressure (Omega PC209-200G5V). This testing was performed by first setting a fixed internal pressure of the FAM, and then cyclically stroking the FAM between its resting length and its pressure-dependent zero force length states. That test sequence was repeated for isobaric pressure tests of 10-100 psi at 10 psi increments. The pressure of the working fluid was set and maintained at fixed pressures (i.e. isobars) using the air pressure control system developed in Chapter 3. The FAM was cycled three times at each pressure at a quasi-static rate of 0.04 in/sec. Throughout the testing sequence, measurement data of the FAM's outer diameter was simultaneously collected at 1 second intervals, by using the photogrammetric acquisition and analysis methods developed in Chapter 4. Observation of the measurements shows an increase in diameter with increases in pressure, that is indicative of what would be expected to occur with stretching of the threads in the braid (Fig. 5.2(b)).

5.2.3 Characterization of the FAM's Braid

The braid and its material properties are of particular interest in this research. The braid characterized in this research, is composed of 144 Kevlar-49 threads woven into a double-helical tubular sleeve (Fig. 5.1(c)). The Kevlar-49 thread is cited as

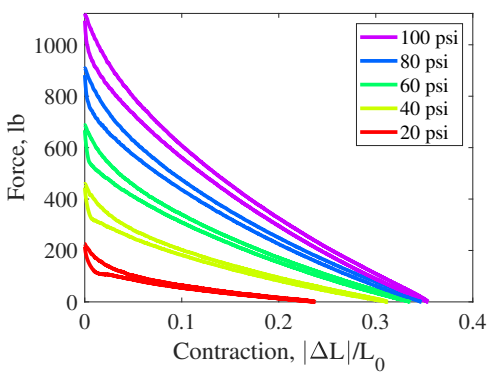

(a) Actuation Force of FAM with respect to contraction at set isobars

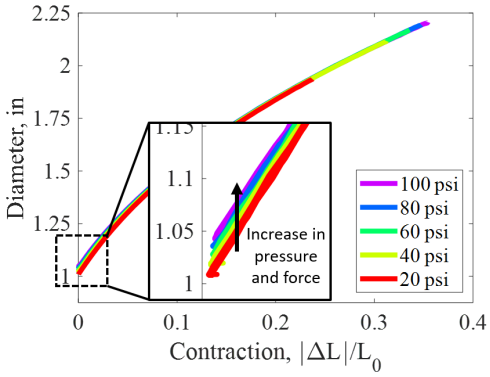

(b) Average diameter of FAM with respect to contraction

Figure 5.2: Characterization testing of the FAM's actuation and geometry

having an elastic modulus of 16.3×10^6 psi, a breaking strength of 59.3 lbf, and an elongation at failure of 2.4% [82]. Each of those threads is composed of 768 fibers and each fiber has a diameter of 0.00047 in, resulting in an overall thread cross-sectional area of $1.332 \times 10^{-4} in^2$.

The material specifications of the Kevlar-49 thread were experimentally validated by conducting a tensile failure test on thread samples from the braid that was used on the FAM. This provides a more complete picture of the stiffness profile of the Kevlar threads, but also ensures that the braid's material properties did not change due to any variation in manufacturing or storage (e.g., degradation due to UV light exposure). Tensile testing of the thread was performed on an Instron 8841 servo-hydraulic testing machine (Fig. 5.3(a)). Thread samples of about 4 in length were prepared by using epoxy to attach tabs for clamping at each end of the thread. Those thread samples were then stretched at a rate of 0.004 in/sec (0.1 mm/sec) until failure.

Test results for three threads are shown in Figure 5.3(b). The experimental

modulus of elasticity was approximated by identifying the slope of the linear portion of each curve. The average elasticity was found to be 16.9×10^6 psi which is within 5% of the cited value for Kevlar-49. Prior to the linear elastic region of each curve, there is a notable nonlinear region that begins at the onset of loading the thread. This nonlinear portion of each curve – which is typically left out of material property reference charts [83] – is due to the initial straightening and uncrimping of the thread fibers, and it continues until all of the fibers in the thread are tensioned and aligned with the thread axis [84]. Note that subsequent analysis of the strain in the braid will find this region of the stress-strain curve to be significant.

(a) Single thread tested on Instron machine

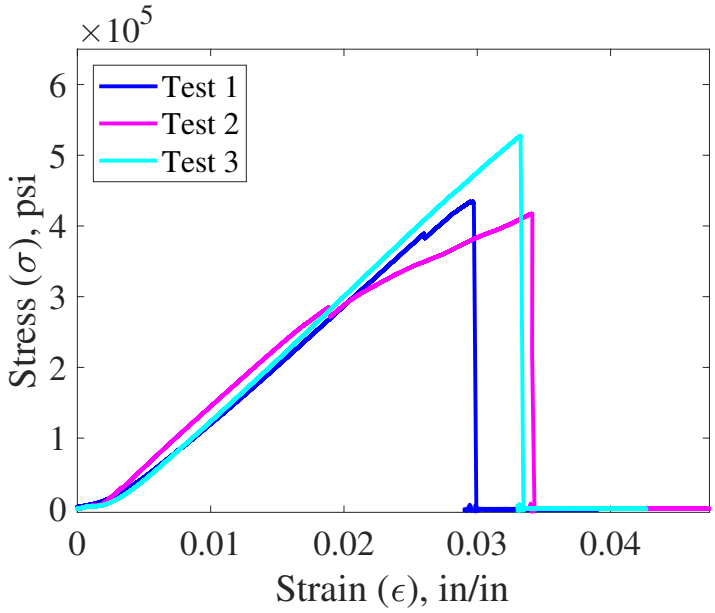

(b) Resulting stress-strain relationships of tested thread samples

Figure 5.3: Testing of Kevlar-49 thread samples

5.3 Analysis of Braid Elasticity Using Measurements of FAM

Characterization data of the FAM's actuation force and diameter is used for *in situ* analysis of the braid's elasticity during actuation of the FAM. The actuation force data is used to estimate the tension in the braid; the diameter measurements of the FAM are used to estimate the stretch in the braid. Typical methods of modeling the braid's dimensions and tension require a cylindrical approximation of the FAM's geometry. This approximation is commonly made despite the FAM's increasingly noncylindrical shape in contracted length states. To ensure the accuracy of our initial investigation of braid tension and stretch, we will focus on the FAM in its resting length state where the cylindrical approximation of the geometry is most accurate.

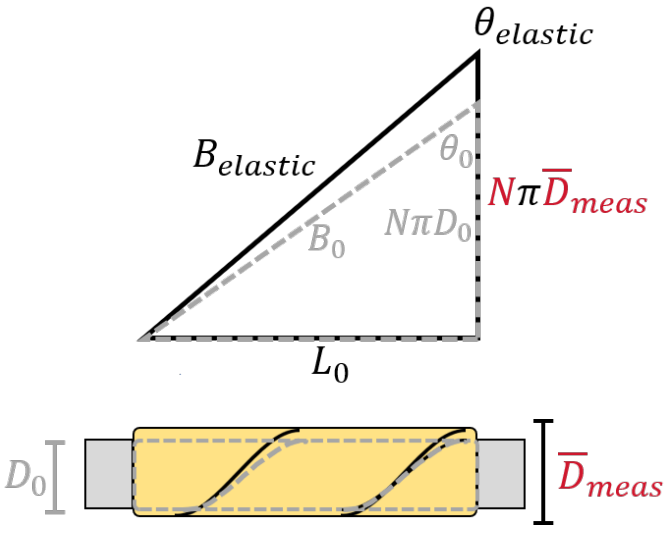

Figure 5.4: Triangle relationship of FAM dimensions, and subsequent effect with consideration of braid elasticity

The cylindrical approximation enables a description of the FAM's geometry

for all contraction states of a FAM through the use of a defined *triangle relationship* (Fig. 5.4). This relationship relates the FAM's length, L, and diameter, D, with variables that describe the braid including the braid angle, θ, the length of each braid thread, B, and the number of turns of each thread about the FAM's circumference, N. With the values of either N or D, and any two of the other dimension variables, the geometry of the FAM can be fully defined using the triangle relationship. For this work, we have known values for L, for the average diameter D, and for N, thus enabling B and θ to be estimated for respective states of contraction. Figure 5.4 shows that an increase in D_{meas} at a fixed-length state of L would result in a stretched length of the braid threads $B_{elastic}$, and a respective change in the braid angle to $\theta_{elastic}$. The stretched thread length can be estimated using the following equation:

$$B_{elastic} = \sqrt{(L^2 + (N\pi\bar{D}_{meas})^2)} \tag{5.1}$$

Estimation of the tension in each thread is based on force equilibrium equations from actuation force models as shown in previous work and as described in Chapter 1. These equations are also based on an assumed cylindrical geometry. Manipulation of the longitudinal force equilibrium equation results in the following equation for the thread tension T_{brd}:

$$T_{brd} = \frac{1}{n_{brd}} \frac{1}{sin\theta} (P\pi R^2 + F_{act} - \sigma_z \frac{V_{bld}}{L}) \tag{5.2}$$

where n_{brd} is the number of threads in the braid ($n_{brd} = 144$), P is the internal pressure of the FAM, and F_{act} is the actuation force. The last term accounts for the portion of the longitudinal force of the FAM that is due to strain in the bladder; it is

a function of the longitudinal stress σ_z, bladder volume V_{bld}, and the instantaneous length L.

Braid stretch and tension are initially investigated in the resting length state where estimates acquired from Equations 5.1 and 5.2 – based on the cylindrical approximation – are most accurate. Figure 5.2(b) showed a slight increase in diameter with pressure in the resting length state. In this state, the average diameter of the FAM increased by 0.043 in with an increase in pressure from 0 to 100 psi (5.5(a)). This increase in diameter creates changes in thread length and braid angle, as seen in Table 5.1. The nominally linear increase in diameter with pressure supports the hypothesis that the increase in diameter is likely due to braid elasticity. There is a notable initial jump in diameter from the 7/8 in resting diameter of the bladder, which indicates some initial tensioning and realignment of the braid upon pressurization of the FAM. The fiber length at each pressure is estimated by inserting the average diameter values at resting length, into Equation 5.1. This results in a calculated braid stretch of up to 0.051 in (0.5% stretch) (Fig. 5.5(b)).

FAM	100 psi	80 psi	60 psi	40 psi	20 psi	0 psi (pred.)
D_{meas}, in	1.044	1.037	1.028	1.020	1.009	1.001
$B_{elastic}$, in	9.945	9.937	9.926	9.916	9.903	9.894
$\theta_{elastic}$, deg.	68.94	69.07	69.22	69.38	69.58	69.73

Table 5.1: Geometric dimensions calculated for the FAM in the resting length state

The tension in the braid threads is estimated using Equation 5.2. Because we are only investigating the resting length state, the form of Equation 5.2 can be simplified to eliminate the last term of the equation by considering that σ_z is negligible when the bladder is in the resting length state. The tension in each thread

of the braid linearly increases with pressure (Fig. 5.5(c)). The maximum force of 8.5 lbf for each thread is well below the cited failure strength of 59.3 lbf for the Kevlar-49 threads.

With the thread stretch and tension estimates, the stress (Eq. 5.3) and strain (Eq. 5.4) of the braid thread is then calculated to obtain a measure of the braid's elasticity while on the FAM. The equations for stress and strain are as follows:

$$\sigma_{brd} = \frac{T_{brd}}{A_{brd}} \tag{5.3}$$

$$\epsilon_{brd} = \frac{B_{elastic}}{B_0} - 1 \tag{5.4}$$

The resulting values produce a nominally linear stress-strain relationship (Fig. 5.5(d)). A linear fit of the data results in an estimated modulus of $E_{brd} = 11.6 \times 10^6 psi$ which is 29% less than the cited value of $E_{brd} = 16.3 \times 10^6$ psi. Closer inspection of the stress-strain trend reveals a slight nonlinearity in the results. Separate linear fits performed on the low pressure and high pressure data points found that the high pressure fit value of $E_{brd} = 15.5 \times 10^6$ psi is significantly closer (within 5%) of the cited value.

5.3.1 Analysis of Measured Elasticity Values

The elasticity found through the *in situ* measurements of the FAM (Fig. 5.3(b)) is compared to the elasticity found from the tensile characterization testing of the Kevlar thread (Fig. 5.5(d)), for agreement, in Figure 5.6. The tested braid material in both cases should have the same stiffness.

The stress values from measurement of the FAM appear to be very close to

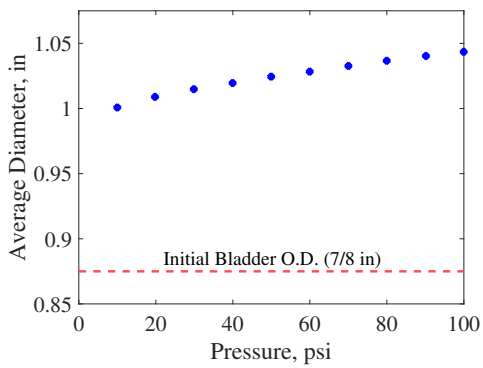

(a) Measured average diameter, $\bar{D}_{meas}$

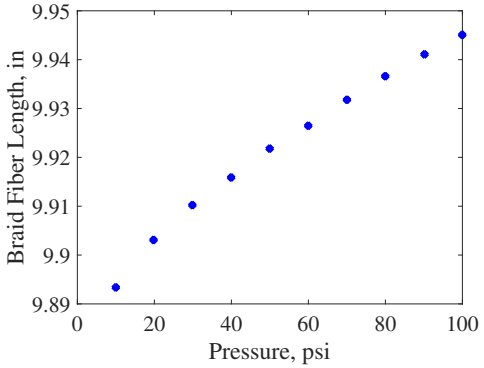

(b) Estimated length of braid threads, B_{meas}

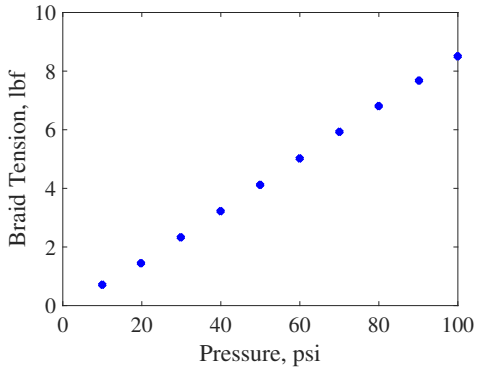

(c) Estimated tension in braid threads, T_{brd}

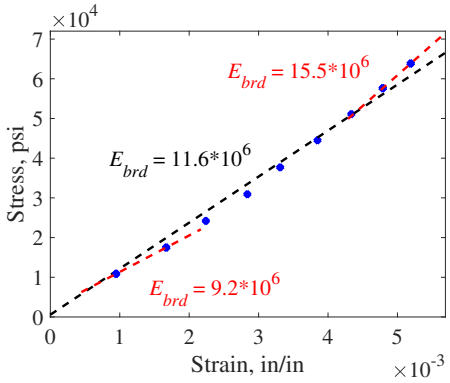

(d) Estimated stress, σ_{brd}, and strain, ϵ_{brd}, with linear fit analysis

Figure 5.5: Analysis of the braid threads through *in situ* analysis

those found in the tensile characterization testing (Fig. 5.6(a)). The maximum braid strain observed on the FAM is $\epsilon_{brd} = 0.0052$ which places it in the low-strain nonlinear region of the tensile test data. This coincides with the nonlinearity observed in the stress-strain relationship found from measurements of the FAM. Comparison of the two sets of data shows that the values are very close in magnitude and have the same basic curvature (Fig. 5.6(b)). Comparing the stress from the FAM measurements against the average curve of the three tensile tests, results in a RMSE for the estimates from the FAM measurements of 3,867 psi. The slight discrepancy between the measurements of the FAM and the tensile test entails the

possibility of a slight overestimation of the tensile loads of the threads on the FAM by 0.57–1.92 lbf. This is much lower than the 1.48–4.50 lbf overestimation of the tensile loads that would be assumed by using the cited linear elastic modulus in the recorded range of strain values.

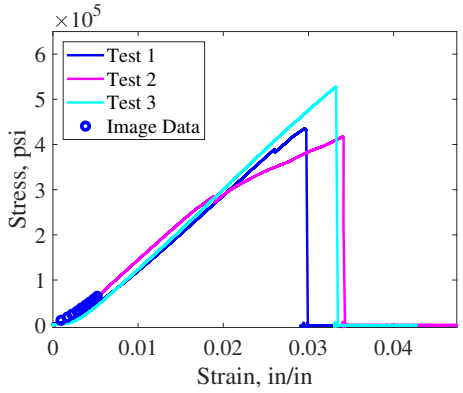

(a) Test data

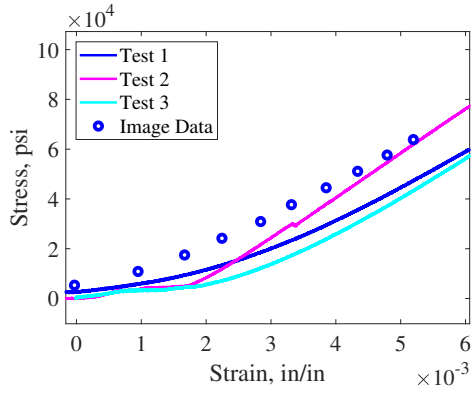

(b) Zoomed-in view of strain region of interest

Figure 5.6: Comparison of the stress-strain relationship calculated from (1) the tensile test measurements of the Kevlar threads, and (2) estimates from the *in situ* measurements of the FAM's braid.

Overall, comparison of the elasticity values found from *in situ* measurements of the FAM, and from tensile testing of individual Kevlar-49 threads, confirms that the source of the fixed-length radial expansion with increases in pressure is, in fact, due to stretching of the braid's threads. The elasticity of the braid observed on the FAM matched closely with what was expected from both cited and tested values. With the elasticity of the braid now fully characterized, the effects of the braid's elasticity on geometry and actuation force can be investigated.

5.4 The Effect of Braid Elasticity on Geometry and Actuation Force

With the stiffness of the braid characterized, the effects of elasticity on the parameters that define the FAM's geometry (D, θ, and B) and actuation force can now be analyzed. This analysis is performed by first estimating the stretch of the braid threads for all pressure-contraction states, and then using the triangle relationship, as shown in Figure 5.4, to calculate the corrected values of B, θ, and D that take the braid's elasticity into account. The effect of the corrected dimensions on the actuation force is then calculated using the Gaylord force equation (Eq. 5.9).

The traditional approach of estimating the dimensions and actuation force of the FAM has relied on the inelastic braid assumption (i.e. a fixed value for B) and a fixed value of N, while assuming a cylindrical geometry for all states of contraction. Using the triangle approximation, values of D and θ are approximated for all length states L of the FAM, using the following basic relations:

$$D = \frac{\sqrt{B^2 - L^2}}{\pi N} \tag{5.5}$$

$$\theta = sin^{-1}\left(\frac{L}{B}\right) \tag{5.6}$$

With this work, we are no longer assuming a fixed value for B. The stretched length of each thread is found through the following equation:

$$\begin{aligned} B_{elastic} &= B_0(1 - \frac{T_{brd}}{A_{brd}E_{brd}}) \\ &= \frac{B_0}{1 - B_0\frac{F_{act}+P\pi R^2}{LE_{brd}A_{brd}n_{brd}}} \end{aligned} \tag{5.7}$$

where T_{brd} is calculated using Equation 5.2; once again, the last term is excluded due to a negligible value of σ_z. For this form of the equation, the interdependence

between the braid's geometry and tension requires an estimation of R and θ based on either the rigid braid assumption, or experimental data. Alternatively, with the insertion of Equation 5.5 into Equation 5.7, a nontrivial solution that is independent of D and θ can be obtained, which requires numerical methods to solve:

$$0 = B_{elastic}^{3}\left(\frac{B_0 P\pi}{4N^2\pi^2 L A_{brd} E_{brd} n_{brd}}\right) + B_{elastic}\left(\frac{B_0}{L n_{brd} A_{brd} E_{brd}}\left(F_{act} - \frac{L^2 P\pi}{4N^2\pi^2} - 1\right)\right) + B_0 \tag{5.8}$$

For this equation, F can be an input from experimental data, or estimated using the Gaylord force. The braid thread tension and length can then be calculated for all pressure-contraction states of the FAM (Fig. 5.7). In this case, the elastic modulus of the braid, E_{brd}, is assumed to be 11.6×10^6 psi which is the value found by performing a linear fit of the stress-strain data obtained from measurement of the FAM (Fig. 5.5(d)). The results of Figure 5.7(b)) show that:

- Stretch of the braid increases with pressure
- Maximum stretch occurs in the block force (i.e. resting length) state where the actuation force is largest

The results show that maximum braid stretch is 0.06 in (0.6%) which occurs at 100 psi.

5.4.1 Effects of Elasticity with Kevlar-49 Braid

With the stretch of the braid threads now understood for all states of FAM length and pressure, the effect of the braid's elasticity on the dimensions and actu-

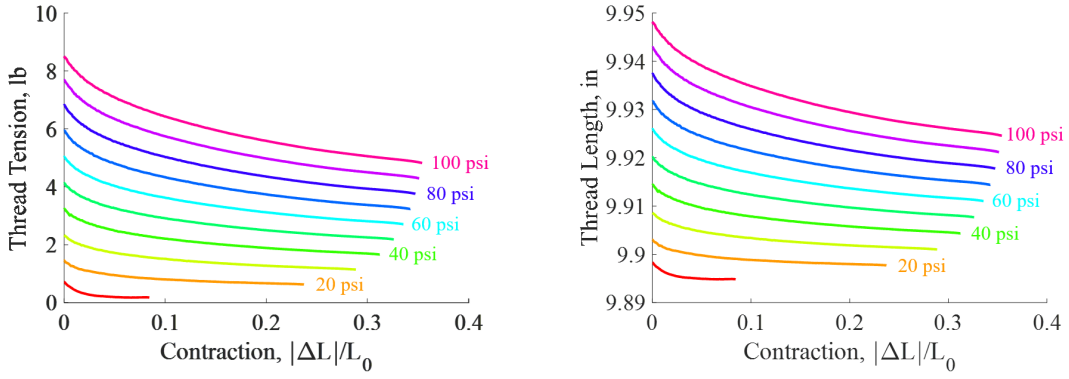

(a) Tension in each thread of braid, T_{brd}

(b) Length of each thread in braid, $B_{elastic}$

Figure 5.7: Thread tension and length with respect to contraction and internal pressure

ation force can now be investigated.

Having known values for $B_{elastic}$, N, and L, the dimensions $D_{elastic}$ and $\theta_{elastic}$ can be estimated using Equations 5.5 and 5.6 (Fig. 5.8(a)). Figures 5.8(b)-5.8(d) compare the dimensions obtained from assuming the braid is elastic versus inelastic. As with the trends shown for $B_{elastic}$, the effects of braid elasticity are largest in the resting length state, and decrease as the FAM contracts. The difference in dimensions between assuming an elastic braid versus an inelastic braid is barely perceptible. Elasticity of the braid resulted in a maximum decrease in braid angle of 0.73 degrees (1.1%), and a maximum increase in diameter of 0.04 in (3.8%).

The effect of the braid's elasticity on actuation force can now be investigated with knowledge of the change in the FAM's dimensions. The Gaylord force F_G – which approximates the actuation force of the FAM – is used to calculate the expected change in actuation force, and is defined as:

$$F_G = P\pi R^2(2tan^2\theta - 1) \tag{5.9}$$

where inputs include internal pressure P, and the dimensions R and θ. The effect of the braid's elasticity on the Gaylord force is shown in Figure 5.9. The relatively small change in the FAM's dimensions with the inclusion of braid elasticity results in a similarly small effect on the actuation force; inclusion of the effects of braid elasticity resulted in a 6 lbf (0.6%) decrease in force in the resting length state, and a 3 lbf (5%) decrease in force in the free contraction state.

The overall effect of the Kevlar braid's elasticity is minimal with only small effects on the resulting dimensions and actuation force of the FAM. Therefore, the inelastic braid assumption could be reasonably assumed for basic modeling efforts of this FAM. Future FAM-related research, however, should be careful to not use this conclusion to universally assume that the inelastic braid assumption is sufficient for other FAMs of different constructions. The Kevlar used in this work, with a cited modulus of 16.3×10^6 psi, has a very high degree of stiffness in comparison to other braid materials that are commonly used such as Nylon and polyethylene terephthalate (PET).

5.4.2 Estimated Effects of Lower Stiffness Braid Materials

FAMs have commonly used braid materials that have a much lower modulus of elasticity than Kevlar-49 [54]. To investigate the effects of a lower stiffness braid material, a case study is performed. This case study assumes a braid modulus that is 10% of the stiffness of the tested Kevlar-49 (from linear fit of nonlinear region) (1.16×10^6 psi) while maintaining the same actuation forces and initial dimensions

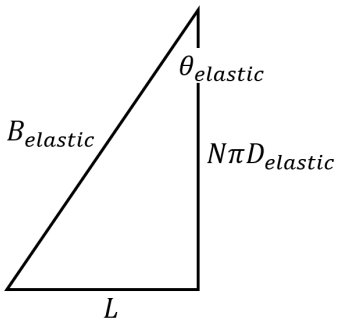

(a) Elastic braid dimension definitions

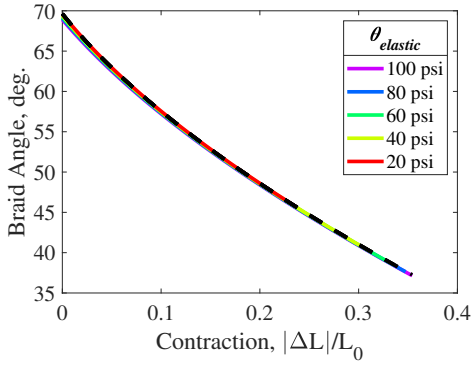

(b) Braid angle estimations, θ

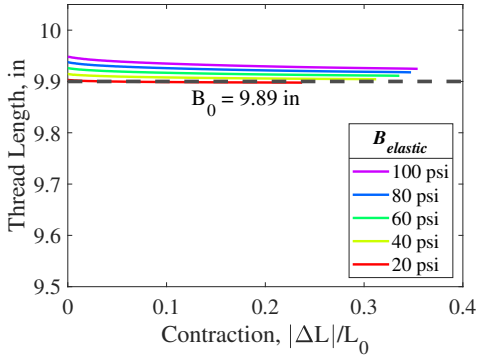

(c) Braid thread length estimations, B

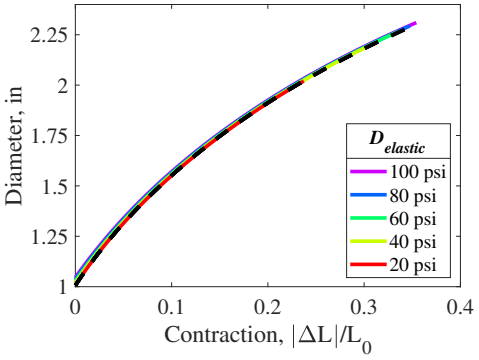

(d) Braid diameter, D

Figure 5.8: Estimated braid dimensions for the Kevlar-49 braid ($E_{brd} = 11.6 \times 10^6\, psi$) – Comparison between elastic (colored lines) and inelastic (black dashed lines) braid assumptions

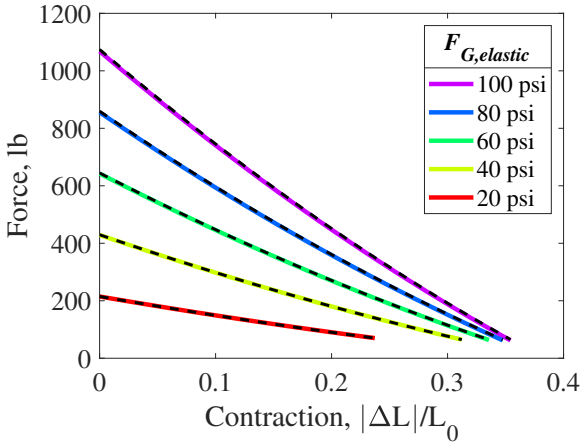

Figure 5.9: Gaylord actuation force estimates for the Kevlar-49 braid ($E_{brd} = 11.6 \times 10^6\, psi$) – Comparison between elastic (colored lines) and inelastic (black dashed lines) braid assumptions

of the tested FAM. This assumed modulus value is much closer to that of commonly used materials such as Nylon (0.5×10^6 psi) [85], and PET (0.62×10^6 psi) [13].

The effect of the braid's elasticity on the FAM's dimensions and actuation force is investigated again for comparison (Table 5.1). In contrast with the previous results – where a stiffer braid was used – the magnitude of stretch estimated for the lower-elasticity material is substantial. The estimated stretch of the braid threads is 0.57 in (5.8%). This results in a substantial decrease in braid angle of 6.3 degrees (12.3%), and an increase in diameter of up to 0.38 in (30.1%). These results are comparable to the work of Davis, where 5% braid stretch and 33% diameter expansion were observed with a FAM that used a Nylon braid [11]. The similarities between the values observed by Davis and the estimated values in this research supports the fidelity of this case study.

The elasticity of the braid, and respective changes in braid dimensions, results in a substantial decrease in actuation force with the inclusion of braid elasticity effects (Fig. 5.11). When compared to the inelastic braid assumption, the force in the resting length state decreases by up to 83 lbf (8%) at 100 psi, while the force at free contraction decreases by up to 47 lbf (70.4%). Through this example case study, it is evident that the elasticity of the braid can have a substantial effect on the resulting dimensions and actuation force of the FAM.

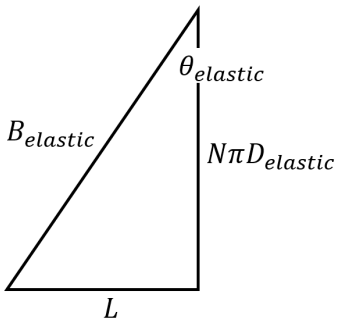

(a) Elastic braid definitions

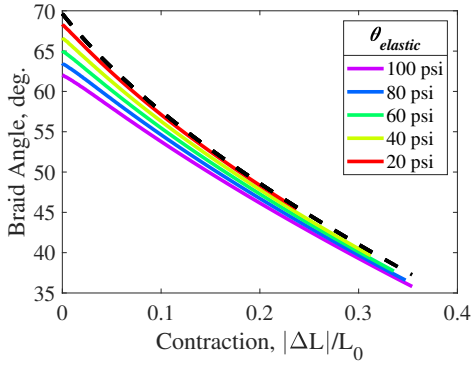

(b) Braid angle estimations, θ

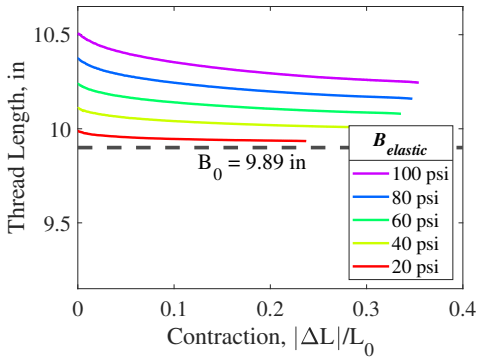

(c) Braid thread length estimations, B

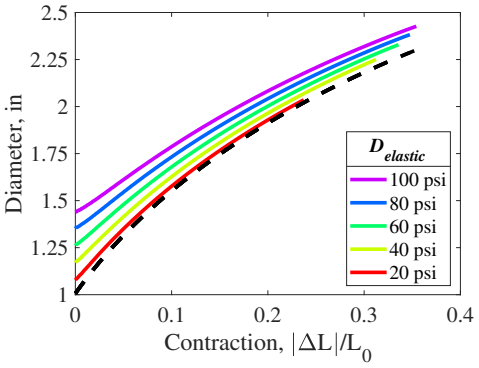

(d) Braid diameter, D

Figure 5.10: Estimated braid dimensions for a lower stiffness braid ($E_{brd} = 1.16 \times 10^6\, psi$) – Comparison between elastic (colored lines) and inelastic (black dashed lines) braid assumptions

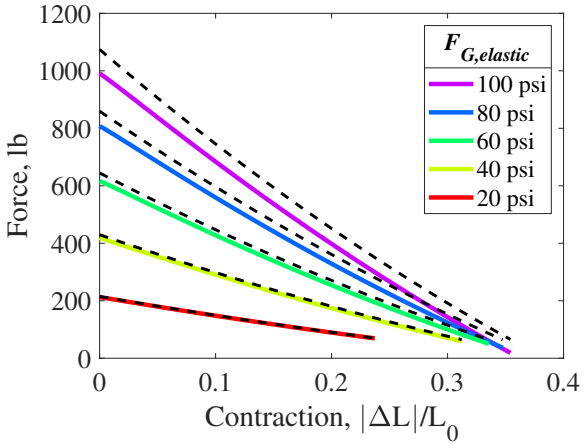

Figure 5.11: Gaylord actuation force estimates for a lower stiffness braid ($E_{brd} = 1.16 \times 10^6\, psi$) – Comparison between elastic (colored lines) and inelastic (black dashed lines) braid assumptions

Max Values	Kevlar-49	Reduced E Kevlar	Nylon [11]
Elastic Modulus	16.3×10^6 psi	1.16×10^6 psi	0.5×10^6 psi (est.)
Tested Pressure	100 psi	100 psi	65 psi
Diameter Change	3.8% (0.04 in)	30.1% (0.38 in)	33% (0.3 in)
Thread Stretch	0.5% (0.05 in)	5.8% (0.57 in)	5% (4 in)
Act. Force Change	0.6% (6 lbf)	8% (83 lbf)	–

Table 5.2: Comparison of effects of braid stretch for different braid materials

5.5 Conclusion

Prior to this work, very little research had been performed on the effects of braid elasticity on FAM actuation characteristics. The inelastic braid assumption has been widely used to simplify analysis. A lack of experimental data to test the effects of braid elasticity has abetted continuation of the use of this assumption, and its validity must be questioned.

The introduction of a photogrammetric method of measuring the dimensions of the FAM opened the door for analysis of braid elasticity and itsg effects on FAM actuation. Photogrammetric measurements showed that the 7/8 in diameter FAM would expand in diameter in its resting length state by 0.043 in with an increase in pressure from 0 to 100 psi. Using the triangle relationship enabled by the cylindrical approximation, this indicated that the Kevlar braid was stretching by up to 0.5%.

Through investigation of the braid's elasticity using measurements of the FAM during actuation, the braid was found to operate primarily in the initial nonlinear region of its stress-strain curve. Furthermore, the stress-strain curve developed from the *in situ* measurements of the FAM were found to closely replicate the nonlinear stress-strain relationship found through tensile testing of individual threads. The

linear modulus of elasticity obtained from measurements of the FAM were within 5% of the cited value of Kevlar-49 which aided in assuring the fidelity of the braid elasticity analysis.

The effects of the braid stretch on the resulting dimensions and actuation force of the FAM were quantified. It was found that the Kevlar braid of the tested FAM had an appreciable, but minimal, effect on the dimensions (3.8% maximum increase in diameter) and actuation force (5% maximum decrease). A case study was performed using a modulus of elasticity value similar to that of other commonly used braid materials, and the study found that these less-stiff braid materials would have a significant effect on the dimensions (30.1% maximum increase in diameter) and actuation force (70.4% maximum decrease) of the FAM. The effects of elasticity were especially noticeable in the blocked force state where the actuation force, and resulting tension on the braid threads, is highest in magnitude.

Overall, it is clear that braid stretch, especially with lower modulus of elasticity braid materials, can have a substantial effect on the dimensions and actuation force of the FAM. This research demonstrates that the inelastic braid assumption cannot be blindly assumed as has commonly been done in previous work with FAMs. To ensure the accuracy of modeling efforts, both the material and loading of the braid must both be considered to ensure that the possible effects of the braid's elasticity on the FAM's actuation are understood.

Chapter 6: Investigation of the Cylindrical Approximation Assumption

6.1 Introduction

The braid of a FAM serves as its main load-bearing component, and it plays a critical role in determining the actuation characteristics of the FAM through its geometry. The braid transforms the pressure force of the internal working fluid into a contractile actuation force, while also enabling a contractile motion of the FAM through the reorientation of its helically wound threads. As the FAM contracts in length, the reorientation of the braid's threads results in a simultaneous radial expansion.

The braid is fixed to end-fittings at each end of the FAM which have diameters that are nominally equal to the initial resting diameter of the braid. As the braid radially expands with contraction, its diameter is constrained in proximity to each end-fitting. This results in a shape of the FAM that, instead of being cylindrical, has a bulbous shape with rounded ends (Fig. 6.1(a)), and a diameter and braid angle that varies along the length of the FAM.

Despite its complex geometry, the modeling and analysis of FAMs – dating

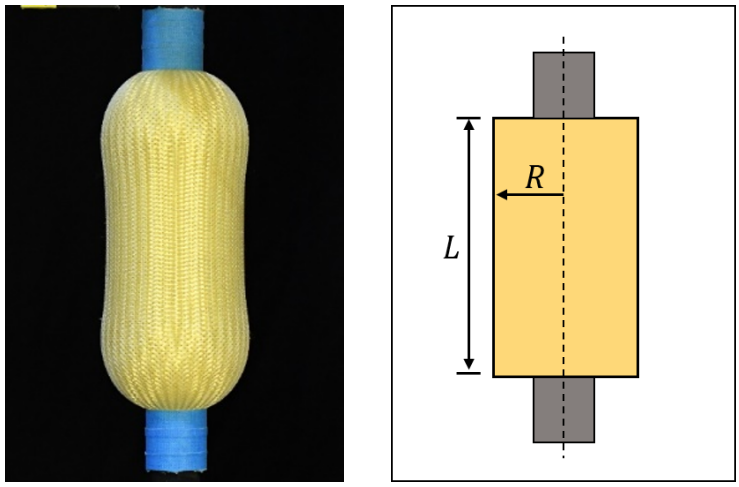

(a) Actual profile of FAM (b) Assumed cylindrical profile

Figure 6.1: Comparison between the profile of the FAM, and the profile assumed with the commonly used cylindrical approximation

back to the invention of the FAM in 1958 – typically assumes a cylindrical shape profile (Fig. 6.1(b)) [1–3, 5, 8–10, 13, 16, 18–21]. This is a simplifying assumption that assumes a constant diameter and braid angle along the length of the FAM. The cylindrical assumption has been used in the derivation of almost every FAM modeling effort, including models of the FAM's internal volume [19], friction [9], bladder strain [13], and actuation force [17]. By using a cylindrical approximation assumption, cylindrical dimensions of the FAM are easily estimated for all states of contraction, and have been used as an input in almost every model formulated for FAMs.

Researchers have long understood that the inaccurate representation of a FAM's geometry – by using the cylindrical approximation – is a likely source of modeling error [13]. For actuation force models, the inaccurate representation of the shape profile – especially in the region near each end-fitting – is said to result

in *end effects* or *tip effects* which are thought to reduce the actuation force of the FAM [13, 17]. To correct for the error induced by the cylindrical approximation, researchers have implemented correction factors that are often used to tune their models to experimental data, but which are based on little phenomenological reasoning. Almost all correction approaches assume a reduction in the effective active length of the FAM, corresponding roughly with the length of the FAM's nominally cylindrical midsection [9]. A few researchers have assumed shape corrections of the cylindrical profile – based only on qualitative observations – with focus on adjusting the cylindrical profile in the region near each end-fitting. Examples of such shape corrections includes replacing the region near each end-fitting with 90 degree [13, 18, 67] or elliptical [20] arcs. However, these geometry corrections only act to reduce the value of active length L – a modeling input – and therefore, still fail to capture any detailed effects of these regions.

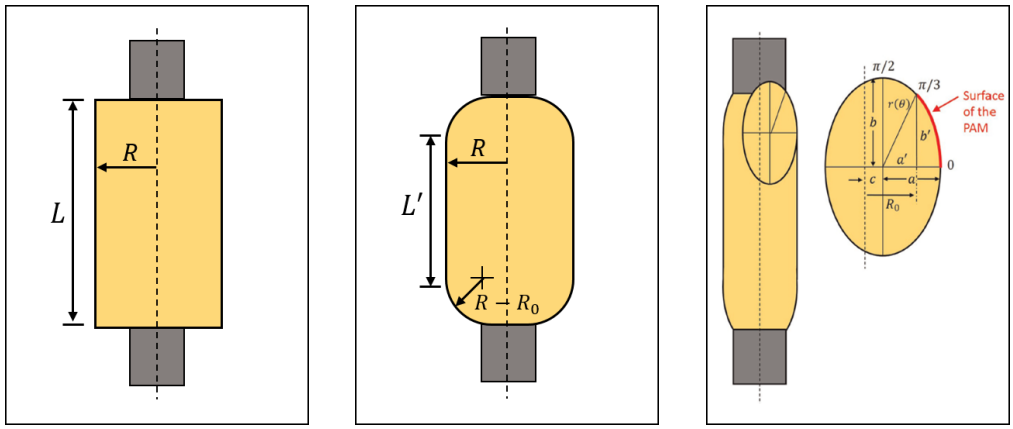

(a) Cylindrical (b) 90 deg. circular arc (c) Elliptical

Figure 6.2: Various assumed geometry profiles used for modeling of FAMs

Ability of the cylindrical approximation to accurately replicate the FAM's true geometry – with or without shape corrections – has not been tested in prior research.

Furthermore, a lack of available methods to directly measure the shape profile of FAMs has stagnated attempts at improving upon the cylindrical approximation; the only method extant was to use a ruler to manually measure the FAM diameter at discrete points along its length, and at a limited number of pressure-contraction states. Now, the invention of the photogrammetric measurement method – detailed in Chapter 4– enables a complete characterization of the FAM's shape profile to be acquired for all states of contraction and pressure, and opens the door for further analysis. Photogrammetric measurements provide the ability to quantify, and possibly eliminate, the degree of modeling uncertainty associated with the inaccurate representation of a FAM's shape profile.

The cylindrical approximation has long been incorporated with FAM modeling work without an understanding of the magnitude of error that it introduces. Here, we attempt to quantify the error induced when using the estimated dimensions derived from use of the cylindrical approximation. The same 7/8 inch diameter, 9-9/32 inch length FAM used in previous chapters will be used here for this analysis. As the first step, the dimensions acquired using cylindrical geometry estimates will be compared to the measured dimensions. These estimated and measured dimensions are then used for a comparison of the bladder's estimated strain state values. The bladder's stiffness is experimentally characterized, and then used, along with the dimensional and strain estimates, to approximate the effect of the cylindrically estimated and measured profiles on the actuation force of the FAM. Through these comparisons, the modeling error assumed in using these estimated dimensions by way of the cylindrical approximation can now be understood, and subsequent cor-

rections in the dimensions and models can then be made.

6.2 Geometric Dimensions Definitions

The geometry of the FAM's braid is defined by the following set of dimensions: length L, diameter D, angle θ, length of each braid thread B, and number of turns of each thread about the circumference of the FAM, N. Of these dimensional parameters, N is always a fixed value. The value of B is also commonly assumed as fixed with the application of the inelastic braid assumption. As seen in Chapter 5, the value of B actually changes due to stretching of the threads when tensioned, and will be taken into consideration in this research. Length L, also known as the *active length*, is measured as the longitudinal length of the braided section of the FAM, and is commonly treated as the main independent variable in models of FAMs. Values of D and θ are left to be determined, based on an *estimated* or a *measured* profile of the FAM. Previous research has obtained dimension estimates by assuming a cylindrical geometry of the FAM. That assumption uses estimated values for the diameter, D_{est} and the braid angle θ_{est}, which are assumed to be constant along the length of the FAM. The photogrammetry measurements, on the other hand, define the diameter of the FAM D_{meas}, along the length of the FAM. A method for directly measuring the braid angle has not yet been developed, so the braid angle θ_{meas}, must be approximated by using the other known dimensions, as will be discussed.

Estimations of bladder dimensions, which will also be investigated, are reliant

on the assumption that the bladder is in continual contact with the inner surface of the braid. This assumption is often true unless the bladder is not initially in contact with the braid in the FAM's resting length state; in that case, a minimum activation pressure is required before this contact condition is satisfied. With the assumption that the bladder is in contact with the braid, the diameter of the bladder, at its mid-thickness, can be written in the following general form:

$$D_{bld} = D_{brd} - 2t_{brd} - t_{bld} \tag{6.1}$$

where D_{brd} is the photogrammetry-measured outer diameter of the braid, t_{brd} is the fixed thickness of the braid ($t_{brd} = 0.011\,\text{in}$ for the tested FAM), and t_{bld} is the instantaneous thickness of the bladder.

The estimated dimensions of the FAM, as used in prior studies, are compared here to the dimensions that are measured using photogrammetry. Previous efforts have estimated the dimensions of the FAM in all states of contraction, using the cylindrical approximation together with the known initial geometry 6.3(a). For this analysis, the measured profile 6.3(b), or a cylindrical approximation of the measured profile 6.3(c), will be used for analysis.

This work uses the same 7/8 inch diameter FAM as in previous chapters for analysis. This FAM has a length L, of $9 - 9/32$ inches, and its dimensions measured to be $N = 1.09$, and $B = 9.89\,\text{inches}$. These values will be used in subsequent sections to analyze the dimensions, actuation force, and bladder strain of the FAM acquired through estimated and measured geometry profiles of the FAM. The geometries to be analyzed, both estimated and measured, are defined in the subsections

that follow.

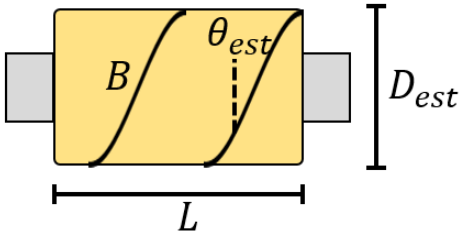

(a) Estimated cylindrical geometry dimensions

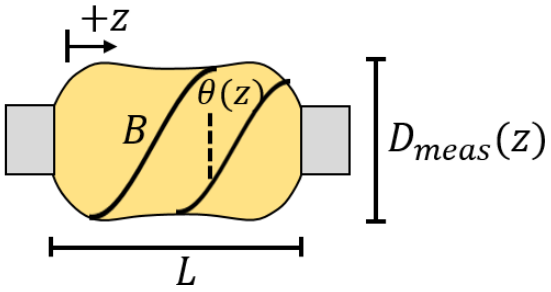

(b) Measured geometry dimensions

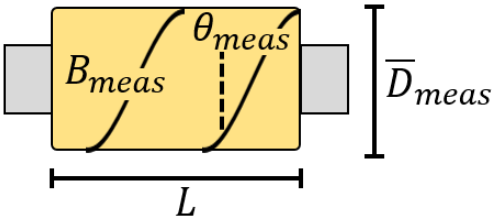

(c) Cylindrical approximation of measured geometry dimensions

Figure 6.3: Definitions of dimensions for the analyzed geometries

6.2.1 Estimated Dimensions – Cylindrical Approximation

Previous modeling efforts have used estimated dimensions for all length states of the FAM (Fig. 6.3(a)). These estimates are derived based on the initial dimensions of the FAM, and the cylindrical approximation enables the use of the *triangle relationship* to define the dimensions (Fig. 6.4). In this case, fixed values of N and

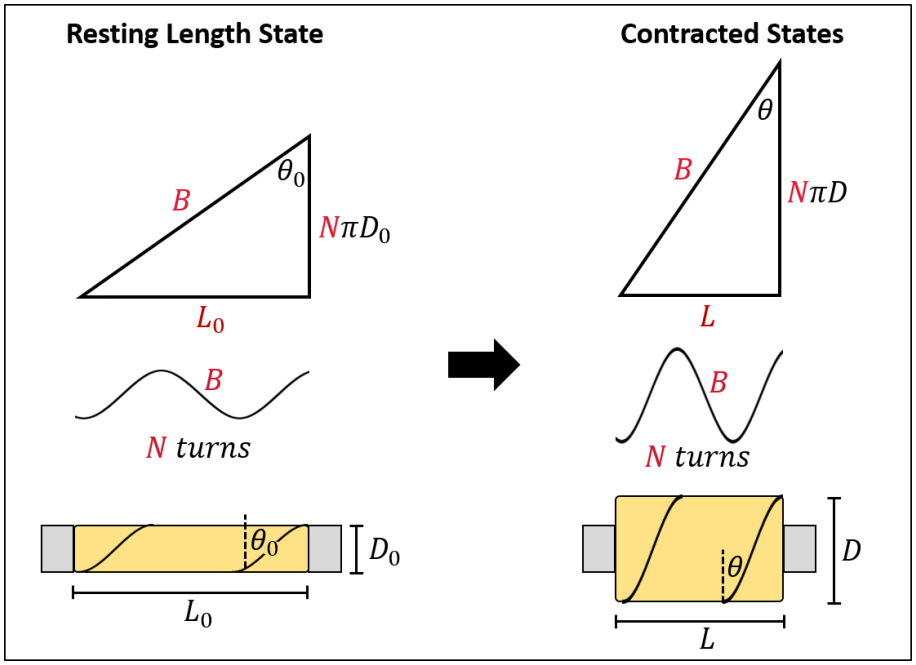

Figure 6.4: The Triangle Relationship, enabled by the cylindrical geometry approximation, used to estimate the dimensions of the FAM between states of contraction

B are determined in the resting length state L_0. The estimated diameter, D_{est}, and braid angle, θ_{est}, are then calculated as a function of L using Equations 6.2 and 6.3, as follows:

$$D_{est}(L) = \frac{\sqrt{B^2 - L^2}}{\pi N} \tag{6.2}$$

$$\theta_{est}(L) = sin^{-1}\left(\frac{L}{B}\right) \tag{6.3}$$

The value of B is either assumed fixed by application of the inelastic braid assumption, or assumed to be elastic with the magnitude of stretch calculated through the methods of Chapter 5. Both elastic and inelastic braid assumptions, and their respective effects on estimated dimensions and actuation force, are also included in this research.

6.2.2 Measured Dimensions

Through a new method of measuring the FAM's diameter (Ch. 4), $D_{meas}(z)$ is known along the entire length of the FAM for all states of contraction and pressure (Fig. 6.3(b)). Just as with the method of estimating dimensions, values of N and B can be calculated or measured directly in the resting length state of the FAM. In contracted length states, N is a fixed value, while B can only be approximated using the other geometric dimensions, or assumed inelastic and fixed. The measured diameter $D_{meas}(z)$, and respective braid angle $\theta(z)$, vary along the length of the FAM and are a function of contraction and pressure. There is no current method for directly measuring the braid angle along the length of the FAM which makes further detailed dimensional analysis of the braid difficult. Analysis of the bladder, however, is enabled to a greater level of detail using the measured dimension, $D_{meas}(z)$, as discussed in subsequent sections.

For the analysis performed using $D_{meas}(z)$ in this work, the raw photogrammetry data is represented by Fourier series equation curve-fits of each profile (Fig. 6.5). As performed in Chapter 4, the radius of each profile, $R_{meas}(z)$, is defined by the equation:

$$R_{meas}(z) = a_0 + \sum_{1}^{n} a_n cos(nzw) + b_n sin(nzw) \tag{6.4}$$

where a_0, a_n, and b_n are parameters used to fit the curve to each profile, and only three terms ($n = 3$) are necessary for a good representation of all profiles of the tested 7/8 inch diameter FAM.

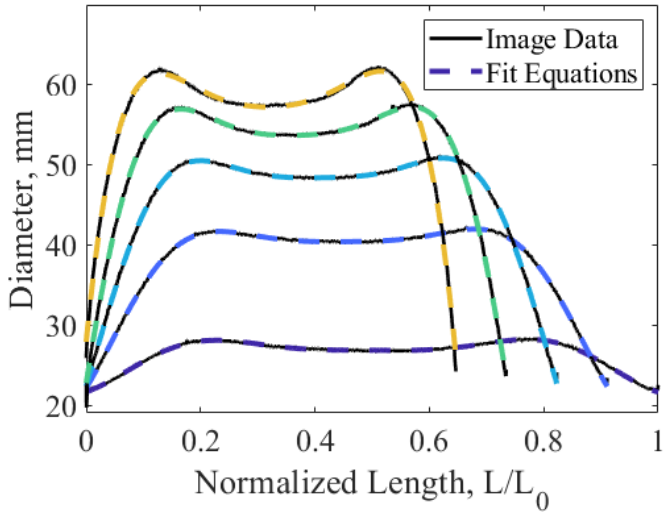

Figure 6.5: Comparison between the profiles defined from acquired image data, and the Fourier-series fit equations that are used to define the profiles for analysis

6.2.3 Measured Dimensions – Cylindrical Approximation

Most established modeling and analysis frameworks for FAMs have been developed to accept only cylindrical dimensions of a FAM. Therefore, especially for comparison to the estimated dimensions, it is more straightforward to approximate the measured dimensions through a cylindrical approximation (Fig. 6.3(c)). The cylindrical approximation of the measured dimensions is calculated by assuming a constant braid diameter that is equal to the average diameter of the measured profile, $\bar{D}_{meas}$. Using known values of N, $\bar{D}_{meas}$, and L, the cylindrical dimensions θ_{meas} and B_{meas} are approximated for all states of contraction and pressure. As will be noted subsequently, the value of B_{meas} is no longer an accurate representation of thread length in this case, but rather is an effective value here when used only to define the cylindrical approximated geometry. With the assumption of a cylindrical profile, the value of B_{meas} is less than that of B due to the loss of curvature along

the FAM's surface.

The key difference between the cylindrical approximation of the measured and the estimated dimensions can be explained as follows. The cylindrical approximation of the measured dimensions assures the accuracy of the measured average diameter, and provides an assumed subsequent improvement in accuracy of the average braid angle. To maintain the triangle approximation, the value of B_{meas} must assume some inaccuracy with respect to the actual value B. In contrast, the estimated cylindrical dimensions use an accurate value of B, but use of the cylindrical approximation leads to error in the estimated diameter and braid angle values. Notably, those dimensions D and θ, are prioritized in this research due to their role in determination of the actuation characteristics of the FAM; therefore, a cylindrical approximation of the measured dimensions should provide the closest thing to a "true" representation of these values while fitting into the cylindrical frameworks that have been previously used.

6.3 Analysis of the Cylindrical and Measured Geometries

Previous research has calculated the FAM's dimensions, actuation force, and bladder strain states using an estimation of its geometric dimensions in all states of contraction. Now, with access to actual measurements of the geometry of the FAM, improvements are made to the accuracy of the dimensions, actuation force, and bladder strain state values. In doing this comparison, the degree of error and uncertainty produced by using the cylindrical approximation of the FAM's geometry

can be understood and greatly reduced, and subsequent modeling improvements can be established.

6.3.1 Comparison of Braid Dimensions

The dimensions from previous estimations are compared to the dimensions obtained through direct measurements of the FAM's geometry profile. For a direct comparison, the cylindrical dimensions of the estimated geometry (Fig. 6.3(a)) are compared to a cylindrical approximation of the measured profile geometry (Fig. 6.3(c)). The measured dimensions ($\bar{D}_{meas}$, θ_{meas}, B_{meas}) are compared to the estimated dimensions (D_{est}, θ_{est}, B_{est}) at each tested pressure (Fig. 6.6). Estimated dimensions with, and without, the use of the inelastic braid assumption are considered for comparison to the dimensions of the measured geometry.

Figure 6.6 includes the estimated geometry with the inelastic braid assumption (black dashed lines), and with braid elasticity effects included (gray lines) (as shown in Chapter 5). This analysis focuses on the comparison between measured geometries, and the estimated geometry with braid elasticity effects included, in an effort to isolate the effects of the cylindrical approximation.

The comparison between the dimensions of the estimated and the measured geometries displays a common trend: the error in the estimated dimensions increases with increases in the contraction of the FAM. This trend stems from the fact that the estimated dimensions, which rely on the cylindrical approximation, become increasingly inaccurate as the actual profile of the FAM becomes increas-

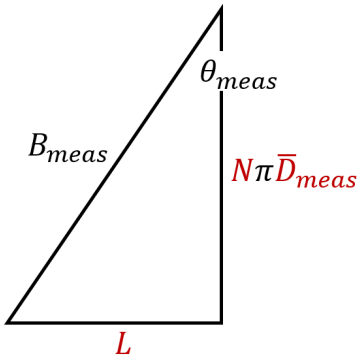

(a) Cylindrical approximation of measured dimensions (Red values measured directly)

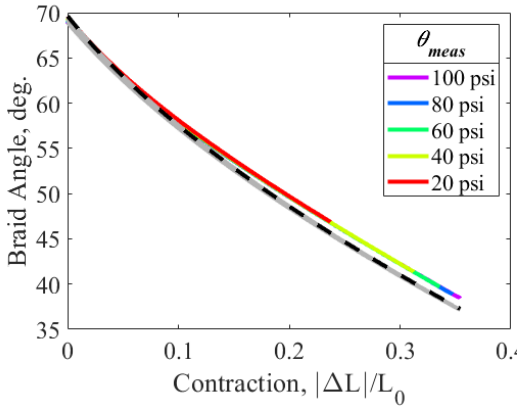

(b) Braid angle estimations, θ

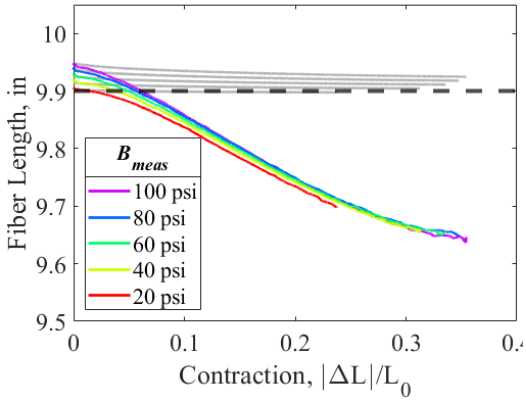

(c) Braid thread length estimations, B

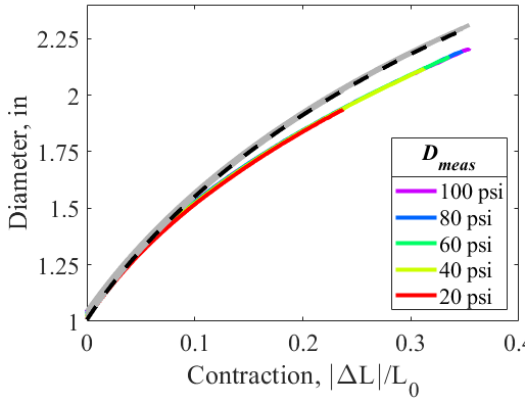

(d) Braid diameter, D

Figure 6.6: Comparison of dimensions obtained from the cylindrical approximation of the measured geometry (colored lines), estimated cylindrical geometry with elastic braid (gray lines), and estimated cylindrical geometry with inelastic braid assumption (black dashed lines)

ingly noncylindrical with contraction. Error in the estimated dimensions peaks at the free-contraction state, where the diameter is overestimated by 0.11 in (4.7%), and braid angle is underestimated by 1.25 deg. (3.3%).

The difference in the value of B between the estimated and the measured geometries is interesting because it depicts the effect of the FAM's curvature on their resulting dimensions (Fig. 6.6(c)). B_{est} is an accurate value of the braid thread length that is then wrapped around the surface of the inaccurate cylindrical

geometry that is assumed. This, in turn, results in inaccurate estimates of D_{est} and θ_{est}. In contrast, the measured geometry D_{meas}, represents an accurate depiction of the geometric profile of the FAM. Simplification to a cylindrical geometry, by going from D_{meas} to $\bar{D}_{meas}$, eliminates the curvature of the geometry resulting in a shorter than actual value of B. Therefore, the difference between B_{est} and B_{meas} quantifies the length of each thread that is "lost" to the curvature along the longitudinal surface of the braid. For the tested FAM, the reduction from B_{est} to B_{meas} is 0.29 in (3%).

6.3.2 Comparison of Bladder Dimensions

Improvements to actuation force models have often focused on better characterizing the energy lost to the radial expansion and strain of the bladder. An accurate depiction of the bladder's geometry, therefore, is important for yielding an accurate depiction of the bladder's strain state; this is, in turn, important for producing estimates of the bladder's stress state, and the respective forces applied to the bladder. The error inherent in the estimated cylindrical geometry of a FAM results in uncertainty of bladder strain estimations. It is hypothesized here that improvements in accuracy of strain estimations, by accounting for the curvature of the FAM, would act to improve the accuracy of actuation force models. Stress, and respective strain values, are defined in the FAM's longitudinal (σ_z, ϵ_z), and circumferential (σ_c, ϵ_c) directions, as illustrated in Figure 6.7.

Relevant to the research conducted in this chapter is the form of the intrinsic

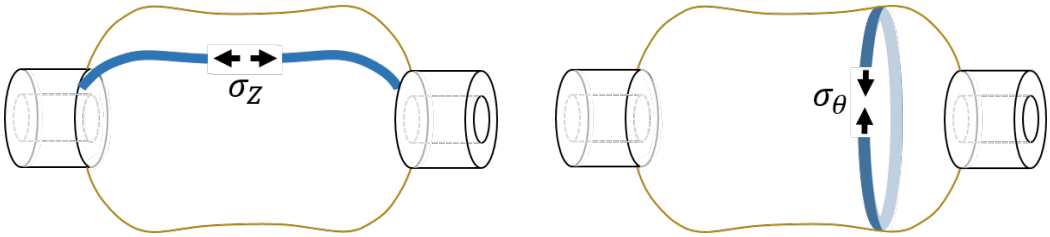

(a) Longitudinal stress (b) Circumferential stress

Figure 6.7: Bladder longitudinal and circumferential stress directions

stress-strain relationship used to define the bladder's material properties. Hyperelastic material models are commonly either strain energy based – such as Mooney-Rivlin and Ogden methods [7, 13, 17, 21]– or based on a polynomial stress-strain relationship [18,86,87]. The polynomial stress-strain relationship (Eqs. 7.6 and 7.5) is the most intuitive stress-strain relationship, and when used in actuation force models, has provided the most accurate fits of experimental data. The polynomial stress-strain relationship is defined as:

$$\sigma_c = \sum_{1}^{n} E_n \epsilon_c^n \tag{6.5}$$

$$\sigma_z = \sum_{1}^{n} E_n \epsilon_z^n \tag{6.6}$$

which requires inputs values for strain, ϵ_z and ϵ_c, and the terms E_n which define the stiffness of the bladder material. Prior works have defined the polynomial stress-strain relationship using up to four terms (4th-order polynomial) [18,48]. Therefore, in this work, we investigate strains up to the fourth power.

In this section, the resultant error in the strain values calculated using the estimated cylindrical geometries will be quantified through comparison with the more accurate strain values calculated using the measured geometries. Strain will be calculated by using the estimated diameter D_{est}, and compared with the strain

calculated using the measured diameter $D_{meas}(z)$. It should be noted that, because the braid is usually very thin – 0.011 inch wall-thickness for the tested FAM – the outer diameter of the bladder is commonly considered to be equivalent to $D_{meas}(z)$ as a simplification. The profile, $D_{meas}(z)$, is defined using the Fourier series fit equations (Eq. 6.4) as described earlier.

6.3.2.1 Comparison of Bladder Thickness

Recent improvements to the calculation of bladder strain take into account the change in bladder thickness with its contraction [13]. Since the thickness of the bladder varies with the amount that it is strained, an estimation of thickness is dependent on the assumed geometry of the FAM. In this section, we investigate the effect of using the measured geometry – instead of the previously used estimated cylindrical geometry – on the resulting estimation of bladder thickness.

The instantaneous thickness of the bladder t_{bld}, is calculated for all states of contraction. The tested FAM has a resting bladder thickness of 1/16 inch. As a simplifying assumption, the bladder is assumed to have a uniform thickness throughout the bladder in all states of strain. Bladder thickness is calculated for the estimated cylindrical geometry, and for the measured profile cases, using the following equations:

$$t_{bld} = R_{est} - \sqrt{R_{est}^2 - \frac{V_{bld}}{\pi L}} \qquad (Cylindrical\ Profile) \qquad (6.7)$$

$$t_{bld} = \frac{V_{bld}}{\int_0^L 2\pi R_{meas}(z)\sqrt{1 + [R'_{meas}(z)]^2}\, dz} \qquad (Measured\ Profile) \qquad (6.8)$$

where R and t_{bld} are the instantaneous radius, and thickness, respectively, of the

bladder at FAM length states L. Equation 6.7 is used for the cylindrical geometry assumption, and assumes the bladder takes on the shape of a constant diameter tube in all length states. This is the standard equation that has been used for the calculation of bladder thickness in prior research. Equation 6.8, on the other hand, uses the arc-length of the measured geometry's profile to obtain a higher fidelity bladder thickness value. Both equations rely on the assumption that the bladder volume V_{bld}, is fixed; this assumption of incompressibility is commonly used for elastomeric materials. Bladder volume is easily defined in the resting length state using the following equation:

$$V_{bld} = L_0 \pi (R_{bld,0}^2 - (R_{bld,0} - t_{bld,0})^2) \tag{6.9}$$

where $R_{bld,0}$ and $t_{bld,0}$ are the initial outer radius and thickness of the bladder, respectively, with the FAM in its resting length state L_0.

Figure 6.8 shows the comparison of the thickness calculated using a cylindrical or a measured geometry. The estimated cylindrical bladder geometry, as used in prior research, produces a minimum bladder thickness value of 0.0339 in (inelastic braid), and 0.0337 in (elastic braid). This is comparable to the measured geometry's minimum thickness of 0.0334 in, which is 53% of the bladder's 0.0625 in resting thickness. These results indicate that the measured bladder thickness in contracted length states is barely thinner than the thickness value obtained by use of the estimated cylindrical geometry – with a calculated decrease in the minimum thickness of 0.0005 in (1.5%).

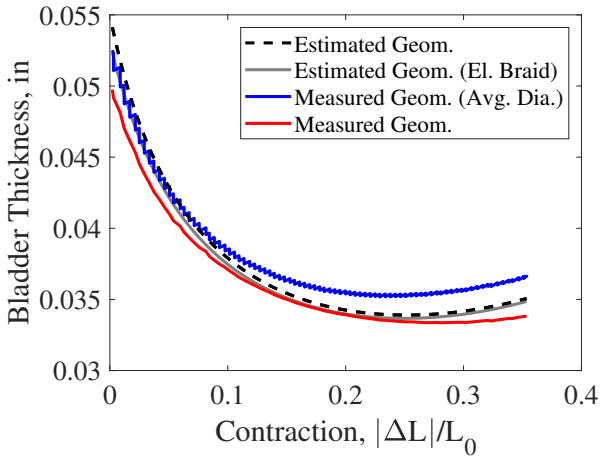

Figure 6.8: Bladder thickness calculated for each geometry ($100\,psi$)

6.3.2.2 Comparison of Longitudinal Strain

The longitudinal strain of the bladder is calculated based on the change in its length in the direction of the longitudinal axis of the FAM. Longitudinal strain is calculated using the following equation:

$$\epsilon_z^n = \left(\frac{L_{bld}}{L_{bld,0}} - 1 \right)^n \tag{6.10}$$

where $L_{bld,0}$ is the resting length of the bladder, equal to that of the FAM's resting length, and n is the order of strain used in the polynomial form of the stress-strain relationship. The instantaneous length of the bladder L_{bld}, is defined depending on whether a cylindrical geometry or a measured geometry is assumed for the calculation of longitudinal stress, as follows:

$$L_{bld} = L \qquad (Cylindrical\ Profile) \tag{6.11}$$

$$L_{bld} = \int_0^L \sqrt{1 + [R'_{meas,bld}(z)]^2}\, dz \qquad (Measured\ Profile) \tag{6.12}$$

where the difference between the two approaches of defining L_{bld} is illustrated in Figure 6.9. For a cylindrical profile (Fig. 6.9(a)), the longitudinal length of the bladder is assumed to be equivalent to the length of the FAM (Eq. 6.11). However, the length of the bladder in the longitudinal direction is more accurately captured by including the curvature of the actual measured profile of the FAM (Fig. 6.9(b)). To include the bladder's curvature in the longitudinal length, the arc length of the profile equation for the bladder $R_{meas,bld}(z)$ is calculated (Eq. 6.12).

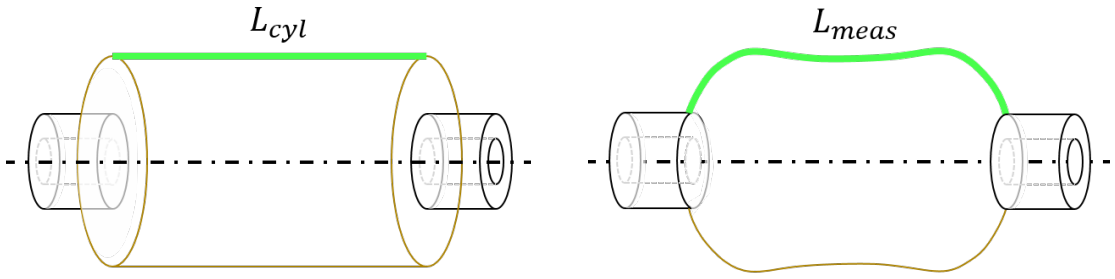

(a) Cylindrical Geometry (b) Measured Geometry

Figure 6.9: Geometry-dependent longitudinal length assumed for longitudinal bladder strain calculations

Analysis of the results show that the cylindrical geometry assumption produces a maximum strain value at free-contraction of about 35.3%, compared to the measured geometry maximum strain value of 28.9%. Therefore, the strain calculation method used in previous works would overestimate the longitudinal strain of this FAM by 0.064 (a 22.2% decrease in strain). Figure 6.10 provides a depiction of the results comparing the two geometries for strain orders 1–4. It is clear that the maximum error in the cylindrical geometry occurs in the free-contraction state. Table 6.1 provides the maximum values for strain orders 1–4, calculated for each geometry with the respective error of the cylindrical geometry assumption shown as

percentages. While the magnitude of that error decreases with increased order of strains, the percentage error increases from 22% up to 129%.

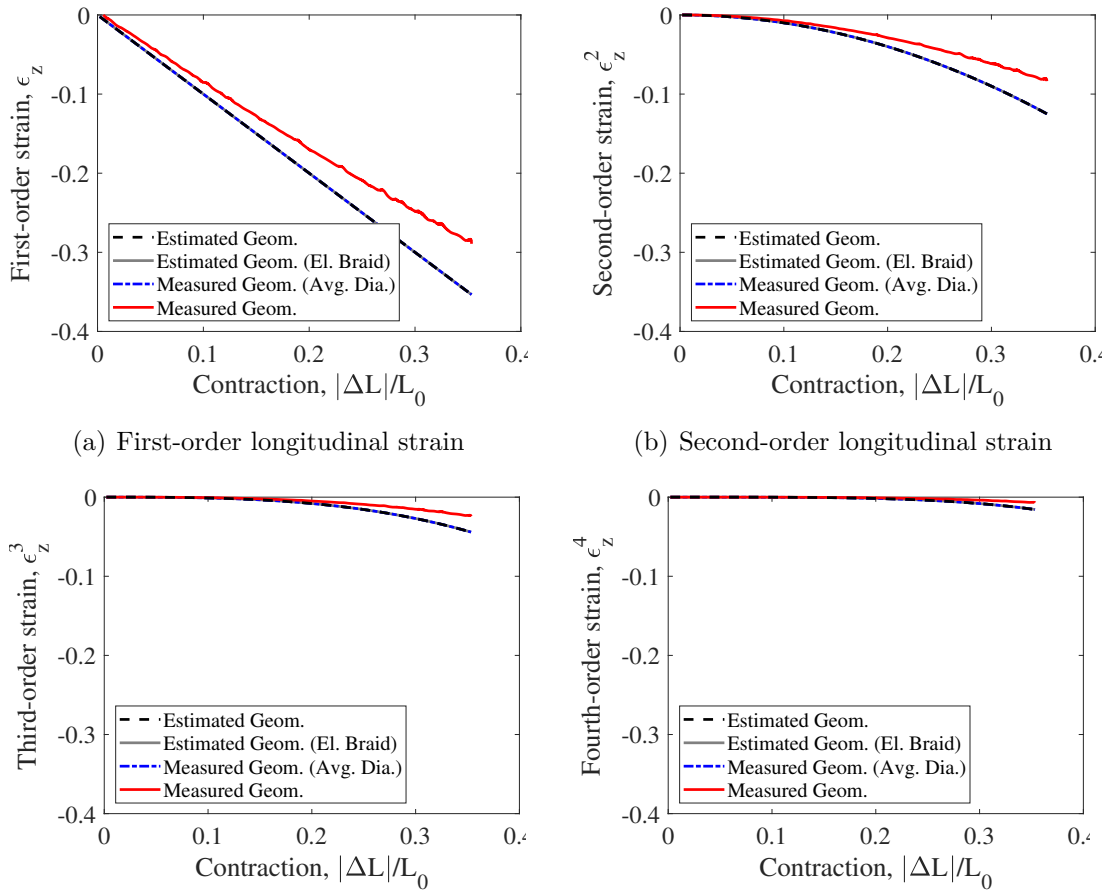

(a) First-order longitudinal strain

(b) Second-order longitudinal strain

(c) Third-order longitudinal strain

(d) Fourth-order longitudinal strain

Figure 6.10: Longitudinal bladder strain calculated for each geometry ($100\,psi$)

Table 6.1: Longitudinal Bladder Strain, ϵ_z^n (Free-contraction, $100\,psi$)

Strain Order (ϵ_z^n)	**Measured Geometry** in/in	**Cylindrical Geometries** $in/in, (error)$
n = 1	0.289	0.353 (22.2%)
n = 2	0.084	0.125 (48.8%)
n = 3	0.024	0.044 (83.3%)
n = 4	0.007	0.016 (128.5%)

6.3.2.3 Comparison of Circumferential Strain

The circumferential strain of the bladder is a measure of the change in its diameter along its length. To have a single value of strain for use in modeling equations, the average of the circumferential strain for the entire length of the FAM is of interest. The average circumferential strain equation can be written as:

$$\epsilon_c^n = \frac{1}{L}\int_0^L \left(\frac{R_{bld} - \frac{t_{bld}}{2}}{R_{bld,0} - \frac{t_{bld,0}}{2}} - 1 \right)^n dz \tag{6.13}$$

where $R_{bld,0}$ is the initial resting diameter of the bladder (equal to 7/8 in for the tested FAM), and $t_{bld,0}$ is the initial resting thickness of the bladder (equal to 1/16 in for the tested FAM). The instantaneous radius of the bladder R_{bld}, is defined depending on whether a cylindrical geometry or a measured geometry is assumed for the calculation of circumferential stress, as follows:

$$R_{bld} = R_{est} \qquad (Cylindrical\ Profile) \tag{6.14}$$

$$R_{bld} = R_{meas,bld}(z) \qquad (Actual\ Profile) \tag{6.15}$$

where the difference between the two approaches of defining R_{bld} is illustrated in Figure 6.11. Previous efforts have assumed that the diameter of the bladder is equal to the estimated dimensions, D_{est} (Eq. 6.14). But, calculating the circumferential strain using a cylindrically assumed profile neglects the variation of strain along the length of the FAM with variation in diameter.

The strain can instead be calculated using an accurate representation of the geometry $D_{meas,bld}$ (Eq. 6.15). If the bladder material were a linear-elastic material, the distinction between using a measured profile, versus using a cylindrical

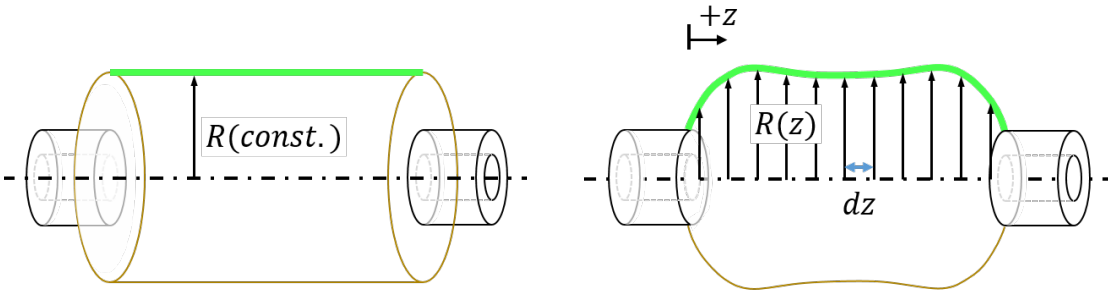

(a) Cylindrical Geometry (b) Measured Geometry

Figure 6.11: Geometry-dependent radial profile assumed for circumferential bladder strain calculations

approximation by calculating the average of the measured profile, would be irrelevant when calculating the average strain. However, that distinction is important with the nonlinear stiffness properties of the bladder used for most FAMs.

A comparison of the circumferential strain calculated using the estimated cylindrical geometry (elastic and inelastic braid), the measured geometry $D_{meas,bld}(z)$, and the average of the measured geometry $\bar{D}_{meas,bld}$ is illustrated in Figure 6.12. For first-order strains, there is very little difference in the calculated circumferential strain values. The differences in magnitude between the tested geometries increase as the strain orders increase. The estimated cylindrical geometry underestimates the circumferential strain at low levels of contraction, and overestimates at high levels of contraction. The difference in circumferential strain magnitude between the different geometries increases as the strain order increases.

Comparison between the measured geometry, and the cylindrical geometry defined using the average of the measured profiles, illustrates the effect of taking the changing radius of the FAM along its length into account (Fig. 6.12) . With exception of first-order strains, neglecting to take into account the actual measured

profile results in an underestimate of strain magnitude for the other orders of strain. This underscores the importance of calculating the actual profile rather than the cylindrical profile for use with the nonlinear bladder materials used.

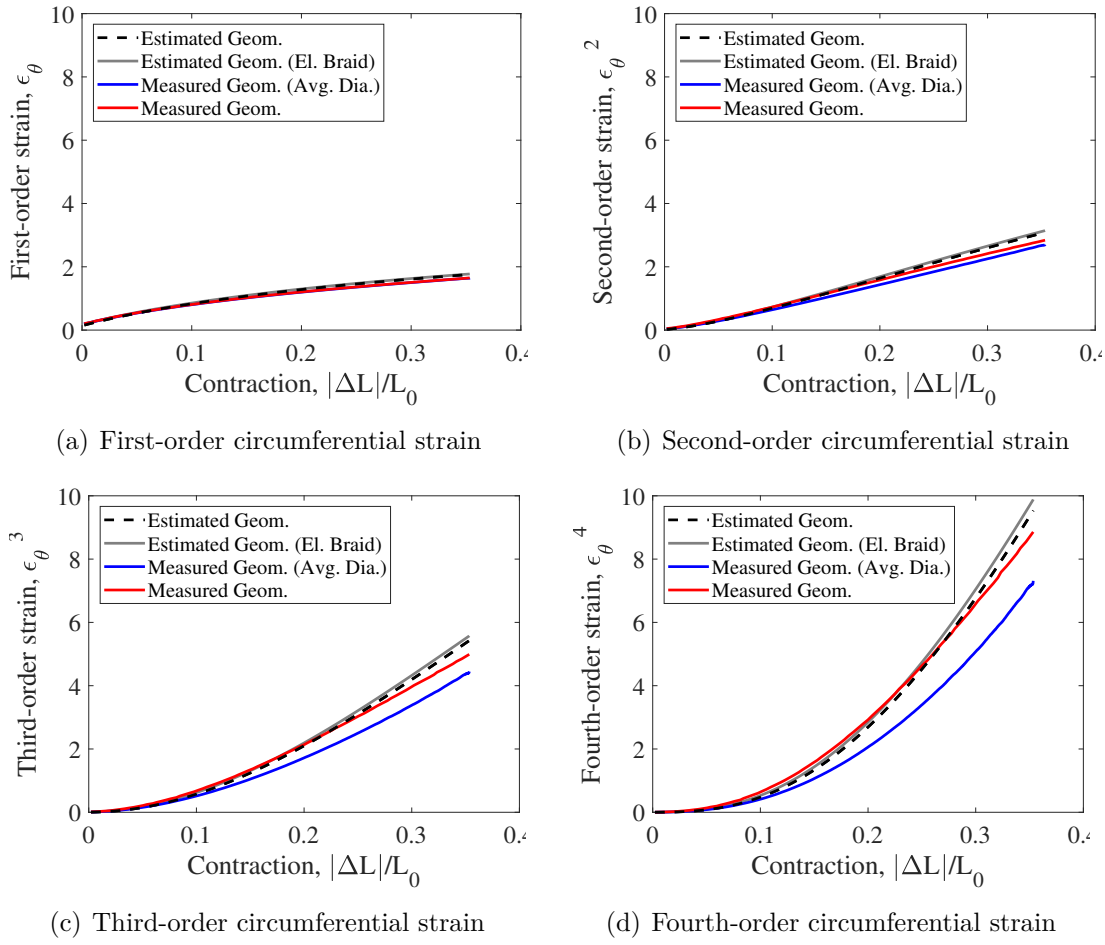

(a) First-order circumferential strain

(b) Second-order circumferential strain

(c) Third-order circumferential strain

(d) Fourth-order circumferential strain

Figure 6.12: Circumferential bladder strain calculated for each geometry ($100\,psi$)

Table 6.2 provides the maximum value of strain calculated for each geometry at strain orders 1–4, and are accompanied by the respective error of each cylindrical geometry expressed as a percentage error through comparison to the measured geometry strain values. The cylindrical assumption of both the estimated geometry, and the measured geometry, are considered to illustrate the effect of using the actual profile in the measurement of circumferential strain. Maximum error induced by us-

ing the cylindrical approximation of the measured geometry ranges from 0–17.5%, while the estimated cylindrical geometry results in maximum errors of 6.6–8.7% (elastic braid). It is evident that correction of the strain calculation by using the measured profile $D_{meas,bld}$, has a significant effect on the magnitude of values for all strain orders, but especially for the higher orders.

Table 6.2: Circumferential Bladder Strain, ϵ_c^n (Free-contraction, $100\,psi$)

		Cylindrical Bladder Geometries		
Strain Order (ϵ_c^n)	**Measured Geometry** in/in	**Measured (Avg. Dia.)** $in/in, (error)$	**Estimated (El. Braid)** $in/in, (error)$	**Estimated (InEl. Braid)** $in/in, (error)$
n = 1	1.65	1.65 (0.0%)	1.77 (7.3%)	1.76 (6.7%)
n = 2	2.84	2.70 (-4.9%)	3.14 (10.6%)	3.09 (8.7%)
n = 3	4.99	4.40 (-11.9%)	5.58 (11.8%)	5.43 (8.7%)
n = 4	8.86	7.31 (-17.5%)	9.89 (11.6%)	9.53 (7.6%)

6.4 Effect of Geometry Profile on Force Model Results

The geometry and respective dimensions assumed for a FAM will have an effect on its predicted actuation force. In this section, we will compare the actuation force predictions for the estimated and the measured geometries. The model used to estimate actuation force is as follows:

$$F_{act} = F_G + F_{bld,z} + F_{bld,c} \tag{6.16}$$

where,

$$F_G = P\pi R^2(2tan^2\theta - 1) \tag{6.17}$$

$$F_{bld,z} = \sigma_z \left(\frac{V_{bld}}{L}\right) \tag{6.18}$$

$$F_{bld,c} = -\sigma_c \left(\frac{tL^2}{2\pi RN^2}\right) \tag{6.19}$$

This actuation force model (Eq. 6.16) has three basic terms. F_G is the Gaylord force – which serves as the original and most basic form of the actuation force model – and it accounts for the actuation force produced by the internal fluid pressure acting on the braid. The Gaylord force is comprised of variables that represent pressure P, and geometric dimensions for radius R and braid angle θ. The second and third terms of Equation 6.16 are bladder force terms $F_{bld,z}$ and $F_{bld,c}$; these terms account for actuation force losses that are due to the stretching of the bladder during actuation. They are a function of the bladder stresses σ_z and σ_c, and dimensions R, N, t, and L. Values of σ_z and σ_c are based on the geometry-dependent bladder strain – as estimated in Section 6.3.2 – and the intrinsic stiffness of the bladder. Defining the nonlinear stiffness of the bladder is nontrivial, but it is required to obtain estimations of $F_{bld,z}$ and $F_{bld,c}$.

In the following sections, the effect of the assumed geometry on the predicted actuation force is analyzed. Analysis of F_G is covered first, followed by an investigation of terms $F_{bld,z}$ and $F_{bld,c}$. The combined effect of these terms is then investigated for each geometry. This will aid in quantifying the force model uncertainty and error that comes with assuming a cylindrical approximation and estimated dimensions of the FAM's geometry.

6.4.1 Gaylord Actuation Force Term (F_G)

The estimated and measured dimension sets are input into the Gaylord force term to obtain a comparison of their respective effects on the actuation force. Because the Gaylord force term requires dimensional inputs in cylindrical coordinates, the measured dimensions of the FAM must be defined in cylindrical terms. The average measured diameter, therefore, will be used to define the measured profile for analysis of the Gaylord force predictions.

A comparison of the Gaylord force term values for each geometry is provided in Figure 6.13. The same basic trends seen in previous geometry comparisons are observed here; the difference in Gaylord force values between the measured and estimated geometries increases with increases in contraction and pressure. The estimated dimensions (elastic braid) result in an underestimation of the FAM's Gaylord force, with a mean absolute error (MAE) of 19.9 lbf, and a maximum difference of 36.5 lbf (37% difference) observed in the free-contraction state at 100 psi. This underestimation of the Gaylord force also leads to an underestimation of the FAM's maximum contraction capabilities by an estimated 1-2% for all pressures. Table 6.3 provides a comparison of the Gaylord force term values – for the each assumed geometry – for 100 psi at free-contraction. Note that the maximum difference in force between each geometry is observed at 100 psi, and decreases with a decrease in pressure due to the respective reduction in geometric differences at lower levels of contraction.

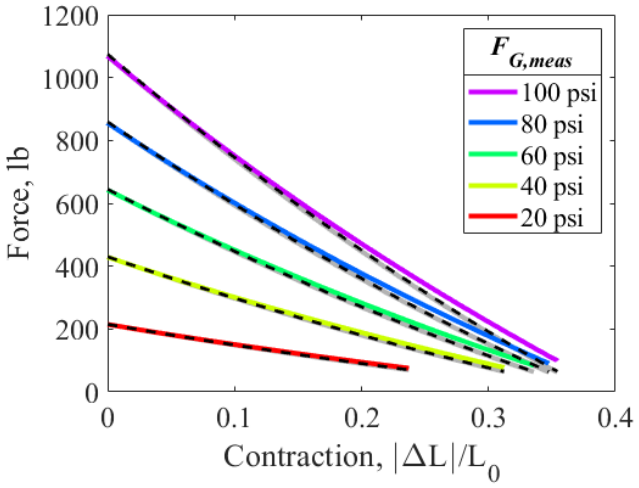

Figure 6.13: Comparison of the Gaylord force term estimates obtained for the cylindrical approximation of the measured geometry (colored lines), the estimated cylindrical geometry with elastic braid (gray lines), and the estimated cylindrical geometry with inelastic braid assumption (black dashed lines)

Table 6.3: Gaylord Force Term, F_G $(100\,psi)$

Length State $(100\,psi)$	**Cylindrical Bladder Geometries** **Measured (Avg. Dia.)** lbf	**Estimated (El. Braid)** $lbf, (error)$	**Estimated (InEl. Braid)** $lbf, (error)$
Resting Length	1068.3	1067.9 (0.0%)	1074.3 (0.6%)
Free-Contraction	98.6	62.1 (-37.0%)	65.4 (-33.7%)
Mean Abs. Error	–	19.9	16.8

6.4.2 Bladder Actuation Force

Energy lost to stretching of the bladder during actuation of the FAM acts to reduce the FAM's actuation force. As previously noted, obtaining values of $F_{bld,c}$ and $F_{bld,z}$ requires estimations of the stress state of the bladder (σ_c, σ_z), and a measure or estimation of the bladder material's stiffness.

Characterization of the bladder's nonlinear stiffness is nontrivial, and often

requires either direct testing of the material using complex testing procedures and equipment, or estimations based on empirical analysis of the FAM's actuation response data. Direct characterization is difficult for multiple reasons: hyperelastic materials can withstand large deformations, so specialized clamping techniques are required to ensure the test sample does not slip or tear in the test fixtures [88]; material stiffness is stress mode dependent, so multiple different tests are often required for a full characterization [89, 90]; and, the material's stiffness can vary from sample-to-sample based on its strain history and environment [37]. These challenges have led many FAM researchers to characterize the FAM's bladder stiffness *in situ* through analysis of the FAM's experimental actuation response. This often involves fitting the actuation force model to experimental data through adjustment of the bladder's material stiffness properties [7, 13, 17, 18, 21]. The model's accuracy with experimental data often still exhibits appreciable error; an unrealistic lack of material property constraints will render the defined stiffness parameters questionable. For these reasons, a direct characterization of the Latex bladder's stiffness – despite the experimental challenges – is attempted in this research to obtain values for $F_{bld,c}$ and $F_{bld,z}$.

6.4.2.1 Bladder Stiffness Characterization

A tensile test is performed on the same latex bladder that was used in the construction of the tested FAM. A tensile test of the bladder has been deemed sufficient to characterize the bladder's stiffness [88, 91]. This bladder measures 7/8

inches in diameter, and has a 1/16 inch wall thickness (Fig. 6.14). Test fixtures were fabricated to hold the bladder in place; these fixtures are cylindrical and have grooves – similar in design to the end-fittings of the FAM – and use hose clamps and epoxy to fix the bladder in place during testing. The resulting bladder sample had a test length between the fixtures of 3 3/32 inches.

Figure 6.14: Latex bladder tensile test specimen

The test specimen was tested using a material testing machine (MTS), and was stretched by 6.5 inches (2.1 strain) at a rate of 0.05 in/sec for a total of five consecutive stretch and relax cycles (Fig. 6.15). Mullins effect, which results in an initial relaxation of the bladder stiffness [87, 92], was observed between the first and second cycles. This resulted in a permanent stretch of the bladder by 3/32 inches to a total resting length of 3 3/16 inches. The response of the bladder stabilized after two cycles. A significant degree of necking of the bladder is observed, with a reduction in diameter to about 0.5 inches in the maximum tested strain state (Figs. 6.15(a) and 6.15(b)).

Engineering stress versus strain was calculated from the test data for comparison to the stress-strain relationship defined in a referenced work by J.G. Niemczura [87] (Fig. 6.16(a)). In that study, a tensile test was performed on a 0.48 mm

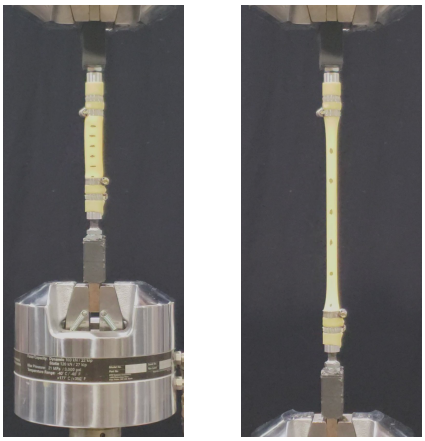

(a) Zero strain

(b) Max strain

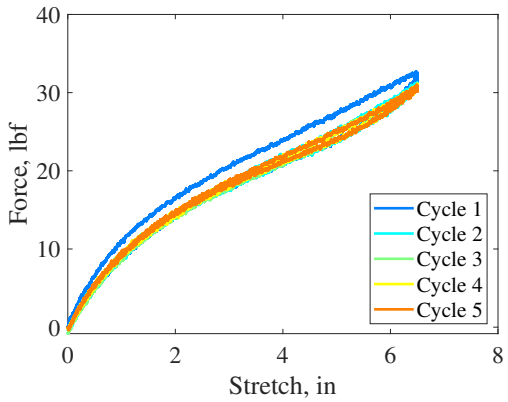

(c) Test results for eccentric-concentric cycling of bladder

Figure 6.15: Tensile testing of the latex bladder used in FAM construction

(0.019 in) thick, 5 mm (0.20 in) wide, 76.2 mm (3.0 in) long latex sample, and its stiffness was then defined by a third-order polynomial fit of the data. A third-order fit of the tensile test data acquired in this research resulted in an average difference of only 5.54 psi (6.24 psi RMSE) from the referenced data, and supported assurance of the accuracy of the acquired experimental stiffness values.

The force model requires an input of true stress, opposed to engineering stress. True stress references the instantaneous (deformed state) cross-sectional area, instead of the resting cross-sectional area. True stress is commonly used to define hyperelastic materials because of their non-negligible change in cross-sectional area as they achieve large deformations. A true stress calculation, therefore, requires an estimate of the instantaneous cross-sectional area of the bladder sample during the experimental test. The cross-sectional area of the bladder is approximated to be uniform along the deformed length of the bladder based on visual observations during testing; each end of the specimen rapidly decreases to a relatively constant

width for most of the deformed length (Fig. 6.15(b)). With a fixed bladder volume of $0.49\,in^3$ for the incompressible material in all length states, the cross-sectional area is calculated by dividing the bladder volume by the instantaneous length. This results in a cross-sectional area reduction from $0.16\,in^2$ at zero strain, to $0.05\,in^2$ at the maximum tested strain. The true stress-strain relationship is then calculated, as shown in Figure 6.16(b). The approximately 200% increase in maximum stress between the engineering and true stress values emphasizes the substantial effect of the changing cross-sectional area and bladder thickness on the calculated stress values.

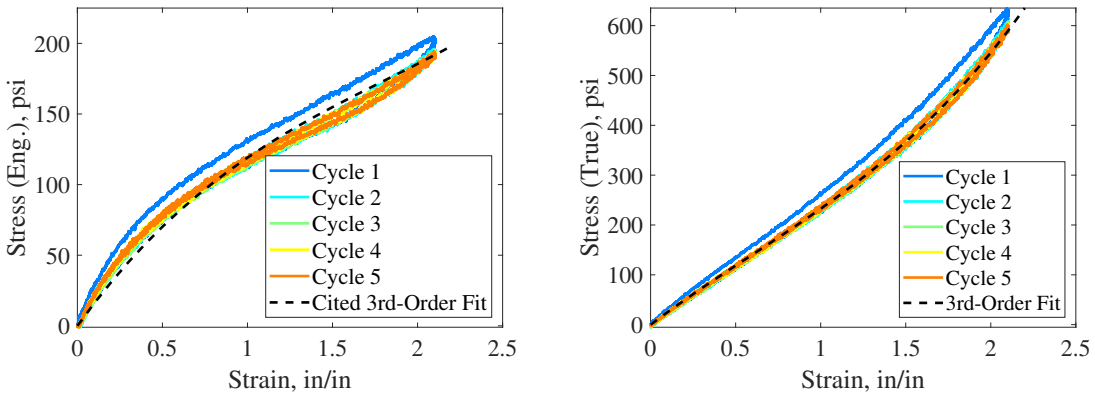

(a) Engineering Stress versus Strain

(b) True Stress versus Strain

Figure 6.16: Engineering and True Stress values acquired from tensile test data

As previously noted, hyperelastic material stiffness is commonly defined using a polynomial fit of experimental data. A third-order polynomial is often used to fit the distinct S-shape that is common for the stress-strain relationship of hyperelastic materials, as seen in Figure 6.16(a). A least-squares polynomial fit was performed on cycles 3-5 of the tensile test (Fig. 6.16(b)), resulting in the following definition

of the Latex's stress-strain relationship:

$$\sigma = E_1\epsilon + E_2\epsilon^2 + E_3\epsilon^3 \tag{6.20}$$

$$E_1 = 257.8\,psi$$

$$E_2 = -57.9\,psi$$

$$E_3 = 32.7\,psi$$

The resulting fit accurately depicts the stiffness of the Latex bladder, as shown in Figure 6.16(b), with a mean absolute error of only 4.4 psi (5.5 psi RMSE). Subsequent analysis will utilize this equation to define the Latex bladder's stiffness.

6.4.2.2 Longitudinal Bladder Force Term ($F_{bld,z}$)

The longitudinal bladder force term $F_{bld,z}$, represents the effect of the bladder's changing longitudinal length on the actuation force of the FAM. $F_{bld,z}$, defined in Equation 7.2, requires geometry-dependent inputs of longitudinal bladder stress σ_z, and FAM length L. The longitudinal bladder stress is calculated using the stress-strain relationship defined for the Latex (Eq. 6.20), and the strain values defined for each geometric profile in Section 6.3.2.2. The resulting bladder stress and respective force values are presented in Figures 6.17(a) and 6.17(b), and are tabulated in Tables 6.4 and 6.5, respectively.

Analysis of the longitudinal stress values shows that the bladder is in tension at the resting length state of the FAM, before shifting to a state of compression that monotonically increases in magnitude with FAM contraction. The initial tension in the bladder is a result of the slight radial expansion of the bladder in the fixed

resting length state of the FAM. The longitudinal force term $F_{bld,z}$, is then calculated as the product of the instantaneous stress state and cross-section area of the bladder (normal to FAM's longitudinal axis).

Comparison of the results for different geometric profiles shows the difference between the cylindrical and measured geometric profiles. As with their strain values, the cylindrical geometric profiles all result in identical values of stress and force; differences in the free-contraction values between cylindrical geometries are a result of slight differences in their other force terms.

Longitudinal force term values are tabulated in Table 6.5 for each geometry (100 psi fluid pressure). The longitudinal force for the measured geometry profile ranges in magnitude from 0.1 lbf (tension) in the resting length state, to -17.9 lbf (compression) in the free-contraction state. Error of the cylindrical geometry profiles is minimal in the resting length state (0.1 lbf), and has a much larger impact in the free-contraction state where the longitudinal force is overestimated by up to 2.2 - 3.7 lbf (12.2 - 20.4%). The mean absolute error of the force calculated for the cylindrical geometry profiles (at 100 psi) is relatively low, at 1.4 lbf.

Table 6.4: Longitudinal Bladder Stress, σ_z $(100\,psi)$

		Cylindrical Bladder Geometries		
Length State $(100\,psi)$	**Measured Geometry** psi	**Measured (Avg. Dia.)** $psi, (error)$	**Estimated (El. Braid)** $psi, (error)$	**Estimated InEl. Braid** $psi, (error)$
Resting Length	0.6	0.0 (100%)	0.0 (100%)	0.0 (100%)
Free-Contraction	-71.6	-86.7 (-21.0%)	-82.8 (-15.6%)	-83.3 (-16.3%)

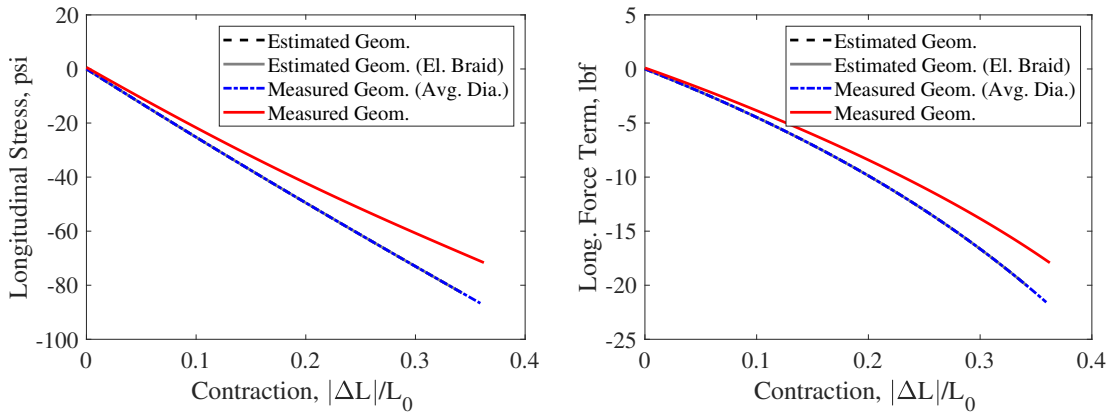

(a) Longitudinal bladder stress, σ_z

(b) Longitudinal bladder force term, $F_{bld,z}$

Figure 6.17: Longitudinal bladder stress, and longitudinal force term, calculated for each geometry (all tested pressures)

Table 6.5: Longitudinal Bladder Force Term, $F_{bld,z}$ $(100\,psi)$

Length State $(100\,psi)$	**Measured Geometry** lbf	**Cylindrical Bladder Geometries**		
		Measured (Avg. Dia.) $lbf, (error)$	**Estimated (El. Braid)** $lbf, (error)$	**Estimated (InEl. Braid)** $lbf, (error)$
Resting Length	0.1	0.0 (100%)	0.0 (100%)	0.0 (100%)
Free-Contraction	-17.9	-21.6 (20.4%)	-20.1 (12.2%)	-20.3 (13.3%)
Mean Abs. Error	–	1.4	1.4	1.4

6.4.2.3 Circumferential Bladder Force Term ($F_{bld,c}$)

The circumferential bladder force term $F_{bld,c}$, represents the effect of the bladder's radial expansion, and respective stretch, on the actuation force of the FAM. $F_{bld,c}$, defined in Equation 6.19, requires geometry-dependent inputs of circumferential bladder stress σ_c, and the instantaneous bladder dimensions of thickness t, radius R, and length L. The circumferential bladder stress is calculated using the stress-strain relationship defined for the Latex (Eq. 6.20), with the strain values

defined for each geometric profile in Section 6.3.2.3.

The resulting stress and force values are shown in Figures 6.18(a) and 6.18(b), and tabulated in Tables 6.6 and 6.7, respectively (100 psi fluid pressure). The circumferential stress monotonically increases in magnitude from a non-zero minimum value in the resting length state; stress is non-zero in the resting length state due to the initial unconstrained radial expansion of the bladder prior to it coming into contact with the braid. In comparison to the stress curves, the circumferential force term values increase in magnitude only up until about 8% contraction of the FAM. The subsequent decrease in force at higher FAM contractions - despite the increase in respective stress values - is primarily due to the effect of the bladder's reducing cross-sectional area that comes with increases in FAM contraction.

Comparison of the circumferential force term values for different geometric profiles shows a distinct difference between the measured geometry profile, and the cylindrical geometry profiles. The measured geometry profile predicts that the circumferential strain acts to reduce the FAM's actuation force by up to 85.8 lbf. The cylindrical geometries - using either measured or estimated dimensions – tend to over-predict the circumferential stress and force values. The estimated geometry used in past research overestimated the circumferential force term by as much as 10.2 lbf (19.0% error) in the resting length state, while using a cylindrical approximation of the bladder's measured dimensions resulted in a slightly lower magnitude of maximum error of 3.4 lbf (5.5%) in the free-contraction length state. Overall, the use of any cylindrical geometry in place of the measured geometry resulted in a mean absolute error of about 3 lbf.

Note that in comparison to the values of the measured geometry, the cylindrical approximation of the measured geometry results in a general underestimation of stress, but an overestimation in force; this occurs despite the fact that the two geometries share the same values for R, L, and N for the calculation of force, and only differ in their value for t. This emphasizes the relatively large effect that the value of t has on the predicted circumferential force term.

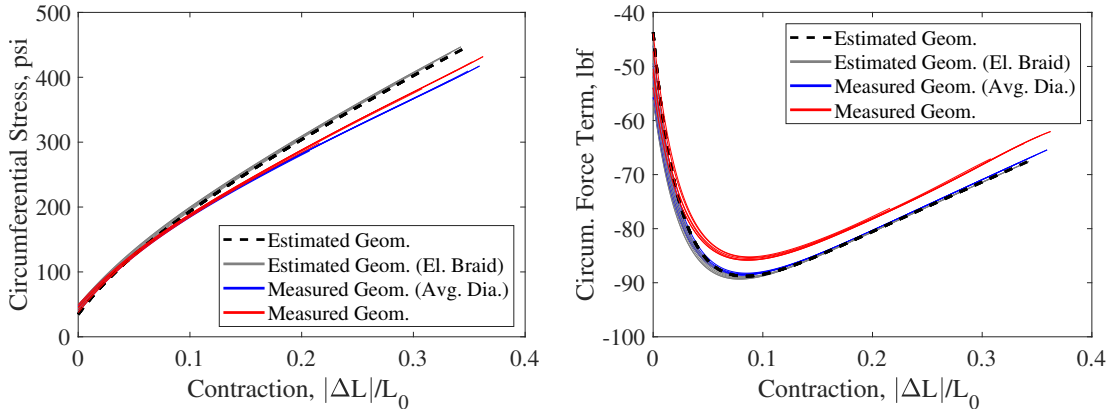

(a) Circumferential bladder stress, σ_c (b) Circumferential bladder force term, $F_{bld,c}$

Figure 6.18: Circumferential bladder stress, and circumferential bladder force term, calculated for each geometry (all tested pressures)

Table 6.6: Circumferential Bladder Stress, σ_c $(100\,psi)$

		Cylindrical Bladder Geometries		
Length State $(100\,psi)$	**Measured Geometry** psi	**Measured (Avg. Dia.)** $psi, (error)$	**Estimated (El. Braid)** $psi, (error)$	**Estimated (InEl. Braid)** $psi, (error)$
Resting Length	49.2	48.2 (-2.0%)	48.7 (-0.9%)	34.5 (-29.9%)
Free-Contraction	431.9	417.4 (-3.4%)	446.9 (3.5%)	443.8 (2.8%)

Table 6.7: Circumferential Bladder Force Term, $F_{bld,c}$ $(100\,psi)$

Length State $(100\,psi)$	**Measured Geometry** lbf	**Cylindrical Bladder Geometries**		
		Measured (Avg. Dia.) $lbf, (error)$	**Estimated (El. Braid)** $lbf, (error)$	**Estimated (InEl. Braid)** $lbf, (error)$
Resting Length	-53.9	-55.7 (-3.3%)	-56.1 (-4.0%)	-43.7 (19.0%)
Free-Contraction	-62.0	-65.4 (-5.5%)	-67.6 (-9.0%)	-67.3 (-8.5%)
Maximum Value	-85.8	-88.6 (-3.2%)	-89.3 (-4.1%)	-88.8 (-3.5%)
Mean Abs. Error	–	2.6	3.1	2.7

6.4.2.4 Combined Effect of Bladder Forces

The combined values of $F_{bld,z}$ and $F_{bld,c}$ represent the overall actuation force losses due to stretch of the bladder during actuation of the FAM. As seen in Figure 6.19, the measured geometry predicts that bladder forces reduce the actuation force at 100 psi by about 53.8 lbf in the resting length state, by a maximum of 89.5 lbf at 10.4% contraction, and by 80.0 lbf in the free-contraction state. The overall trend reflects a substantial increase in bladder force effects from 0% to 10% contraction, and then a relatively consistent effect on actuation force from 10% contraction to free-contraction. Figure 6.19 includes the results for pressures of 20-100 psi with each geometry; the relative width of the curves indicates that the variation in force values is slightly noticeable in the resting length state, and decreases with contraction. Comparing the circumferential and longitudinal bladder force terms shows the dominance of the circumferential term. The maximum circumferential force term value is 85.8 lbf, which is 4.8 times the maximum magnitude of the longitudinal force term value of 17.9 lbf.

Table 6.8 provides a comparison between the measured geometry profile, and the cylindrical approximation profiles. The cylindrical bladder geometries overpredict the combined bladder force effects, and are all nearly identical in magnitude with a mean absolute error of about 4 lbf. The estimated geometry with the elastic braid assumption generally has the largest error in comparison to the measured geometry profile. However, the inclusion of braid elasticity does reduce error in the resting length state from 18.9% down to 4.3% (12.4 lbf difference). The cylindrical approximations of the measured geometry and the estimated geometry (elastic braid) never differ by more than 1 lbf for all contraction states. Cylindrical bladder geometries differ from the measured geometry profile by 1.9 lbf (3.5%) to 7.7 lbf (9.7%) for all states of contraction.

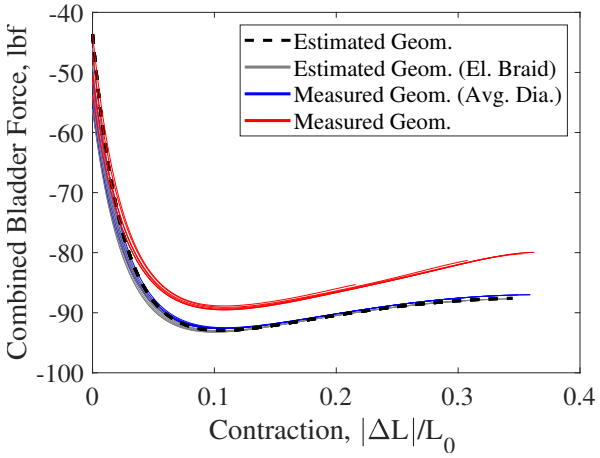

Figure 6.19: Combined bladder force calculated for each geometry (all test pressures)

6.4.3 Overall Effect of Geometry on Estimated Force

Values for the Gaylord and bladder force terms obtained in the preceding sections are combined here to form the overall FAM actuation force model predictions

Table 6.8: Combined Bladder Force, F_{bld} $(100\,psi)$

Length State $(100\,psi)$	**Measured Geometry** lbf	**Cylindrical Bladder Geometries** **Measured (Avg. Dia.)** $lbf, (error)$	**Estimated (El. Braid)** $lbf, (error)$	**Estimated (InEl. Braid)** $lbf, (error)$
Resting Length	-53.8	-55.7 (-3.5%)	-56.1 (-4.3%)	-43.7 (18.9%)
Free-Contraction	-80.0	-87.0 (-8.8%)	-87.7 (-9.7%)	-87.6 (-9.6%)
Maximum Value	-89.5	-92.7 (-3.5%)	-93.2 (-4.2%)	-93.0 (-3.8%)
Mean Abs. Error	–	4.0	4.5	4.1

(Eq. 6.16). Figure 6.20 compares the investigated geometries. Figure 6.20(a) provides a comparison between the Gaylord force term, and combined bladder force terms, for all pressures and geometric profiles. As previously noted, the bulk of the FAM's actuation force is accounted for with the Gaylord force term. The effects of differences in geometric profiles, therefore, are much more noticeable in the Gaylord force term than they are with the bladder force terms. The noticeable differences in force between geometries in Figure 6.19 appear to to be almost negligible when viewed in Figure 6.20(a).

Figure 6.20(b) shows the actuation force model results (Gaylord and bladder force terms combined). Table 6.9 provides mean absolute error, resting length (blocked force) and free-contraction values of the resulting actuation force curves for the 100 psi case. The measured geometry profile produces a blocked force that is only 2 lbf greater (0.3%) than the cylindrical approximation of the measured geometry, and the estimated geometry (elastic braid). This result is not surprising considering the FAM has a relatively cylindrical shape and minimal bladder strain

in the resting length state. The estimated geometry (inelastic braid) has the largest magnitude of error in the resting length state out of all the geometries (17 lbf, 1.7% error). Assuming an inelastic braid neglects the effect of braid stretch on the radial expansion, braid angle, and the respective effects on actuation force.

Larger differences in the resulting values between geometries are seen in their predicted maximum contraction values. The measured geometry predicts the largest free-contraction value of 36.2% contraction; the cylindrical approximation of the measured geometry – which only differs in its calculated bladder force values – predicts a free-contraction that is only 0.3% less. The estimated geometry profiles predict free-contraction values that are substantially lower (close to 2% lower) than the measured geometry. Overall, we can see that the differences between the measured geometry and the cylindrical geometries increase with contraction as the cylindrical approximation of the FAM's geometry becomes increasingly non-representative of the FAM's actual geometry. In comparison to the results from the measured geometry (at 100 psi), the cylindrical assumption of the measured geometry has the lowest mean absolute error (4.0 lbf), while the estimated geometry (elastic braid) has the highest mean absolute error (23.8 lbf).

6.4.4 Comparison To Experimental Data

Model results for each geometry are compared to experimental data of the tested FAM (Fig. 6.21). Comparison of the model results and experimental data show that the model overpredicts the actuation force over much of the FAM's con-

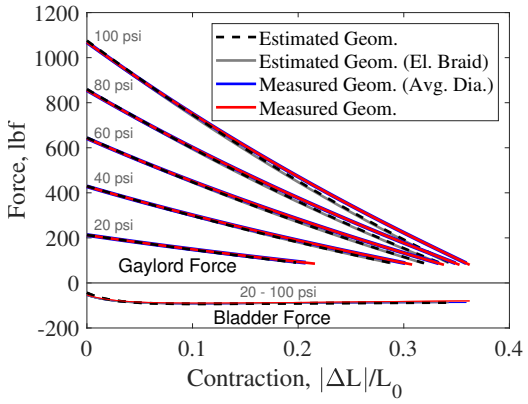

(a) Components of actuation force model, Gaylord Force (F_G) and bladder force terms (F_{bld})

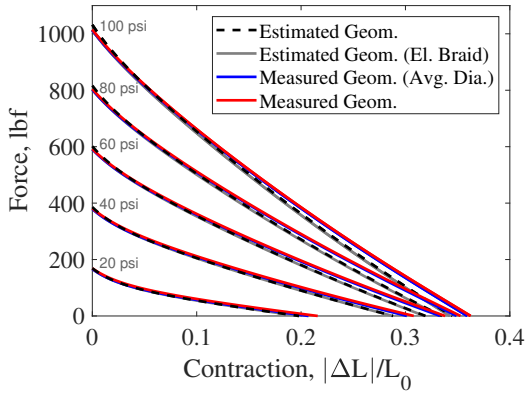

(b) Actuation force model results (F_{act})

Figure 6.20: Combining individual actuation force model terms to obtain overall model results for each geometry

Table 6.9: FAM Actuation Force (Model), F_{act} ($100\,psi$)

		Cylindrical Bladder Geometries		
Length State ($100\,psi$)	**Measured Geometry** lbf	**Measured (Avg. Dia.)** $lbf, (error)$	**Estimated (El. Braid)** $lbf, (error)$	**Estimated (InEl. Braid)** $lbf, (error)$
Resting Length	1015	1013 (-0.2%)	1012 (-0.3%)	1032 (1.7%)
Free-Contraction	36.2%	35.9% (-0.9%)	34.3% (-5.5%)	34.5% (-4.9%)
Mean Abs. Error	–	4.0	23.8	19.6

traction range. The model results are most accurate for the regions near the resting and free-contraction length states. Error is greatest at around 50% contraction. Model error is also pressure-dependent, with error increasing as working fluid pressure is increased. The mean absolute error (MAE) of the force model values at each tested pressure are compared to the experimental force values in Table 6.10. The measured geometries have larger MAE values than the estimated geometries at high pressures, but lower MAE values than the estimated geometries at low pressures ($< 40\,$psi). The RMSE values of the model are similar in magnitude to the MAE

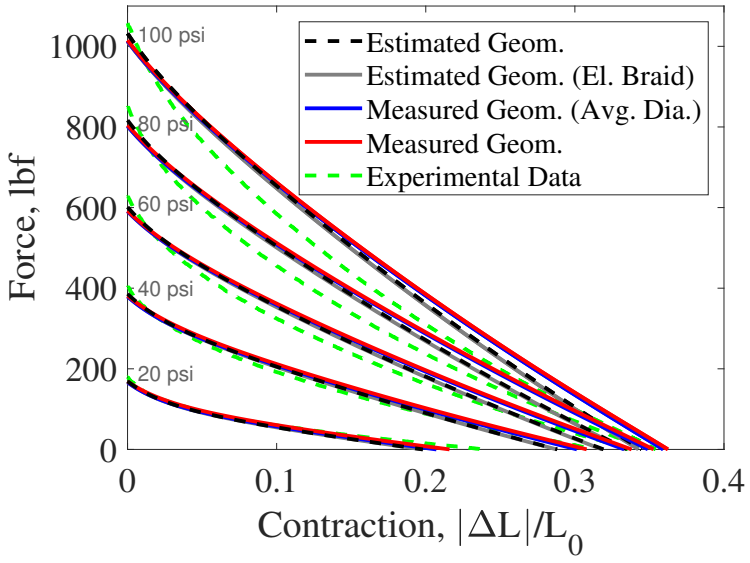

(a) Actuation response comparison

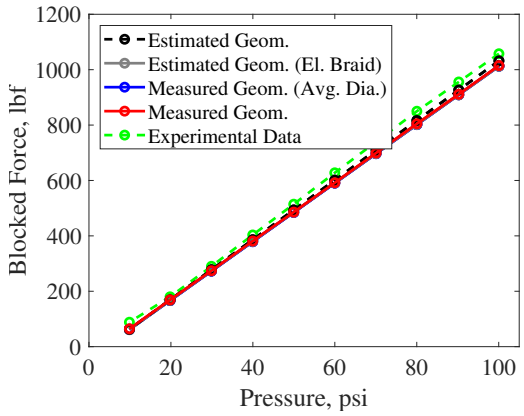

(b) Blocked force results

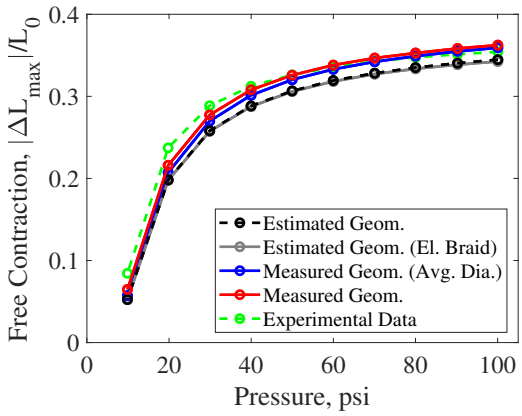

(c) Free-contraction results

Figure 6.21: Comparison between model and experimental test results

values (as expected); for the measured geometries, the RMSE of the model is 61.7 lbf at 100 psi; 44.3 lbf at 80 psi; 28.4 lbf at 60 psi; 13.7 lbf at 40 psi; and 4.5 lbf at 20 psi.

Analysis of the model predictions for the blocked force state is given in Figure 6.21(b), and detailed in Table 6.11. The estimated geometry resulted in the lowest error in the blocked force state, with an average blocked force error for all pressures of 22.8 lbf (3.9% average error). The remaining three geometries all resulted in similar accuracies, with the measured geometry performing slightly better than the

others with an average blocked force error of 31.4 lbf (5.2% average error) . Measured geometry error ranged from 45 lbf (-5.2% error) at 80 psi, to 11 lbf (-5.9% error) at 20 psi. With increases in pressure, the geometries each showed an increase in their magnitude of error, and a decrease in their percent error.

Analysis of the model predictions in the free-contraction state are provided in Figure 6.21(c), and detailed in Table 6.12. Improvements in modeling accuracy due to improvements in geometric accuracy are most apparent in the free-contraction state. The measured geometry profile resulted in the lowest error in the free-contraction state, with an average absolute error of 0.8% (3.0% error). Measured geometry error ranged from 0.2% contraction (0.7% error) at 60 psi, to 2.1% contraction (-9.0% error) at 20 psi. The estimated geometries did not perform as well; with an inelastic braid, they had an average free-contraction error of 2.0% (7.1% error). The error at free-contraction had the overall trend of increasing with decreasing pressure.

The error that remains between the experimental force and model predictions indicates that there is still room for modeling improvements. Improvements to the model's accuracy – through the use of the accurate measured geometries – is most apparent near the free-contraction states. These improvements are mostly attributed to the geometry's effect on the Gaylord force term; improvements in dimensional accuracy had only a small impact on the results of the bladder force terms. This observation, combined with the pressure-dependent nature of the force error, suggests it is unlikely that further improvements to the model's bladder force terms would yield significant improvements in the model's accuracy.

Table 6.10: Mean Absolute Error (MAE) - Experimental versus Model Results

Test Pressure	**Tested (Exp.)** *lbf*	**Measured Geometry** *lbf*	**Measured (Avg. Dia.)** *lbf*	**Estimated (El. Braid)** *lbf*	**Estimated (InEl. Braid)** *lbf*
100 psi	–	58.4	54.5	37.9	41.8
80 psi	–	41.7	37.7	27.0	29.1
60 psi	–	26.0	22.6	16.9	17.8
40 psi	–	12.3	10.0	8.8	9.0
20 psi	–	3.1	5.1	7.0	6.7

Table 6.11: Blocked Force - Experimental versus Model Results

Test Pressure	**Tested (Exp.)** *lbf*	**Measured Geometry** *lbf*, (*error*)	**Measured (Avg. Dia.)** *lbf*, (*error*)	**Estimated (El. Braid)** *lbf*, (*error*)	**Estimated (InEl. Braid)** *lbf*, (*error*)
100 psi	1058	1015 (-4.1%)	1013 (-4.2%)	1012(-4.3%)	1032 (-2.4%)
80 psi	850	805 (-5.2%)	802 (-5.5%)	802 (-5.5%)	817 (-3.7%)
60 psi	628	592 (-5.5%)	590 (-5.7%)	591 (-5.7%)	601 (-4.0%)
40 psi	403	381 (-5.1%)	379 (-5.7%)	380 (-5.5%)	386 (-3.9%)
20 psi	180	169 (-5.9%)	166 (-7.3%)	167 (-7.2%)	169 (-5.7%)

Table 6.12: Free-Contraction - Experimental versus Model Results

Test Pressure	**Tested (Exp.)** %	**Measured Geometry** %, (*error*)	**Measured (Avg. Dia.)** %, (*error*)	**Estimated (El. Braid)** %, (*error*)	**Estimated (InEl. Braid)** %, (*error*)
100 psi	35.4	36.2 (2.3%)	35.9 (1.4%)	34.3 (-3.3%)	34.5 (-2.7%)
80 psi	34.8	35.3 (1.5%)	34.9 (0.4%)	33.4 (-4.0%)	33.5 (-3.6%)
60 psi	33.6	33.8 (0.7%)	33.3 (-0.8%)	31.8 (-5.2%)	31.9 (-4.9%)
40 psi	31.2	30.8 (-1.4%)	30.1 (-3.5%)	28.8 (-7.9%)	28.8 (-7.7%)
20 psi	23.7	21.6 (-9.0%)	20.7 (-12.7%)	19.8 (-16.6%)	19.8 (-16.5%)

These results emphasize the fact that further improvements should be made to the Gaylord force term in the model. Analysis of the braid's effect on actuation force is still constrained to the assumption of a cylindrical geometry by the Gaylord force term of the model, and the current framework of the model is unable to take full advantage of the high-fidelity geometry measurements provided by the photogrammetric method. Future studies, therefore, should focus on investigating improvements to the model that do a better job of accounting for the complex geometry of the braid.

6.5 Conclusion

Previous research on the modeling of FAMs has relied on a cylindrical approximation of the FAM's geometry for estimations of dimensions and actuation force. It has long been understood that dimensions estimated using the cylindrical approximation misrepresent the actual geometry of the FAM, and have served as a major source of error and uncertainty in the modeling of FAMs. In this research, the results of using measured FAM dimensions were compared to the results produced with the estimated dimensions used in previous FAM modeling efforts. This comparison was used to quantify the accuracy improvements in geometric and actuation force modeling by using an accurate representation of the FAM's geometry. The photogrammetric method of measuring the geometric profile of FAMs is a tool that can provide a high-fidelity representation of the FAM's geometric dimensions. This research showed how the photogrammetric method can now be used to improve

upon previous modeling efforts by reducing modeling error previously introduced by using the cylindrical approximation.

Initial analysis compared the dimensions of the estimated and measured geometries. The estimated dimensions are based on a cylindrical approximation of the FAM's geometry, however, the FAM's geometric shape becomes increasingly non-cylindrical with contraction. This fosters a consequent increase of the error – inherent in the estimated dimensions – with increases in contraction of the FAM. Accordingly, by neglecting the curvature of the FAM, the estimated dimensions were found to overestimate the diameter of the FAM by up to 4.7%, and underestimate the braid angle by up to 3.3%. These dimensions were then used to compare estimates of bladder strain. Use of the estimated cylindrical geometry was found to overestimate the longitudinal strain by up to 22–129%, and overestimate circumferential strain values by up to 7–12% (maximum error varies with strain order).

The effect of the FAM's geometry on the model's actuation force values was investigated piece-wise through isolation of each term of the model. For the Gaylord force term, when compared to the measured geometries (at 100 psi), the estimated geometries underestimated force by as much as 37%, and had a mean absolute error of 19.9 lbf. For the bladder force terms, when compared to the measured geometries (at 100 psi), the estimated geometries overestimated the bladder effects by 4.2% - 9.7% (elastic braid), and all cylindrical geometries resulted in a mean absolute error of about 4 lbf – relatively less than the magnitude of error in the Gaylord force term. When the force terms were combined to observe their cumulative effects, variations in force between geometries were minimal in the resting length state (3 lbf, 0.3%

maximum difference between tested geometries), but variations were relatively large with the predicted maximum contractions (1.9% contraction, a 5.5% difference). The mean absolute error for the cylindrical geometries (at 100 psi) ranged from 4.0 lbf (cylindrical approximation of measured geometries) to 23.8 lbf (estimated geometry with elastic braid).

The results of the force model were then compared to experimental force response data of the tested FAM, with a focus on the performance of the force model when using the measured geometry profiles. In the blocked force state, the model error using the measured geometries ranged from 45 lbf (-5.2% error) at 80 psi, to 11 lbf (-5.9% error) at 20 psi. Improvements in modeling accuracy by using the measured geometries was most apparent in the free-contraction state with an average contraction error of 0.8% (3.0% error), which was much better than the average free-contraction error of 2.0% (7.1% error) for the estimated geometries. Analysis of the mean absolute error of the model fit to experimental data found that the measured geometries had larger mean absolute error values than the estimated geometries at high pressures, but lower MAE values than the estimated geometries at low pressures (< 40 psi). From this analysis, the error that remains in the model – even with the use of the measured geometric dimensions – motivates the need for future improvements to the model.

Overall, this research has quantified much of the uncertainty associated with the use of a cylindrical approximation in acquiring dimension and actuation force estimates of the tested FAM. The previously used estimated dimensions (acquired through application of the cylindrical approximation) were replaced by measured

dimensions, and the error and uncertainty induced by the cylindrical approximation in the previous force models was largely quantified. Moreover, error due to the cylindrical approximation was also fully quantified for the bladder force terms, however, analysis of the Gaylord force term was limited by the term's requirement for dimensional inputs to be presented in cylindrical coordinates. Nonetheless, the error in the Gaylord force was partially quantified by using a cylindrical approximation of the accurate measured dimensions in place of the estimated dimensions. The current form of the actuation force model still has room for further improvements in accuracy. This work presents evidence that future improvements should focus on modification of the Gaylord force term to better represent the effects of the braid's complex curvature on actuation force.

Chapter 7: Modeling Improvements

7.1 Introduction

In the previous chapter, we found an undesirable amount of error in the actuation force model despite the use of accurate inputs for the geometric and material properties. Additional modification to the model is required to improve the fit and predictive nature of the model. Until this happens, *fit-parameters* – terms used to adjust the model to match the FAM's physical force response – are needed. These fit-parameters are typically identified through optimization techniques. While fit-parameters are phenomenological in nature, they can be defined and constrained in ways that reflect the FAM's underlying physical mechanisms. The current challenge, therefore, is defining the fit-parameters in a way that reflects the physical mechanisms of the FAM, while also ensuring the model accurately represents the FAM's actuation response.

Previous FAM modeling research has developed modeling approaches that embed fit-parameters within the bladder's material stiffness term of the force model [18]. Placement of the fit-parameters within the material's stiffness definition alleviates the need for a difficult-to-obtain experimental characterization of the bladder's material stiffness. However, initial implementations of this form of the model

allowed for unrealistic bladder stiffness definitions that were free of the actual material's physical constraints. Subsequent research has moved towards applying realistic constraints to these material-based fit-parameters, while still attempting to retain model accuracy.

A model using this approach will be investigated in this research. While past research has used this model approach with dimensional inputs that were estimated using a cylindrical approximation of the FAM's geometry, we will improve the fidelity of the model here, by instead utilizing the geometric measurements acquired using photogrammetric methods (established in Chapters 4-6) to ensure accurate dimensional inputs to the model. This work will then aim to improve the fidelity and fit of the model by: (1) improving the material stiffness constraints that are applied to candidate fit-parameter values; and, (2) identifying the necessary number of fit-parameters to use along with their dependencies, if any, on the internal pressure of the FAM (as used in previous works). As a gauge of the physical accuracy of obtained fit-parameters, they will be compared to the analogous bladder material stiffness coefficients obtained in Chapter 6. The 7/8 inch diameter, 9 9/32 inch length FAM used for analysis in previous chapters is also used here. The model is updated to make it more mechanistic in form, while also striving to provide a model fit that is true to the experimental response of the FAM; the computational complexity of the model will also be considered for its application in control schemes.

7.2 Background on Model

The force-balance form of the actuation force model used in this work was originally derived by Ferraresi (2001) [1]. Many authors have since improved upon that model by adding or adjusting terms to better represent the dimensions, interactions, or material properties of the braid or bladder. The specific form of the model used in this research was originally developed by Hocking (2012) [18]. The

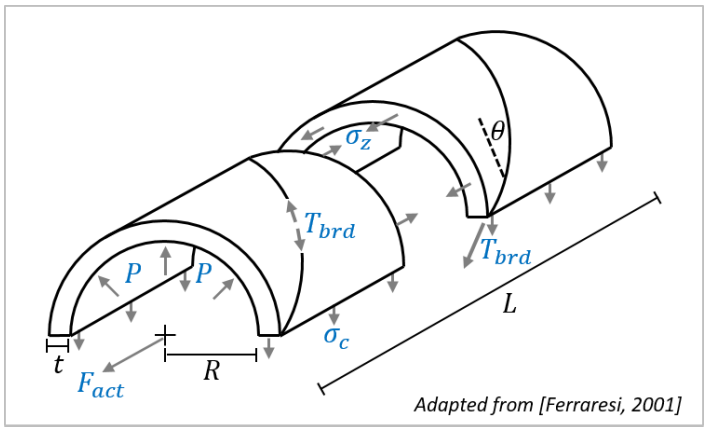

Figure 7.1: Free-body diagram of the FAM used in derivation of the force model [1]

model takes a mechanistic approach, and is based on a free-body diagram (shown in Figure 7.1) which accounts for pressure, bladder, and braid forces. From this, force-balance equations for equilibrium in the FAM's longitudinal (z) and circumferential (c) directions are obtained:

$$PRL = \sigma_c t_{bld} L + N T_{brd} cos(\theta) \tag{7.1}$$

$$F_{act} + \pi R^2 P = \sigma_z (V_{bld}/L) + T_{brd} sin(\theta) \tag{7.2}$$

These equations include: unknown values of actuation force (F_{act}) and braid thread tensions (T_{brd}); working fluid parameters for pressure (P); bladder parameters for

volume (V_{bld}), bladder thickness (t_{bld}), longitudinal stress (σ_z), and circumferential stress (σ_c); and braid geometry-based parameters for active length (L), radius (R), braid angle (θ), and number of turns of each thread about the circumference of the FAM (N). Through substitution of the unknown value of T_{brd}, the system of equations is used to solve for F_{act}. The following expression for actuation force of the FAM – as a function of length L – is then defined as follows:

$$F_{act} = P\pi R^2(2tan^2\theta - 1) + \sigma_z\left(\frac{V_{bld}}{L}\right) - \sigma_c\left(\frac{t_{bld}L^2}{2\pi RN^2}\right) \tag{7.3}$$

The model requires an estimation or measurement of the FAM's geometric dimensions in each length-state to define many of its input parameters. These dimensions are commonly estimated using the triangle approximation [5], but can also be defined based on photogrammetric measurements of the FAM's geometry, as covered in Chapter 4.

The model also requires an estimation of bladder stress in the longitudinal (σ_z) and circumferential (σ_c) directions. As covered in Chapter 6, obtaining these values requires an estimation of the bladder's strain state (commonly based on geometric dimensions) and its material stiffness. The bladder's stiffness, however, is difficult to accurately characterize for multiple reasons; testing to the high strain-states of hyperelastic materials can require specialized clamping fixtures, testing equipment, and multi-directional testing. Furthermore, even after a hyperelastic bladder material is fully characterized, its stiffness can vary depending on storage and working conditions (e.g. temperature, light or fluid exposure), strain history, or variations in manufacturing methods [19, 92].

Because of those challenges, the bladder's stiffness is commonly defined using indirect empirically-based methods instead of through direct characterization. These methods typically involve fitting the force model to experimental force-response data by adjusting the bladder material's stiffness coefficients, and in effect, turning them into fit-parameters [18, 20, 34]. These fit-parameters are typically identified through optimization techniques.

Initial efforts used a single fit-parameter – often connected to the Gaylord force term – to account for unmodeled phenomena, and inaccuracies in the bladder stiffness term [9]. The first applications to place the fit-parameter within the bladder stiffness terms used a single fit-parameter; this simplistic form defined the hyperelastic stiffness of the bladder as a linear-elastic material [1, 13], and struggled in matching the model to the nonlinear response of the FAM.

Hocking (2012) developed a method of defining the bladder stress input to the model as a polynomial function of strain, as follows [18]:

$$\sigma_c = \sum_{1}^{n} E_n \epsilon_c^n \tag{7.4}$$

$$\sigma_z = \sum_{1}^{n} E_n \epsilon_z^n \tag{7.5}$$

where n defines the order of the polynomial – and the corresponding number of material stiffness coefficients E_n – used to define the nonlinear stress-strain relationship of the bladder. Values of E_n can be experimentally defined or, in this case, used as fit-parameters that are defined by an optimization function. This method of model fitting was developed to improve model accuracy by not only better representing the bladder's stiffness, but by also capturing unmodeled physical mechanisms of

the FAM. The multiple degrees-of-freedom that these fit-parameters provide aid in ensuring a good fit of the model to the experimental force response of the FAM.

When used as fit-parameters, the stiffness coefficients (E_n) are design variables that are identified by fitting the model to empirical force-response data of the FAM; E_n values are identified to minimize the error between the model and experimental results. In this work, the built-in MATLAB optimization function *fmincon* is used to determine E_n values that minimize the error between the model output and the average force data from each experimentally obtained response curve. The objective function that the optimizer is tasked with minimizing is a least-squares regression error, defined as:

$$f(x) = \frac{1}{N_P} \sum_{p} \sqrt{\frac{1}{N_i} \sum_{i} \left[(F_{act})_{p,i} + (F_{exp})_{p,i} \right]^2} \tag{7.6}$$

where F_{act} is the model force, F_{exp} is the experimental force, N_p is the number of experimentally tested pressures, and N_i is the number of data points at each tested pressure.

The initial modeling effort by Hocking provided a very good fit of her experimental data by using a fourth-order polynomial stress-strain relationship (E_{1-4}). Unique values of E_n were defined to fit the experimental data at each of the ten tested pressures; material coefficient values were defined at each discrete pressure without any imposed constraints, resulting in a total of forty unique E_n values. This variation with respect to pressure is not representative of the material's intrinsic properties, and also requires assumptions to be made to obtain E_n values at experimentally untested pressures (as needed in control schemes).

The lack of optimization constraints imposed on values of E_n motivated subsequent research. Both Pillsbury (2015) and Robinson (2015) used the same basic form of the model, but with the values of E_n constrained to be defined as a linear function of pressure [20, 34]; while still not representative of the material's intrinsic properties, this approach does reduce the computation required to identify the pressure-dependant E_n values (through interpolation) for use in control schemes. The stress-strain relationship of materials has a true-stress state that increases with increases in strain; this results in a curve that monotonically increases up to a point of failure. Pillsbury (2015) was the first to introduce an additional constraint to the model to ensure that the value(s) of E_n do not violate this inherent stress-strain trend. In his work, this was implemented by requiring all optimized values of E_n to be positive. This constraint makes the model more physically realistic, but is also rather strict. The research presented in this chapter will improve upon this constraint.

The order of the polynomial stress-strain equation required to obtain a good model fit has also previously been investigated. The stress-strain curve of a hyperelastic material typically produces a S-curve which is characteristic of a third-order polynomial (as seen in Chapter 6). To improve the degrees-of-freedom for fitting the model to experimental data, researchers have typically used up to a fifth-order polynomial relationship.

In this research, the model's fit will be investigated using experimental data of the tested 7/8 inch diameter FAM. Geometric dimensional inputs of R, N, θ, t, for all length-states L are obtained from the previously acquired photogrammetric

measurements of the FAM (from Chapter 4). These dimensions account for the actual geometry of the bladder, and use a cylindrical approximation of the braid geometry (required for use in the model). The experimentally obtained bladder stiffness coefficients from Chapter 6 are compared to, and replaced by, the material fit coefficients obtained by the optimization function. The model is then investigated with E_n values that are: a function of pressure; a linear function of pressure; or are fixed with respect to pressure.

7.2.1 Baseline Modeling Results

To pinpoint areas of potential improvement, the model's fit is first tested using the model constraints established by Hocking (2012) and Pillsbury (2015) [18,34]. In both works, a fourth-order stress-strain relationship was used to define the bladder stiffness.

Hocking defined unique values of E_{1-4} for each experimentally tested pressure. Having E_{1-4} values that vary arbitrarily with pressure does not represent the intrinsic fixed stiffness properties of the bladder that are independent of pressure, but does allow them to compensate for unmodeled effects that vary with pressure. The values of E_{1-4} found using the optimization function are also not bound by realistic stress-strain relations of hyperelastic materials; these materials should, at the least, be defined by a monotonically increasing stress-strain relationship. For the 7/8 inch FAM, the model fit achieved by using the model which lacks a stress-strain constraint is shown in Figure 7.2(a). The resulting model fit is very accurate.

Averaged across pressures, the model has a root-mean-square error (RMSE) of only 2.0 lbf, a mean absolute error (MAE) of 2.7 lbf, blocked force error of 16.0 lbf, and a free contraction error of only 0.003 in/in. The values of E_{1-4} identified by the optimization function to produce this model fit are shown in Figure 7.2(b). With the exception of the 10 psi case, many of the E_n values nominally trend as a linear function of pressure; this entails that a linear constraint of E_n with pressure would result in a minimal penalty in model accuracy. The pressure-dependent stress-strain relationship curves produced by these E_{1-4} values, shown in Figure 7.2(c), are tested up to the maximum estimated circumferential bladder strain (ϵ_c) at each respective pressure. Circumferential strain of the bladder is much larger than the maximum magnitude of longitudinal strain, and therefore is the focus of the stress-strain analysis. Many of these curves violate the positive-monotonic stress-strain relationship requirement by having points that have a negative slope. Constraints should be applied to avoid obtaining E_n values that create this condition.

Pillsbury improved the model by defining values of E_n as a linear function of pressure. This constraint aids in interpolating stiffness coefficients for untested pressures. While this results in a model that is slightly more constrained, it still enables the values of E_n to compensate for unmodeled effects of pressure. In an effort to ensure a positive-monotonic stress-strain relationship, the model was constrained to allow only positive values of E_n. The resulting model fit – which uses a fourth-order polynomial fit – is shown in Figure 7.3(a). The resulting model fits fairly well, but exhibits appreciable pressure-dependent error in the resting, mid-contraction, and free contraction length states. Averaged across pressures, the model has a RMSE

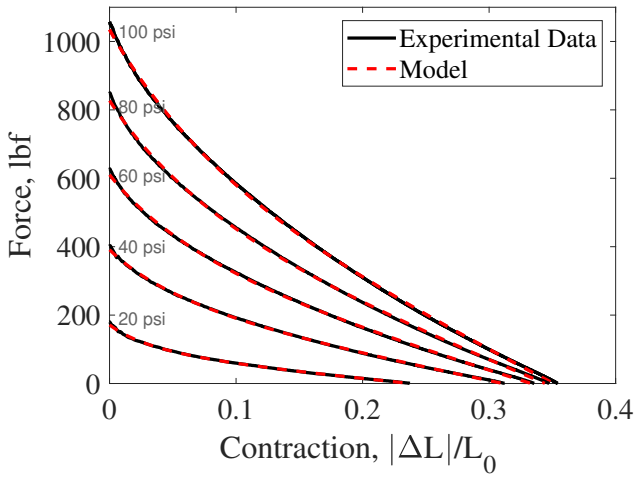

(a) Comparison between model and experimental data (shown at pressure increments of 20 psi for clarity)

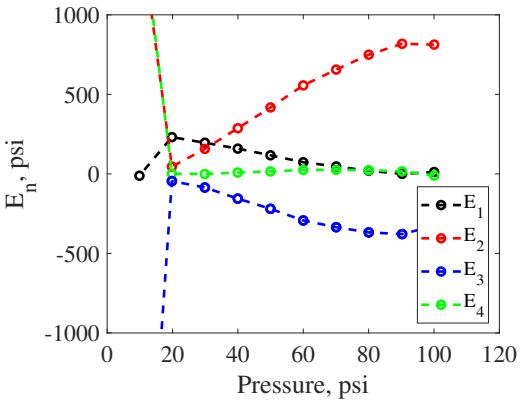

(b) Optimized E_{1-4} values used in the model

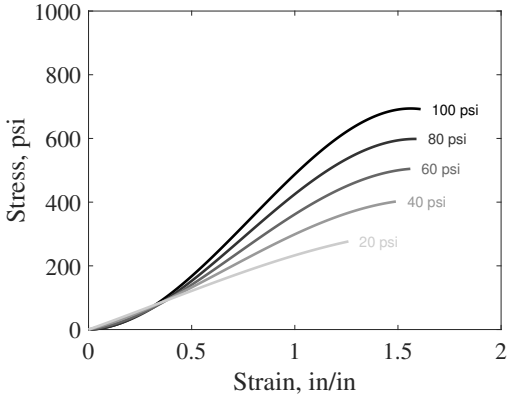

(c) Stress-strain curves using E_{1-4} values

Figure 7.2: Model results (7/8 inch FAM) using the approach of Hocking (2012) to define E_n values. E_{1-4} values are defined with respect to pressure, and without any constraints on their resulting stress-strain relationships.

of 10.3 lbf, MAE of 8.3 lbf, blocked force error of 40.9 lbf, and a free-contraction error of 0.013 in/in. Error increases with increases in pressure in the blocked force state by about 0.8 lbf/psi. The E_{1-4} values used to obtain the model fits are shown in Figure 7.3(b). It is evident that constraining the optimization to allow for only positive values of E_{1-4} severely limited the domain of possible fit values; only the E_1 term was used, while E_{2-4} were effectively inactive. This results in a linear-elastic model

that varies in stiffness with pressure. The constraint on the bladder's stress-strain relationship needs adjustment (as covered in this chapter) to improve the model fit by enabling higher-order terms to be active.

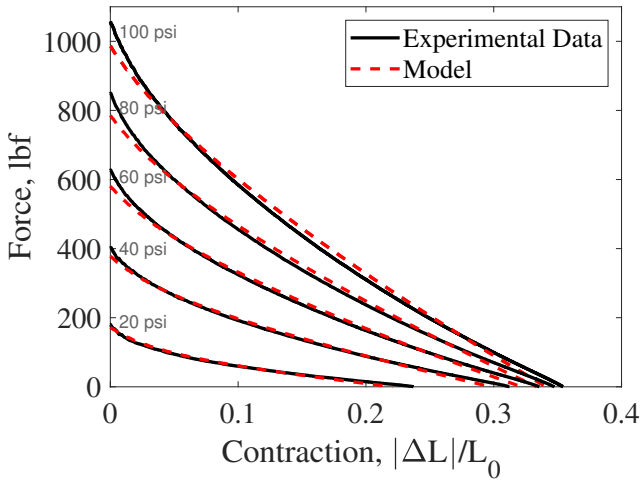

(a) Comparison between model and experimental data (shown at pressure increments of 20 psi for clarity)

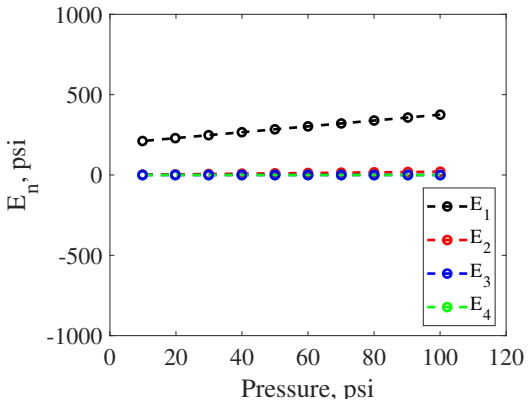

(b) Optimized E_{1-4} values used in the model

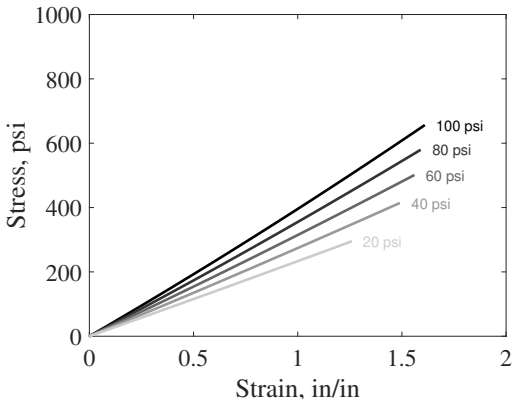

(c) Stress-strain curves using E_{1-4} values

Figure 7.3: Model results (7/8 inch FAM) using the approach of Pillsbury (2015) to define E_n values. E_{1-4} values are constrained to be positive, and as a linear function of pressure.

7.3 Model Improvements

In this section, improvements to the model are made by adjusting the optimization constraints on candidate E_n values. Constraints are imposed on E_n values to ensure that they produce a stress-strain relationship that obeys the constitutive laws of hyperelastic materials. A feasible nonlinear stress-strain relationship should ensure material stability [93]; this means that, in defining a stress-strain relationship, an applied load to the material does not result in an arbitrary deformation state. Material stability can be established by: (1) requiring a stress-strain relationship that monotonically increases with strain (slope > 0); or, (2) satisfying the Drucker Stability criterion.

The fit of the model without constraints will be compared to the model with added constraints (Fig. 7.4). In this section, the optimization function fits the model to the experimental data using a bladder material defined by four stiffness coefficients (fourth-order polynomial), and are defined to vary linearly with pressure. The stiffness coefficients are defined with respect to pressure, in these cases, to enable the degrees of freedom required to obtain a model fit that is sufficiently accurate for comparison of the constraints. Without any constraints imposed on the allowable stress-strain relationship, the model (labeled "Free") provides a good fit of the experimental data, with a low degree of average error in the blocked force state (16.6 lbf) and the free-contraction state (0.003 in/in). The average RMSE and MAE across tested pressures is 3.1 lbf and 2.3 lbf, respectively.

As previously described, Pillsbury (2015) ensured a positive-monotonic stress-

strain relationship of the bladder within the model by constraining the optimization function to allow for only positive values of E_{1-4}. Although that constraint is simple, it is overly strict because it is possible to have some negative E_n values while still obeying one of the stability conditions as stated above. The results of using that constraint on model fit are provided in Figure 7.4 with the label "Pos. E-Vals". Because the optimization function is overconstrained, there is a significant drop-off in model accuracy that is especially visible in the blocked force and free-contraction states; the average respective errors are much higher at 40.9 lbf and 0.013 in/in, respectively. RMSE averaged across pressures is 10.3 lbf, while MAE is 8.3 lbf.

In this work, we first modify the constraint to ensure a positive-monotonic stress-strain relationship (stability condition 1). The developed inequality constraint calculates the differential (i.e. slope) of the polynomial stress-strain equation, and ensures that it is greater than or equal to zero in all strain states ($\epsilon \leq \epsilon_{max}$). This nonlinear constraint is applied to the optimization function, and rejects sets of E_n values that produce a stress-strain curve with a negative slope at any point. The resultant model, shown in Figure 7.4 (labeled "Pos. Slope"), improves the fit of the model in comparison to the previous "Pos. E-Vals." constraint. The average blocked force error is reduced by 14.1 lbf (down to 26.9 lbf error), average free-contraction error is reduced down by 0.007 in/in (down to 0.006 in/in error), overall RMSE is reduced by 5.3 lbf (down to 5.0 lbf error), and the overall MAE is reduced by 4.8 lbf (down to 3.5 lbf error). Distinct regions of error near the blocked force and free-contraction states still remain however.

In an attempt to further reduce the error in the blocked force and free-

contraction states, a third constraint approach is introduced. In this iteration, the constraint was developed in accordance with the Drucker Stability criterion (stability condition 2). This criterion ensures stability by requiring that a material's incremental energy only increases with increases in strain state magnitude, for the developed stress-strain relationship. This is defined through the following equation:

$$d\sigma : d\epsilon \geq 0 \tag{7.7}$$

,where $d\sigma$ is the stress increment tensor associated with the strain increment tensor $d\epsilon$. This condition is identical to the previous slope constraint in the uniaxial strain case. For the case of the FAM bladder, this postulate considers the combined effects of the longitudinal and circumferential stress-strain states together. This has the effect of slightly loosening the constraint in comparison to the previous slope constraint; a slightly negative slope at a point is allowed where the overall internal energy of the bladder still increases. The incremental improvement in model fit afforded by this constraint is visible in Figure 7.4, where it is labeled as "Drucker". In comparison to the slope constraint, the Drucker Stability constraint further reduces the average error in the blocked force state by 12.1 lbf (down to 14.8 lbf error), reduces average free-contraction error by 0.003 in/in (down to 0.003 in/in error), reduces overall RMSE by 1.7 lbf (down to 3.3 lbf error), and reduces overall MAE by 0.9 lbf (down to 2.5 lbf error). At this point, the stress-strain constraint has a minimal effect on model fit, while still ensuring the fidelity of the model.

The effect of each stress-strain constraint on model accuracy is tabulated for the model fit at 100 psi (Table 7.1), and as an average over all tested pressures (Table

7.2). The constraints have the largest effect on the model at higher strains, and therefore, have the most prominent effect on model fit at the highest tested pressure of 100 psi. Figure 7.5 shows the difference between the stress-strain curves using each constraint (at 100 psi). The effect of loosening the stress-strain constraint on the resulting curves is evident: moving from the positive E_n values constraint, to the slope constraint, and then to the Drucker Stability constraint, the curvature of the FAM gradually approaches the curvature of the model that is free from constraints. Overall, the stress-strain constraint is important in ensuring material stability for the developed stress-strain curves, but often does not need to be very active in the optimization.

Table 7.1: Model Error with Respective Stress-Strain Constraints – 100 psi (Experimental Blocked Force: 1058 lbf, Experimental Free-Contraction: 0.354)

	Free	**Pos. E-Vals.**	**Pos. Slope**	**Drucker**
Blocked Force, *lbf*	17.1 (1.6%)	71.4 (6.8%)	43.3 (4.1%)	11.9 (1.1%)
Free-Contr.	0.003 (0.8%)	0.013 (3.7%)	0.010 (2.7%)	0.006 (1.7%)
MAE, *lbf*	3.7	15.6	7.0	4.2
RMSE, *lbf*	4.5	18.7	9.2	5.2

Table 7.2: Model Error with Respective Stress-Strain Constraints – Averaged Across All Pressures

	Free	**Pos. E-Vals.**	**Pos. Slope**	**Drucker**
Blocked Force, *lbf*	16.6 (5.0%)	40.9 (7.9%)	26.9 (5.7%)	14.8 (5.0%)
Free-Contr.	0.003 (1.5%)	0.013 (4.2%)	0.006 (2.8%)	0.003 (1.4%)
MAE, *lbf*	2.3	8.3	3.5	2.5
RMSE, *lbf*	3.1	10.3	5.0	3.3

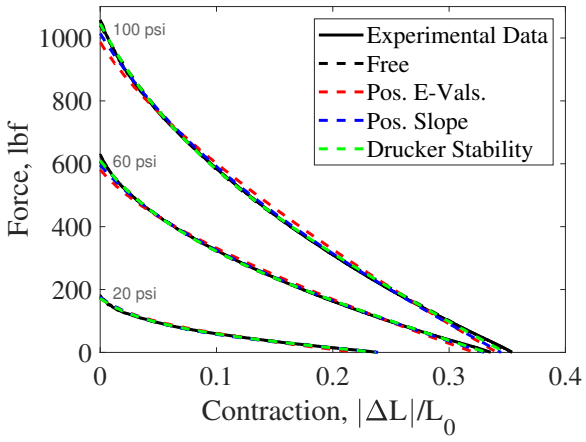

(a) Force Response

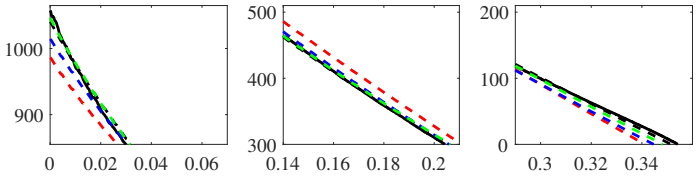

(b) Zoomed-in views of results in subfigure (a) (100 psi test). Regions of focus are near (left) zero-contraction/blocked force, (middle) mid-contraction, and (right) free-contraction

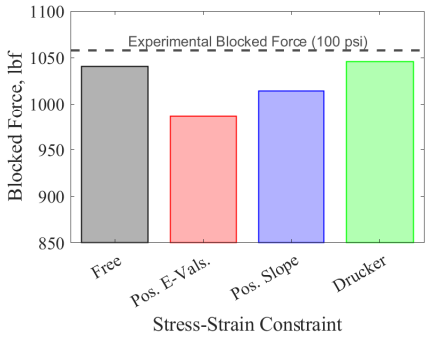

(c) Blocked force results (100 psi)

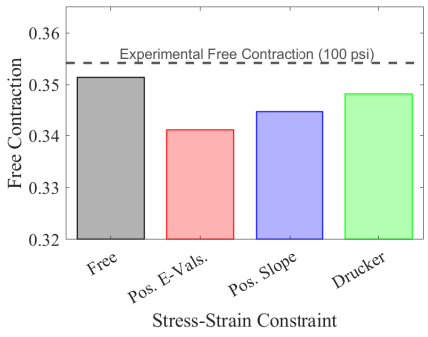

(d) Free-contraction results (100 psi)

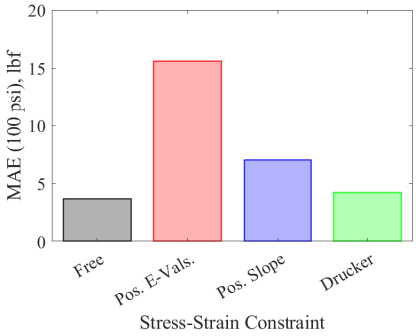

(e) MAE results (100 psi)

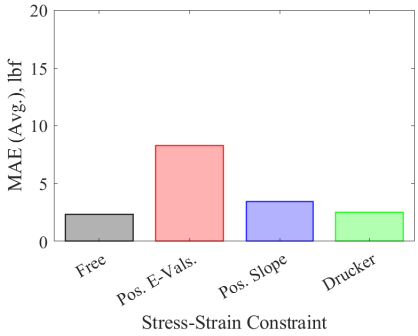

(f) MAE results (avg.)

Figure 7.4: Comparison of model results using different stress-strain constraints

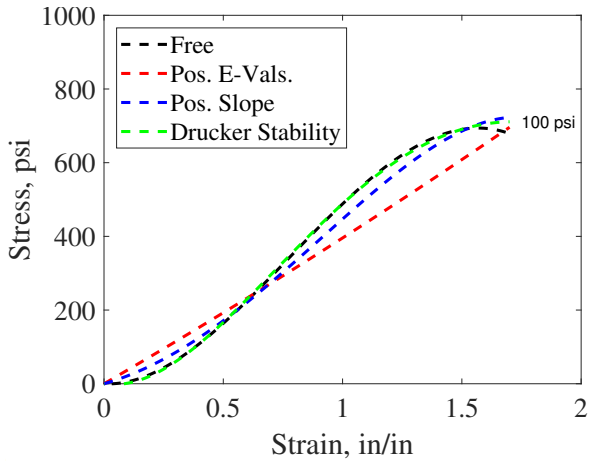

Figure 7.5: Stress-strain curves with the use of the respective constraints for the model at 100 psi (curves vary with pressure)

7.4 Model Results and Analysis

The performance of the updated model is now analyzed. In comparison to the form of the model used in prior studies [18, 20, 34], this model includes the updated Drucker Stability stress-strain constraint and accurate geometry inputs acquired from photogrammetric measurements. The model fit is first tested using E_n values that are constrained to be fixed with respect to pressure; this is the most realistic case, and allows for a direct comparison between the experimental stiffness coefficient values obtained in Chapter 6 and the E_n values obtained using the optimization function. Fixed E_n values result in an unsatisfactory model fit, so subsequent analysis focuses on improvements to the model with E_n values that vary with pressure. The performance of the model fit is analyzed while varying: (1) the number of E_n terms used to define the bladder's stress-strain relationship; and, (2) the relationship of E_n with respect to pressure. The model fit is analyzed using up to four material coefficient terms, with the terms defined as: a free function

of pressure; a linear function of pressure; and fixed with respect to pressure. The model is fit to experimental data acquired for the 7/8 inch diameter, 9 9/32 inch length FAM used in the previous chapters, which was tested at pressures from 10 to 100 psi in 10 psi increments.

7.4.1 Comparison of Experimental and Model Values of E_n

The optimization is first set to define values of E_n that are fixed with respect to pressure. These values are then compared to the experimentally obtained values from Chapter 6. An accurate fit of the model using optimized E_n values, together with correspondence to the experimentally obtained E_n values, would provide assurance of the model's fidelity in its current form.

The optimized and experimental E_n values are compared using a third-order polynomial stress-strain relationship; the respective values are provided in Table 7.3. The two sets of E_n values appear to be very different. To clarify the comparison, the stress-strain curves produced by the two sets of E_n are provided in Figure 7.6(b). The curves are not as different as the E_n values would entail, but they do deviate from one another at strains above 0.75.

Table 7.3: Material Coefficient Values, E_n (Fixed with respect to pressure)

	E_1	E_2	E_3
Experimental Values, *psi*	257.8	-57.9	32.7
Optimized Values, *psi*	131.9	340.7	-146.0

The resulting model fits are compared in Figure 7.6(a). Neither model fit

matches the nonlinearity of the FAM's experimental response very well, especially at higher pressures. Table 7.4 provides a clear comparison of the average error in each model fit. The optimized E_n values provide a slightly better fit than the experimental values. Error of each model also increases with increases in pressure; this observation emphasizes the need for optimal E_n values that vary with pressure to obtain an accurate model fit.

Table 7.4: Average Model Error Using Experimental Versus Optimized E_n Values (E_{1-3} Fixed With Respect to Pressure)

	Experimental Values	**Optimized Values**
Blocked Force, *lbf*	31.1 (7.5%)	18.7 (3.9%)
Free-Contr.	0.008 (4.5%)	0.020 (10.5%)
MAE, *lbf*	25.4	18.1
RMSE, *lbf*	27.7	19.7

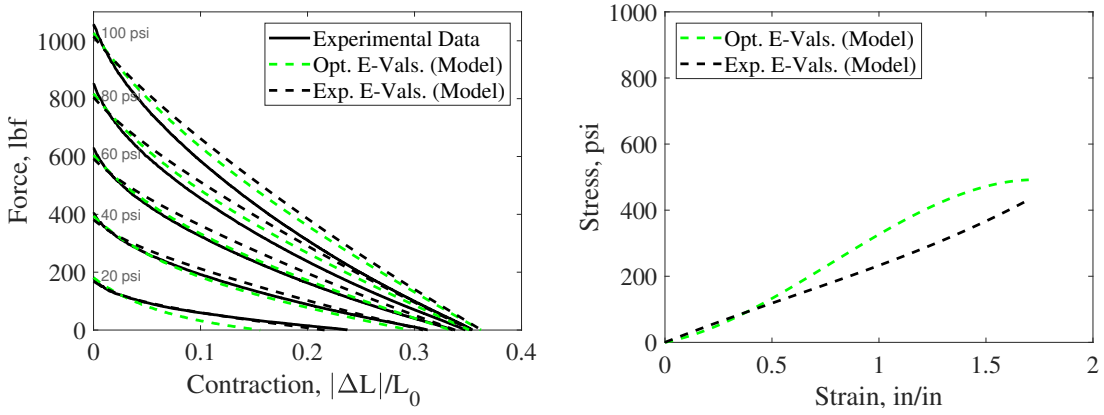

(a) Model comparison to experimental data

(b) Comparison of stress-strain curves

Figure 7.6: Comparison between E_{1-3} values obtained through experimental characterization, and those found through optimization. Values of E_{1-3} are independent of pressure.

7.4.2 Parametric Analysis for Optimal Model Fit

Prior studies have adjusted the bladder's polynomial stress-strain relationship to improve the fidelity and computational ease of the model; both the order of the stress-strain relationship – defined by the number of E_n terms used – and the relationship of the E_n terms with respect to pressure, have been adjusted. Using the updated form of the model developed in this research, different permutations of the material coefficient definitions are analyzed for their effect on the accuracy of the model.

The model is tested using the following polynomial stress-strain relationship definitions: First-order (i.e. linear) (E_1), second-order (E_1, E_2), third-order (E_1, E_2, E_3), and fourth-order (E_1, E_2, E_3, E_4). Each material coefficient value is defined by the optimization function to be: (1) a function of pressure $(f(P))$; (2) a linear function of pressure $(f(P)(linear))$; or, (3) a fixed value that is independent of pressure $(Fixed)$.

Figure 7.7 provides a comparison between the experimental data, and each permutation of the model; the average error over all tested pressures is provided. These results are accompanied by figures that illustrate the change in model fit by varying the number of E_n terms used (Fig. 7.8), and the effect of changing the relationship of E_n with respect to pressure (Fig. 7.9).

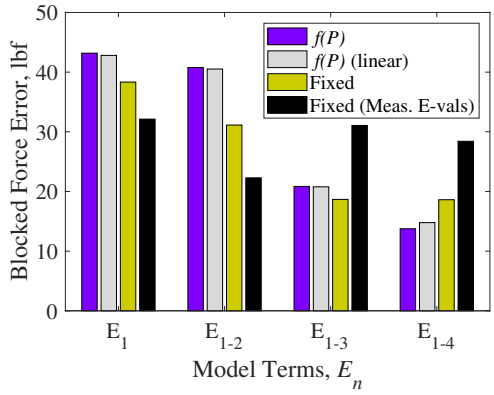

(a) Average force error in blocked force state

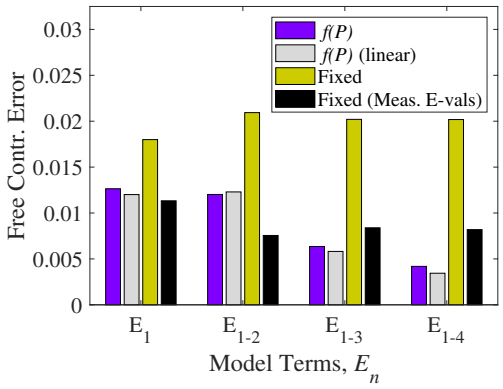

(b) Average error in free-contraction states

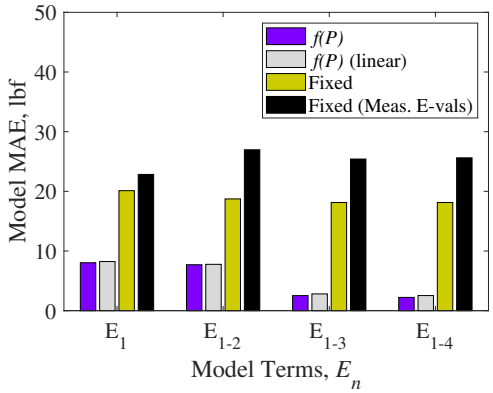

(c) Mean absolute error (MAE) over entire contraction range

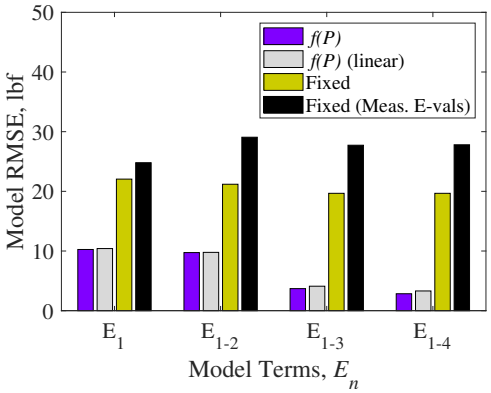

(d) Root-mean-square error (RMSE) over entire contraction range

Figure 7.7: Model fit error – averaged over all tested pressures – for all tested permutations of defining the material coefficients, E_n

7.4.2.1 Effect of Number of E_n Terms Used

Increasing the number of E_n terms generally acts to improve model fit by increasing the degrees of freedom that the optimization function has to fit the model to experimental data. The results in Figure 7.7 show the effects of varying the number of E_n terms. The resultant model fit accuracy is dependent on the freedom of E_n to vary with respect to pressure. Here, increasing the number of E_n terms while also fixing their values with respect to pressure results in a minimal and

inconsistent effect on model accuracy. However, when the E_n terms are allowed to vary with respect to pressure, there is a clear improvement in model fit by increasing the number of E_n terms; a distinct jump in accuracy is observed when a third-order or higher ($n > 2$) stress-strain relationship is used.

Figure 7.8 illustrates the effect that the number of E_n terms has on model accuracy. For this comparison, the values of E_n are defined as a linear function of pressure. The results show a visible step increase in accuracy when $n > 2$, as observed in Figure 7.7; between E_{1-2} and E_{1-3}, there is a 64% decrease in MAE, 49% decrease in blocked force error, and a 53% decrease in free-contraction error. Figure 7.8(c) shows a comparison of the stress-strain curves with variations in E_n terms. Note that multiple pressure-dependent stress-strain curves are produced by defining the E_n terms as a function of pressure. A distinct change in strain-strain curvature is observed when $n > 2$ which coincides with the respective improvement in model accuracy. Also of interest in Figure 7.8(c) is the magnitude that the stress increases with respect to pressure (as allowed by E_n varying with pressure). This provides an indication of how much the model's bladder stiffness term – and respective E_n terms that vary with pressure – are compensating for unmodeled effects of pressure in the FAM's force response. The value of E_1 increases by about 2 psi per each psi increase of internal pressure.

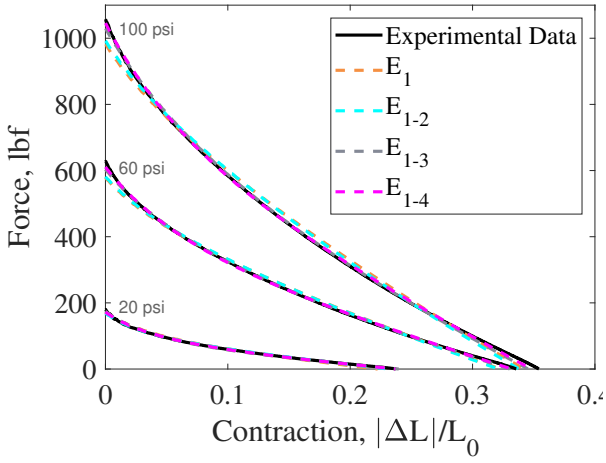

(a) Comparison of model fits and experimental data

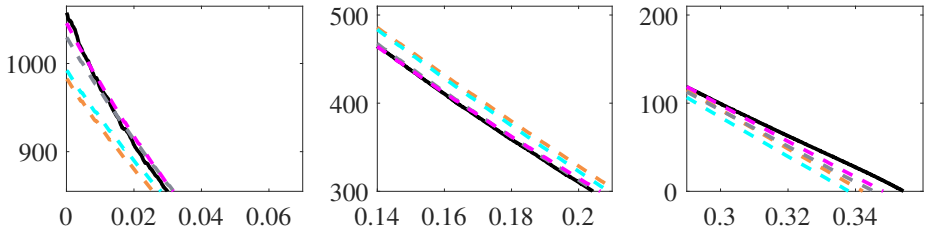

(b) Zoomed-in views of results in subfigure (a) (100 psi test). Regions of focus are near (left) zero-contraction/blocked force, (middle) mid-contraction, and (right) free-contraction

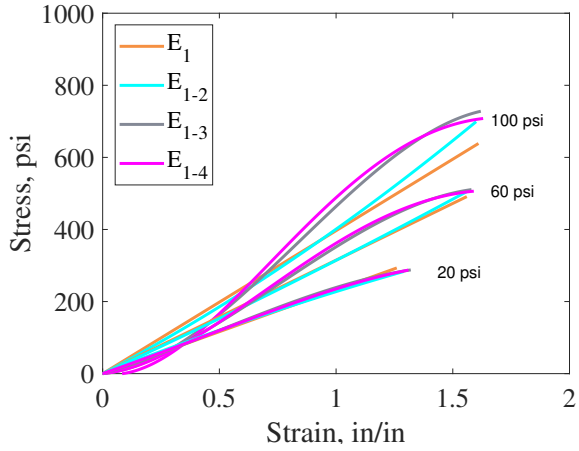

(c) Stress-strain curves produced by optimized E_n values

Figure 7.8: Comparison of model fits with variation in the number of E_n terms used (with respect to pressure)

7.4.2.2 Effect of Variation of E_n with Pressure

As noted earlier, the physical bladder material should not have stiffness properties – and respective E_n values – that vary with respect to pressure. However, unmodeled effects of pressure within the model require the alleviation of this material constraint to obtain an accurate model fit. Allowing the E_n terms to vary with pressure provides a marked improvement in model accuracy; alleviating this constraint reduces the MAE of the model by up to 86% (Figure 7.7). Requiring E_n values to be a linear function of pressure – opposed to being completely free with respect to pressure – carries only a minimal penalty in model accuracy. The concomitant decrease in required computation effort, occasioned by making E_n terms vary linearly with pressure, is likely a worthwhile approach for applications of the model in control schemes. Note that Figure 7.7 indicates that when using E_n values that are fixed with respect to pressure, the effect is the lowest error for the blocked force and free-contraction states; however, these improvements in accuracy are misleading, and are only local to these two length-state regions.

Figure 7.9 presents a direct illustration of the effect of varying the pressure-dependencies of the E_n terms. These model fits use a fourth-order stress-strain relationship (E_{1-4}) while varying the relationship of E_n with respect to pressure. Here, the improvement in accuracy, by allowing E_n values to vary with pressure, is evident. It is interesting to note how the accuracy of the model fit for each case varies with respect to pressure. When E_n values are allowed to vary with respect to pressure, the model fit is very accurate in all pressure states (0.6-4.1 lbf MAE).

Notably, the model that uses the experimentally measured E_n values (fixed with respect to pressure) is also able to provide a very good fit at low pressures (3.5 lbf MAE at 20 psi), but the accuracy of the fit decreases with increases in pressure (58.2 lbf MAE at 100 psi). This observation supports the assertion that the model is missing a pressure-dependent term that, if added, could eliminate the need for E_n to vary with pressure.

7.4.2.3 Best-fit Model Selection

From the parametric study above, a "best fit" form of the model is selected as the final demonstration of the model's accuracy in its current form. This model uses a stress-strain relationship defined by a third-order polynomial, and with fit-coefficient terms (E_{1-3}) that are both constrained to vary linearly with pressure, and constrained to obey the Drucker Stability criterion. Previous analysis showed that the relatively small decreases in modeling error that would come with adding an additional material fit coefficient (0.3 lbf MAE improvement), removing the linear pressure-dependence of the E_n terms (0.3 lbf MAE improvement), and removing any stress-strain stability constraint (0.5 lbf MAE improvement), are likely not worth the additional cost in model complexity, or the departure from accurately representing the intrinsic properties of the bladder material.

A detailed illustration of the resulting model is provided in Figure 7.10. Figure 7.10(a) shows the model fit to the averaged response of each isobaric test. These averaged experimental curves represent the complete set of data that the model

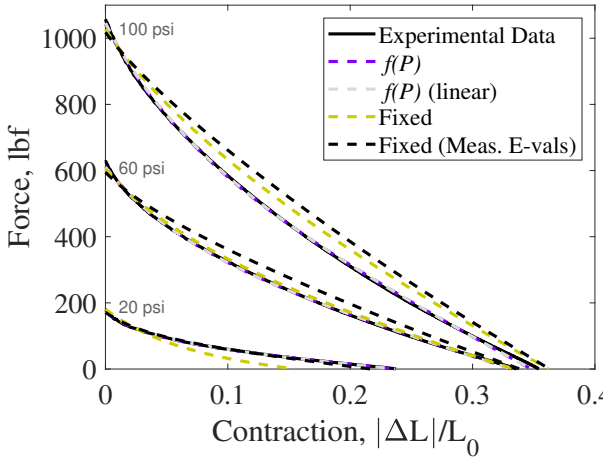

(a) Comparison of model fits and experimental data

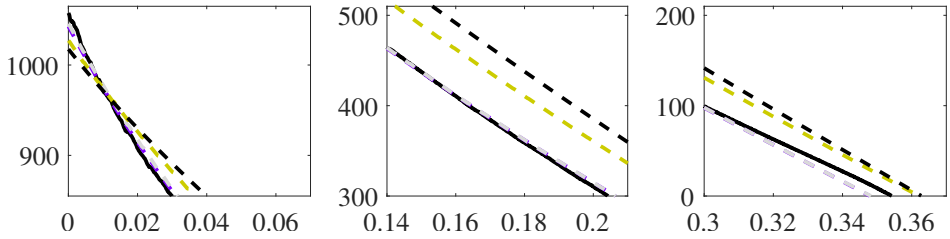

(b) Zoomed-in views of results in subfigure (a) (100 psi test). Regions of focus are near (left) zero-contraction/blocked force, (middle) mid-contraction, and (right) free-contraction

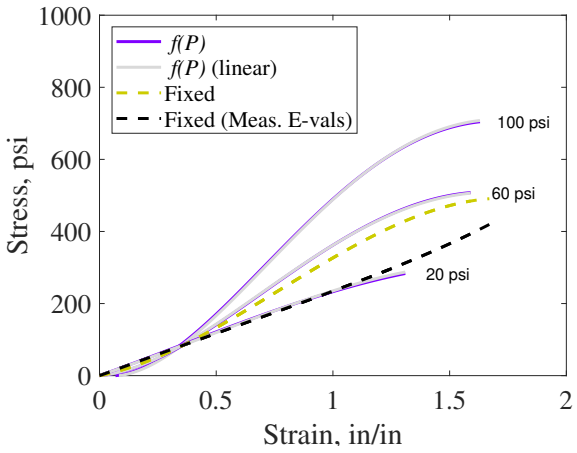

(c) Stress-strain curves produced by optimized E_n values

Figure 7.9: Comparison of model fits with variation in the relationship between E_n and pressure

is fit to, and they provide a more complete depiction of the model's fit (figures are commonly reduced to show curves in only 20 psi increments for visual clarity).

Figure 7.10(b) shows how the model fit compares to the raw experimental data. The model developed in this work can be adapted to take into account the hysteresis of the FAM's response through the use of an additional modeling term, as detailed in Hocking (2012) [18]. Figure 7.10(c) provides a depiction of the optimized values of E_{1-3} that are constrained to vary linearly with pressure; slope and y-intercept values for each of these linear curves are provided in Table 7.5. The pressure-dependent stress-strain relationships produced by values of $E_{1-3}(P)$, and constrained by the Drucker stability criterion, are shown in Figure 7.10(d). Again, note that the same stress-strain relationship is used for the material in both tensile and compressive stress states; however, the compressive strain due to longitudinal stresses ranges up to a maximum of only 0.28 in/in (for 10 to 100 psi, respectively).

A detailed report of the model's accuracy with respect to the experimental data is provided in Table 7.6. Averaged over all pressures, the MAE is low at 2.8 lbf. Average error in the blocked force and free-contraction states is also fairly good, at 20.8 lbf and 0.005 in/in, respectively. The optimization function has the most apparent difficulty in fitting the model near the resting length and maximum contraction states. If further improvements in accuracy are desired in certain regions of the contraction range, the least-squares cost function of the optimizer can be weighted towards these regions at the expense of reduced model fit in other regions.

Table 7.5: Fit Coefficient Values, E_n, For "Best-Fit" Model

$E_n = m_n * P + b_n$	E_1	E_2	E_3
Slope (m_n)	257.8	-57.9	32.7
y-intercept (b_n)**,** psi	131.9	340.7	-146.0

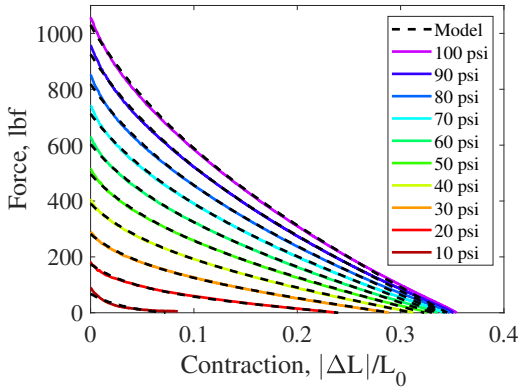

(a) Model comparison to experimental data (averaged for each pressure)

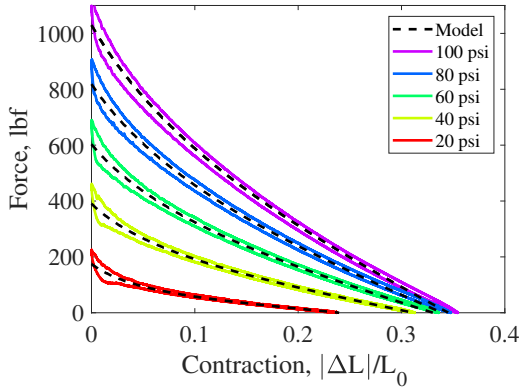

(b) Model comparison to raw experimental data (includes hysteresis in force response)

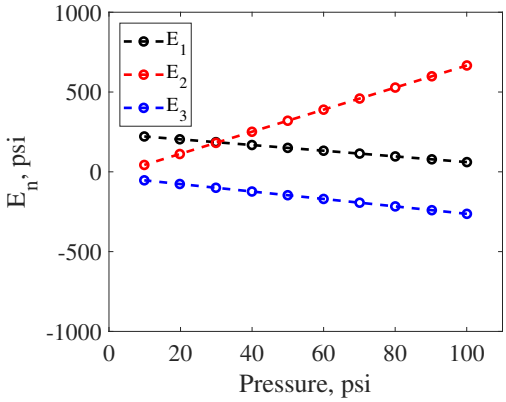

(c) Fit optimized E_{1-3} values used for the model

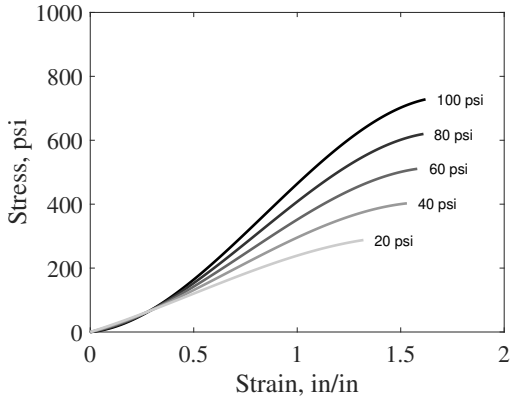

(d) Pressure-dependent stress-strain curves produced by $E_{1-3}(P)$

Figure 7.10: Modeling results for the "best-fit" model, which uses terms E_{1-3} that are constrained to vary linearly with pressure, and constrained to comply with the Drucker stability criterion.

7.5 Conclusion

The research presented in this chapter works to improve the model by better representing the mechanisms of the FAM while also improving the accuracy of the model. Previous chapters in this work have set a foundation for this effort, providing an accurate characterization of the FAM by ensuring true isobars during testing, and then developing a photogrammetric method for acquiring accurate di-

Table 7.6: Error of the "Best-Fit" Model with Respect to Experimental Data for All Tested Pressures

Test Pressure *psi*	**Blocked Force Error** *lbf*, (%)	**Free-Contraction Error** $\mid \Delta L_{max} \mid / L_0$, (%)	**RMSE** *lbf*	**MAE** *lbf*
100	-28.0 (-2.6%)	-0.009 (-2.6%)	7.36	5.58
90	-30.5 (-3.2%)	-0.008 (-2.4%)	6.42	4.24
80	-31.5 (-3.7%)	-0.008 (-2.4%)	5.75	3.65
70	-27.8 (-3.8%)	-0.007 (-2.0%)	4.64	2.82
60	-24.4 (-3.9%)	-0.005 (-1.6%)	3.58	2.08
50	-18.5 (-3.6%)	-0.003 (-1.0%)	2.56	1.68
40	-13.1 (-3.2%)	-0.001 (-0.3%)	1.82	1.26
30	-8.5 (-2.9%)	0.001 (0.5%)	1.43	1.09
20	-5.5 (-3.0%)	0.002 (1.0%)	1.70	1.14
10	-20.1 (-22.8%)	-0.012 (-14.1%)	5.75	4.55
Total Avg.	**-20.8 (-5.3%)**	**0.005 (-2.5%)**	**4.1**	**2.8**

mensional measurements of the FAM. By employing the developed photogrammetric method, accurate dimensional inputs to the model can now replace the previously used cylindrical approximations.

With those previous improvements in-hand, the model was tested here for associated improvements in its accuracy. The results illuminated distinct regions of modeling error near the blocked force and free-contraction states of the FAM. The stress-strain relationship constraint placed on the model's fit-parameters (i.e. E_n values) to ensure material stability – which in its prior form was thought to be over-constraining the model – was investigated for its potential to improve model accuracy. Two approaches were taken to ensure material stability: a constraint that ensures a positive monotonic stress-strain relationship, and a constraint that

ensures Drucker Stability. Replacing the prior constraint with either of these new constraints resulted in a mean reduction in error from 8.3 lbf down to 3.5 lbf, or 2.5 lbf, respectively.

With the optimization function updated to include the accurate dimensional inputs to the model – along with the addition of the Drucker Stability constraint – the overall accuracy of the model fit was then tested. For the first test of potential improvements to the model, E_n values were constrained to be fixed with respect to pressure. These results were then compared to the experimentally obtained E_n values from Chapter 6. While this fixed-value case represents the most physically realistic definition of the bladder's material properties, the resulting fit of the model was not very accurate, with a mean model error of 25.4 lbf using the experimental values, and 18.1 lbf for the optimized values. The inability of the model to match the FAM's response when using fixed material coefficient values demonstrates that unmodeled phenomena still exist, and suggests that the model is not ready to be used in a predictive manner. Values of E_n, and the respective bladder stiffness, must still be allowed to vary with respect to pressure in order to obtain an accurate fit of the model.

With no further model improvements to be made in this study, it was in our best interest to determine how to provide the best performance of the model in its current form. The model was tested for fit while adjusting the number of E_n terms used (polynomial order), and by varying the relationship of the E_n values with respect to pressure. A parametric study was performed to find the combination of parameters that provides the most accurate fit of the model. The number of

E_n terms was varied from one to four terms, and they were allowed to vary as a free function of pressure, as a linear function of pressure, or fixed with respect to pressure. Increasing the number of E_n terms generally improved the fit of the model by providing it with more degrees of freedom; a distinct jump in model fit improvement was observed when more than two E_n terms were used. An accurate fit required the E_n terms to vary with respect to pressure, but only a minimal 0.3 lbf average error penalty came with constraining them to be a linear function of pressure. Finally, a best-fit model was produced which used three E_n terms that were each defined as a linear function of pressure. The resultant model provided an accurate fit with an average error across all pressures of only 2.8 lbf.

So, in its current form, this model is able to provide a very good fit of experimental data, overall. Even though this model still relies on fit-parameters (E_n) that cannot produce a very accurate model fit when they are fixed – as is physically expected of the bladder material – steps were accomplished here in improving the overall fidelity of the model through the use of accurate inputs and constraints. Reliance on pressure-dependent E_n values for an accurate model fit points to an opening for future works to develop an additional pressure-dependent term within the model.

Chapter 8: Conclusion

8.1 Summary of Key Work and Conclusions

In this research, significant contributions were made towards the characterization and modeling of FAMs. A 7/8 inch diameter FAM was developed, and in the process, the design and fabrication methods for making swaged end-fitting FAMs were improved. Experimental characterization data was improved by (1) ensuring accurate control of pressure during testing, and by (2) developing a method of measuring the FAM's shape profile during testing. This characterization data was used to test the accuracy of long-held modeling assumptions – the cylindrical geometry approximation, and the inelastic braid assumption. Subsequent adjustments were made to the actuation force model, and the model was then tested for improvements in its accuracy.

8.1.0.1 FAM Design and Fabrication

A 7/8 inch diameter FAM with a swaged end-fitting design was produced in this work. Through the development of this FAM, a standard method of scaling swaged end-fitting design was developed that considers the desired actuation

characteristics, the compression required in each end-fitting, as well as constraints imposed by the limited availability of component sizing. Difficulties with the safety and consistency of the existing fabrication method led to modifications that resulted in strengthening of the FAM through a 10% increase in braid compression in the end-fittings. The resulting 7/8 inch diameter FAM improved upon the capabilities of previous swaged end-fitting FAMs; with a feed pressure of 100 psi, the new FAM provides a maximum force of 1050 lbf (a 100 lbf increase over previous swaged FAMs), a maximum contraction of 35%, and a safety factor of greater than two. Since the completion of this work, the developed methods have been used in the design and fabrication of additional swaged end-fitting FAMs with diameters of 1.5 inches, 2.25 inches, and a 7/8 inch extensile FAM – the first extensile FAM with swaged end-fittings.

8.1.0.2 Characterization Improvements - Pressure Control

Pressure control systems for air and water working fluids were developed to provide accurate feed-pressures to the FAM during characterization testing. The previous pneumatic system could only control set-pressures within 8 psi. The new pneumatic and hydraulic systems provided average feed-pressure errors of only 0.1 psi for a small scale FAM (3/16 inch dia.), and 0.4 psi for a large scale FAM (7/8 inch dia.). Subsequent analysis of characterization testing results found that inaccuracies in the old pressure control system would result in overestimations of the FAM's maximum force by 5-30%, underestimations of maximum contraction by up

to 3%, and overestimations of hysteresis (resulting in overestimations of the FAM's internal friction). The developed pneumatic pressure control system was used in all of the FAM testing performed (as detailed in the subsequent chapters), to ensure the accuracy of the characterization data used for model development.

The new pressure systems were used to test the quasi-static response of FAMs when driven by working fluids with different compressibilities (e.g. air and water). Nominally identical responses of FAMs with air or water working fluids resulted in a confirmation of the independence of the FAM's quasi-static response to working fluid compressibility. This conclusion elevates the ability to transition between different working fluids for FAM actuation.

8.1.0.3 Characterization Improvements – Profile Measurements

A method for measuring a FAM's shape profile was developed to enable the acquisition of geometric measurements during characterization testing. The photogrammetry-based method was designed to be inexpensive and easy to implement. Photographs are taken during testing at a regular interval, and measurements are then extracted from the images using automated analysis techniques. This measurement system was tested during the characterization of a 7/8 inch diameter FAM. While the FAM was stroked during testing, photographs were taken at the rate of once-per-second to obtain measurements for every 0.04 inches of the FAM's contraction range. The resulting measurements had a 0.004 in/pixel resolution. For analysis of the acquired data, the profile measurements were represented as either an average diameter, or as

a highly-accurate Fourier-series fit of the profile. Initial analysis found evidence of inaccuracies in the cylindrical approximation and inelastic braid assumption, which motivated the work documented in subsequent chapters. A new method of acquiring volume measurements was also presented, which can now replace prior methods that were intrusive to the FAM and required elaborate test setups.

8.1.0.4 Testing the Inelastic Braid Assumption

The inelastic braid assumption, commonly used in the prediction of a FAM's geometric dimensions – was investigated in this chapter. This assumption came into question when measurements of the FAM's shape profile captured a 0.043 inch (4%) increase in braid diameter (in the FAM's resting length state) as feed-pressure was increased from 0 to 100 psi. Upon further investigation, it was estimated that this increase in diameter was a result of the braid's threads stretching by 0.5% (while seemingly minuscule, even small changes in diameter and braid angle can have a magnified effect on actuation force). A Kevlar thread – as used in the FAM's braid – was tensile tested in isolation for comparison to the observed measurements. Agreement between the stress-strain curves obtained from the photographic measurements, the tensile test, and the cited elastic modulus of the Kevlar, confirmed that the observed changes in diameter at fixed length-states were, in fact, due to stretching of the braid. The effect of braid elasticity on the actuation force response of FAMs was then investigated. The effects of the Kevlar's elasticity was found to be greatest in the resting length state, and was estimated to cause a 5% decrease in

force (braid elasticity has typically been accounted for with the common use of the inelastic braid assumption). To test the response of FAMs with softer braid materials (e.g. PET, Nylon), a case study was performed using a braid with a hypothetical stiffness that was closer to that of PET or Nylon (about 10% of Kevlar's stiffness). For these cases, the study estimated a decrease in actuation force of up to 70%, and a fixed-length increase in diameter of up to 30%. This exemplifies the large impact potential that braid elasticity has on the actuation of FAMs, and supports the assertion that there are cases where an inelastic braid should not be assumed.

8.1.0.5 Testing the Cylindrical Approximation

The cylindrical approximation – an assumption used in almost every model of FAMs – was tested in this chapter. First, estimated dimensions provided by the cylindrical approximation were compared to the photographic measurements of the FAM's dimensions. Errors in the estimated dimensions were found to increase as a FAM becomes increasingly less cylindrical in shape with increases in contraction. Estimated geometries overestimated the FAM's diameter by up to 4.7%, and underestimated braid angle by up to 3.3%. These geometric errors of the estimated dimensions resulted in force model estimates that had a mean absolute error of up to 23.8 lbf (for all contraction states at 100 psi) when compared to force estimates found using the measured dimensions. However, when the force model with measured dimensional inputs was compared to the experimental response of the FAM, the model still had appreciable mean absolute errors ranging from 3 lbf (at 20 psi) to

58 lbf (at 100 psi). While improvements were surely made to improving the accuracy of the model by replacing the cylindrical approximation dimensions with measured dimensions, there was still a clear need for further corrections to the model.

8.1.0.6 Analysis of Improved Actuation Model

Further improvements were made to the model to improve its accuracy and fidelity. To improve the model's accuracy, the bladder's material stiffness was defined using fit-coefficients found through least-squares-fit optimization techniques (in place of empirically-based constants), as has been used in previous works. An optimization constraint in previous renditions of the model, used to ensure stability of the bladder's optimized stress-strain curve, was modified in this research in accordance with the Drucker stability criterion. Modification of this constraint improved the fidelity of the model, and was shown to provide a 70% reduction in the model's mean absolute error. The force model now included the following improvements: accurate dimensional inputs (from measurements); removal of the cylindrical approximation from the model's bladder force terms, with partial removal from the Gaylord force term (by using measured dimensions); and, addition of the Drucker stability criterion constraint to ensure the stability of the bladder's optimized material stiffness. To test this new version of the model, the optimized material coefficient values were compared to the empirical material coefficients found in Chapter 6. The optimized model did not provide sufficient accuracy, with a mean absolute error of 18.1 lbf that was only marginally better than the 25.4 lbf mean absolute

error achieved by the model when using the empirically-based material coefficient values. To improve the model's fit, the fit-parameters (i.e. the material coefficient values), were allowed to vary with respect to pressure – as has been allowed in previous FAM modeling work – while the number of material coefficients needed for a good model fit was also identified through a parametric sweep. The selected form of the model used three optimized material coefficients (a third-order stress-strain polynomial relationship), that were each allowed to vary linearly with respect to pressure. This form of the model provided a very accurate fit of experimental data, with a mean absolute error of only 2.8 lbf. The overall final form of the model proved to be very accurate while also improving the representation of the FAM's physical mechanisms within the model. However, the model's continuing reliance on pressure-dependent material coefficient terms, which is not mechanistically accurate, emphasizes the need for further modification of the model to directly account for this pressure dependency.

8.1.1 Contributions to Literature

This dissertation makes a number contributions to fluidic artificial muscle literature. The major contributions of this work are as follows:

1) Developed method for measuring the FAM's geometry: A novel method of accurately measuring a FAM's geometry during its actuation was developed in this research. The method provides geometric measurements of the FAM that were not previously available, and can now be used as an asset in the research and anal-

ysis of FAMs, or in defining design requirements for the implementation of FAMs in robotic mechanisms. The photogrammetry-based measurement method was designed to be easily adopted for future work, with minimal equipment or expertise requirements, and the ability to measure a wide-range of FAM sizes. The measurements were shown to provide very high resolution and accuracy measurements that enable detailed analyses of a FAM's actuation. Many of the findings for this research were enabled by access to this advancement in the measurement of FAMs.

2) Assessment of the inelastic braid assumption: Elasticity of the braid can affect the geometry and actuation force of a FAM. However, the braid is often assumed as being inelastic in FAM models because of the modeling simplifications provided by that assumption, and because its effects are often visually imperceptible, and hence assumed to be inconsequential. The effects of braid elasticity became apparent through analysis of the detailed geometric measurements of a tested FAM. Analysis showed that the effects of braid elasticity, even for very stiff materials such as Kevlar – can affect the actuation force by as much as 5%. Commonly used braids are often more compliant, and could affect actuation by as much as 70%. Overall, the research demonstrated that the braid's elasticity can have a significant effect on a FAM's actuation.

3) Removal of model uncertainty due to the cylindrical approximation: Since the initial inception of the FAM, the cylindrical approximation of the FAM's geometry has been relied upon for simplified dimensional and actuation force estimates. This assumption has long been understood as a source of model error, and could not be quantified due to a lack of dimensional measurement methods.

The photogrammetric measurement method enables a comparison between the measured dimensions, and the estimated cylindrical geometry dimensions. Error in the estimated geometry was found to increase as the FAM becomes increasingly less cylindrical in shape with contraction of the FAM. For a 7/8 inch diameter FAM, the estimated geometry underestimated diameter by as much as 4.7%, and underestimated the Gaylord actuation force by as much as 37%. Due to its method of derivation, the Gaylord force term of the model cannot be completely divorced from the cylindrical approximation, however, the assumption has been completely removed from the bladder force terms of the model. Removal of the cylindrical approximation from FAM models results in a significant reduction in the degree of uncertainty within them.

Additional contributions of this work include:

- Further development of methods for the design and fabrication of swaged end-fitting FAMs
- Highlights the importance of accurate pressure control during characterization testing
- Proof of the FAM's quasi-static force independence from working fluid
- Introduction of a Drucker stability constraint into the force model optimization of material stiffness coefficients

The chart in Figure 8.1 (which is an updated version of 1.11), exhibits the actuation mechanisms within the force model that this dissertation addresses, in

comparison to previous works (column header: Chambers Dissertation, 2021). The updated form of the actuation force model includes terms and dimensional inputs that accurately capture both the elasticity and geometry of the bladder and braid. FAM characterization data that uses accurate pressure control ensures that the model is based on an accurate representation of the FAM. The deadband pressure term was also effectively accounted for by capturing the initial strain of the bladder. The current model does not include a term for friction, however, the model can be easily appended with one of the many friction models developed in previous works.

8.1.2 Future Work

This dissertation serves as a foundation for subsequent research to build upon. A natural extension of this research would include making further improvements to the actuation force model. That would likely involve removing the current pressure-dependency within the bladder's optimized material coefficient terms (that are currently required for a good model fit) through modification of the model's Gaylord force term, and would require further investigation into the FAM's actuation mechanisms. Next steps towards this goal would likely require further improvements in the characterization and fabrication of FAMs, as described below.

In this research, dimensional parameters D, L, N, and B were all accurately defined. However, braid angle (θ) was never directly measured, and had to be assumed as fixed along the length of the FAM. Future research could adapt the photogrammetric measurement method to also capture braid angle measurements

KEY:

●	Included
○	Partially Included
	Not Included
–	Not Specified

Actuation Force Models (Terms/effects included)	Gaylord, 1958	Schulte, 1961	Chou and Hannaford, 1994	Chou and Hannaford, 1996	Tondu, 1997	Klute and Hannaford, 2000	Tsagarakis and Caldwell, 2000	Tondu, 2000	Ferraresi, 2001	Colbrunn, 2001	Davis et al, 2003	Davis and Caldwell, 2006	Kothera, 2009	De Volder, 2011	Solano, 2011	Tiwari, 2012	Tondu, 2012	Hocking, 2012	Meller, 2014	Robinson, 2015	Wang, 2015	Chambers Dissertation, 2021
1) Modeling Approach (F=Force Balance; E=Energy Methods)	–	E/F	E	E	E	E	E	E	F	E	–	–	E/F	E/F	F	E	E	F	E	F	F	F
2) Gaylord Force - Cylindrical Approx.	●	●	●	●	●	●	●	●	●	●	●	–	●	●	●	●	●	●	●	●	●	●
4) Bladder Stiffness		○				●	○		○		–	–	●	○	○		●	●		●	●	●
5) Bladder Geometry												–										●
6) Bladder Thickness												–	●		●			●		●	●	●
7) Bladder Deadband pressure							○					–		●	●			●		●		●
8) Braid Elasticity											○	–	○									●
9) Braid Geometry							○				–	–	○			○	○	○		○		●
10) Friction		○	○	○			○	○				●				●	●	○		○		
11) Pressure Control	–	–	–	–	–	–	–	–	–	–	–	–	–	○	–	○	–	–	–	–	–	●

Figure 8.1: Overview of the FAM's actuation force model development through the following representative literature: Gaylord (1958) [2], Schulte (1961) [3], Chou and Hannaford (1994) [4], Chou and Hannaford (1996) [5], Tondu (1997) [6], Klute and Hannaford (2000) [7], Tsgarakis and Caldwell (2000) [8], Tondu (2000) [9], Ferraresi (2001) [1], Colbrunn (2001) [10], Davis et al. (2003) [11], Davis and Caldwell (2006) [12], Kothera (2009) [13], De Volder (2011) [14], Solano (2011) [15], Tiwari (2012) [16], Tondu (2012) [17], Hocking (2012) [18], Meller (2014) [19], Robinson (2015) [20], Wang (2015) [21]

along the length of the FAM. These measurements would ensure accurate braid angle values for model inputs, but would also enable discretized analysis of the braid's forces along its length; sections of the FAM with distinct diameter-braid angle dimensions could then be analyzed individually and as an interconnected whole.

In the Chapter 4 work, variation in the shape profiles of otherwise identically constructed FAMs was observed. These shape profiles also appeared to transform through time before eventually settling into a consistent shape. It is assumed that this phenomenon is due to the subtle migration of braid threads that occurs until the braid and bladder forces within the FAM equilibrate. Analysis of the FAM's dimensions over repeated cycles could help uncover why this occurs, to what extent it occurs, and how it may effect the actuation force of the FAM.

Finally, the development and analysis of FAMs could be boosted with the ability to better control their actuation characteristics through their construction process. The FAM's characteristics are driven by their braid angle and diameter, but control of these parameters is currently limited by the availability of component sizes through vendors. The inability to directly control braid angle often results in an incoherence between the braid and bladder's sizing that can convolute the FAM's actuation mechanisms and characteristics. Preliminary research at the University of Maryland has investigated a filament-winding fabrication process of FAMs; this process weaves braid fibers directly onto the bladder, with the ability to control the angle of the braid threads. This offers many opportunities, including the ability to: control the actuation characteristics of the FAM; reduce or eliminate actuation (i.e. deadband) pressure by eliminating initial slack in the braid; have accurate knowledge

of braid parameters B, N, D_0, and θ_0 as model inputs; and, select from a wider-range of braid materials for preferred properties. This fabrication method could also allow for the braid to be contained within a bladder mold to produce a single composite component. which would protect the braid from external abrasion, and keep the braids from shifting on the surface of the bladder. The maturation of this fabrication technique could aid in the modeling and analysis of FAMs by reducing the number of complex interactions between the bladder and braid. Investigation of individual actuation mechanisms would benefit from the ability to better control individual aspects of the FAM's construction.

Bibliography

[1] Walter Franco Carlo Ferraresi, W Walter Franco, and A Bertetto. Flexible pneumatic actuators: a comparison between the McKibben and the straight fibres muscles. *J. Rob. Mechatronics*, 13(1):56–63, 2001.

[2] R.H. Gaylord. Fluid actuated motor system and stroking device, July 22 1958. US Patent 2,844,126.

[3] Hal F Schulte, J Raymond Pearson, et al. Characteristics of the braided fluid actuator. Technical report, 1961.

[4] Ching-Ping Chou and Blake Hannaford. Static and dynamic characteristics of McKibben pneumatic artificial muscles. In *Proceedings of the 1994 IEEE international conference on robotics and automation*, pages 281–286. IEEE, 1994.

[5] Ching-Ping Chou and Blake Hannaford. Measurement and modeling of McKibben pneumatic artificial muscles. *IEEE Transactions on robotics and automation*, 12(1):90–102, 1996.

[6] Bertrand Tondu and Pierre Lopez. The McKibben muscle and its use in actuating robot-arms showing similarities with human arm behaviour. *Industrial Robot: An International Journal*, 24(6):432–439, 1997.

[7] Glenn K Klute and Blake Hannaford. Accounting for elastic energy storage in McKibben artificial muscle actuators. *J. Dyn. Sys., Meas., Control*, 122(2):386–388, 2000.

[8] N Tsagarakis and Darwin G Caldwell. Improved modelling and assessment of pneumatic muscle actuators. In *Proceedings 2000 ICRA. Millennium Conference. IEEE International Conference on Robotics and Automation. Symposia Proceedings (Cat. No. 00CH37065)*, volume 4, pages 3641–3646. IEEE, 2000.

[9] Bertrand Tondu and Pierre Lopez. Modeling and control of McKibben artificial muscle robot actuators. *IEEE control systems Magazine*, 20(2):15–38, 2000.

[10] Robb W Colbrunn, Gabriel M Nelson, and Roger D Quinn. Modeling of braided pneumatic actuators for robotic control. In *Proceedings 2001 IEEE/RSJ International Conference on Intelligent Robots and Systems. Expanding the Societal Role of Robotics in the the Next Millennium (Cat. No. 01CH37180)*, volume 4, pages 1964–1970. IEEE, 2001.

[11] Steve Davis, N Tsagarakis, J Canderle, and Darwin G Caldwell. Enhanced modelling and performance in braided pneumatic muscle actuators. *The International Journal of Robotics Research*, 22(3-4):213–227, 2003.

[12] Steve Davis and Darwin G Caldwell. Braid effects on contractile range and friction modeling in pneumatic muscle actuators. *The International Journal of Robotics Research*, 25(4):359–369, 2006.

[13] Curt S Kothera, Mamta Jangid, Jayant Sirohi, and Norman M Wereley. Experimental characterization and static modeling of McKibben actuators. *Journal of Mechanical Design*, 131(9), 2009.

[14] Michaël De Volder, AJM Moers, and Dominiek Reynaerts. Fabrication and control of miniature McKibben actuators. *Sensors and Actuators A: Physical*, 166(1):111–116, 2011.

[15] Belen Solano and Christine Rotinat-Libersa. Compact and lightweight hydraulic actuation system for high performance millimeter scale robotic applications: modeling and experiments. *Journal of Intelligent Material Systems and Structures*, 22(13):1479–1487, 2011.

[16] Rashi Tiwari, Michael A Meller, Karl B Wajcs, Caris Moses, Ismael Reveles, and Ephrahim Garcia. Hydraulic artificial muscles. *Journal of Intelligent Material Systems and Structures*, 23(3):301–312, 2012.

[17] Bertrand Tondu. Modelling of the McKibben artificial muscle: A review. *Journal of Intelligent Material Systems and Structures*, 23(3):225–253, 2012.

[18] Erica G Hocking and Norman M Wereley. Analysis of nonlinear elastic behavior in miniature pneumatic artificial muscles. *Smart Materials and Structures*, 22(1):014016, 2012.

[19] Michael A Meller, Matthew Bryant, and Ephrahim Garcia. Reconsidering the McKibben muscle: Energetics, operating fluid, and bladder material. *Journal of Intelligent Material Systems and Structures*, 25(18):2276–2293, 2014.

[20] Ryan M Robinson, Curt S Kothera, and Norman M Wereley. Quasi-static nonlinear response of pneumatic artificial muscles for both agonistic and antagonistic actuation modes. *Journal of Intelligent Material Systems and Structures*, 26(7):796–809, 2015.

[21] Gang Wang, Norman M Wereley, and Thomas Pillsbury. Non-linear quasi-static model of pneumatic artificial muscle actuators. *Journal of Intelligent Material Systems and Structures*, 26(5):541–553, 2015.

[22] Thomas E Pillsbury, Norman M Wereley, and Qinghua Guan. Comparison of contractile and extensile pneumatic artificial muscles. *Smart Materials and Structures*, 26(9):095034, 2017.

[23] Ryan M Robinson, Curt S Kothera, and Norman M Wereley. Control of a heavy-lift robotic manipulator with pneumatic artificial muscles. In *Actuators*, volume 3, pages 41–65. Multidisciplinary Digital Publishing Institute, 2014.

[24] Thomas Edward Pillsbury. *Soft Robotic Appendages Using Pneumatic Artificial Muscles*. PhD thesis, University of Maryland, College Park, 2018.

[25] Bertrand Tondu and Sergio Diaz Zagal. McKibben artificial muscle can be in accordance with the Hill skeletal muscle model. In *The First IEEE/RAS-EMBS International Conference on Biomedical Robotics and Biomechatronics, 2006. BioRob 2006.*, pages 714–720. IEEE, 2006.

[26] Taro Nakamura, Norihiko Saga, and Kenji Yaegashi. Development of a pneumatic artificial muscle based on biomechanical characteristics. In *IEEE International Conference on Industrial Technology, 2003*, volume 2, pages 729–734. IEEE, 2003.

[27] Mayuko Mori, Koichi Suzumori, Syukushi Seita, Masayuki Takahashi, Takashi Hosoya, and Koji Kusumoto. Development of very high force hydraulic McKibben artificial muscle and its application to shape-adaptable power hand. In *Robotics and Biomimetics (ROBIO), 2009 IEEE International Conference on*, pages 1457–1462. IEEE, 2009.

[28] Jonathan M Chambers, Craig R Carignan, and Norman M Wereley. Powering a lower limb exoskeleton using pneumatic artificial muscles. In *ASME International Mechanical Engineering Congress and Exposition*, volume 50534, page V003T04A051. American Society of Mechanical Engineers, 2016.

[29] Ashby Huber, Fleck. The selection of mechanical actuators based on performance indices. *Proceedings of Royal Society of London. Series A: Mathematical, physical and engineering sciences*, 453(1):2185–2205, 1997.

[30] Darwin G Caldwell, N Tsagarakis, and GA Medrano-Cerda. Bio-mimetic actuators: polymeric pseudo muscular actuators and pneumatic muscle actuators for biological emulation. *Mechatronics*, 10(4-5):499–530, 2000.

[31] Frank Daerden. Conception and realization of pleated pneumatic artificial muscles and their use as compliant actuation elements. *Vrije Universiteit Brussel, Belgium*, 1999.

[32] Michaël De Volder and Dominiek Reynaerts. Pneumatic and hydraulic microactuators: a review. *Journal of Micromechanics and microengineering*, 20(4):043001, 2010.

[33] Michele Focchi, Emanuele Guglielmino, Claudio Semini, Alberto Parmiggiani, Nikos Tsagarakis, Bram Vanderborght, and Darwin G Caldwell. Water/air performance analysis of a fluidic muscle. In *2010 IEEE/RSJ international conference on intelligent robots and systems*, pages 2194–2199. IEEE, 2010.

[34] Thomas E. Pillsbury, Curt S. Kothera, Norman M. Wereley, and David L. Akin. Pneumatically power assisted extra-vehicular activity glove. In *45th International Conference on Environmental Systems*, pages 1–9, 2015.

[35] Sylvie Adams DeLaHunt. Variable recruitment in bundles of miniature pneumatic artificial muscles and space qualified pneumatic artificial muscles. Master's thesis, University of Maryland, Dept. Aerospace Engineering, 2016.

[36] Larry D Peel, James Mejia, Ben Narvaez, Kyle Thompson, and Madhuri Lingala. Development of a simple morphing wing using elastomeric composites as skins and actuators. *Journal of Mechanical Design*, 131(9), 2009.

[37] Benjamin KS Woods, Michael F Gentry, Curt S Kothera, and Norman M Wereley. Fatigue life testing of swaged pneumatic artificial muscles as actuators for aerospace applications. *Journal of intelligent material systems and structures*, 23(3):327–343, 2012.

[38] Benjamin Woods, Edward Bubert, Curt Kothera, Jayant Sirohi, and Norman Wereley. Experimental testing of pneumatic artificial muscles for trailing edge flap actuation. In *48th AIAA/ASME/ASCE/AHS/ASC Structures, Structural Dynamics, and Materials Conference*, page 1718, 2007.

[39] J Marcincin and A Palko. Negative pressure artificial muscle-an unconventional drive of robotic and handling systems. *Translations-VE Riecansky*, 1994.

[40] R.C. Pierce, 1940. US Patent 2,211,478.

[41] Hugh De Haven. Tensioning device for producing a linear pull, September 27 1949. US Patent 2,483,088.

[42] A.H. Morin, 1953. US Patent 2,642,091.

[43] J.L. McKibben. Artificial muscle. *Life* magazine, March 14 1960.

[44] Bridgestone Corporation. Rubbertuators and applications for robots, technical information, 1987.

[45] Bridgestone Corporation and Taicubo Engineering. Soft arm: Advanced painting system unit, technical information., 1993.

[46] Shadow Robot Group. The shadow air muscle. available at http://www.shadow.org.uk, 1994.

[47] Festo. *Fluidic Muscle DMSP Product Catalog*, May 2018.

[48] Thomas E Pillsbury, Curt S Kothera, and Norman M Wereley. Effect of bladder wall thickness on miniature pneumatic artificial muscle performance. *Bioinspiration & biomimetics*, 10(5):055006, 2015.

[49] Bong-Soo Kang, Curt S Kothera, Benjamin KS Woods, and Norman M Wereley. Dynamic modeling of McKibben pneumatic artificial muscles for antagonistic actuation. In *2009 IEEE International Conference on Robotics and Automation*, pages 182–187. IEEE, 2009.

[50] Bertrand Tondu, Vincent Boitier, and Pierre Lopez. Naturally compliant robot-arms actuated by McKibben artificial muscles. In *Proceedings of IEEE International Conference on Systems, Man and Cybernetics*, volume 3, pages 2635–2640. IEEE, 1994.

[51] Benjamin KS Woods, Curt Kothera, and Norman M Wereley. Fluidic artificial muscle actuator and swaging process therefor, November 13 2012. US Patent 8,307,753.

[52] Ryan M Robinson, Curt S Kothera, Benjamin KS Woods, Robert D Vocke III, and Norman M Wereley. High specific power actuators for robotic manipulators. *Journal of intelligent material systems and structures*, 22(13):1501–1511, 2011.

[53] H Dabiryan and MS Johari. Analysis of the tensile behavior of tubular braids using energy method, part i: theoretical analysis. *The Journal of The Textile Institute*, 107(5):553–561, 2016.

[54] Shilpa N Raja, Sandip Basu, Aditya M Limaye, Turner J Anderson, Christina M Hyland, Liwei Lin, A Paul Alivisatos, and Robert O Ritchie. Strain-dependent dynamic mechanical properties of kevlar to failure: Structural correlations and comparisons to other polymers. *Materials Today Communications*, 2:e33–e37, 2015.

[55] WEST SYSTEM. *Technical Data Sheet: 105 Epoxy Resin/206 Slow Hardener*, Oct 2014.

[56] Robert D Vocke III, Curt S Kothera, Anirban Chaudhuri, Benjamin KS Woods, and Norman M Wereley. Design and testing of a high-specific work actuator using miniature pneumatic artificial muscles. *Journal of intelligent material systems and structures*, 23(3):365–378, 2012.

[57] S Davis and Darwin G Caldwell. Biologically inspired damage tolerance in braided pneumatic muscle actuators. *Journal of intelligent material systems and structures*, 23(3):313–325, 2012.

[58] Frank Daerden and Dirk Lefeber. Pneumatic artificial muscles: actuators for robotics and automation. *European journal of mechanical and environmental engineering*, 47(1):11–21, 2002.

[59] Kenneth KK Ku, Robin Bradbeer, Katherine Lam, and Lam Yeung. Exploration for novel uses of air muscles as hydraulic muscles for underwater actuator. In *OCEANS 2008-MTS/IEEE Kobe Techno-Ocean*, pages 1–6. IEEE, 2008.

[60] H Yoshinada, T Yamazaki, T Suwa, T Naruse, and H Ueda. Seawater hydraulic actuator for subsea manipulator. *Proceedings of the ISART*, pages 559–566, 1991.

[61] DeLaHunt S. A., Pillsbury T. E., and Wereley N. M. Variable recruitment in bundles of miniature pneumatic artificial muscles. *Bioinspiration and Biomimetics*, 11(5):056014, 2016.

[62] JF Blackburn, G Reethof, and JL Shearer. Fluid power control. *Cambridge.*, 1960.

[63] Gary W Krutz and Patrick SK Chua. Water hydraulics–theory and applications 2004. In *Workshop on Water Hydraulics, Agricultural Equipment Technology Conference (AETC'04)*, pages 8–10, 2004.

[64] Dongseok Ryu, Kyung-Won Moon, Hyungdo Nam, Yongkwun Lee, Changmook Chun, Sungchul Kang, and Jea-Bok Song. Micro hydraulic system using slim artificial muscles for a wearable haptic glove. In *Intelligent Robots and Systems, 2008. IROS 2008. IEEE/RSJ International Conference on*, pages 3028–3033. IEEE, 2008.

[65] Danial Sangian, Sina Naficy, Geoffrey M Spinks, and Bertrand Tondu. The effect of geometry and material properties on the performance of a small hydraulic McKibben muscle system. *Sensors and Actuators A: Physical*, 234:150–157, 2015.

[66] Peter Beater. *Pneumatic drives*. Springer, 2007.

[67] Benjamin KS Woods, Curt S Kothera, and Norman M Wereley. Wind tunnel testing of a helicopter rotor trailing edge flap actuated via pneumatic artificial muscles. *Journal of Intelligent Material Systems and Structures*, 22(13):1513–1528, 2011.

[68] Wilfried Linder. *Digital photogrammetry*. Springer, 2009.

[69] Thomas Luhmann, Stuart Robson, Stephen Kyle, and Ian Harley. Close range photogrammetry: Principles. *Methods and Applications*, pages 97–130, 2006.

[70] Darrin Cardani. Adventures in hsv space. *Laboratorio de Robótica, Instituto Tecnológico Autónomo de México*, 2001.

[71] Wladyslaw Skarbek, Andreas Koschan, Technischer Bericht, Zur Verofentlichung, et al. Colour image segmentation-a survey. 1994.

[72] Michael W Schwarz, William B Cowan, and John C Beatty. An experimental comparison of rgb, yiq, lab, hsv, and opponent color models. *ACM Transactions on Graphics (TOG)*, 6(2):123–158, 1987.

[73] Alvy Ray Smith. Color gamut transform pairs. *ACM Siggraph Computer Graphics*, 12(3):12–19, 1978.

[74] GN Srinivasan and G Shobha. Segmentation techniques for target recognition. *International Journal of Computers and Communications*, 1(3):313–333, 2007.

[75] PM Nishad. Various colour spaces and colour space conversion. *Journal of Global Research in Computer Science*, 4(1):44–48, 2013.

[76] John Canny. A computational approach to edge detection. *IEEE Transactions on pattern analysis and machine intelligence*, (6):679–698, 1986.

[77] Dongju Liu and Jian Yu. Otsu method and k-means. In *2009 Ninth International Conference on Hybrid Intelligent Systems*, volume 1, pages 344–349. IEEE, 2009.

[78] Nobuyuki Otsu. A threshold selection method from gray-level histograms. *IEEE transactions on systems, man, and cybernetics*, 9(1):62–66, 1979.

[79] P Rajashekar Reddy, V Amarnadh, and Mekala Bhaskar. Evaluation of stopping criterion in contour tracing algorithms. *International Journal of Computer Science and Information Technologies*, 3(3):3888–3894, 2012.

[80] Ratika Pradhan, Shikhar Kumar, Ruchika Agarwal, Mohan P Pradhan, MK Ghose, et al. Contour line tracing algorithm for digital topographic maps. *International Journal of Image Processing (IJIP)*, 4(2):156–163, 2010.

[81] Marc Doumit, Atef Fahim, and Michael Munro. Analytical modeling and experimental validation of the braided pneumatic muscle. *IEEE transactions on robotics*, 25(6):1282–1291, 2009.

[82] Kevlar aramid fiber technical guide, 2017.

[83] Standard Test Method for Tensile Properties of Single Textile Fibers. Standard, American Society for Testing and Materials (ASTM), West Conshohocken, PA, 2000.

[84] E Tapie, VPW Shim, and YB Guo. Influence of weaving on the mechanical response of aramid yarns subjected to high-speed loading. *International Journal of Impact Engineering*, 80:1–12, 2015.

[85] Edited by James E Mark. Polymer data handbook, 1999.

[86] Oon H Yeoh. Some forms of the strain energy function for rubber. *Rubber Chemistry and technology*, 66(5):754–771, 1993.

[87] Johnathan Greenberg Niemczura. On the response of rubbers at high strain rates. 2009.

[88] Erick Ball and Ephrahim Garcia. Effects of bladder geometry in pneumatic artificial muscles. *Journal of Medical Devices*, 10(4), 2016.

[89] Ronald S Rivlin and DW Saunders. Large elastic deformations of isotropic materials vii. experiments on the deformation of rubber. *Philosophical Transactions of the Royal Society of London. Series A, Mathematical and Physical Sciences*, 243(865):251–288, 1951.

[90] Paul Steinmann, Mokarram Hossain, and Gunnar Possart. Hyperelastic models for rubber-like materials: consistent tangent operators and suitability for treloar's data. *Archive of Applied Mechanics*, 82(9):1183–1217, 2012.

[91] Glenn K Klute and Blake Hannaford. Fatigue characteristics of McKibben artificial muscle actuators. In *Proceedings. 1998 IEEE/RSJ International Conference on Intelligent Robots and Systems. Innovations in Theory, Practice and Applications (Cat. No. 98CH36190)*, volume 3, pages 1776–1781. IEEE, 1998.

[92] Julie Diani, Bruno Fayolle, and Pierre Gilormini. A review on the Mullins effect. *European Polymer Journal*, 45(3):601–612, 2009.

[93] Allan F Bower. *Applied mechanics of solids*. CRC press, 2009.